First Principle Investigations of

Bio-oil Hydrodeoxygenation (HDO) over $Ru/TiO_2(110)$

A Dissertation

Presented to

the Faculty of the Department of

Chemical and Biomolecular Engineering

University of Houston

In Partial Fulfillment

of the Requirements for the Degree

Doctor of Philosophy

by

Byeongjin Baek

December 2015

First Principle Investigation of

Bio-oil Hydrodeoxygenation (HDO) over $Ru/TiO_2(110)$

Byeongjin Baek

Approved:

Chair of the Committee
Lars C. Grabow, Assistant Professor
Chemical & Biomolecular Engineering

Committee Members:

Michael P. Harold, Professor
Chemical & Biomolecular Engineering

William Epling, Professor
Chemical & Biomolecular Engineering

Jakoah Brgoch, Assistant Professor,
Chemistry

Istvan Lengyel, Research Fellow,
SABIC Americas

Suresh K. Khator, Associate Dean,
Cullen College of Engineering

Michael P. Harold, Professor and Chair
Chemical & Biomolecular Engineering

Acknowledgments

First and most importantly, I would like to express my special thanks to God. He had a plan ahead of me and made everything possible by giving me strength and courage to do this work. When I was feeling down and in trouble, he raised me up and led to a place where I could take a rest and refresh myself.

During the degree in University of Houston, I have met many great people for which I am gratefully thankful. First, I want to thank my advisor Dr. Lars Grabow. He has been always a great mentor and sometime a brother taking care of me and my family. I have been able to broaden my research backgrounds by learning density functional theory (DFT) calculations and kinetic analysis from him. He has also strengthened me with words of encouragement and guidance, and took the initiative in solving problems. I also would like to thank Dr. Michael Harold, Dr. William Epling, Dr. Jakoah Brgoch, and Dr. Istvan Lengyel for putting their effort and time as my committee member. I have met great experimental colleagues who shared their thoughts and data and advised me with the most valuable feedback, which improved the quality of my theoretical results. They are Ryan C. Nelson, Brian G. Frederick, Rachel N. Austin, and Steven P. Crossley. I appreciate their supports and contributions to my dissertation.

Gratitude is expressed to all my group members including Hieu, Arian, Sashank, Yuying, Quan Do, Quan Vo, Tran, Shengguang. Sharing their experiences smoothened my research progress.

Last but not least, special thanks with all my heart go to my family which includes Youngsil, Jungwha, Jungsook, Jaesik, Byeongsoo, Kangim, and Seongil for their emotional and financial supports. I'd also like to express thanks to Sang and Han-cheon for letting me be part of their family, so living in Houston was full of joy and happiness. Most importantly, I truly thank my loved ones, Soojung and Jaden, for always being there for me with the greatest support and encouragement.

First Principle Investigation of

Bio-oil Hydrodeoxygenation (HDO) over $Ru/TiO_2(110)$

An Abstract

of a

Dissertation

Presented to

the Faculty of the Department of

Chemical and Biomolecular Engineering

University of Houston

In Partial Fulfillment

of the Requirements for the Degree

Doctor of Philosophy

in Chemical Engineering

by

Byeongjin Baek

December 2015

Abstract

Biomass can be converted to bio-oil, which contains hundreds of oxygenated species that are detrimental to its use as transportation fuel. Hydrodeoxygenation (HDO) is a promising technology to reduce the oxygen content of bio-oil and improve its properties. From the many oxygenated compounds in real bio-oils we chose acetaldehyde, phenol, and m-cresol as model compounds to investigate reaction mechanisms and active sites on $Ru/TiO_2(110)$ using density functional theory (DFT).

Acetaldehyde HDO was explored on Ru(0001), $RuTiO_2(110)$, 1 ML $RuO_2/TiO_2(110)$, $RuO_2(110)$, $TiO_2(110)$, and $Ru_{10}/TiO_2(110)$. HDO of the phenolic compounds, phenol and m-cresol, was investigated on Ru(0001), $TiO_2(110)$, and $Ru_{10}/TiO_2(110)$. Our overall findings suggest that vacancy sites on $TiO_2(110)$ have high selectivity for the desired C-O bond cleavages steps, but the formation of vacancy sites is limited by hydrogen activation. In contrast, the metallic Ru(0001) surface activates hydrogen easily, but leads to undesired decarbonylation reactions for acetaldehyde and ring hydrogenation reactions for phenolic compounds.

Our simulations show that the active site responsible for the desired direct C-O scission reaction is the Ru/TiO_2 interface, which is supported by experimental evidence showing a linear relationship between the rate of m-cresol HDO and the perimeter of Ru clusters supported on TiO_2. Furthermore, we have proposed a proton-assisted direct deoxygenation for phenol HDO, which is well agreement with isotopic labeling experiments performed by our collaborators. Finally, we hypothesize that the amphoteric nature of the metal-oxide support, i.e., its ability to accept and donate protons, is the key characteristic of an efficient HDO catalyst. The proton is provided through heterolytic bond cleavage across the Ru/TiO_2 interface and subsequently assists in the C-O bond cleavage step in alcohols.

Table of Contents

List of Figures

List of Tables

Chapter 1. Introduction

1.1. Future Feedstock: Biomass

Ever since crude oil has been discovered in the 19th century, this cheap liquid fuel source has rapidly boosted industrialization and has improved our quality of living. However, over the past decades, the rapid growth of the world's population and the increased demand for petroleum by new emerging technologies raise concerns such as declining petroleum resources and environmental issues. Hence, it is imperative to develop eco-friendly processes for sustainable fuel production[1]. In this respect, a significant amount of research is being carried out to replace fossil fuels with alternative energy sources, which require not only compatibility with current infrastructure, but also sustainability to reduce greenhouse gas (e.g. CH_4, CO, CO_2) emissions. To this end, bio-oils derived from biomass are at the center of attention for the development of alternative energy sources, because it is the only currently sustainable energy sources of organic carbon with a friendlier carbon balance than that of current fossil fuels. The generated greenhouse gases could be offset completely, if an efficient process for bio-fuels production were developed as seen in Figure 1-1 in which CO_2, H_2O, and light are used for bio-fuels production, and energy and edible biomass are produced as their outputs[2].

The U.S Department of Agriculture (USDA) and Oak Ridge National Laboratory (ORNL) estimated that sustainable biomass resources in the U.S could be 1.3×10^9 metric tons of dry biomass per year, which include 72 % of agricultural and 28 % of forest resources[3]. These amounts of biomass correspond to the amount of energy of ca. 3.8×10^9 boe (barrels of oil energy), which is almost half of the total energy consumption of the U.S per year ($\approx 7.0 \times 10^9$ boe). The estimated worldwide raw biomass energy in 2050 will reach approximately 79.0×10^9 boe[3]. The Billion-Ton Study (BTS) funded by the U.S Department of Energy (DOE) predicted that the annual biomass produced in the U.S can replace 30 % of the U.S petroleum with bio-fuels and 25 % of chemicals with renewable bio-chemicals and set them as targets by 2025.

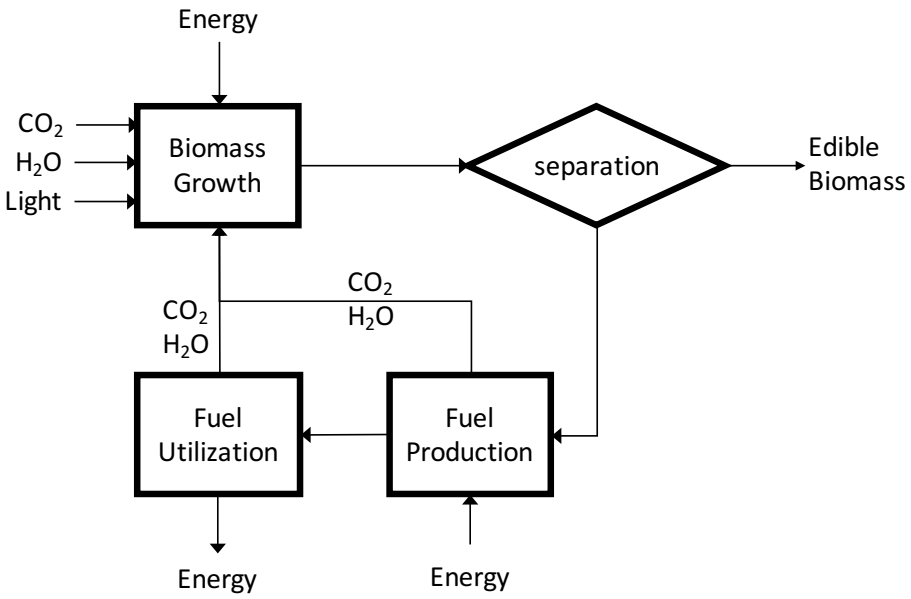

Figure 1-1. Energy efficient process for bio-fuels production from biomass.

1.2. Biomass Conversion

First generation bio-fuels such as bio-ethanol and biodiesel generally refer to fuels that have been produced from sugar, corn, vegetable oil, animal fats, and starch[1]. They are typically produced via processes called esterification and fermentation[1]. However, due to the fact that these bio-fuels are mainly from food grade biomass, they face strong criticism and poor acceptance give the lack of food in many areas of the world.

Consequently, the main focus for the second generation bio-fuels is aimed at using feedstock derived from agricultural wastes, wood, black liquor, forest wastes, etc[1]. Typical strategies for the production bio-oil from these second generation of bio-fuels are summarized in Figure 1-2, and can be mainly classified as gasification, pyrolysis and liquefaction, and hydrolysis[3].

Gasification is one of the oldest technology which converts solid biomass into syngas (CO, H_2, and CH_4) under high temperature (> 700 ℃). Syngas is currently used for the production of valuable chemicals and fuels via water-gas shift (WGS), Fischer-Tropsch Synthesis (FTS), and methanol synthesis. Chemicals and fuels being produced from synthesis gas include hydrogen, methanol, dimethyl ether, olefins, gasoline, and formaldehyde[4].

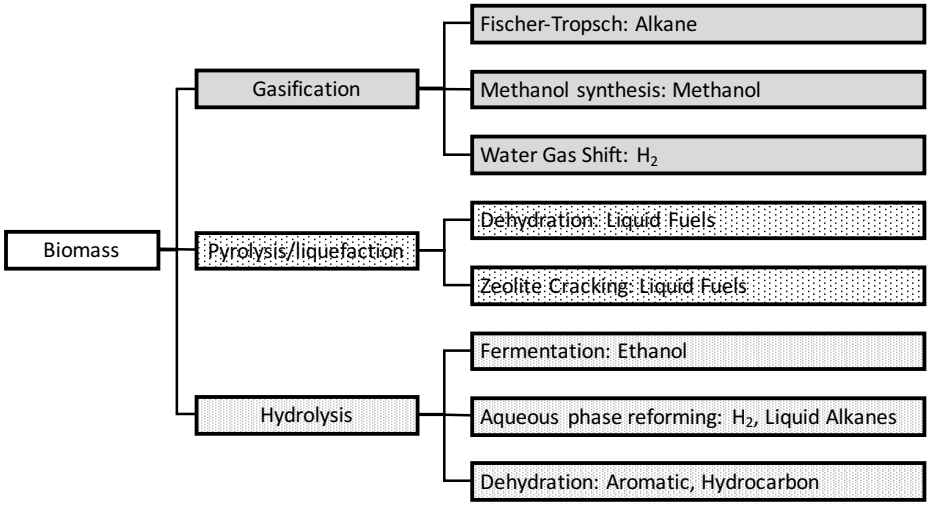

Figure 1-2. Different strategies for the conversion of biomass into valuable chemicals and bio-fuels.

Pyrolysis and liquefaction are processes that are able to convert solid biomass into liquid form of bio-oils under short residence time (0.5 ~ 2 sec) and fast heating rates in the absence of oxygen at T = 250 ~ 500 ℃. Generally, pyrolysis oils contain more oxygen than liquefaction oils, but requires less energy than liquefaction due to the fact that pyrolysis is carried out under much lower pressure condition than liquefaction. Therefore, pyrolysis is more common in current biomass conversion technologies than the liquefaction process. These two processes commonly require one single reactor and can convert solid biomass into ca. 50 ~ 90 % of liquid bio-oils, but its composition depends on initial feedstock, residence time, heating rate, and temperature [1,3]. The liquid bio-oils have low heating values, are viscous and incompatible with fossil fuels. These problems are caused by the presence of more than ca. 400 different oxygenated organic or inorganic compounds including dominantly water (10 ~ 30 wt%), acids, alcohols, aldehydes, esters, ketones, char, furan, and aromatic compounds[5]. Milne *et al.* analyzed the composition of bio-oils (see Figure 1-3) and reported that the dominant components of bio-oils have acid and aldehyde functional groups[3]. The existence of these multiple components in bio-oils is resulted from the depolymerization and fragmentation of cellulose, hemicellulose, and lignin in lignocellulose.

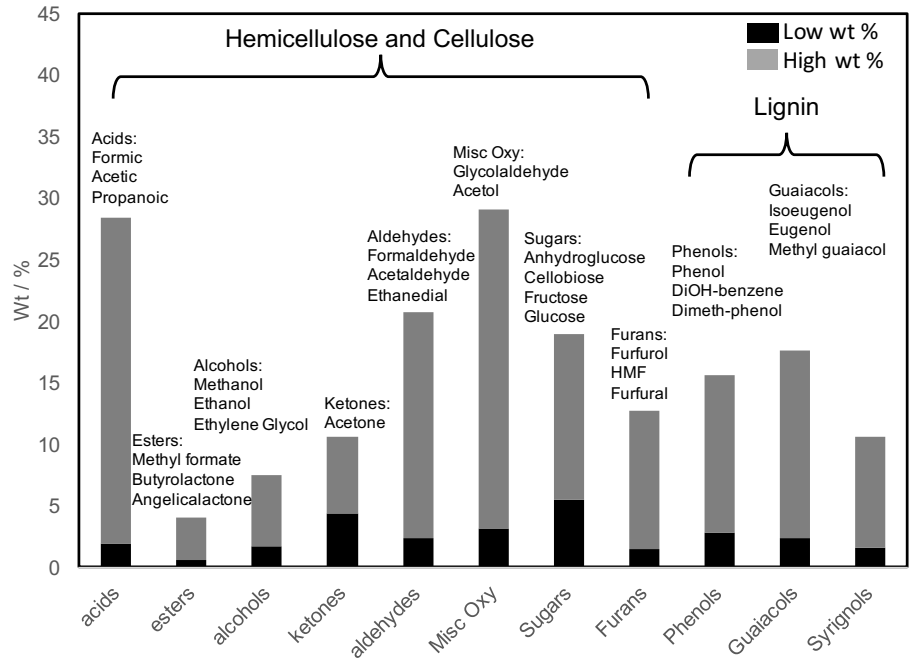

Figure 1-3. Composition of bio-oils after pyrolysis of lignocellulosic biomass.

Hydrolysis is related to an enzyme and acid catalysis for cellulose conversion into sugar monomer units[1]. Enzymes known as cellulase are able to catalyze the depolymerization of cellulose with a conversion of 100 % at 50 ℃, but such process takes generally hours or days. The formed aqueous sugar is further processed by fermentation, dehydration, and aqueous-phase processing to produce ethanol, and olefins, and gasoline.

1.3. Catalytic Bio-oil Upgrading to Oxygen-free Compounds

Among many different biomass conversion strategies summarized in Figure 1-2, fast pyrolysis is technologically and economically favorable, because it results in high liquids yields up to 50 ~ 90 % in short residence time (0.5 ~ 2 sec) and increases the energy density via partial deoxygenation. Yet, bio-oil derived from such fast pyrolysis of biomass is still far from being commercially useful because of difficulties related to its transportation to local refineries, complexity, and instability[1]. Jones *et al.* proposed that biomass transportation costs can be minimized by building decentralized small plants near natural biomass sources to facilitate the supply of bio-oil to bio-refineries[6]. Hence, a key for the success of bio-oil commercialization would be the development of a method to produce high quality and stable bio-oils. One of the main

challenge for this development is associated with the difficulties of oxygen removal from the 300 ~ 400 different oxygenated compounds, which lead to undesirable properties such as high viscosity, chemical instability, immiscibility with petroleum fuels, and low energy density[1]. The high contents of water and oxygenated compounds render bio-oil a polar in nature, making it immiscible with crude oils; its acidic character causes corrosion issues for equipment, pipe lines, and machinery. During the storage of bio-oils, the highly reactive species like aldehydes, acids, and ketones react with each other leading to repolymerization, which ultimately prompts phase separation over time.

Table 1-1. Examples of catalytic bio-oils upgrading processes: (a) cracking, (b) decarbonylation (DCN), (c) decarboxylation (DCX), (d) hydrocracking, (e) hydrodeoxygenation (HDO), and (f) hydrogenation (HYD).

no.	Reaction
(a) Cracking	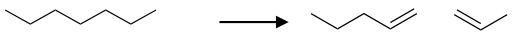
(b) Decarbonylation	 → R-H + CO
(c) Decarboxylation	 → R-H + CO_2
(d) Hydrocracking	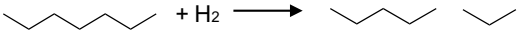
(e) Hydrodeoxygenation	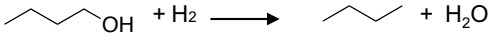
(f) Hydrogenation	

Because of these challenges, substantial amounts of research are currently being aimed toward the catalytic bio-oil upgrading processes with the purpose of catalytic removal of oxygen from bio-oils. In fact, such catalysis is complicated due to the variety of organic compounds in bio-oil and the broad range of potential reactions. Thus, a good catalyst for bio-oil upgrading process has to work in difficult, complex environments and fulfills multiple functions at a time. Examples of processes that can possibly occur during bio-oil upgrading are cracking, hydrocracking, hydrodeoxygenation (HDO), decarboxylation (DCX), decarbonylation(DCN), and hydrogenation (HYD) as given in Table 1-1. The selectivity between HDO versus HYD/DCN/DCX depends primarily on the catalyst's tendency for preferentially breaking C-O or C-C bonds or forming C-H

bond in oxygenated molecules. For the production of liquid fuels from bio-oil it is clearly desirable to maintain the carbon content of the reactant species to maintain the heating value and only break C-O bonds via the HDO reaction. In addition, for the production of valuable chemicals, it is useful to have unsaturated hydrocarbons that can be easily transformed into more valuable chemicals with less H_2 consumption. Therefore, common criteria for the best bio-oil upgrading catalyst are whether they can maintain the carbon contents in the product and use minimal amounts of H_2.

The removal of oxygen from bio-oil is largely classified into two groups (see Table 1-1): (1) DCN and DCX: oxygen atoms are removed in form of CO and CO_2, respectively, and (2) HDO: an oxygen atom is selectively removed in form of H_2O. The difference between these two groups is whether the number of carbon remains the same before and after the reaction. Table 1-2 presents the list of catalysts tested for bio-oil upgrading processes[1]. Common choices are promoted sulfides ($CoMoS_2$ and $NiMoS_2$), precious metals (Pt, Pd, Ru, and Rh), and zeolites (HZSM-5 and SAPO)[7]. Other examples for single model compounds include HDO of aliphatic ester on $NiMoS_2$[8], HDO of guaiacol on transition metal phosphide[9], HDO of furan on MoS_2[10], and glycerol conversion over zeolites such as ZSM-5 and SAPO-11[7,11,12].

Table 1-2. List of catalysts investigated for bio-oil upgrading process.

Catalyst	Time / h	P / bar	T / ℃	[a]DOD / %	O/C	H/C	[b]Y_{oil} / wt%
$CoMoS_2/Al_2O_3$	4	200	350	81	0.8	1.3	26
$NiMoS_2/Al_2O_3$	4	200	350	74	0.1	1.5	28
Pd/C	4	200	350	85	0.7	1.6	65
$Pt/Al_2O_3/SiO_2$	0.5	85	400	45	-	-	81
Ru/Al_2O_3	4	200	350	78	0.4	1.2	36
Ru/C	4	230	350-400	73	0.1	1.5	38
Ru/TiO_2	4	200	350-400	77	1	1.7	67
HZSM-5	0.32	1	380	50	0.2	1.2	24
SAPO-11	0.28	1	370	-	-	-	20

[a]Degree of deoxygenation $= (1 - \frac{wt\%\ of\ oxygen\ in\ product}{wt\%\ of\ oxygen\ in\ feed}) \times 100$. [b]Oil yield: $(Y_{oil}) = (\frac{m_{oil}}{m_{feed}}) \times 100$

The prevalent problems for the listed catalysts is deactivation caused by poisoning with nitrogen or water, sintering of active sites, metal deposition, and coking[1,13,14]. Although the extent

of these problems depends on the catalyst and reaction conditions, coking by carbon formation remains a central issue for the catalytic bio-oil upgrading. Carbon is mainly formed via polymerization and polycondensation and covers the active sites of the catalyst, consequently decreasing catalytic activity. Because of rapid carbon formation during HDO, catalyst lifetimes of more than 200 hours have not yet been achieved with the catalysts listed in Table 1-2. Another pronounced problem when using sulfide catalysts is sulfur stripping, which adds sulfur contamination to the final product and also leads to deactivation[15].

In the literatures it has been suggested that the existing oxygen functionalities in bio-oil can be used to make stable intermediates with longer hydrocarbon chains. This advantageously improves the quality of the resulting fuel and simultaneously eliminates existing oxygen without any additional hydrogen requirements before hydrotreatment[16,17]. One such example is the ketonization reaction between two carboxylic acids on reducible oxide catalysts, in which a total of three oxygen atoms are eliminated as CO_2 and H_2O. In the subsequent HDO step, only one oxygen atom is needed to be removed from the ketone group via hydrotreating to convert the ketone into an oxygen free compound. For the purpose of stabilization at an early stage, mild hydrotreating processes have been suggested to transform bio-oil into a product that is suitable for incorporation into existing petrochemical refineries[18–20]. During this mild hydrotreating, the most active species, such as aldehyde functionalities, are converted to the stable alcohol functional group.

1.4. Investigation of Bio-oil Upgrade using Computation

Over the past decades, state-of-art computational techniques have been successfully applied to many heterogeneously catalyzed reactions of small molecules, such as CO / NO oxidation, ammonia synthesis[21,22], and methanol synthesis[23], but the applications to biomass derived molecules were confronted with big challenges caused by the plethora of reaction pathways, the sheer size of biomass molecules, and the presence of solvents. Even to date, there are relatively few theoretical studies related to catalytic bio-oil upgrade. The examples are propanoic acid on Pd(111)[24], furfural conversion to furan on Pd(111)[25], guaiacol HDO on Ru(0001)[15], phenolate

HDO on Ru(10 $\bar{1}$ 5)[26] and a mechanistic deoxygenation study on Ni-promoted MoS_2 bulk catalysts[27]. Recent progress in density functional theory (DFT) calculation and rapid increases in computational capabilities have enabled us to study catalytic bio-oil upgrade at the atomic-scale using computational screening approaches[28] and microkicetic modeling (MKM)[15]. These methods can be applied to small oxygenated molecules (e.g. acetaldehyde, propanal)[29,30] up to relatively big oxygenated molecules (e.g. guaiacol, phenol, and m-cresol) [15, 32]. This results from these model studies can then be extrapolated for the design of a novel catalysts for bio-oil upgrade.

1.5. Electronic Structure Theory

This section gives a brief summary of electronic structure calculations. We have used periodic density functional theory (DFT), which has become the state-of-the-art predictive tool for diverse materials modeling in chemistry, physics, materials science, and chemical engineering[33]. This is easily illustrated by performing a keyword search on the "Science Citation Index" for papers with the word "Density Functional Theory". The citation index has increased by more than 100 times in 2015 compared to 1996[34]. This significant increase of DFT simulations in many areas of science and engineering is due to the fact that it can give us reasonable accuracy and predictive capability with acceptable computational requirements that are much less demanding than other simulation methods[35]. One of the main areas of interest in the recent literature are electronic structure calculations of solid-state systems that are relevant for heterogeneous catalysis and rational catalyst design. Readers who are interested in more detailed information about DFT are referred to read well-organized books and reviews[36].

1.5.1. The Schrödinger Equation

The time-independent Schrödinger equation, which contains all quantum mechanical properties such as energy and position of nuclei and electrons of a system, is given by

$$\hat{H}\Psi = E\Psi, \tag{1-1}$$

where $\hat{H}$ is the Hamiltonian operator, Ψ is the many-particle wave function, and E is the total energy of the quantum mechanical system. The wavefunction $\Psi=\Psi(r_1,r_2,\ldots r_N)$ contains all information with respect to the internal degrees of freedom. Eq. (1-1) can be simplified by the Born-Oppenheimer approximation based on the large mass difference between the nuclei and electrons[37], i.e., each proton or neutron in a nucleus are 1800 times heavier than the mass of an electron. Hence, electrons are much more sensitive to changes in their surroundings than nuclei. As a result, we can solve Eq. (1-1) assuming fixed positions of the nuclei and only describe the electrons' motion in the external potential determined by the positively charged nuclei. In other words, the degrees of freedom of the electrons can be decoupled from that of the nuclei. The approximated result for the Hamiltonian operator is then given by

$$\hat{H} = -\frac{1}{2}\sum_{i=1}^{N}\nabla_i^2 + \sum_{i=1}^{N}\sum_{J>i}^{N}\frac{1}{|r_j-r_i|} + \sum_{i=1}^{N}\sum_{i=1}^{N}\frac{Z_a}{|r_i-R_a|}, \quad (1\text{-}2)$$

where R is the position of the nuclei, r is the position of the electrons, and Z is the charge of the nuclei, respectively. Using the shorter form of notation, Eq. **Error! Reference source not found.** can be simplified as

$$\hat{H} = \hat{T} + \hat{V}_{ee} + \hat{V}_{ext}, \quad (1\text{-}3)$$

where first term, $\hat{T}$, is a kinetic energy of the electrons, the second term, $\hat{V}_{ee}$, is the repulsive interaction between the electrons, and the third term, $\hat{V}_{ext}$, is a attractive interaction between the fixed nuclei and the electrons, which can be conceptually interpreted as the interaction with an external potential caused by the fixed nuclei.

1.5.2. Density Functional Theory

DFT relies on two basic theorems proven by Kohn and Hohenberg that were further developed by Kohn and Sham in the 1960s. The idea behind DFT is that the electronic energy of a system can be written in terms of the electron density, $\rho_{(r)}$, which reduces the problem of 3N degrees of freedom to 3 degrees of freedom, but contains the same energetic information as the full wave function of Eq. (1-1).

1.5.3. The Hohenberg-Kohn Theorem

The first Hohenberg-Kohn theorem states, “The ground state energy from Schrödinger’s equation is a unique functional of the electron density”. Hence, it is possible to calculate the ground state energy corresponding to the ground state wave function, if the ground state electron density is known. The ground state energy can then be expressed as E[$\rho_{(r)}$], which is important because it allows Eq. (1-1) to be solved using only three spatial variables of the electron density rather than solving it with 3N degrees of freedom. This theorem, however, does not provide an exact mathematical definition of the functional form that related the energy to the electron density and it only proves that such a functional exists. The second Hohenberg-Kohn theorem states, “The electron density that minimizes the energy of the overall functional is the true electron density corresponding to the full solution of the Schrödinger Equation”. According to this theorem, if we can find the “true” functional, then the energy of the system can be minimized by variation of electron density (Variational Principle).

In summary, the Hohenberg-Kohn theorem can be simply expressed as a function of the electron density as given by the following equation,

$$\mathrm{E}\left[\rho_{(\mathrm{r})}\right] = \langle \Psi\left[\rho_{(\mathrm{r})}\right] | H | \Psi\left[\rho_{(\mathrm{r})}\right] \rangle, \tag{1-4}$$

$$= \mathrm{T}[\rho] + \mathrm{V_{ee}}[\rho] + \int v(r)_{\mathrm{ext}} \rho(\mathrm{r}) \mathrm{dr}, \text{ and} \tag{1-5}$$

$$= \mathrm{F}[\rho] + \int v(\mathrm{r})_{\mathrm{ext}} \rho(\mathrm{r}) \mathrm{dr}\,, \tag{1-6}$$

where the functional is divided into a part that depends on the external potential, $\int v(\mathrm{r})_{\mathrm{ext}} \rho(\mathrm{r}) \mathrm{dr}$, and a part which does not depend on the external potential, $\mathrm{F}[\rho]$. This expression is exact and is valid for a system with any number of particles and with any external potential, $v(\mathrm{r})_{\mathrm{ext}}$. However, an analytical solution exists only for systems with one electron and for systems of technical interest, iterative solution schemes must be employed. Hence, approximation and simplification must be made to enable the solution for larger systems while maintaining the accuracy of the result. This presents the major challenge for DFT calculations in practice.

1.5.4. The Kohn-Sham Equation

In 1965, Kohn and Sham (KS) presented an idea to approximate the solution to the many-body electronic structure problem. In their approach, the problem of interacting electrons is replaced with an independent particle system by assuming that the ground state density of the non-interacting system can represent the ground state density of interacting system by defining an appropriate effective potential, $v_{\mathrm{eff}}(\mathrm{r})$. As a result, Hohenberg and Kohn suggest that the real electron density can be obtained from single electron wave functions, $\psi_i(\mathrm{r})$, and all the many body effects are grouped into an exchange correlation functional. Thus, the total energy functional of N electron is given by

$$E[\psi_i] = E_{\mathrm{known}}[\psi_i] + E_{\mathrm{xc}}[\psi_i], \tag{1-7}$$

where the $E_{\mathrm{known}}[\psi_i]$ is the collection of terms we can calculate analytically and $E_{\mathrm{xc}}[\psi_i]$ is everything else including many body effects. The $E_{\mathrm{known}}[\psi_i]$ is then expressed as

$$E_{\mathrm{known}}[\psi_i] = -\frac{h^2}{m}\sum_i \int \psi_i^* \nabla^2 \psi_i d^3r + \int V(r)\,\rho(r) d^3r + \frac{e^2}{2}\iint \frac{\rho(r)\rho'(r)}{|r-r'|} d^3r d^3r' + E_{\mathrm{ion}}, \tag{1-8}$$

where the first term represents the kinetic energies of the electrons, the second term represents Coulomb interactions between electrons and nuclei, the third term are Coulomb interactions between electron, and the last term represents Coulomb interactions between nuclei. The remaining term in eq. (1-7), $E_{xc}[\psi_i]$, is the exchange–correlation functional, which includes all the quantum mechanical effects that are not included in the "known" terms. The total electron density of the system can then be found from the one-electron wave functions given by

$$\rho(\mathrm{r}) = 2\sum_{\mathrm{i}=1}^{\mathrm{N}} |\psi_i(\mathrm{r})|^2, \tag{1-9}$$

in which the factor 2 results from the spin up and down states according to Pauli's exclusion principle. The one-electron wave functions are obtained by solving the single particle Kohn-Sham (KS) equations as given by

$$\left[-\frac{h^2}{2m}\nabla^2 + V(\mathrm{r}) + V_H(\mathrm{r}) + V_{\mathrm{xc}}(\mathrm{r})\right]\psi_i(\mathrm{r}) = \varepsilon_i \psi_i(\mathrm{r}), \tag{1-10}$$

where the first potential *V* describes interactions between an electron and the collection of atomic nuclei, the second potential is called Hartree potential and accounts for Coulomb repulsions between electrons, and the third term is the exchange-correlation potential. Since the single electron itself in Eq. (1-10) belongs to the total electron density, the Hartree potential should be corrected for self-interaction errors. Therefore, not only these unphysical interactions, but also many body effects, are grouped into the $V_{\mathrm{xc}}(\mathrm{r})$, which is the functional derivative of the exchange-correlation energy, $E_{\mathrm{xc}}[\rho(\mathrm{r})]$, as expressed as

$$V_{xc}(r) = \frac{\delta E_{xc}[\rho(r)]}{\delta \rho(r)}. \tag{1-11}$$

1.5.5. Exchange-correlation

Finding an accurate exchange-correlation functional is the main challenge for DFT calculations, and several empirical and semi-empirical functionals with different strengths and weaknesses have been proposed[38–40]. The most commonly used approximations in solid-state physics are the Local Density Approximation (LDA) and the Generalized Gradient Approximation (GGA). The LDA functional uses only the local density of a uniform electron gas. On the other hand, the GGA takes into account both the local electron density and the local gradient of the electron density. However, it is not necessarily always the case that the GGA is more accurate than the LDA, only because the GGA contains for more physical information. In this dissertation, a GGA functional based on the revised Perdew-Burke-Ernzerhof (RPBE) and Perdew-Wang (PW91) functionals are rigorously applied, which has been shown to give a good description of the energetics for adsorbed species on surfaces[40,41].

1.5.6. Self-Consistent-Field Cycle

In order to solve the KS equations self-consistently, an iterative method must be applied. This iterative method is called the Self-Consistent Field (SCF) Cycle. The cycle is terminated when a pre-defined convergence criterion for changes in the electron density is met. A full description of the solution strategy is illustrated in the literatures[35]. The cycle can be briefly described as follows:

1. Guess the trial electron density, $\rho(r)_{\mathrm{trial}}$.
2. Apply the $\rho(r)_{\mathrm{trial}}$ in the KS equations and solve for the single-electron wave functions, $\psi_i(r)_{\mathrm{initial}}$.
3. Plug in Eq. (1-9) to find the KS electron density, $\rho(r)_{\mathrm{KS}}$.
4. Compare $\rho(\mathrm{r})_{\mathrm{KS}}$ to $\rho(\mathrm{r})_{\mathrm{trial}}$ and if the two densities are equal, this is the ground state electron density. This electron density can then be used to compute the total energy. If the densities are not equal, go back to step 1 with an updated $\rho(\mathrm{r})_{\mathrm{trial}}$.

1.6. Objective of My Research Projects

Main goal of my research projects is to find a better catalyst for bio-oil upgrade process through first principle investigations. Mainly, I was looking into active sites and reaction mechanisms of HDO reactions over Ru/TiO_2. Since the understanding of atomic-scale surface chemistry is very important over metal oxide surface, we first adopted the constrained thermodynamic method to predict a surface phase diagram of rutile oxide surfaces (Chapter 1). The surrogated bio-oil compounds studied herein are acetaldehyde (Chapter 3), m-cresol (Chapter 4), and phenol (Chapter 5). In Chapter 3, I focus on the mechanistic study of acetaldehyde HDO on model surfaces including TiO_2, $RuTiO_2$, 1 ML RuO_2/TiO_2, RuO_2, and Ru/TiO_2. It is followed by the study of active sites on Ru/TiO_2 for m-cresol HDO in Chapter 4. In Chapter 5, I elucidate the water effect on phenol HDO on Ru/TiO_2. Because the production of hydrogen is also another important factor for efficient HDO reaction, catalytic processes such as partial and complete methane oxidation, steam and dry methane reforming were investigated by microkinetic (MKM) modeling in Chapter 6.

Chapter 2. Rapid Prediction Method for Surface Phase Diagrams of Rutile (110) Surfaces from DFT Calculations

2.1. Introduction

There are many different classes of transition metals oxides such as rutile, perovskite, anatase, hematite, brookite, and spinel[42]. Among them, the rutile structure has been considered as the most interesting material due to its stability and unique chemical properties[43]. The rutile bulk structure is similar to the '*hcp*' structure and has a metal atom at the Wyckoff 2(a) site and a oxygen atom at the Wyckoff 4(f) sites[44]. The well studied rutile surfaces are RuO_2, IrO_2, SnO_2, VO_2, and TiO_2. These rutile surface are successfully employed for heterogeneous catalysis as given: (1) NO and CO oxidation on RuO_2[45], methane and NH_4 oxidation on IrO_2[46,47], hydrogenation and methylation on SnO_2[44], and methanol oxidation on TiO_2[44,48–50]. Such diverse applications are derived from unique chemical properties that is associated with their own electronic structures[44].

Since the discovery of high catalytic activity of surface oxide layers over metal surfaces, numerous experimental techniques such as low-energy electron diffraction (LEED), scanning tunneling microscopy (STM), electron energy loss spectroscopy (EELC), and temperature-programed reduction (TPR) have been used to understand the growth of oxide layers over metal surfaces and their chemical properties under ultra high vacuum (UHV)[51–53]. However, atomistic information about oxide layers is scarce and the transitions between active metal/oxide phases are still debated because of the difficulties of making well-defined oxide layers over metals and low atomistic resolution under the ambient conditions[54–56].

Comprehensive theoretical studies on the other hand can provide precise atomistic information of oxide layers (i.e. equilibrated surface terminations) and can be used to extrapolate experimental observations under UHV conditions to predict surface terminations under ambient conditions. One successful approach is the constrained thermodynamic method, which uses density functional theory (DFT) calculations to enumerate ground state configurations under

ambient conditions, and then relates the calculated surface free energies (γ) to practical reaction conditions (T, *p*). This approach has been successfully applied for the discrimination of active phases among transition metal oxides[45,57]. For example, Getman *et al.* used this method to determine whether the pure Pt(111) metal surface or oxygen covered Pt(111) is active for NO oxidation[58]. Reuter *et al.* have applied this approach to identify the onset reaction conditions of oxide formation over the 4-*d* transition metals[59]. However, the fact that the evaluation of many possible surface terminations through DFT calculations limits the size of unit cells, restricts the approach to simple systems such as clean metal surface with one or two adsorbates. Furthermore, this method incorporates surface adsorbate-adsorbate interactions only implicitly. These interactions often plays a crucial role when the surface intermediates are present at high coverages. To take these interactions explicitly into account, the cluster expansion (CE) method is an alternative approach in which a series of parameters are estimated through the different configurations of adsorbates to evaluate effective cluster interaction parameters[60,61]. Most recently, the CE method has been combined with kinetic Monte Carlo (kMC) simulation to predict the spatial distribution of adsorbates for CO oxidation, ammonia synthesis, and water-gas-shift reactions on Pt surfaces[60,62]. Yet, this method is computationally expensive, because effective cluster interaction parameters have to be determined via fitting with pair, triplet, and higher order interaction models[60].

In this chapter, we introduce a rapid method for the prediction of *ab-initio* surface phase diagrams of rutile MO_2(110) surfaces with M = Ru, Ti, Ir, Rh, Sn, Pt, Pd, V, and the binary RuO_2/TiO_2 mixed metal oxide. This new method requires only the oxygen vacancy formation energy ($\Delta E_v = E_{slab} + E_{H_2O} - E_v - E_{H_2}$), and relies on linear scaling correlations to predict the stability of other surface terminations. The effect of the surface adsorbate-adsorbate interactions with an extended surface interaction model on the prediction of phase diagram has been also investigated. The reliability of our rapid prediction method for surface phase diagram using a combination of scaling relationships and interaction parameters is verified by comparison to a sophisticated kinetic phase diagram obtained from kinetic Monte Carlo simulations for both RuO_2 and RuO_2/TiO_2.

2.2. Computational Details

We applied first principles density functional theory (DFT) calculations using Vienna Ab-initio Simulation Package (VASP) in conjunction with the Atomic Simulation Environment (ASE)[35,63]. The projector augmented wave (PAW) method and pseudopotentials were used to describe interaction between core electrons and valence electrons with cutoff energy = 400 eV[64,65]. The revised Perdew-Burke-Ernzerhof (RPBE) was chosen as exchange-correlation functional[66]. The Brillouin zone was sampled with a Monkhorst-Pack $(10 \times 10 \times 10)$ k-points grids for bulk calculations and a (8×8×1) k-points grids for the slab relaxations[67]. The optimized bulk lattice constants are in good agreement with experimental data as tabulated in Table 2-1[44,68,69].

Table 2-1. Optimized lattice constants for different rutile structures (a=b, and c in Å)

	Experimental		DFT		Error / %	
	a	c	a	c	a	c
RuO_2	4.641	3.202	4.589	3.149	1.12	1.66
TiO_2	4.593	2.958	4.723	2.971	-2.83	-0.44
IrO_2	4.510	3.150	4.587	3.201	-1.71	-1.62
RhO_2	4.487	3.089	4.601	3.145	-2.54	-1.81
PtO_2	4.600	3.240	4.672	3.246	-1.57	-0.19
PdO_2	4.483	3.101	4.656	3.229	-3.86	-4.13
VO_2	4.555	2.855	4.634	2.794	-1.73	2.14
SnO_2	4.734	3.185	4.875	3.249	-2.98	-2.01

Surface slabs were represented in p(2×2) unit cell using MO_2 layers (M = Ru, Ti, Ir, Rh, Pt, Pd, V, Sn), keeping all metal atoms and subsurface oxygen atoms fixed at their bulk positions, because we encountered severe surface reconstruction problems. These issues were addressed by adding additional constraints. All atomic hydrogen atoms were allowed to move freely and the top six oxygen atoms were allowed to move only in z-direction. To avoid the interactions between periodically repeated layers, the unit cell included 16 Å of vacuum along the normal direction of the surfaces. A dipole correction was applied to compensate for the effect of adsorbing molecules only on one side of surface[70]. The conjugated gradient algorithm was used for surface relaxations until the forces between atoms converged below 0.05 eV $Å^{-1}$. A Fermi temperature of k_BT = 0.1 / 0.01 eV was chosen for surface slabs / gas phase molecules (H_2O and H_2), and the energies were extrapolated to zero electronic temperature[71].

All binding energies (E_{BE}) and vacancy formation energies (ΔE_{vac}) were referenced to the energies of the stoichiometric rutile surfaces and the gas molecules (H_2O and H_2). The climbing image nudged elastic band (cNEB) method was employed to determine transition states (TS) of elementary reaction steps[72]. Vibrational analysis was subsequently performed to verify the existence of a single imaginary mode, corresponding to the transition state mode along the reaction path using the scheme implemented in the ASE[63].

We use a constrained thermodynamic approach to predict surface phase diagrams of rutile surfaces as a function of chemical potentials of H_2O and H_2. Such method enables us to extrapolate DFT energies calculated for UHV and T = 0 K to realistic reaction conditions, i.e., 'pressure gap' can be bridged. As reported elsewhere, the thermodynamic formulation of the equilibrated surface energy depends on the reservoir conditions[57,59]. Here, we find out the most stable surface phase under certain reaction conditions from the surface free energy $\gamma(T, p_i)$ as evaluated by[57]

$$\gamma(T, p_i) = [E_s(MO_2 + N_H H) - N_M E_{MO2}^{bulk} + (2N_M - N_o)\mu_o - N_H \mu_H], \tag{2-1}$$

where E_s and E_{MO2}^{bulk} are the DFT energies of the slab and bulk, and μ_i and N_i are chemical potentials and the number of species 'i' in the unit cell, respectively. The chemical potential of H_2O and H_2, which are in equilibrium with metal oxides surfaces, can be expressed as [57]

$$\mu_{\mathrm{O}} = \mu_{\mathrm{H_2O}} - \mu_{\mathrm{H_2}}, \tag{2-2}$$

$$\text{with } \mu_{\mathrm{H_2O}} - \mu_{\mathrm{H_2}} = \left[\Delta h_{\mathrm{H_2O}}(\mathrm{T}, p^0) - \Delta h_{\mathrm{H_2}}(\mathrm{T}, p^0)\right] + [E_{\mathrm{H_2O}}^{\mathrm{vib}}(\mathrm{T} = 0K) - E_{\mathrm{H_2}}^{\mathrm{vib}} - \left(E_{\mathrm{H_2O}} - E_{\mathrm{H_2}}\right) - \mathrm{T}[s_{\mathrm{H_2O}}(\mathrm{T}, p^0) - s_{\mathrm{H_2}}(\mathrm{T}, p^0) + k_{\mathrm{B}}\mathrm{T}ln\left(\frac{p_{\mathrm{H_2O}}}{p_{\mathrm{H_2}}}\right), \tag{2-3}$$

$$\text{and } \mu_{\mathrm{H}} = \frac{1}{2}\mu_{\mathrm{H_2}} = \frac{1}{2}\Delta h_{\mathrm{H_2}}(\mathrm{T}, p^0) + E_{\mathrm{H_2}}^{\mathrm{vib}}(\mathrm{T} = 0K) + E_{\mathrm{H_2}} - \mathrm{T}s_{\mathrm{H_2}}(\mathrm{T}, p^0) + k_B\mathrm{T}ln\left(\frac{p_{\mathrm{H_2}}}{p^0}\right), \tag{2-4}$$

where E_i are DFT energies, $E_i^{\mathrm{vib}}(\mathrm{T} = 0\ \mathrm{K})$ denotes the zero point energies of H_2O and H_2, h is enthalpy, s is entropy, k_{B} is Boltzmann's constant, and p^0 is our reference pressure = 1.0 bar. We used tabulated values for $\Delta h_{\mathrm{H_2O}}(T, p^0)$, $\Delta h_{\mathrm{H_2}}(T, p^0)$, and $s_{\mathrm{H_2O}}(T, p^0)$ [73,74]. Through the evaluation

of Eq. (2-1) and Eq. (2-3) and (2-4), we can find the surface terminations with the lowest surface free energy and predict a thermodynamic phase diagram (TPD) for rutile surfaces were predicted.

The predicted thermodynamic phase diagrams were validated with a kinetic phase diagram (KPD) obtained from sophisticated kinetic Monte Carlo (kMC) simulations. Kinetic input parameters for the kMC simulations were calculated over p(2×3) RuO_2 and RuO_2/TiO_2. These values are summarized in Table 2-2. We consider our kMC simulations to be the most accurate benchmark result; kMC has been successfully implemented to simulate the time evolution of elementary processes occurring on various surfaces and to explore sequences of thermally activated rare events such as diffusion, reaction, desorption, and adsorption[75,76]. It provides not only detailed information of the stochastic interplay of all elementary reactions taking place on the surface, but it also accounts for correlations, fluctuations, and spatial distributions on the surface[75,77]. For our purposes we adopted the general lattice kinetic Monte Carlo Simulation framework *kmos*[78].

Table 2-2. DFT-derived energies for kinetic Monte Carlo (kMC) simulations on RuO_2(110) and RuO_2/TiO_2. All tabulated energies are calculated with respect to gas phase H_2 and H_2O.

no.	Elementary steps	RuO_2		RuO_2/TiO_2	
		E_{BE} / eV	E_a / eV	E_{BE} / eV	E_a / eV
M1	H_2Ru^{cus}	-0.11	.	-0.19	
M2	H_2O^{br}	-0.25	.	0.16	
M3	$HRu^{cus} + O^{br} \leftrightarrow Ru^{cus} + HO^{br}$	.	0.48	.	0.92
M4	$HRu^{cus} + Ru^{cus} \leftrightarrow Ru^{cus} + HRu^{cus}$	.	1.58	.	1.15
M5	$HO^{br} + HO^{br} \leftrightarrow H_2O^{br} + O^{br}$	.	1.32	.	1.26
M6	$H_2Ru^{cus} + O^{br} \leftrightarrow HRu^{cus} + HO^{br}$	.	0.29	.	0.47
M7	$HRu^{cus} + HO^{br} \leftrightarrow Ru^{cus} + H_2O^{br}$	.	0.93	.	1.38
M8	$HO^{br} + H_2Ru^{cus} \leftrightarrow H_2O^{br} + HRu^{cus}$	.	0.45	.	0.57

2.3. Results and Discussion

We will limit our discussion in this section to the data obtained for the RuO_2(110), and binary RuO_2/TiO_2 surface, because the main aspects and findings throughout the other rutile surfaces are almost identical. Detailed information about the other surfaces is summarized in the Appendix.

The RuO_2 surface is of specific interest because of a still ongoing debate whether the oxide, a surface oxide, or metallic surface is the active phase for CO oxidation. Goodman *et al.* reported that one-monolayer oxygen covered Ru, (1X1)O-Ru, is the active surface phase for CO oxidation, while Over *et al.* argued that RuO_2 is the active surface phase for Ru catalyst[79]. Thanks to this debate, however, the properties of RuO_2 have been extensively studied and precise surface information has been obtained through the various surface chemistry techniques.

The p(2×2) RuO_2(110) surface consists of six oxygen sites including two bridging oxygen sites (O^{br}) and four three-fold sites (O^{3f}). Further, there are two coordinatively unsaturated Ru sites (Ru^{cus}). It is well known that atomic hydrogen binds preferentially to the O^{br} site rather than the Ru^{cus} site, and the bridging hydroxyls (HO^{br}) are dominant above T = 350 K as confirmed by the combination of TPR and HREELS[80]. Jacob *et al.* also reported that the free Ru^{cus} site is only needed for H_2 dissociation to form H-Ru^{cus} and HO^{br} on RuO_2(110)[51,81].

Although hydrogen adsorption on the O^{3f} site has not been experimentally observed, we adopted both the O^{3f} and O^{br} sites as the possible hydrogen adsorption sites. Those sites might be occupied at higher H_2 pressure outside the typical operating pressure for surface science techniques. Under highly reducing conditions, we allowed for the removal of all six surface oxygen atoms. Further oxidation of RuO_2 at the Ru^{cus} site was considered due to the fact that the oxidation only occurs under extremely high p_{H_2O} condition through water dissociation, but water desorbs from the Ru^{cus} site starting at T ≈ 400 K[82].

Figure 2-1 is a grid representation of all RuO_2 p(2×2) surface configurations included for the prediction of the thermodynamic phase diagram. The *x*-axis and *y*-axis represent the level of reduction (oxygen removal) and hydrogenation, respectively. The two key examples for reduction and hydrogenation steps are expressed as $H_{2(g)} + O^{br} \rightarrow V_o + H_2O_{(g)}$ and $H_{2(g)} + 2O^{br} \rightarrow 2HO^{br}$. We analyzed the stable surface structures in Figure 2-1 and the equivalent graphs for all other rutile surfaces and noticed common features regarding the preferred structure of rutile surfaces upon reduction and hydrogenation.

First, the adsorption of atomic hydrogen always begins at the O^{br} site, and subsequent adsorption of hydrogen on the O^{3f} site happens if there is no available O^{br} site (see the '+1H/-0O' ~ '+1H/-6O' in Figure 2-1). Second, when surface reduction (i.e. oxygen vacancy defect formation) occurs, the O^{br} site is first reduced, then followed by the reduction of the O^{3f} site (see the '+0H/-1O' ~ '+0H/-6O' in Figure 2-1). The reason is that the defect formation at the O^{br} site (ΔE = -0.33 eV) is thermodynamically preferred over the O^{3f} site (ΔE = 0.93 eV). This result agrees well with other DFT calculations and experimental results[82,83].

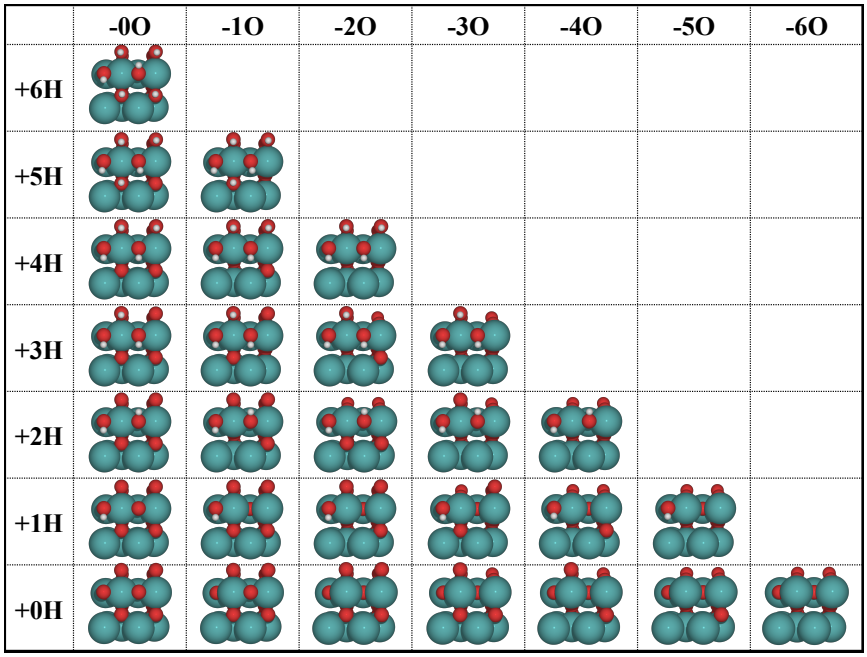

Figure 2-1. Stable surface configurations on the p(2×2) RuO_2(110) surface. '+0H' ~ '+6H' denotes the degree of surface hydrogenation, and '-0O' ~ '-6O' denotes the degree of surface reduction. Color code: white - hydrogen / red – oxygen / teal - ruthenium.

The third common aspect is that adsorbed hydrogen atoms tend to stay far away from each other to minimize their repulsion. For example, in the case of '+2H/-0O', two hydrogen atoms adsorbed on adjacent O^{br} sites are pointing to opposite direction, i.e. one is up and the other one is down.

Using the calculated formation energies of the surface structures shown in Figure 2-1, we are able to reduce the complexity of the parameter space and derive linear scaling relations as shown in Figure 2-2. We observe that the first vacancy formation energy, ΔE_v: $O^{br} + H_2 \leftrightarrow H_2O + V_o$, at the O^{br} site corresponding to '+0H/-0O' in Figure 2-1 is a good descriptor for all other calculated energies, which include the ΔE of reduction (e.g. the ΔE when moving from the left to the right in

Figure 2-1) and hydrogenation (e.g. the ΔE when moving from the bottom to the top in Figure 2-1). Moreover, this descriptor does not only work for pure rutile surfaces, but it also captures energy variations across the binary mixed oxide RuO_2/TiO_2. The average mean absolute error (MAE) between fitted lines and calculated energies shown in Figure 2-2 is 0.44 eV, meaning that the correlations are not perfect, but within an reasonable error range[84].

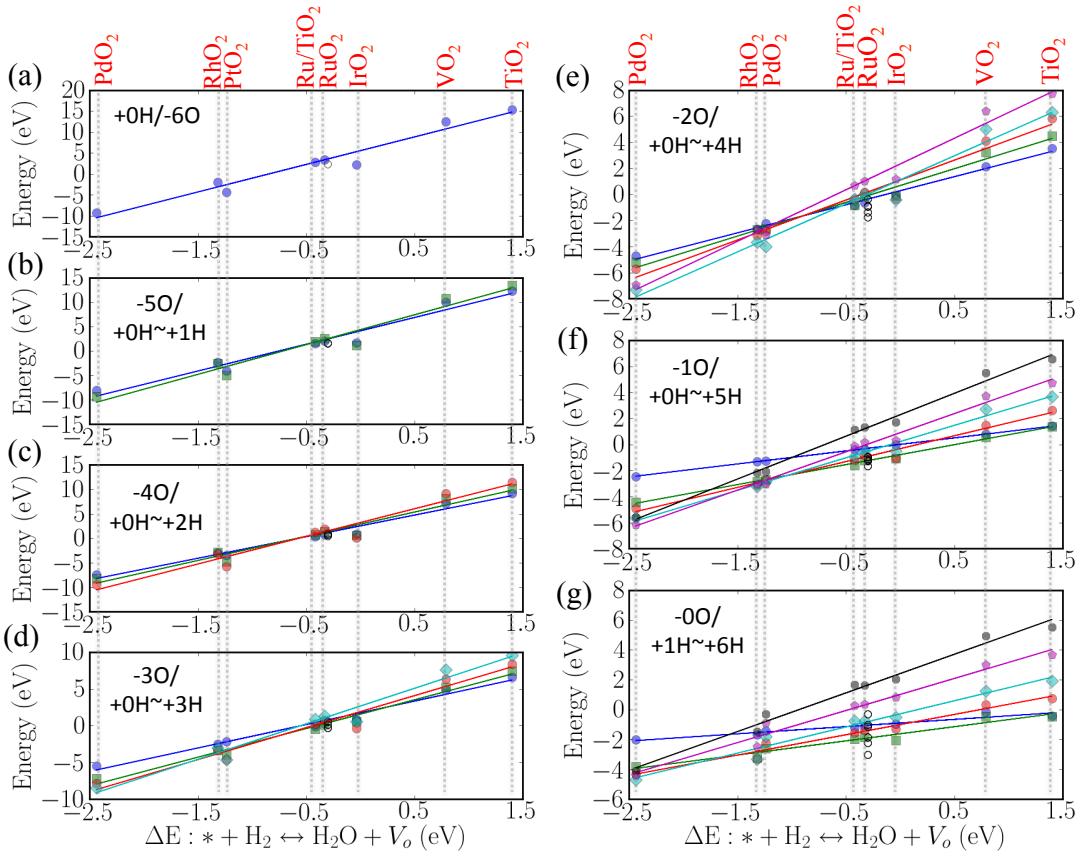

Figure 2-2. Linear scaling relations as a function of a single descriptor value (ΔE_v). The black empty circles are ΔE on SnO_2 and other surfaces are labeled on top of this figure. Each panel corresponds to the one of the column in Figure 2-1.

Another important finding is that coverage-dependent binding energies, $\Delta E(\theta_i, i = H \text{ or } V_o)$, can be easily predicted from these scaling correlations. Calculations of $\Delta E(\theta_i)$ on transition metals (TMs: Pt, Ru, Rh, Cu, Pd, and Au) have been known to be very important topic for decades, because it is be able to provide information about surface adsorbate-adsorbate interactions, which are of widespread and growing interest for improving the description of heterogeneously catalyzed reactions[84–86]. For example, Kitchin *et al.* discovered a linear relation for $\Delta E(\theta_i, i =$

oxygen) on Pt and Au with respect to the value of *d*-band center, providing more realistic surface information on both transition metal surfaces[87]. However, to the best of our knowledge this is the first DFT study introducing coverage-dependent binding energies, $\Delta E(\theta_i, i = H \text{ or } V_O)$, on rutile surfaces with single descriptor value (ΔE_v). Note that values for SnO_2 (empty black circles in Figure 2-2) deviate significantly from our scaling correlations, and the stable configurations also do not even follow the trends discussed in Figure 2-1. In addition, some points for PtO_2, PdO_2, RhO_2, and IrO_2 also deviate significantly from the scaling correlations. We speculate that these outliers are a result of the fact that the rutile phase is not the most stable crystal phase for PtO_2, PdO_2, and RhO_2 and it is not directly relevant for traditional catalytic conditions. Forcing these oxides to assume the rutile crystal structure resulted in severe surface reconstructions during their structure relaxation, and is ultimately responsible for the large deviation as observed in Figure 2-2[88,89].

Our discovery of the oxygen vacancy formation energy as universal descriptor for the stability of rutile surfaces supplements various related studied. In recent years there has been significant progress in a descriptor-based search methods for the estimation of binding energies and energy barriers on transition metal catalysts, which is slowly being extended to transition metal oxide surfaces for atomic adsorption (H, O, N, and S)[66,88]. For transition metal catalysts, the *d*-band model provides fruitful information with regard to catalytic activity. However, according to its derivation and physical origin it is technically restricted from describing trends in catalytic activity on transition metal oxides, because of the difficulties stemming from self-interactions for localized *d* and *f* electrons in metal oxide[66]. Nonetheless, the progress in descriptor-based screening approaches for the transition metal oxides has been recently reported by Suntivich *et al.* who described the electrochemical activity of oxygen reduction and evolution (ORE) with a function depending on the filling of the e_g orbitals of perovskite oxides[90]. Other descriptors such as the *p*-band center of the atomic oxygen on the transition metal oxides and the number of outer electrons (valence electron) have also been applied to describe catalytic activity[91,92]. To the best of our knowledge, a descriptor that can represent all energetic information for coverage-dependent binding energies on rutile surfaces has not been discovered. This discovery man be

specific to rutile surfaces, but we hypothesize that it can be translated to other metal oxide surfaces as well.

From the variations in reduction and hydrogenation energies across the structures in Figure 2-1, it is evident that strong interactions between vacancy sites and surface adsorbates including HO^{br} and HO^{3f} on metal oxides exist. Such interactions should be carefully studied to obtain more precise surface information on metal oxides. Hence, to investigate these surface adsorbate-adsorbate interactions [E_{BE} (θ_H, θ_{vac})], an extended interaction model has been applied for this study. The adsorbate-adsorbate interactions including an interaction between the same species (O^{br}-O^{br}, O^{3f}-O^{3f}, HO^{br}-HO^{br}, HO^{3f}-HO^{3f}) and an interaction between the different species (O^{br}-O^{3f}, O^{br}-HO^{br}, O^{br}-HO^{3f}, O^{3f}-HO^{br}, O^{3f}-HO^{3f}, HO^{br}-HO^{3f}) are fitted to a piecewise continuous interaction model as reported elsewhere[93,94]. This model predicts the integral binding energies (E^{int}) of surface intermediates per site as a function of coverage given the multiple adsorbates, and theE^{int} can be derived as

$$E_{\mathrm{i}}^{\mathrm{int}}(\theta_{\mathrm{i}}) = E_{\mathrm{i}}^{0}, \text{ with } (|\theta| \leq \theta_0) \text{ and} \tag{2-5}$$

$$E_{\mathrm{i}}^{\mathrm{int}}(\theta_{\mathrm{i}}) = E_{\mathrm{i}}^{0} + \sum_{\mathrm{j}} f\varepsilon_{\mathrm{ij}}\theta_{\mathrm{j}}, \text{ with } (|\theta| > \theta_0 \; and, \; f = \tfrac{(|\theta| - \theta_0)}{|\theta|}). \tag{2-6}$$

The $E_{\mathrm{i}}^{\mathrm{int}}(\theta_{\mathrm{i}})$ is integral-binding energy with regard to coverage of 'i' (θ_{i}), E_{i}^{0} is the binding energy below a threshold coverage θ_0, $\varepsilon_{\mathrm{ij}}$ is a pairwise interaction parameter (IP) between different species 'i' and 'j' ($\varepsilon_{\mathrm{ij}}$ < 0: attraction, and $\varepsilon_{\mathrm{ij}}$ > 0: repulsion), and |θ| is the sum of all coverages[93]. Below the threshold coverage ($\theta_{\mathrm{i}} < \theta_0$), we assumed that binding energies are constant, because the interaction-interaction between adsorbates is negligible. Finally, the extended surface interaction model for rutile oxide surfaces to take all combinations of interactions into account is expressed as[93]

$$E^{\mathrm{int}}\left(\theta_{\mathrm{O^{br}}}, \theta_{\mathrm{HO^{br}}}, \theta_{\mathrm{O^{3f}}}, \theta_{\mathrm{HO^{3f}}}\right) = \sum E_{\mathrm{i}}^{0}\theta_{\mathrm{i}} + \sum \theta_i^2 \varepsilon_{\mathrm{ii}} + \sum \theta_{\mathrm{i}}\theta_{\mathrm{j}}\varepsilon_{\mathrm{ij}}, \tag{2-7}$$

where $\varepsilon_{\mathrm{ii}}$ (pairwise interaction between the same surface species) and $\varepsilon_{\mathrm{ij}}$ (pairwise interaction between different surface species) are included as required.

Using this extended interaction model, Eq. (2-7), we estimated the IPs from the original binding energies (OBE) for RuO_2. In addition, since all energetic parameters can be also calculated with our scaling correlations shown in Figure 2-2, the IPs are also estimated with scaled binding energies (SBE) to provide further validation of the agreement between OBE and SBE. The obtained IPs are summarized in Table 2-3.

Table 2-3. The fitted interaction parameters with the extended interaction model on the RuO_2(110) surface.

	[a]OBE / eV ML^{-1}	[b]SBE / eV ML^{-1}	Error / eV ML^{-1}
$E_{O^{br}}$	-0.42	-0.40	0.02
$E_{O^{3f}}$	0.16	0.21	0.05
$E_{HO^{br}}$	-1.01	-0.97	0.04
$E_{HO^{3f}}$	0.41	0.25	-0.16
$\varepsilon_{O^{br}O^{br}}$	0.64	0.85	0.21
$\varepsilon_{O^{3f}O^{3f}}$	0.87	0.52	-0.35
$\varepsilon_{HO^{br}HO^{br}}$	0.09	-0.08	-0.17
$\varepsilon_{HO^{3f}HO^{3f}}$	0.63	0.82	0.19
$\varepsilon_{O^{br}O^{3f}}$	0.60	1.04	0.44
$\varepsilon_{HO^{br}HO^{3f}}$	0.13	0.28	0.15
$\varepsilon_{HO^{br}O^{3f}}$	-0.61	0.54	1.15
$\varepsilon_{HO^{br}O^{br}}$	0.50	-0.18	-0.68
$\varepsilon_{HO^{3f}O^{3f}}$	0.99	0.21	-0.78
$\varepsilon_{O^{br}HO^{3f}}$	-1.43	-1.51	-0.08

[a]Original binding energies (OBE) were taken from DFT calculations. [b]Scaled binding energies (SBE) were taken from linear scaling lines shown in Figure 2-2.

Both fittings produce consistent IPs suggesting largely repulsive interactions, although a few exceptions exist. As studied elsewhere, strong repulsion between $V_{O^{3f}}$-$V_{O^{3f}}$, HO^{3f}-O^{3f}, and HO^{3f}-HO^{3f} is found and makes the formation of vacancy at the O^{3f} site or the adsorption of hydrogen on the O^{3f} site thermodynamically unlikely[95,96]. To better understand the effect of IPs on the integral-binding energies, we plotted 2D binding energy maps in the presence and absence of IPs (see Figure 2-3). The high coverage domains are indicated at each corner at (θ_H = 0, θ_{vac} = 0), (θ_H = 0, θ_{vac} = 1), and (θ_H = 1, θ_{vac} = 0). In the absence of IPs, coverage-dependent integral binding energies maps shown Figure 2-3(a) and (b) are discontinuous, because of the discrete coverages data points obtained from p(2×2) unit cell, which limited possible coverage points to 0.0, 0.17,

0.33, 0.50, 0.67, and 0.83 ML. These discrete coverage-dependent binding energies can be extended to continuous binding energies maps by incorporation of IPs fitted to OBE and SBE. Namely, Figure 2-3(c) and (d) present coverage-dependent integral binding energies maps that become continuous after the inclusion of the fitted IPs.

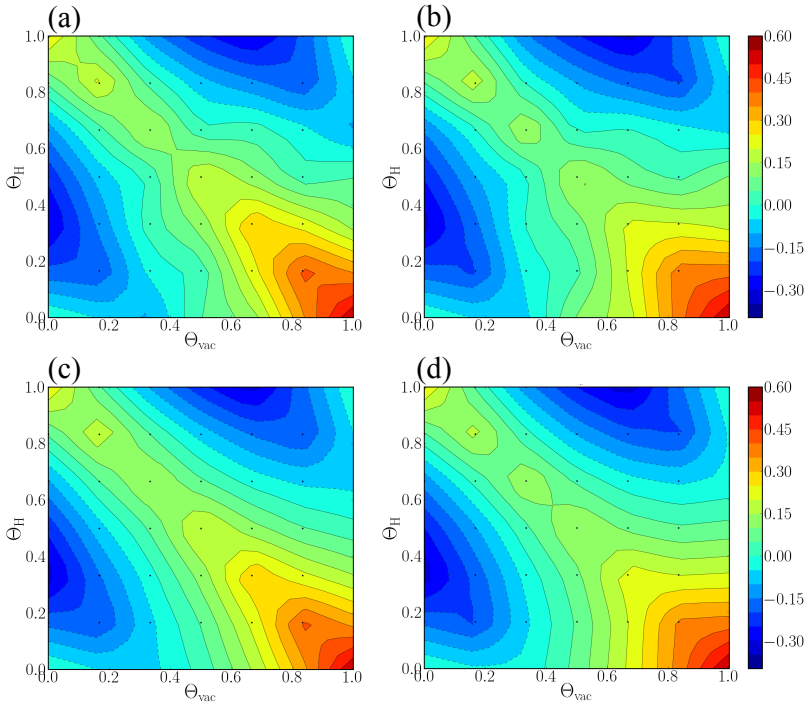

Figure 2-3. Coverage-dependent integral binding energies (E^{int}) maps on the RuO_2(110) surface: (a) E^{int} from original binding energies (OBE), (b) E^{int} from scaled binding energies (SBE), (c) E^{int} with OBE and interaction parameters (IP) fitted to OBE, (d) E^{int} with IPs fitted to SBE.

The calculation of surface free energies via Eq. (2-1) with OBE and SBE enables us to predict the thermodynamic phase diagram (TPD) of the RuO_2(110) surface with respect to the pressure of H_2 and H_2O (see Figure 2-4). TPDs for other rutile surfaces are given in the Appendix. Different surface phases in Figure 2-4 are shown in different colors: the major three phases include the fully hydroxylated RuO_2, stoichiometric RuO_2, and fully reduced RuO_2 shown in blue, green, and red, respectively. The surface phases in Figure 2-4 are denoted with different color and number as (1) +0H/-6O, (2) +1H/-5O, (3) +0H/-5O, (4) +3H/-4O, (5) +1H/-4O, (6) +0H/-4O, (7) +3H/-3O, (8) 2H/-3O, (9) +1H/-3O, (10) +0H/-3O, (11) +0H/-2O, (12) +3H/-2O, (13) +1H/-1O, (14) +2H/-0O, (15) +1H/-0O, and (16) +0H/-0O. The four panels correspond to surface free energy calculations

using four different input strategies: (a) OBE, (b) SBE, (c) interaction model with IPs from OBE (OBE+IP), and (d) interaction model with IPs from SBE (SBE+IP).

Despite the use of different input energies for the calculation of surface free energies, all TPDs look similar, and have only minor differences at the phase boundaries. In general, we can say that (1) at p_{H_2} > ca. 10^{-13} bar and p_{H_2O} > ca. 10^{-3} bar (phase 14): all O^{br} sites of RuO_2 are hydroxylated and form HO^{br}, (2) at p_{H_2} < ca. 10^{-13} bar (phase 15 and 16): RuO_2 is stoichiometric or partially hydroxylated, and (3) at p_{H_2} > ca. 10^{-13} bar and p_{H_2O} < ca. 10^{-3} bar (from phase 1 to 13): RuO_2 starts to reduce and exhibits surface oxygen vacancies (V_O). We note that the applicability of this TPD for H_2-rich (strongly reducing) conditions is limited. In the meta-stable region (p_{H_2} > ca. 10^{-13} bar and the p_{H_2O} < ca. 10^{-3} bar), where we see severe surface reduction, oxygen diffusion from the bulk toward the surface to heal oxygen vacancy defects V_O are further expected, eventually leading to a transformation into metallic Ru as predicted in other works [59,82]. The metallic surface phase was not included as possibility for the derivation of the TPD and can therefore not be found.

The TPD based on OBE, Figure 2-4(a), has the smallest number of phases mainly because of the limited data points from the small unit cell. The TPD with SBE, Figure 2-4(b), is essentially identical to Figure 2-4(a) except for minor differences for phases 9 and 13. After smoothening out the energy variations from one phase to the next by employing IPs based on OBEs we start to observe additional phases not found in Figure 2-4(a). Even more additional phases are found when the IPs are derived from SBEs, which results in even more continuity of the energy input data. The reason for this increase in the number of phase is attributed to the piecewise continuous fitting in Eq. (2-6). Thus, this smoother integral binding energy maps results in a more gradual energy variation from one phase to another and is ultimately responsible for the appearance of the extra phases in Figure 2-4(c) and (d). It is noted that most of the additional phases appear in the area defined as meta-stable region (p_{H_2} > ca. 10^{-13} bar and p_{H_2O} < ca. 10^{-3} bar), where significant surface reconstruction occurs. We speculate that the severe reconstruction strongly favors certain surface phase, such that many of the intermediate phases cannot be

identified in a direct search using small unit cells. With the interpolated functions, however, we can obtain the continuous progression from one phase to another, which seems more realistic and is a possible improvement of the standard approach.

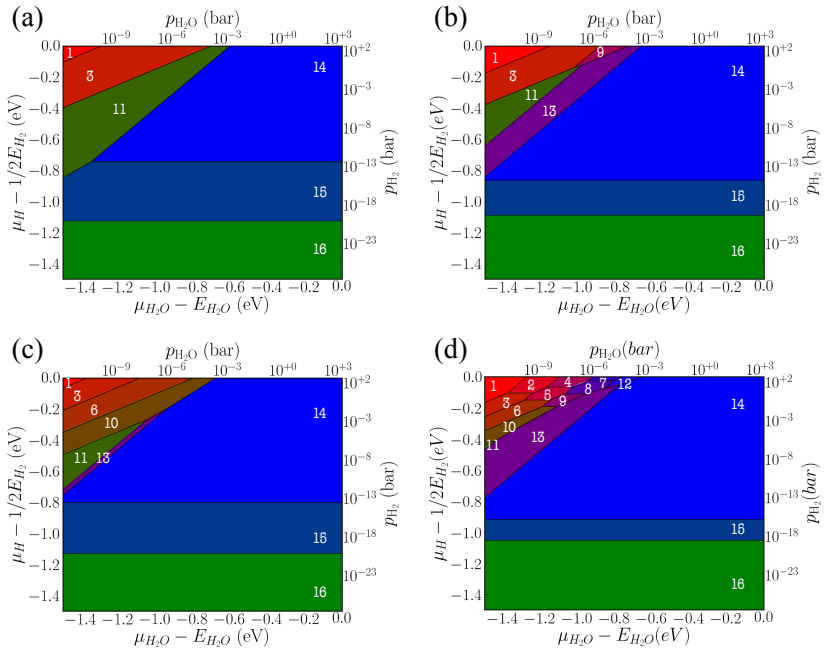

Figure 2-4. Thermodynamic surface phase diagram of the RuO_2(110) as a function of H_2 and H_2O chemical potentials at T= 500 K: (a) original binding energy (OBE), (b) scaled binding energy (SBE), (c) OBE with IPs fitted to OBE, and (d) SBE with IP fitted to SBE.

Among the many phases shown in Figure 2-4, the relevant surface termination for the catalysis at realist pressure for H_2 and H_2O is predicted to be phase 14 (+2H/-0O), independent of which one of the four TPDs is consulted (Figure 2-4). Thus, our scaling relations are clearly sufficient to make useful predictions regarding the most relevant surface terminations, which we define as our ultimate goal in this process.

The final test of the robustness of our rapid prediction approach for TPD is a comparison between the thermodynamic limit with a full kinetic description. Therefore, kinetic Monte Carlo (kMC) simulations were, performed on a p(20×20) RuO_2(110) surface with 25 different pressure conditions (p_{H_2}, p_{H_2O}) at T = 500 K. In this kMC model the gas-phase H_2 and H_2O are treated as ideal-gases in a reservoir by keeping the same temperature and partial pressures of the gas phase species. The sticking coefficients for both species are assumed to be 1. Lateral interactions are not included in the kMC model.

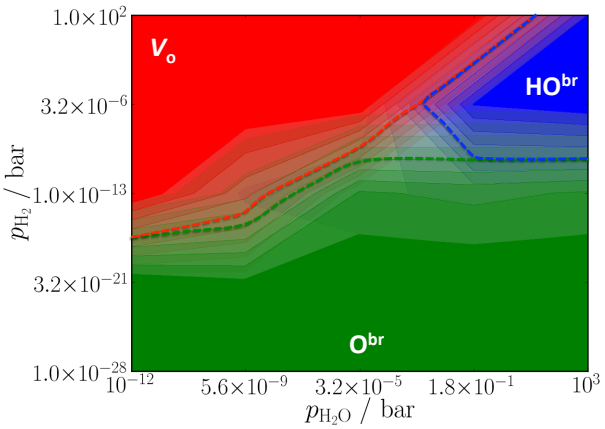

Figure 2-5. Steady state kinetic phase diagram of the RuO_2(110) surface as a function of H_2O and H_2 pressure at T = 500 K. The dotted lines for each color indicate a surface coverage (θ_i) = 0.5 ML.

The kinetic values shown in Table 2-2 are calculated on the hydroxylated p(3×2) RuO_2 surface. A total of 10 elementary steps such as two hydrogen diffusion pathways, four vacancy formation pathways, desorption and adsorption of H_2 and H_2O are included. The calculated energy barrier for disproportionation (M5) suggested by Ertl *et al.*[96] is good agreement with other DFT studies[96]. Since vacancy formation at the O^{3f} sites is thermodynamically unfavorable[51,97], this site was excluded for vacancy formation in our kMC model. Thus, only phase 11 in Figure 2-4 can be obtained under highly reducing conditions.

The kinetic phase diagram (KPD) for RuO_2(110) is shown Figure 2-5, where each color corresponds to the coverage of different surface intermediates: red - coverage of vacancies (θ_{vac}); blue - coverage of HO^{br} ($\theta_{HO^{br}}$); and green - coverage of O^{br} ($\theta_{O^{br}}$). The dotted lines indicates coverage θ_i = 0.5 (i = V_o, O^{br}, and HO^{br}). We observed that the KPD reproduces nearly the same surface terminations as the various TPDs at similar pressure conditions, except for phase boundaries where the configurational entropy becomes important[98]. Specifically, below the p_{H_2} < ca. 10^{-13} bar almost all surface oxygen sites were clean (≈ stoichiometric surface), above p_{H_2}> ca. 10^{-6} bar and p_{H_2O} > ca. 0.1 bar the O^{br} sites were either partially or fully hydroxylated (forming HO^{br}), and below p_{H_2O}< ca. 0.1 and above p_{H_2}> ca. 10^{-13} bar V_O become dominant. Since we have not included the possibility of $V_{O^{3f}}$ formation in our kMC model, the complex surface terminations associated with the $V_{O^{3f}}$ shown in the TPDs were not observed in this KPD

under the region below the p_{H_2O}< ca. 0.1 bar and above the p_{H_2}> ca. 10^{-13} bar. It is also found that the area corresponding to phase 14 (fully hydroxylated surface at bridging oxygen sites HO^{br}) in Figure 2-4 is predicted to be smaller in the KPD. Even though there are small differences between KPD and TPD from the phase boundaries, it clearly shows that the inclusion of kinetics would not significantly change the dominant surface terminations with respect to the pressure of H_2 and H_2O.

We mentioned earlier that the scaling relations work not only for pure rutile surfaces, but also for a mixed rutile surface. It means that all surface free energies (total 28 parameters) needed to predict TPD for binary rutile surface like RuO_2/TiO_2 [see Figure 2-6(a)] can be estimated only with first the vacancy formation energy, ΔE_v: $O^{br} + H_{2(g)} \leftrightarrow H_2O_{(g)} + V_o$, without performing a full series of DFT calculations. To see how this argument applies to the mixed RuO_2/TiO_2 surface, we compared its TPD derived from SBE with KPD. The calculated ΔE_v on RuO_2/TiO_2 is -0.42 eV which is in turn lower than on RuO_2 (-0.33 eV). Using this value with our linear relations, we can estimate the remaining total of 28 energetic parameters required for the prediction of surface free energies. For the KPD we calculated explicitly the kinetic parameters for the same steps investigated on RuO_2 over RuO_2/TiO_2 as summarized in Table 2-2. The comparison between KPD and TPD for RuO_2/TiO_2 is shown in Figure 2-6(b) where the TPD is drawn with white dotted lines.

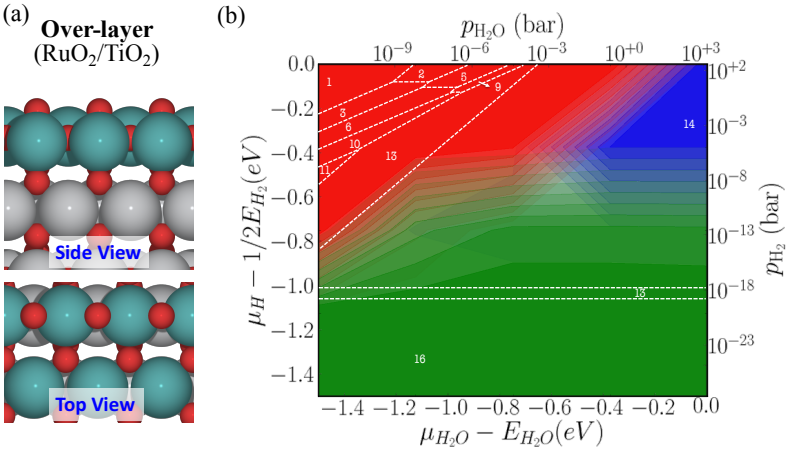

Figure 2-6. (a) Side and top view of the RuO_2/TiO_2(110) surface [teal: Ru, red: O, grey: Ti], (b) steady state kinetic phase diagram (KPD) with thermodynamic phase diagram (TPD) predicted with OBE+IP as a function of chemical potentials H_2 and H_2O at T = 500 K.

As in Figure 2-5, each colors in Figure 2-6 represents the different coverages of a different surface species and the surface phases are denoted with different color and number as (1) +0H/-6O, (2) +1H/-5O, (3) +0H/-5O, (4) +3H/-4O, (5) +1H/-4O, (6) +0H/-4O, (7) +3H/-3O, (8) 2H/-3O, (9) +1H/-3O, (10) +0H/-3O, (11) +0H/-2O, (12) +3H/-2O, (13) +1H/-1O, (14) +2H/-0O, (15) +1H/-0O, and (16) +0H/-0O. Overall, the KPD and TPD of RuO_2/TiO_2 are very similar just as in the case of RuO_2.In particular, for p_{H_2} < ca. 10^{-18} bar: RuO_2/TiO_2 has a stoichiometric surface termination; above p_{H_2}> ca. 10^{-5} bar and p_{H_2O} > ca. 1.0 bar: the O^{br} sites were either partially or fully hydroxylated (forming HO^{br}); and below p_{H_2O}< ca. 0.1 and above p_{H_2}> ca. 10^{-13} bar: V_{vac} become dominant. The KPD shows a smaller area for $\theta_{HO^{br}}$ and a large area for the reduced surface and stoichiometric surface than the TPD [see Figure 2-6(b)]. Yet, the overall agreement is good and confirms that the new scaling relations work well for the binary RuO_2/TiO_2 surface.

In conclusion, surface free energies derived from both OBE and SBE predict similar surface phase diagrams and the energy description can be further interpolated by intruding IP, indicating that: (1) our scaling correlations have enough accuracy to predict the most dominant surface terminations under the practical catalysis conditions; and (2) discrete results obtained under the constraints of small unit cells can be interpolated by introducing a model based on interaction parameters. This last point suggest that cumbersome cluster expansion methods may not be necessary to complete the phase space outside the easily accessible region of DFT simulations. We also anticipate that our scaling relations would work for the other transition metal oxides such as WO_3, Mn_3O_4, MoO_3, Cr_2O_3, Fe_2O_3, etc. and transition metal sulfides. For both materials surface vacancy sites are paramount for their catalytic activity.

2.4. Conclusions

We suggest a novel and rapid method to predict surface phase diagrams of rutile surfaces including MO_2(110) with M = Ru, Ti, Ir, Rh, Sn, Pt, Pd, and V. This method requires only the vacancy creation energy (ΔE_v: $O^{br} + H_2 \leftrightarrow H_2O + V_o$) at a bridging oxygen site as input and otherwise relies on linear scaling relations. Thus, this method can greatly reduce the amount of DFT calculations necessary to develop a full phase diagram. We used an extended interaction

model to estimate the adsorbate-adsorbate interaction parameters, which allows us to interpolate our discrete data points and add continuity to the derived phase diagrams, which then show the existence of additional intermediate phases. We also derived a kinetic phase diagram using kinetic Monte Carlo simulations and compared it with the thermodynamic phase diagram derived from scaled binding energies. Both phase diagrams predicted similar phase behavior under the same reaction conditions, indicating that our linear relations have sufficient accuracy for the prediction of dominant surface terminations. Under typical hydrotreating conditions, we find that rutile surfaces are fully hydrogenated at the bridging oxygen sites. Notably, the linear scaling relations can be extended to treat mixed oxides, as we have demonstrated for the $RuO_2/TiO_2(110)$ surface.

Chapter 3. First-principles Investigation of the Active Site and the Reaction Mechanism of Acetaldehyde Hydrodeoxygenation over $Ru/TiO_2(110)$

3.1. Introduction

As introduced in Chapter 1 HDO catalysis can be separated into two main categories: (i) hydrogenation (HYD) / direct deoxygenation (DDO), a reaction in which oxygen atoms are removed as H_2O from oxygenated molecules in the presence of high pressure hydrogen gas, and (ii) decarbonylation (DCN) or decarboxylation (DCX) where oxygen is removed in the form of CO and CO_2, respectively. The selectivity between HYD/DDO and DCN/DCX depends primarily on the catalyst's tendency for preferentially breaking C-O or C-C bonds in oxygenated molecules. For the production of liquid fuel, it is clearly desirable to maintain the carbon content of the reactants, which makes the HYD and DDO routes more attractive than DCN or DCX.

Most recently, Ru/TiO_2 draws attention as catalyst for HDO of phenolic compounds such as cresol, guaiacol, acetic acid, and phenol, because good catalytic activity and selectivity toward ideal HDO products can be achieved[99–101]. However, the nature of the active site or the preference of certain sites to catalyze specific reaction steps is still debated. More specifically, it remains unknown which sites [e.g. TiO_2, metallic Ru, oxidized Ru (RuO_x), or the Ru/TiO_2 interface] catalyze preferentially DDO over HYD or DCN. Here, we use acetaldehyde (CH_3CHO) to study possible reaction pathways at different reaction sites by periodic DFT calculations on model surface describing the experimentally known Ru/TiO_2 catalyst. CH_3CHO is a good surrogate molecule for aldehydes and ketones, which form the third largest functional class in biomass fast pyrolysis oil. It also allows us to address the issue of selectivity, because it contains both C-C and C-O bonds. Preferential bond scission would indicate the overall catalytic selectivity of a catalyst for HYD, DDO, or DCN.

The three major HDO reaction pathways are summarized in Figure 3-1. The first pathway is HYD, which requires multiple hydrogenation steps and consumes more hydrogen than the other

pathways. In the HYD pathway CH_3CHO is converted to ethanol (CH_3CH_2OH), followed by rapid dehydration and hydrogenation to ethane (CH_3CH_3) and water (green line in Figure 3-1). It is generally believed that the dehydration step over solid acid catalysts is fast and facile, and thus we have not explicitly investigated[102]. The second pathway is DDO, in which CH_3CHO is converted to CH_2CH_2 (black line in Figure 3-1). Because DDO consumes less hydrogen than HYD and keeps the number of carbon atoms in CH_3CHO constant, it is considered to be the ideal HDO pathway. The third pathway is DCN and produces by-products such as CO, methane (CH_4), or coke. DCN often leads to catalyst deactivation (red line in Figure 3-1). Figure 3-1 clearly indicates that hydrogen consumption and the number of carbon atoms in the deoxygenated products are important factors for the design of HDO catalysts.

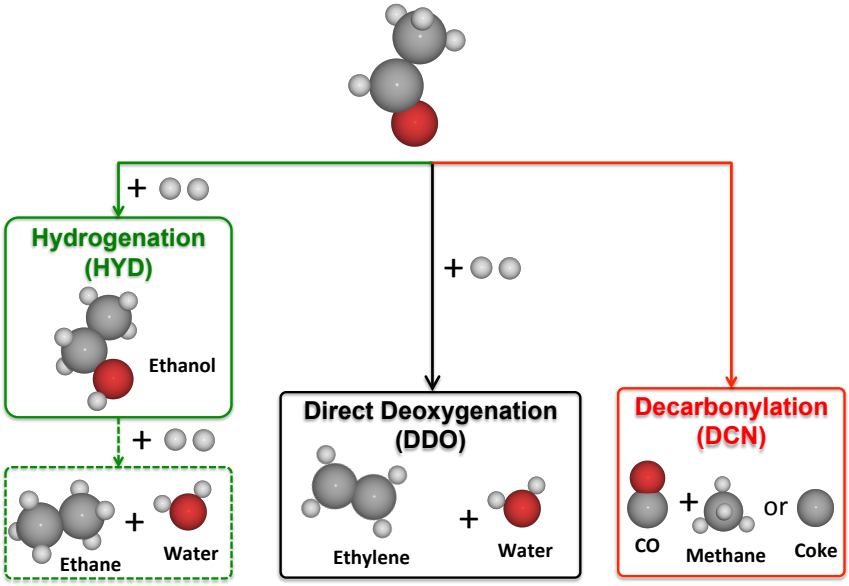

Figure 3-1. Three main reaction pathways of CH_3CHO (white – hydrogen / red – oxygen / gray – carbon). The colors (green, black, and red) indicate hydrogenation, direct deoxygenation, and decarbonylation, respectively.

To identify the nature of the active site and develop a reaction mechanism for HDO pathways of CH_3CHO over Ru/TiO_2, we considered six different model systems such as metallic Ru(0001), TiO_2(110), doped-Ru/TiO_2, RuO_2/TiO_2(110), RuO_2(110), Ru_{10}/TiO_2(110). The goal of this chapter is twofold. We aim to identify the active site for HDO reaction pathways of CH_3CHO over these model systems, and determine trends in bond activation preference (C-O, C=O, and C-H), which

would directly answer the aforementioned selectivity question. Ultimately, these results can be used to guide the design of novel HDO metal or metal-oxide catalysts with desired properties.

3.2. Computational methods

All density functional theory (DFT) calculations (adsorption energies, activation energy barriers and vibrational frequencies) reported here have been calculated using the Vienna Ab-initio Simulation Package (VASP) in combination with the Atomic Simulation Environment (ASE) [63,64,103,104]. The revised Perdew – Burke – Ernzerhoff - generalized gradient approximation (RPBE - GGA) was used as exchange-correlation functional[40,105]. The interactions between core and valence electrons were represented by the projected augmented wave (PAW) method[65,103,106], and the cut-off energy of 400 eV for plane wave was selected for this study. For accurate electronic state descriptions we treated Ti(3s,3p,3d,4s), doped-Ru(4p,5s,4d), overlaid Ru(4p,5s,4d), metallic Ru(4d,5s), and O(2s,2p) as valence electrons, whereas the remaining electrons were kept frozen as core state. Spin polarization was included except for RuO_2(110) and Ru(0001), which both have metallic character. A Fermi temperature (k_BT) of 0.1 eV and 0.01 eV was chosen for all slab calculations and gas phase molecules (CH_3CHO, H_2, H_2O, C_2H_4, CH_3CH_2OH, CO, and CH_4), respectively, and the resulting energies were extrapolated to zero electronic temperature[71]. The conjugate gradient algorithm with a force convergence criterion of 0.05 eV/Å was used for ionic relaxations of equilibrium geometries. The optimized bulk lattice constants are a = 2.689 Å, c/a = 1.637 for the Ru(0001), a = 4.589 Å, c/a = 0.686, u = 0.306 for the RuO_2(110), and a = 4.712 Å, c/a = 0.640, u = 0.306 for the TiO_2(110), which are in good agreement with experimental data[107–110].

It is well known that DFT fails to describe correct electronic structure for strongly correlated systems due to errors associated with on-site Coulomb and exchange interactions. TiO_2 is one of example belong to this category having highly localized Ti 3d states, i.e., electrons occupying conduction band experiencing strong Columbic repulsion (strong local interaction) which is poorly described with standard GGA functionals[111]. Hence, in order to resolve this problem, we applied a Hubbard-U correction (DFT+U) for model systems associated with TiO_2(110) surface [TiO_2,

doped-Ru_1/TiO_2, RuO_2/TiO_2, Ru_{10}/TiO_2]. We estimated the value of U_{eff} = U – J from the experimentally determined reaction enthalpy of the reaction (ΔH), $2TiO_2 + H_2 \rightarrow Ti_2O_3 + H_2O$[112,113]. The fitted value of U_{eff} = 2.0 eV yielded good agreement with the experimental heat of reaction and is in good agreement with other studies[114].

All slabs consist of four atomic layers with the top two layers are fully relaxed and the bottom two layers fixed at their bulk positions. To avoid interaction between successive slabs due to the periodic boundary conditions, the unit cell included 16 Å of vacuum along the normal direction of the surface. A dipole correction was applied to compensate the effect of adsorbing molecules only on one side of each surface[70]. The Brillouin zone was sampled with (8×8×1) for Ru(0001), (6×8×1) for RuO_2(110) and TiO_2(110), and (2×2×1) for Ru_{10}/TiO_2(110) Monkhorst-Pack k-point grids[67]. Binding energies (E_{BE}) are calculated with respect to the clean surface and the gas phase molecules (H_2, CH_4, CH_3CHO) according to

$$E_{\mathrm{BE}} = E_{\mathrm{slab+adsorbate}} - (E_{\mathrm{slab}} + E_{\mathrm{molecule}}), \tag{3-1}$$

where $E_{slab+adsorbate}$ is total energy of the slab with adsorbates, E_{slab} is the energy of clean surface, and $E_{molecule}$ is the energy of reference gas phase molecules. A negative value of the E_{BE} means favorable (exothermic) binding. The climbing image nudged elastic band (cNEB) method[72] was implemented to determine transition state (TS) of elementary reaction steps and reactions paths were interpolated with five or six intermediate images, which were fully optimized to a force criterion of 0.1 eV $Å^{-1}$. Vibrational analysis was performed to confirm the existence of a single imaginary mode, corresponding to the reaction coordinate along the reaction path.

The top and side view of our model surfaces on which we have investigated acetaldehyde HDO are shown in Figure 3-2: (a) stoichiometric p(3 × 2) TiO_2(110), (b) Ru_1TiO_2(110) where one of the coordinatively unsaturated Ti atom is replaced only doped with a Ru atom, (c) 1 ML RuO_2/TiO_2 where the top layer of TiO_2 was replaced with RuO_2(110), (d) stoichiometric p(3 × 2) RuO_2(110), and (e) supported-Ru_{10}/TiO_2(110). In addition, we also used a p(3 × 3) Ru(0001) surface to assess the reactivity of Ru alone (not shown). The most stable rutile phase was chosen for both RuO_2 and TiO_2, and in case for the Ru_{10}/TiO_2(110) 10 Ru atoms were placed on

top of partially reduced TiO_2(110) surface to anchor the Ru nano-cluster[88,115]. Ten Ru atoms contain the smallest number of Ru atoms that can form the *hcp* structure, yet it is larger enough to approximate the hemispherical cluster shape that was observed in experiments[116]. After Ru doping, the Ru_1TiO_2 exhibits two different adsorption sites, the coordinatively unsaturated Ti (Ti^{cus}) and Ru site (Ru^{cus}) see Figure 3-2(b)), which we have treated separately.

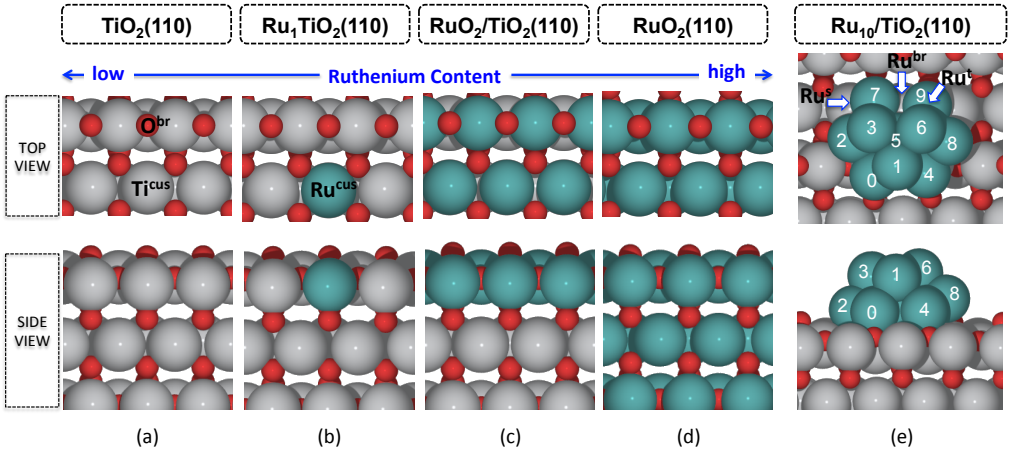

Figure 3-2. Model surfaces (gray: Ti, teal: Ru, and red: O): (a) TiO_2(110), (b) doped-Ru_1/TiO_2, (c) 1 ML RuO_2/TiO_2(110), (d) RuO_2(110), and (e) supported-Ru_{10}/TiO_2(110). The O^{br}, Ti^{cus}/Ru^{cus}, Ru^{s}, Ru^{br}, and Ru^{t} mean bridging O, coordinatively unsaturated Ru/Ti, side of Ru, Ru bridge site, Ru top site, respectively.

3.3. Results and Discussion

3.3.1. Acetaldehyde HDO on metallic Ru(0001)

Table 3-1. Major elementary steps studied on the Ru(0001) surface[a].

no.	Reaction	E_{int}^{IS}	E_{int}^{FS}	E_a	ΔE	[b]ν
M0	H_2 + 2* ↔ 2H*				-0.76	
M1	CO + * ↔ CO*				-1.52	
M2	CO_2*↔ CO_2 + *				-2.93	
M3	CH_3CHO + * ↔ CH_3CHO*				-0.09	
M4	CH_2CH_2 + * ↔ CH_2CH_2*				-0.77	
M5	CH_3CHO* + * ↔ CH_3CO* + H*	0.00	0.26	0.20	-0.84	352
M6	CH_3CHO* + * ↔ CH_2CHO* + H*	0.00	0.27	0.46	-0.47	84
M7	CH_2CHO* + * ↔ CH_2CO* + H*	0.00	0.17	0.31	-0.38	788
M8	CH_3CO* + * ↔ CH_2CO* + H*	0.00	0.43	0.84	-0.02	868
M9	CH_2CO* + * ↔ CH_2* + CO*	0.45	0.41	0.52	-0.69	141
M10	CH_2* + H* ↔ CH_3* + *	0.27	0.00	0.75	0.26	845
M11	CH_3* + H* ↔ CH_4 + 2*	0.32	0.00	1.11	-0.13	942
M12	CH_2* + * ↔ CH* + H*	0.00	0.28	0.12	-0.62	760
M13	CH* + * ↔ C* + H*	0.00	0.23	1.00	0.08	854

Table 3.1 continued

M14	$CH_2CHO^* + H^* \leftrightarrow CH_2CH_2O^* + *$	0.32	0.22	1.16	0.66	638
M15	$CH_2CH_2O^* + * \leftrightarrow CH_2CH_2^* + O^*$	0.00	0.31	0.55	-0.70	471
M16	$CH_2CH_2^* \leftrightarrow * + CH_2CH_2$	0.00	0.00	0.54	0.47	80
M17	$CH_3CHO^* + H^* \leftrightarrow CH_3CH_2O^* + *$	0.28	0.00	0.86	0.07	196
M18	$CH_3CH_2O^* + H^* \leftrightarrow CH_3CH_2OH + 2^*$	0.10	0.00	1.32	0.45	1220
M19	$H^* + O^* \leftrightarrow OH^* + *$	0.41	0.04	1.77	0.80	1371
M20	$H^* + OH^* \leftrightarrow H_2O + 2^*$	0.65	0.00	1.70	0.39	1124
M22	$CH_3CHO^* \leftrightarrow CH_3^* + CHO^*$	0.00	-0.45	1.10	0.46	381
M23	$CH_3CHO^* \leftrightarrow CH_3CH^* + O^*$	0.00	0.67	0.91	-0.77	405
M24	$CH_3CO^* \leftrightarrow CH_3^* + CO^*$	0.00	0.27	1.11	-0.44	381
M25	$CH_3CO^* \leftrightarrow CH_3C^* + O^*$	0.00	0.25	1.06	-0.89	53
M26	$CH_3C^* \leftrightarrow CH_3^* + C^*$	0.10	-2.03	1.84	3.67	173
M27	$CH_3C^* \leftrightarrow CH_2C^* + H^*$	0.10	0.29	0.80	0.06	854
M28	$CH_2C^* \leftrightarrow CH_2^* + C^*$	0.00	-2.60	1.89	3.39	339
M29	$CH_2C^* \leftrightarrow CHC^* + H^*$	0.00	0.29	1.04	0.05	755
M30	$CHC^* \leftrightarrow CC^* + H^*$	0.00	0.00	1.53	0.70	1074
M31	$CH_2CHO^* \leftrightarrow CH_2^* + CHO^*$	0.00	-0.35	0.97	0.67	348
M32	$CH_2CHO^* \leftrightarrow CH_2CH^* + O^*$	0.00	0.31	1.32	-0.70	446
M33	$CH_2CHO^* \leftrightarrow CHCHO^* + H^*$	0.08	0.33	0.61	-0.52	651
M34	$CH_2CO^* \leftrightarrow CH_2C^* + O^*$	0.00	0.25	1.44	-0.81	507
M35	$CH_2CO^* \leftrightarrow CHCO^* + H^*$	0.00	0.26	0.75	-0.34	907

[a] $E_{\mathrm{int}}^{\mathrm{IS}}$, $E_{\mathrm{int}}^{\mathrm{FS}}$, E_a, and ΔE are in eV. E_{int} denotes the interactions between adsorbates in the IS and FS during NEB calculations. ΔE and E_a are the total energy change and activation energy barriers without ZPE correction. [b] ν denotes the frequency of the imaginary mode at the TS in cm^{-1}.

In this section, HDO mechanism of CH_3CHO on the metallic Ru(0001) surface has been discussed. Because of the large number of elementary steps for CH_3CHO HDO on Ru(0001), we limit our discussion only on the key elementary steps in Table 3-1. The adsorption configurations of major intermediates involved in these key elementary steps are depicted in Figure 3-3. Due to the complex adsorption geometries of the intermediates, commonly used standard adsorption site naming, i.e. top, bridge, 3-fold, etc., do not provide a detailed enough description. Hence, we used the extended notation, $\mu^i\eta^j$ where 'i' and 'j' indicate the number of atoms interacting between adsorbates (i) and the surface (j), respectively.

The Ru(0001) metal surface has four different high-symmetry adsorption sites (top, bridge, hcp, and fcc). Although Iker del Rosal *et al*. have reported a total of seven different adsorption sites including three extra sites (two tetrahedral and octahedral), these are discarded in our study because these sites are energetically unfavorable for high coverage of hydrogen[110]. CH_3CHO can

adsorb on the metallic Ru(0001) surface in multiple configurations and we identified the $\mu^2\eta^3$ adsorption as the most stable adsorption geometry with E_{BE} = -0.09 eV shown in Figure 3-3(a). In this configuration, the oxygen and αC atom of CH_3CHO bind to the bridge site and top site, respectively. The C=O axis of CH_3CHO is nearly parallel to the Ru(0001) surface, indicating that π-bonding of the C=O orbitals and lone pair electrons of the oxygen are interacting with d-band electrons of Ru surface atoms[117,118].

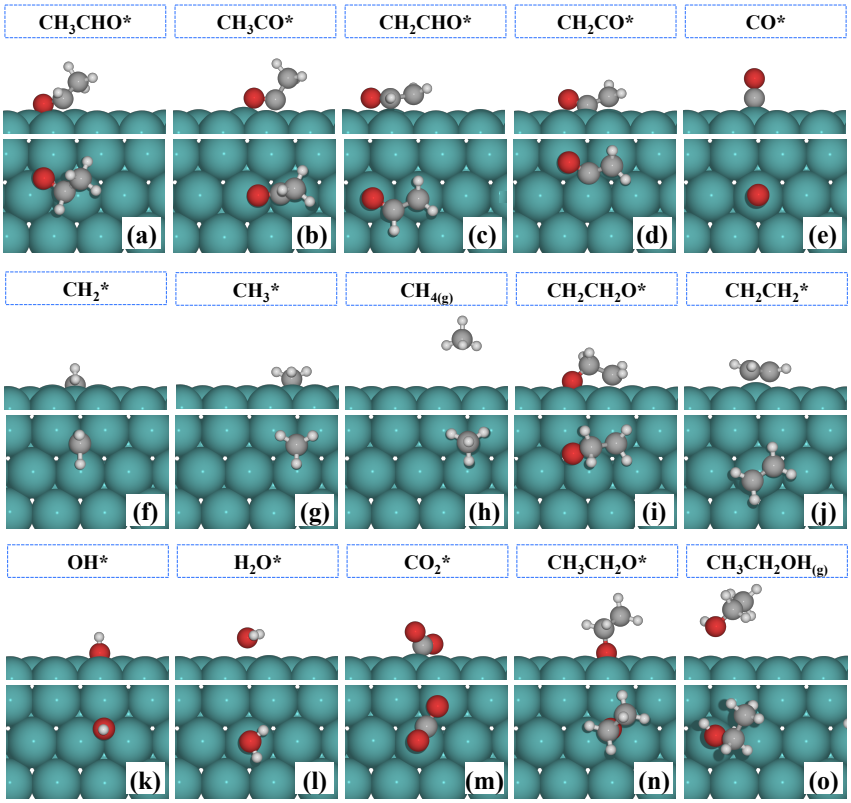

Figure 3-3. Most stable surface intermediates during CH_3CHO DDO on the Ru(0001) (white – hydrogen / red – oxygen / gray – carbon / teal – ruthenium). (a) CH_3CHO*, (b) CH_3CO*, (c) CH_2CHO*, (d) CH_2CO*, (e) CO*, (f) CH_2*, (g) CH_3*, (h) $CH_{4(g)}$, (i) CH_2CH_2O*, (j) CH_2CH_2*, (k) OH*, (l) H_2O*, (m) CO_2*, (n) CH_3CH_2O*, and (o) $CH_3CH_2OH_{(g)}$.

After molecular adsorption of CH_3CHO on the Ru surface, the calculated bond distances $d_{C=O}$ and d_{C-C} of CH_3CHO are elongated by 16 % to 1.421 Å and by 0.79 % to 1.523 Å with respect to the gas-phase CH_3CHO molecule, respectively. This result is consistent with adsorption configuration of CH_3CHO on Mo(110), Pt(111), Pd(110/111), and Rh(111) where CH_3CHO adsorbs with both $\mu^1\eta^1$ and $\mu^2\eta^3$ configurations at low temperature primarily through interaction of the oxygen atom and the transition metal surface[29,53,118,119]. The $\mu^1\eta^1$ adsorption configuration is only stable at low

temperatures and as temperature increases, only the more stable $\mu^2\eta^3$ configuration remains on the surface. These results are further supported by extended Hückel calculations that also predict the $\mu^2\eta^3$ configuration to be more stable over the $\mu^1\eta^1$ geometry[119]. The kinetically and thermodynamically preferred initiation of possible HDO pathways are the two αC-H and ßC-H scission steps (reaction M5 and M6 in Table 3-1). Reaction M5 is the αC-H scission in CH_3CHO^* leading to CH_3CO^* with E_a = 0.20 eV and ΔE = -0.84 eV as depicted in Figure 3-4(a). At the TS, the calculated $d_{C\text{-}H}$ is elongated to 1.14 Å, and the elongated hydrogen is pointing towards the fcc site. Following the reaction coordinate further, the H adatom diffuses to the hcp site due to repulsion between hydrogen and the acetyl [CH_3CO^*, Figure 3-3(b) - $\mu^2\eta^2$] intermediate. Reaction M6 describes the ßC-H bond scission in CH_3CHO^*, producing adsorbed vinoxy [CH_2CHO^*, Figure 3-3(c) - $\mu^6\eta^3$] with E_a = 0.46 eV and ΔE = -0.47 eV, respectively. Although the energy barrier of reaction M6 is a slightly higher than that of reaction M5, reaction M6 must be considered as a feasible step under the practical HDO reaction temperatures. Hence, we took reaction M5 and M6 into account as competitive pathways. The adsorption configurations of the two resulting intermediates, CH_3CO^* and CH_2CHO^* are shown in Figure 3-3(b) and (c). The CH_2CHO^* intermediate can further decompose along four different pathways to form CH_2^* + COH* (reaction M31), CHCHO* + H* (reaction M32), CH_2CH^* + O* (reaction M33), and CH_2CO^* + H* (reaction M7). Reaction M7 leading to CH_2CO^* and H* is the kinetically preferred pathway with E_a = 0.31 eV and ΔE = -0.38 eV. The other possibilities (reaction M31, M32, and M33) have significantly higher energy barriers as listed Table 3-1. The alternative decomposition product of CH_3CHO^* is CH_3CO^*, which can also be dehydrogenated to CH_2CO^* via reaction M8 in Table 3-1. At the TS, the C-C axis of CH_3CO^* tilts towards the Ru surface to facilitate the ßC-H bond activation, and the calculated $d_{C\text{-}H}$ is elongated to 1.155 Å as shown in Figure 3-4(b). This reaction is quasi thermo-neutral (ΔE = -0.02 eV) and the calculated energy barrier is 0.84 eV. Although we are unable to determine the exact order of the first two C-H bond activation steps on the basis of our DFT results, we note that both reactions M7 and M8 lead to the same ketene [CH_2CO^*, Figure 3-3(d) - $\mu^3\eta^3$] intermediate.

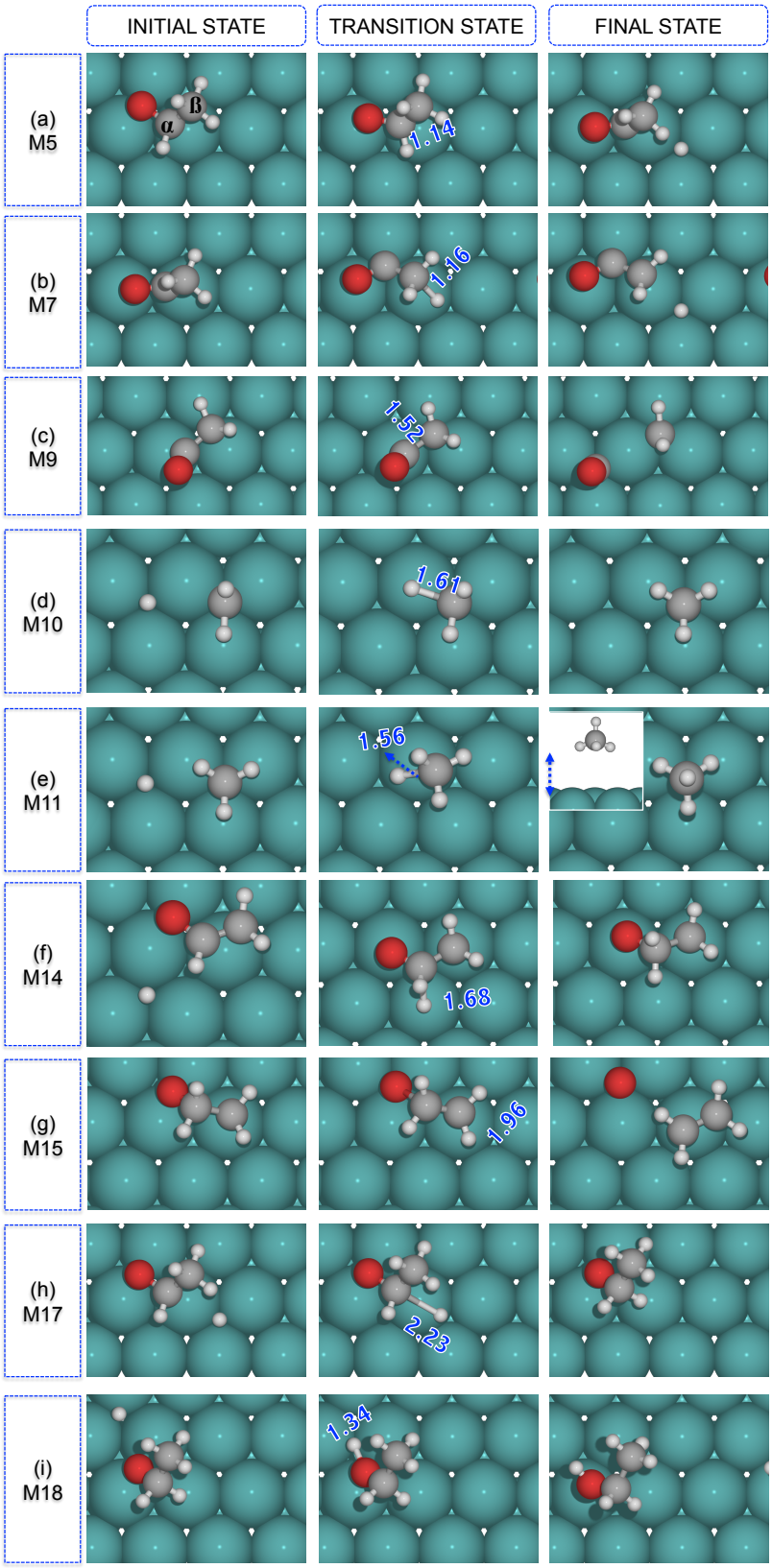

Figure 3-4. Calculated reaction pathway of CH_3CHO HDO on the Ru(0001) (white – hydrogen / red – oxygen / gray – carbon / teal – ruthenium). (a) M5; (b) M8; (c) M9; (d) M10; (e) M11; (f) M14; (g) M15; (h) M17; (i) M18.

The calculated binding energy of CH_2CO^* is E_{BE} = 0.28 eV. At this point of the mechanism, the C-C bond of CH_2CO^* is easily broken via the DCN reaction, leaving behind carbon monoxide (CO*) and methylene (CH_2^*) on Ru surface via step M9 [E_a = 0.52 eV, ΔE = -0.69 eV]. The carbon monoxide (CO*) fragment of CH_2CO^* is strongly adsorbed through its carbon atom on top of the Ru [E_{BE} = -1.52 eV, Figure 3-3(e) - $\mu^1\eta^1$], which is in good agreement with other theoretical and experimental data[120,121]. The CH_2^* fragment, however, is unfavorably bound to the hcp site with E_{BE} = 1.12 eV with respect to gas phase CH_4 and H_2 [see Figure 3-3(f) - $\mu^2\eta^3$], which also agrees well with previous DFT results[122]. The intermediate CH_2^* can proceed either through a hydrogenation or dehydrogenation pathway, which may depend on the reaction conditions. The former hydrogenation pathway leads to methane (CH_4) in the gas-phase, while the latter dehydrogenation pathway results in carbon deposition on the Ru(0001) surface. Before we discuss the hydrogenation process occurring through reaction M10 and reaction M11 in Table 3-1, we note that the binding preference of hydrogen in the presence of co-adsorbed CH_2^* and CH_3^* is altered. On the clean Ru(0001) surface, H atom adsorbs on fcc sites with E_{BE} = -0.61 eV, but when CH_2^* and CH_3^* intermediates are co-adsorbed, the hcp site is found to be the most favorable adsorption site for H adatom. These adsorption site preferences are in good agreement with other DFT and experimental data[122]. The adsorbed CH_2^* can be hydrogenated with an H* atom from the *hcp* site to methyl [CH_3^*, Figure 3-3(g) - $\mu^4\eta^3$] and the corresponding energetics are E_a = 0.75 eV and ΔE = 0.26 eV [see Figure 3-4(d)]. The resulting CH_3^* intermediate can be further hydrogenated to CH_4 through reaction M11 with E_a = 1.11 eV and ΔE = -0.13 eV as shown in Figure 3-4(e). At the TS, the calculated $d_{C\text{-}H}$ is 1.61 Å in case of the reaction M10 and 1.56 Å in case of the reaction M11. The second hydrogenation of CH_3^* to CH_4 has a higher energy barrier than the first hydrogenation of CH_2^*, which is consistent with other DFT studies of the methanation reaction over various transition metal catalyst surfaces[123,124]. Along the hydrogenation coordinate ($C^* + 4H^* \rightarrow CH^* + 3H^* \rightarrow CH_2^* + 2H^* \rightarrow CH_3^* + H^* \rightarrow CH_4$), the total energy of the TS keeps increasing, suggesting that the last CH_3^* hydrogenation is the rate-determining step, which also is associated with the highest individual reaction barrier in this

reaction sequence[125]. Once the CH_3* forms a bond with the surface hydrogen, the formed CH_4 desorbs spontaneously from the surface.

Alternatively, the CH_2* intermediate can also be dehydrogenated to methylidyne (CH*) and H* (via reaction M12), followed by CH* decomposition into C* and H* (via reaction M13) on the surface. In both reactions, the separated hydrogen atom moves to the fcc site, while the CH_2* and CH* species stay at the hcp site during the reactions. The calculated E_a and ΔE are 0.12 eV and -0.63 eV for reaction M12 and 1.00 eV and 0.08 eV for reaction M13, respectively. From a thermodynamic and kinetic perspective, the dehydrogenation of CH_2* to surface carbon is preferred over the hydrogenation pathway leading to CH_4. Hence, carbon or CH* poisoning on Ru surface is expected, which can eventually lead to catalyst deactivation. These predictions are in agreement with a study done by Cheng *et al.*, reporting that among Re, Fe, Co, Rh and Ru, the Ru catalyst is the least suited catalysts for methanation because of a high effective energy barrier for CH_4 formation[123]. On the other hand, the same study reports that Ru is the best catalyst for C-C coupling reaction and if we invoke the concept of microscopic reversibility this may further suggest that C-C bond scission is also effectively catalyzed.

Kinetically and thermodynamically preferred reaction pathways of CH_3CHO on the Ru(0001) discussed up to this point suggest that unselective C-O bond breaking, or in the most optimistic scenario, DCN to methane would take place. The desired product ethylene (CH_2CH_2) is unlikely to be formed on the metallic Ru(0001) surface, but one of the powerful advantages of computational catalysis tools is the possibility to investigate mechanism even for unselective pathways. The mechanism leading to CH_2CH_2 formation starts from adsorbed CH_2CHO* and the necessary steps are shown in Figure 3-4(f) and (g). Hydrogenation at the ßC through reaction M14 forms CH_2CH_2O* [$\mu^2\eta^3$, E_{BE} = 0.09 eV] displayed in Figure 3-3(i). The calculated E_a and ΔE are 1.16 eV and 0.66 eV, respectively, and the calculated $d_{C\text{-}H}$ at the TS is 1.68 Å. The resulting CH_2CH_2O* intermediate is then deoxygenated through step M15 as shown in Figure 3-4(g). The dissociated oxygen moves to the hcp site in the FS and CH_2CH_2* [Figure 3-3 (j) - $\mu^2\eta^1$] preferentially adsorbs on the top site with E_{BE} = -0.77 eV. At the TS, the calculated $d_{C\text{-}O}$ is elongated from 1.46 Å to 1.96 Å. The E_{BE} of co-adsorbed CH_2CH_2* and O* is exothermic by -0.87

eV with respect to the energy of gas phase CH_3CHO and CH_4. This configuration of CH_2CH_2 adsorption is consistent with previous DFT calculations[117]. The desorption step of the formed CH_2CH_2* has an energy barrier of 0.54 eV and is endothermic by 0.47 eV. After CH_2CH_2* desorption, surface O* is left on the hcp site of the Ru surface with E_{BE} = -2.83 eV, referenced to energy of gas phase H_2, CH_4, and CH_3CHO. Surface O* binds even more strongly than surface CO* (E_{BE} = -1.52 eV), which is attributed to the high oxygen affinity of Ru metal to the oxygen atom [126]. Removal of surface O* can be achieved either via M19 – 20 to form H_2O, or M21 to form CO_2. To form H_2O the surface O* reacts with an H adatom adsorbed on the fcc site [via reaction M19 in Table 1] to from hydroxyl [OH*, Figure 3-3(k) - $\mu^1\eta^3$], further followed by another hydrogenation via reaction M20 in Table 3-1, forming water at the top site [H_2O*, Figure 3-3(l) - $\mu^3\eta^1$]. The calculated energy barriers are 1.77 eV (reaction M19) and 1.70 eV (reaction M20), respectively. The alternative option, removal of surface O* via CO_2 formation, is required the reaction between surface O* and CO* adsorbed on the top site. The calculated energy barrier and change for the CO oxidation steps are E_a = 1.77 eV and ΔE = 1.43 eV, respectively. It clearly shows that removal of surface O* is extremely unfavorable because of the strong affinity of Ru to oxygen, which may lead to surface poisoning or phase transition to a surface or bulk metal oxide[126].

It is also established that HYD of CH_3CHO to form ethanol (CH_3CH_2OH) occurs under elevated H_2 pressure over transition metal catalysts such as Au, Pt, Rh, Ru, and Au [127,128]. Among these catalysts, Ru is considered as the most active catalyst for aqueous phase hydrogenation (APH) of non-furanic carbonyl groups which include acetaldehyde, propanal, acetone, and xylose [128]. This experimental evidence motivates our study of ethanol formation via HYD of CH_3CHO. The reaction starts with a hydrogenation of CH_3CHO to the βC as shown in Figure 3-4(h) through reaction M17 in Table 3-1, which forms ethoxy [CH_3CH_2O*, Figure 3-3(n) - $\mu^1\eta^3$]. The calculated E_{BE} of ethoxy specie is -0.64 eV. It is then followed by another hydrogenation step, reaction M18 shown in Figure 3-4(i), producing the final product gas-phase ethanol [CH_3CH_2OH, see Figure 3-3(o)]. The calculated E_a and ΔE are 0.86 eV and 0.07 eV for reaction M17, and 1.32 eV and 0.45 eV for reaction M18, respectively. The calculated $d_{C\text{-}H}$ and

$d_{O\text{-}H}$ distance at the TS are 2.23 Å in reaction M17, and 1.36 Å in reaction M18, respectively. The formed ethanol desorbs slightly after reaction M18, and forms a physisorbed state with E_{BE} = -0.80 eV. Ethanol can be further hydro-treated, and converted into ethane (C_2H_6) and water via dehydration on acid supports as explained before (see Figure 3-1). Since dehydration of alcohol is considered facile over acidic catalysts, we did not study the remainder of the reaction pathway[129].

A summary of the all elementary steps leading to surface coking, CH_4 and CO, CH_3CH_2OH and CH_2CH_2 starting from CH_3CHO on the Ru(0001) surface are summarized in a form of potential energy surface (PES) in Figure 3-5. Intermediate states are (1) Ru (clean surface), (2) CH_3CHO* (CH_3CHO adsorption), (3) CH_3CO* + H*, (4) CH_2CO* + 2H*, (5) CH_2* + CO* + 2H*, (6) CH* + CO* + 3H*, (7) C* + CO* + 4H*, (8) C* + 4H*(after CO desorption), (9) CH_3* + CO* + H*, (10) $CH_{4(g)}$ + CO*, (11) Ru (clean surface after CO desorption), (12) CH_2CHO* + H*, (13) CH_2CH_2O*, (14) CH_2CH_2* + O*, (15) $CH_2CH_{2(g)}$ + O*, (16) O* + 2H* (H_2 adsorption), (17) OH* + H*, (18) H_2O*, (19) H_2O(g) (after H_2O desorption), (20) O* + CO* (CO adsorption), (21) CO_2*, and (22) $CO_{2(g)}$ (after CO_2 desorption). CH_3CHO molecule adsorbs on the Ru surface through the C=O group [state (2) in Figure 3-5] and then proceeds through two competitive dehydrogenation pathways [αC-H (reaction M5) / ßC-H (reaction M6)] leading to the same intermediate, CH_2CO* [state (4) in Figure 3-5]. This is followed by C-C bond breaking resulting in CO* and CH_2* [state (5) in Figure 3-5]. The intermediate, CH_2*, can be either successively hydrogenated to CH_4 via reaction M10 and M11 [state (11) in Figure 3-5] or even more readily dehydrogenated to surface carbon via reaction M12 and M13 [state (7) in Figure 3-5]. The unselective DDO pathways are also included with black line in Figure 3-5, and branch from the main pathway at the CH_2CHO* intermediate [state (12) in Figure 3-5]. This intermediate can be hydrogenated to CH_2CH_2O* via reaction M14, [state (13) in Figure 3-5] with a relatively high barrier E_a = 1.16 eV, which is then deoxygenated to CH_2CH_2* on the surface via reaction M15, [state (14) in Figure 3-5]. The chemisorbed CH_2CH_2* eventually desorbs form the surface into the gas phase with a barrier of E_a = 0.54 eV (reaction M16). The oxygen atom left behind on the Ru(0001) surface [state (15) in Figure 3-5] must also be removed in order to close the catalytic cycle. For this, we have

considered stepwise hydrogenation to H_2O [state (16) → state (19) in Figure 3-5] and the reaction from CO* to CO_2 [state (20) → state (22) in Figure 3-5]. Both pathways have large barriers of ca. 1.8 eV, which is significantly higher than the barriers for the steps required for $CH_2CH_{2(g)}$ formation. Hence, the removal of surface O* from Ru(0001) is the slowest step and unless the temperature is high enough to overcome the barrier for H_2O or CO_2 formation, the surface will slowly accumulate chemisorbed oxygen and may evolve into a surface oxide as studied elsewhere[79,130]. In our above analysis we assumed CO to be a reaction product that desorbs after its formation or it scavenges surface O* atom to produce CO_2. However, the Ru(0001) is not only known to be an active catalyst for CO oxidation[121], but also for Fischer-Tropsch (FT) synthesis, which may lead to CH_4 and higher alkanes through syngas reactions[121,122,131]. Because of its general catalytic importance, adsorption and dissociation of CO on Ru(0001) have been extensively studied. According to the CO adsorption and dissociation study on Ru(0001) surface at elevated pressures[121], the saturation CO coverage is ca. 0.66 ML under UHV conditions and adsorbed CO* on top is stable up to 450 K. Upon temperature increase to 485 K the CO coverage decreases to 0.58 ML, indicating molecular CO desorption from the surface. At higher temperatures (> 520 K), a significant amount of carbon deposits on the surface is observed and attributed to CO dissociation. A sizeable number of studies report that during FT synthesis hydrocarbons (C_xH_y) or even polymeric chains could be formed via the carbide mechanism over Co, Fe, and Ru catalysts[123,132]. However, recent DFT calculations on Co and Ru catalysts have shown that there are non-dissociative FT pathways that involve carbon-carbon coupling, rather than carbide mechanism[131]. Regardless of the still debated details of the FT mechanism, we note here that CO can be further hydrogenated at practical HDO conditions with high partial pressures of H_2. As a result, CO may be converted to either liquid hydrocarbons or methane as suggested by others[122,133]. Although these open questions are certainly relevant for a complete process design, we will not attempt to address these issues in our present work and keep our focus on understanding reaction pathways on metal and metal-oxide catalyst surfaces that preferentially break C-O bonds rather than C-C bonds.

Through the HYD pathway, CH_3CHO can also be converted into ethanol, which is depicted with the green solid line in Figure 3-5. It proceeds along a series of hydrogenation steps in which adsorbed CH_3CHO^* is hydrogenated to $CH_3CH_2O^*$, successively followed by another hydrogenation. This sequential HYD pathway is kinetically and thermodynamically unfavorable compared to DCN pathway. As we mentioned earlier, Huber's group has reported that metallic Ru surface is the best catalyst for APH of acetaldehyde, preferably leading to formation of ethanol [128]. Their conclusions differ from our DFT results as we propose that surface deactivation, formation of surface carbon, is more likely to occur than HYD on the Ru(0001) [128]. This discrepancy may be explained by difference in the coverage of surface intermediates and different surface facets or active sites. Furthermore, Huber *et al.* ranked the catalytic activity of transition metal catalysts based on initial turn over frequencies; give the thermodynamic preference for DCN to form coke (see Figure 3-5), we expect that coking and deactivation would be observed after running APH for a long enough time.

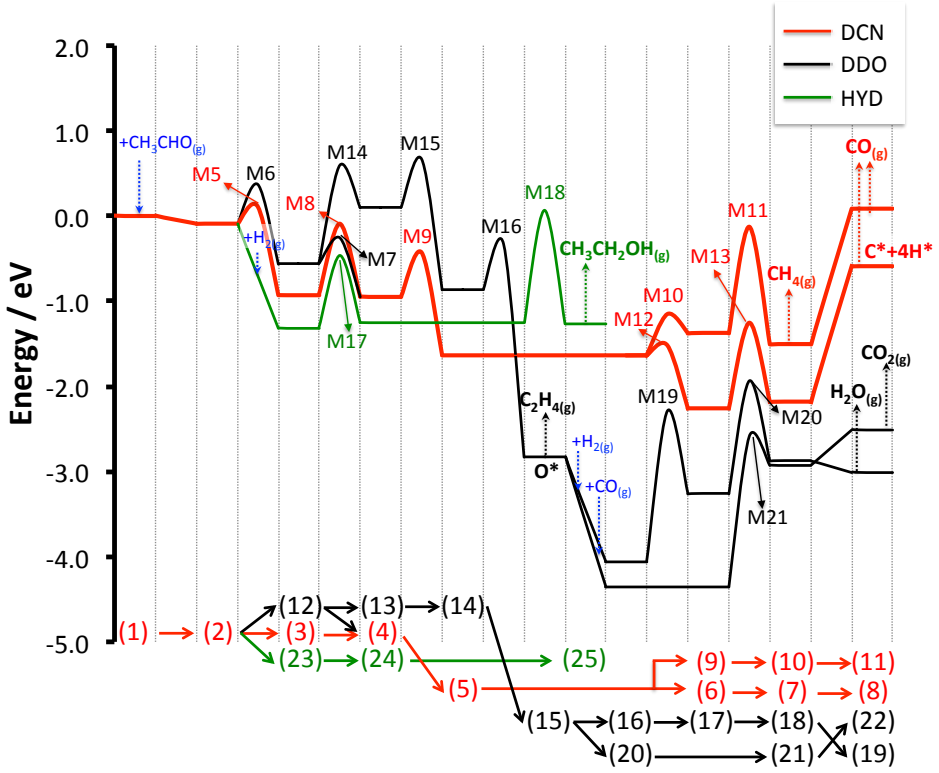

Figure 3-5. Potential energy surface of CH_3CHO HDO on the Ru(0001) surface. The black, blue, and red lines represent the most preferred DDO, HYD, and DCN, respectively.

3.3.2. Acetaldehyde HDO on Metal-Oxide Surfaces

3.3.2.1. Vacancy Formation Pathways under HDO Conditions

It is generally accepted that on stoichiometric rutile surfaces [MO_2(110): M = Ti and Ru], coordinately unsaturated metal atoms (M), referred to as the M^{cus} site, are the preferred adsorption sites for small molecules such as CO, O_2, N_2O and CH_3CHO with fairly high adsorption energies (≤ -0.7 eV) because of its localized electronic properties [97,134,135]. However, at elevated temperature and pressure conditions under which all practical catalysis is performed the most active oxide surface may significantly deviate from the stoichiometric MO_2(110) [M = Ti or Ru] surface. Hence, it is necessary to bridge the zero pressure and temperature conditions of DFT results with practical HDO conditions (e.g. $p_{\mathrm{H_2}}$ > 200 bar, T > 400 K) where surface modification can easily occur on metal-oxides as a result of partial surface reduction or vacancy formation through H_2 adsorption and subsequent H_2O desorption.

In Chapter 2 we provided details for generating a constrained thermodynamic surface phase diagram of rutile surfaces as a function of chemical potential of H_2O (μ_{H_2O}) and H_2 (μ_H)[136]. The conclusions of the Chapter 2 aid in finding the most relevant surface termination (i.e. equilibrated surface) under the practical HDO conditions. According to Chapter 2, the most stable surface termination of TiO_2(110) under typical HDO conditions (500 K and 200 bar of H_2 corresponding to μ_{H} = -0.18 eV, $\mu_{\mathrm{H_2O}}$ = 0.01 eV) is predicted to be a surface on which all bridging oxygen (O^{br}) sites are hydroxylated. Similarly, many studies reported that natural state of TiO_2 under high pressure of H_2 is not the stoichiometric surface, but it is hydroxylated or even further reduced and exhibits surface vacancies[137]. While some experimental results suggest that the TiO_2 is hydroxylated under H_2 atmosphere, there are only a few fundamental studies investigating the kinetics of how TiO_2 is hydroxylated or reduced to form surface oxygen vacancy sites. Thus, studying the formation of hydroxyls is by itself an important topic to understand the surface chemistry on TiO_2.

Surface hydroxyl and vacancy formation on RuO_2 were explored by many groups, while there is much less reliable information available for TiO_2, particularly regarding the adsorption sites for

hydrogen molecules on TiO_2[51]. Moreover, hydrogen molecules are not even expected to stick to the stoichiometric TiO_2 surface at room temperature[138]. Prior studies attempted to form surface hydroxyls deliberately on TiO_2 and used severe conditions (high temperature and high pressure of H_2) to obtain 20 ~ 100 % of hydroxylated bridging oxygen sites[139]. The study was inconclusive regarding the hydroxyl formation mechanism, but stated that hydroxyl formation on the TiO_2 is unlikely under water-free H_2 atmosphere. A simpler way to form surface hydroxyls is by dosing water on reduced TiO_2[140]. Although there is still controversy about H_2O's interaction with stoichiometric TiO_2 in UHV, it is generally agreed upon that a vacancy site can catalyze H_2O dissociation, forming in turn two neighboring bridging hydroxyls ($V_o + H_2O \rightarrow 2HO^{br}$), or H_2O splitting occurs at the Ti^{cus} site, hydroxylating both the O^{br} site and the Ti^{cus} site ($H_2O + Ti^{cus} + O^{br} \rightarrow HO^{br} + HOTi^{cus}$)[141]. Hydroxyls on TiO_2 may then proceed to create surface oxygen vacancy sites. This step is considered to be the most important step during a catalytic reactions not only over TiO_2, but also over other metal oxide surfaces[142,143], because the formed vacancy site acts as an active site for many catalytic reaction [144]. In other words, the ability to create a vacancy site is strongly believed to determine the catalytic activity on metal oxide surfaces. There is ample amount of experimental evidence, showing that RuO_2 surfaces can form a surface oxygen vacancy under H_2 exposure; however, the mechanism of the vacancy formation and its kinetics under realistic conditions on TiO_2 are not completely understood. To the best of our knowledge, we provide the first systematic DFT study for hydroxyl and vacancy formation on TiO_2, Ru_1TiO_2, RuO_2/TiO_2, and RuO_2 under considerations of both kinetics and thermodynamics for multiple formation pathways.

Before discussing of vacancy formation kinetics, we discuss the two distinct and most stable adsorption sites for H_2 molecules on TiO_2, Ru_1TiO_2, RuO_2/TiO_2, and RuO_2, namely the the M^{cus} (M = Ru or Ti) site and the O^{br} site. The calculated binding energies on the Ru^{cus} site of Ru_1TiO_2, RuO_2/TiO_2, and RuO_2 are -0.08 eV, -0.59 eV, and -0.15 eV, respectively. In contrast, the Ti^{cus} site of TiO_2 does not interact with a H_2 molecule. When a H_2 molecule binds to the O^{br} site, dissociative adsorption forms two neighboring HO^{br}. The calculated binding energies for this dissociative adsorption are -0.12 eV on TiO_2, -1.43 eV on Ru_1TiO_2, -1.97 eV RuO_2/TiO_2, and -

1.85 eV on RuO_2. Overall, H_2 molecules preferentially adsorb on the O^{br} site rather than the M^{cus} (M = Ti or Ru) site, which is consistent with numerous experimental results[51,145]. According to literatures, H_2 adsorbs weakly on the Ru^{cus} site in the absence of oxygen or strongly binds to the O^{br} site, forming an H_2O-like surface intermediate referred to as dihydride[145]. This dihydride species is stable only below 90 K, and upon heating, the formation of two neighboring HO^{br} is observed[145]. Surface hydroxyls formed on these metal oxides can undergo disproportionation and form a H_2O at the O^{br} site. Once the formed H_2O desorbs from the O^{br} site, a surface oxygen vacancy site (V_o) remains.

Three different vacancy formation pathways were tested. First, H_2O can be produced via the disproportionation mechanism (WF1) as suggested by Ertl's group under UHV conditions [96]. It is a reaction between two neighboring HO^{br} (reaction O1 in Table 3-2). This reaction is feasible as long as two adjacent HO^{br} exist. An example of WF1 on TiO_2(110) is shown in Figure 3-6(a). At the IS, the O^{br} sites are fully hydroxylated, and the FS consists of one bare O^{br} site and H_2O^{br} as shown in Figure 3-6(a). At the TS, the calculated $d_{O\text{-}H^*\text{-}OH^*}$ are 1.27 Å (O-H^{br}) and 1.23 Å (H-OH^{br}), respectively. The calculated barrier for this WF1 mechanism increases in the order of TiO_2 (1.03 eV) < Ru_1TiO_2 (1.06 eV) < RuO_2 (1.32 eV) < RuO_2/TiO_2 (1.54 eV), and the calculated ΔE increases in the order of RuO_2 (-0.35 eV) < Ru_1TiO_2 (0.50 eV) < TiO_2 (0.82 eV) < RuO_2/TiO_2 (0.89 eV). These results show that Ru promotion of TiO_2 does not change the kinetics of WF1 considerably, while 1 ML RuO_2 on TiO_2 renders the kinetics to be close to the RuO_2 surface. The calculated desorption energy for H_2O^{br} is 0.42 eV from TiO_2, ca. 0.59 eV on from Ru_1TiO_2, 0.39 eV from RuO_2/TiO_2 and 0.45 eV from RuO_2, indicating that the removal of water does not strongly depend on the Ru content of the surface.

The second possibility is the reactions O3 and O4 in Table 3-2. It is a vacancy formation path (WF2) involving two successive hydrogen diffusion steps. An example of this WF2 on RuO_2 shown in Figure 3-6 (b) and (c). It starts with an adsorbed H_2 molecule on the Ru^{cus} site. After H_2 binds to the Ru^{cus} site, the diatomic bond length $d_{H\text{-}H}$ of gas-phase H_2 (0.748 Å) is elongated to 0.791 Å due to hybridization of Ru-d_{z^2} with H_2-σ orbitals, whereby a small amount of charge transfer from hydrogen to the backbone of the Ru^{cus} site occurs [95]. This charge transfer

strengthens the H_2-Ru^{cus} bond, while weakening the H-H bond [51]. A similar phenomenon is seen on both Ru_1TiO_2 and RuO_2/TiO_2 after H_2 adsorption on their Ru^{cus} site. The elongated H-H distance facilitates H_2 dissociation, and leads to one H diffusion to the neighboring O^{br} site.

This H diffusion requires only a small activation barrier E_a of 0.29 eV, indicating that it can occur even at low temperature. At the TS, the distances between RuH^{cus}-HO^{br} and H-O^{br} are 0.93 Å and 1.50 Å, respectively. These calculated distances are consistent with other DFT calculations[40]. The calculated E_a for this H diffusion step decrease in the order of Ru_1TiO_2 (0.82 eV) > RuO_2/TiO_2 (0.66 eV) > RuO_2 (0.29 eV), and the calculated ΔE decreases in the order of Ru_1TiO_2 (0.19 eV) > RuO_2/TiO_2 (-0.50 eV) > RuO_2 (-0.57 eV), suggesting that H_2 dissociation becomes kinetically less hindered with increasing Ru content. As explained, an H_2 molecule does not bind to the Ti^{cus} site, so this WF2 path is unlikely to be relevant for TiO_2. As alternative, we studied dissociative H_2 adsorption as expressed as $H_{2(g)} + Ti^{cus} + O^{br} \rightarrow HTi^{cus} + HO^{br}$; however, its calculated energy barrier is E_a = 1.03 eV (reaction O2 in Table 3-2). The H atom left on the Ru^{cus} site completes the WF2 mechanism by diffusing over to the HO^{br} site as shown in Figure 3-6(c). The IS is similar to the IS of reaction O1 except for the extra H adatom on the Ru^{cus} site. At the TS, the calculated $d_{Ru\text{-}H^*\text{-}O}$ are 1.75 Å (Ru^{cus}-H) and 1.43 Å (RuH^{cus}-HO^{br}), respectively. The calculated E_a decreases in the order of TiO_2 (1.73 eV) > Ru_1TiO_2 (1.68 eV) > RuO_2/TiO_2 (1.40 eV) > RuO_2 (0.93 eV), and the calculated ΔE increase in the order of RuO_2 (0.26 eV) < TiO_2 (0.29 eV) < RuO_2/TiO_2 (0.89 eV) < Ru_1TiO_2 (1.39 eV), respectively. As for the previous H diffusion step, it becomes more facile with increasing Ru content in metal-oxide surface and remains unfavorable on TiO_2.

A third WF3 mechanism is shown in Figure 3-6(d), in which all O^{br} sites are hydroxylated (reaction O5 in Table 3-2). An example for this WF3 on RuO_2 is also illustrated in Figure 3-6(d). In the IS, an extra H_2 molecule on the Ru^{cus} site is required, followed by the diffusion of one H atom to the neighboring HO^{br}, forming a H_2O^{br}. At the TS, the calculated $d_{Ru\text{-}H\text{-}H^*\text{-}OH}$ are 1.79 Å (Ru-H), 1.03 Å (H^{cus}-H), and 1.30 Å (H-O^{br}H), respectively. The calculated ΔE and E_a for this WF3 are ΔE = 0.67 eV and E_a = 0.85 eV on Ru_1TiO_2, ΔE = 0.29 eV and E_a = 0.65 eV on RuO_2/TiO_2, and ΔE = 0.26 eV and E_a = 0.45 eV on RuO_2, respectively.

Table 3-2. Major elementary steps studied on TiO_2, Ru_1TiO_2, RuO_2/TiO_2, and RuO_2[a].

no.	Reaction	TiO_2(110)			Ru_1TiO_2(110)						RuO_2/TiO_2(110)			RuO_2(110)		
					Ru^{cus} site			Ti^{cus} site								
		ΔE	E_a	[b]ν	ΔE	E_a	[b]ν	ΔE	E_a	[b]ν	ΔE	E_a	[b]ν	ΔE	E_a	[b]ν
O0	$H_{2(g)} + M^{cus} \leftrightarrow H_2\text{-}M^{cus}$	.	.	.		.	.		.	.		.	.	-0.15	.	.
O1	$HO^{br} + HO^{br} \leftrightarrow H_2O^{br} + O^{br}$	0.82	1.03	1071	0.50	1.06	893	0.50	1.06	893	0.89	1.40	1015	-0.35	1.32	1041
O2	$H_2 + M^{cus} + O^{br} \leftrightarrow H\text{-}M^{cus} + HO^{br}$	0.59	1.03	1040	.	.	.	0.59	1.03	1040	.	.	.	.	.	.
O3	$H_2M^{cus} + O^{br} \leftrightarrow H\text{-}M^{cus} + HO^{br}$	.	.	.	0.19	0.82	1176	.	.	.	-0.50	0.66	1022	-0.57	0.29	870
O4	$H\text{-}M^{cus} + HO^{br} \leftrightarrow M^{cus} + H_2O^{br}$	0.29	1.73	1568	1.39	1.54	912.8	0.29	1.73	1568	0.89	1.40	1151	0.26	0.93	765
O5	$H_2\text{-}M^{cus} + HO^{br} \leftrightarrow H\text{-}M^{cus} + H_2O^{br}$	.	.	.	0.67	0.85	951	.	.	.	0.29	0.65	999	0.26	0.45	965
O6	$H_2O^{br} \leftrightarrow H_2O + V_o$	1.26	0.00	.	-0.20	0.00	.	-0.33	0.00	.	0.23			0.25	0.00	.
O7	$CH_3CHO_{(g)} + V_o \leftrightarrow CH_3CHO^{br}$	-0.40	0.00	.	-0.30	0.00	.	-0.24	0.00	.	-0.34	0.00	.	-0.45	0.00	.
O8	$CH_3CHO^{br} + M^{cus} \leftrightarrow CH_3CHO^{br}\text{-}M^{cus}$	-0.17	0.26	103	-1.05	.	.	.	.	.	-0.09	0.10	58	-0.10	0.06	160
O9[c]	$CH_3CHO^{br} + M^{cus} \leftrightarrow CH_3CH\text{-}M^{cus} + O^{br}$	.	.	.	-1.99	0.00	.	0.77	1.13	172	-0.14	0.50	353	0.49	0.75	244
O10[d]	$CH_3CHO^{br}\text{-}M^{cus} \leftrightarrow CH_3CH\text{-}M^{cus} + O^{br}$	-0.08	0.65	382	-0.94	0.15	376	.	.	.	-0.06	0.52	330	0.59	0.83	243
O11	$CH_3CHM^{cus} + O^{br} \leftrightarrow CH_2CH\text{-}M^{cus} + HO^{br}$	-0.06	0.87	1422	0.63	1.14	1317	-0.57	0.48	572	-0.21	0.77	1434	-0.51	0.52	976
O12[e]	$CH_3CHM^{cus} \leftrightarrow C_2H_{4(g)} + M^{cus}$	-1.18	1.11	1085	.	.		-1.89	0.67	796	.	.	.	-0.27	1.35	1077
O13	$CH_2CHM^{cus} + HO^{br} \leftrightarrow C_2H_{4(g)} + O^{br}$	-1.67	0.42	1040	0.12	1.17	1372	-1.30	0.37	893	0.40	1.17	1128	0.25	0.93	1220
O14	$CH_2CHM^{cus} + H_2\text{-}M^{cus} \leftrightarrow C_2H_{4(g)} + H\text{-}M^{cus}$	.	.	.	.	.	.	-1.22	0.51	1021	-0.23	0.77		-0.52	0.88	1080
O15	$CH_3CHO^{br} + H\text{-}M^{cus} \leftrightarrow CH_3CH_2O^{br} + Mcus$	-2.01	0.07	109	-0.86	0.00	.	-1.83	0.00	.	-0.61	0.31	.	-0.97	0.11	439
O16	$CH_3CH_2O^{br} + H\text{-}M^{cus} \leftrightarrow CH_3CH_2O^{br}H + M^{cus}$	0.31	1.82	1495	1.08	1.53	1163	-0.37	1.54	1084	0.45	1.28	1305	0.37	0.96	1192
O17	$CH_3CH_2O^{br} + HO^{br} \leftrightarrow CH_3CH_2O^{br}H + O^{br}$	0.60	0.89	839	.	.	.	.	.	.	.	.	.	1.05	1.35	1033
O18	$CH_3CH_2O^{br}H \leftrightarrow CH_3CH_2OH_{(g)} + V_o$	0.16	.	.	0.38	.	.	0.23	.	.	0.11	.	.	0.18	.	.

[a]ΔE and E_a (in eV) are the total energy change and activation energy barriers without ZPE correction. V_o and M^{cus} indicate a surface oxygen vacancy site and undercoordinated metal atoms (Ru or Ti), respectively. [b]ν denotes the frequency of the imaginary mode at the transition state in cm^{-1}. [c]C-O bond scission from singly-bonded configuration. [d]C-O bond scission from bidentate configuration ($CH_3CHO^{br}\text{-}M^{cus}$). [e]Intramolecular hydrogen diffusion.

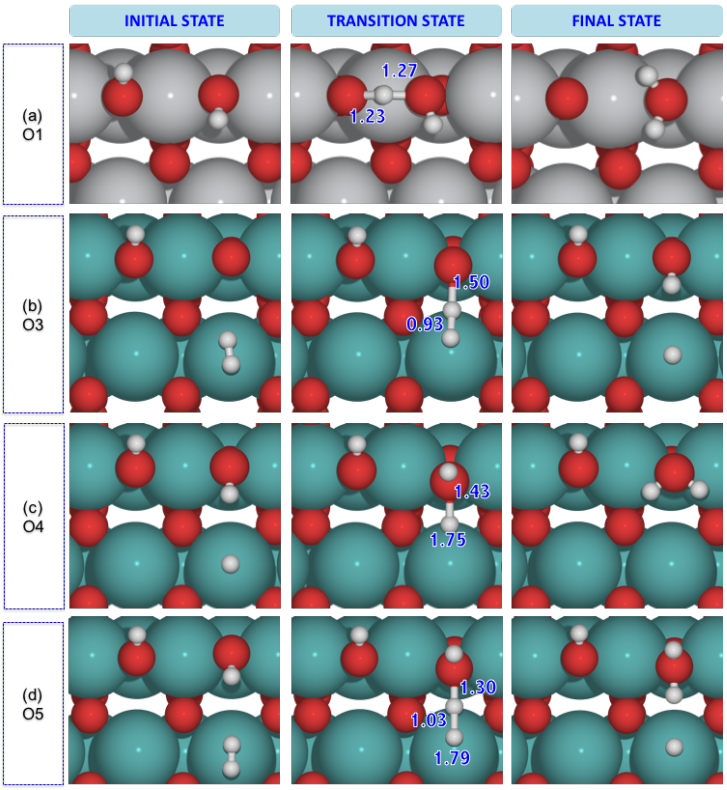

Figure 3-6. Different water formation (WF) pathways. (a) WF1 (disproportionation), $2HO^{br} \rightarrow H_2O^{br} + O^{br}$; (b) H_2 dissociation, $H_2Ru^{cus} + O^{br} \rightarrow HRu^{cus} + HO^{br}$; (c) WF2: $HO^{br} + HRu^{cus} \rightarrow H_2O^{br} + Ru^{cus}$; (d) WF3: $HO^{br} + H_2Ru^{cus} \rightarrow H_2O^{br} + HRu^{cus}$.

Again, this WF3 pathway becomes more relevant with increasing Ru content in metal oxide surfaces. This pathway is not suitable for TiO_2 because of the nonexistence of H_2-Ti^{cus}. In addition to these three WF pathways, we have also considered two Eley-Rideal type reaction pathways on the RuO_2 surface: (i) dissociative hydrogen adsorption on the same O^{br} site leading directly to H_2O^{br}, and (ii) dissociative hydrogen adsorption on the two neighboring O^{br} sites; however, they are all unlikely due to high activation barriers (> 2.0 eV).

In summary, three vacancy formation pathways on TiO_2(110), Ru_1TiO_2(110), RuO_2/TiO_2(110), and RuO_2(110) can be summarized as

$$\text{WF1 O1: } MO_2 + 3/2H_{2(g)} \leftrightarrow MO_{(2-x)} + H_2O_{(g)} + O^{br}\text{-H}, \quad (3\text{-}2)$$

$$\text{WF2 O2/O3+O4: } MO_2 + 2H_{2(g)} \leftrightarrow MO_{(2-x)} + H_2O_{(g)} + 2O^{br}\text{-H}, \quad (3\text{-}3)$$

$$\text{and WF3 O5: } MO_2 + 5/2H_{2(g)} \leftrightarrow MO_{(2-x)} + H_2O_{(g)} + 2O^{br}\text{-H} + \text{H-}M^{cus}. \quad (3\text{-}4)$$

Here, $MO_{(2-x)}$ is MO_2 (M = Ti or Ru) with a surface vacancy (V_o), H* is surface hydrogen, and M^{cus} is the metal 'cus' site. These three pathways are graphically described as PES in Figure 3-7(a - d). Intermediate states during vacancy formation pathways are (1) stoichiometric surface, (2) $3HO^{br}$, (3) $3HO^{br}$, (4) $HO^{br} + H_2O^{br}$, (5) $HO^{br} + V_o + H_2O_g$; (6) $2HO^{br} + H_2$-M, (7) $3HO^{br} + H$-M^{cus}, (8) $2HO^{br} + H_2O^{br}$, (9) $2HO^{br} + V_o + H_2O_g$; (10) $3HO^{br} + H_2$-M^{cus}, (11) $2HO^{br} + H_2O^{br} + H$-M^{cus}, and (12) $2HO^{br} + H_2O_g + H$-$M^{cus} + V_o$.

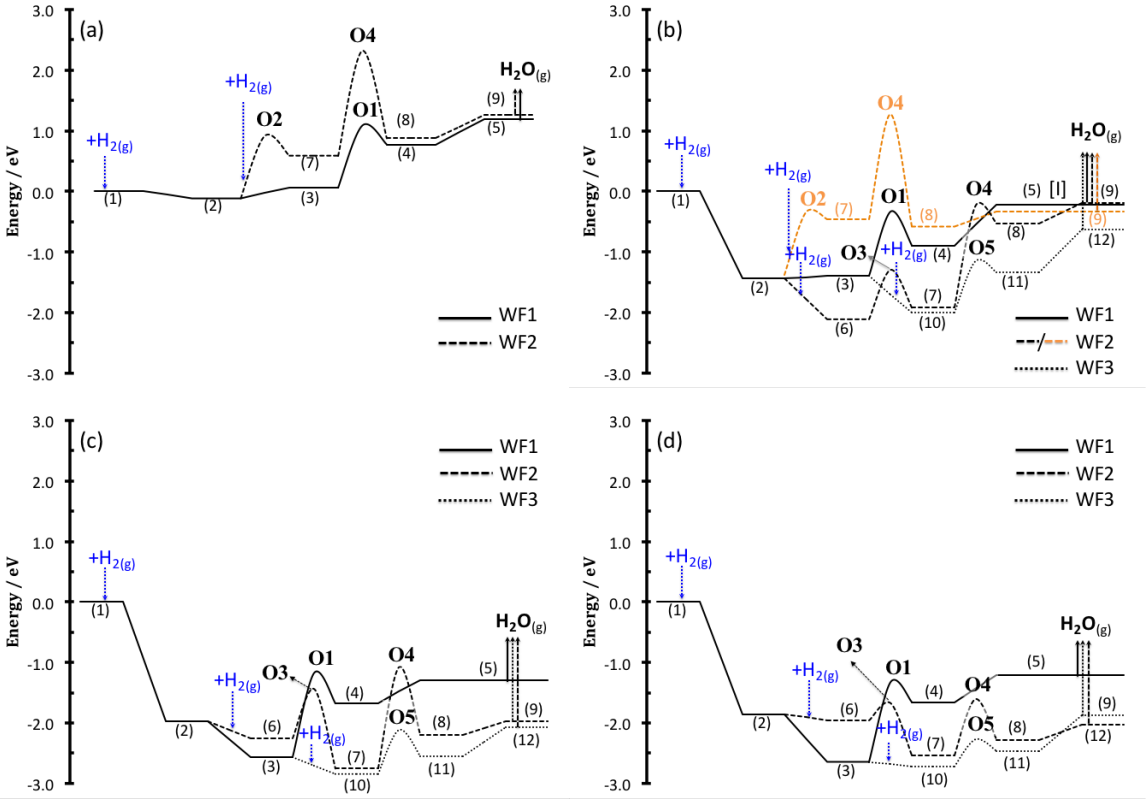

Figure 3-7. Potential energy surface of vacancy formation on four metal oxide surfaces: (a) TiO_2(110), (b) Ru_1/TiO_2(110), (c) RuO_2/TiO_2(110), (d) RuO_2(110). The orange dotted line in (b) indicates the mechanism on the Ti^{cus} site.

On TiO_2, only two pathways, WF1 and WF2, are available. Both require an activation energy of at least E_a = 1.0 eV and are endothermic by more than than 1.2 eV. Disproportionation on TiO_2 starts with state (3) in Figure 3-7(a), where all O^{br} sites are hydroxylated. Then, H_2O^{br} is formed via WF1 [state (4) in Figure 3-7(a)] and leaves behind a V_O vacancy on TiO_2 after desorption [(5) in Figure 3-7(a)]. The second vacancy formation pathway, WF2 has to overcome an activation energy of 1.03 eV for dissociative H_2 adsorption leading to a fully hydroxylated O^{br} row and an H atom on the Ti^{cus} site [(7) in Figure 3-7(a)]. The H atom adsorbed on the Ti^{cus} diffuses to the

neighboring HO^{br} and forms H_2O^{br} [(8) in Figure 3-7(a)]. This diffusion step requires an even higher activation barrier (E_a = 1.73 eV) than the preceding H_2 dissociation. As shown in Figure 3-7(a), WF1 and WF2 are endothermic by more than ΔE > 1.0 eV. Overall, our results in Figure 3-7(a) suggest that vacancy formation on TiO_2 is kinetically and thermodynamically limited, and the formation of surface hydroxyls, the precursor state to from a surface vacancy, is the bottleneck during TiO_2 surface reduction. This conclusion is in good agreement with Barteau *et al.*'s experimental data, which reported that isothermal reduction of rutile TiO_2(110) under H_2 atmosphere is barely measurable even at 573 K[146]. They further postulated a very similar reduction mechanism consisting of (1) dissociative H_2 adsorption, (2) sequential hydrogenation to produce surface hydroxyls and H_2O, and (3) diffusion of oxygen from bulk positions to heal the surface vacancy[146]. They concluded that the rate of surface reduction is initially limited by the availability of surface H atoms, i.e., the formation of surface hydroxyls, and is then autocatalytically accelerated as an additional oxygen vacancy sites are available for subsequent H_2 dissociation[146].

The three Ru containing metal oxides surfaces (b) Ru_1TiO_2(110), (c) RuO_2/TiO_2(110), and (d) RuO_2(110) show similar reaction kinetics and thermodynamics; they can catalyze three vacancy formation pathways (WF1, WF2, and WF3) with activation barrier of ca. 0.5 eV, and are exothermicity. A comparison of three PESs in Figure 3-7 concludes that WF3 is the most likely vacancy formation pathway as we considered the practical HDO conditions (P_{H_2} > 200 bar). Interestingly, it is also found that surface reduction becomes easier with increasing Ru content; *i.e.*, RuO_2 is the easiest surface to create a vacancy[146], but TiO_2 is the hardest surface to reduce.

3.3.2.2. Acetaldehyde HDO on Vacancy Site of TiO_2(110)

In the previous section, we argued that surface oxygen vacancies are easily formed on Ru_1TiO_2, RuO_2/TiO_2, and RuO_2, while their formation is kinetically limited on TiO_2. Under practical HDO conditions (T > 500 K, P_{H_2} > 200 bar), however, the vacancy formation on TiO_2 is plausible, but is expected be slow. For now, we assumed that some sites exist on TiO_2 and continue with exploring HDO pathways on the reduced TiO_2(110) surface. Herein, we limit our discussion to

elementary steps on TiO_2 as a representative surface, because the main pathways leading to different products are essentially identical on RuO_2/TiO_2, Ru_1TiO_2, and RuO_2.

CH_3CHO HDO on TiO_2 starts with CH_3CHO adsorption on a vacancy site through the oxygen end of CH_3CHO, forming a single bonded precursor CH_3CHO^{br} with E_{BE} = -0.40 eV (reaction O7 in Table 3-2). As reported elsewhere, CH_3CHO can adsorb on the vacancy site as well as on the Ti^{cus} site as CH_3CHO-Ti^{cus} [144]. CH_3CHO-Ti^{cus} is only stable at low temperature and may diffuse along a Ti^{cus} row, ultimately scavenged into the V_O site. Upon its adsorption, the calculated $d_{C\text{-}O}$ of CH_3CHO^{br} is slightly elongated by 7 % to 1.31 Å, whereas the calculated $d_{C\text{-}C}$ is kept essentially constant compared to gas-phase CH_3CHO. The surface CH_3CHO^{br} can be transformed into a more energetically favorable intermediate state via isomerization (reaction O8 in Table 3-2), leading to CH_3CHO^{br}-Ti^{cus} where the αC carbon in CH_3CHO^{br} interacts with the Ti^{cus} site. Its energy level places the stable state at E_{BE} = -0.57 eV as shown in Figure 3-8(a). This adsorption geometry is often called a bidentate configuration. At the TS, the calculated $d_{O^*\text{-}C^*\text{-}Ru}$ are 1.36 Å (O*-αC*) and 3.02 Å (αC*-Ti^{cus}), respectively. The calculated E_a and ΔE for this isomerization are 0.26 eV and -0.17 eV, which are energetically and kinetically facile even at very low temperature. An interesting observation regarding the bond distances during the isomerization is the following; the bond distances of αO*-C and αC*-C in bidentate configuration are 1.46 Å and 1.52 Å, respectively. A comparison of these values to those of gas-phase CH_3CHO provides that the $d_{O^*\text{-}C^*}$ is increased by 19 %, while the $d_{C^*\text{-}C}$ is approximately constant. Since bond lengths can be taken as a first order approximation as a measure of bond strength, this indicates that the strength of αC-O bond is weakened as the CH_3CHO^{br} transforms into the bidentate CH_3CHO^{br}-Ti^{cus}. Mei *et al*. published similar results for CH_3CHO adsorption on MoO_3 where they referred to the bidentate configuration as a doubly-bonded CH_3CHO that is also more stable than the singly bonded CH_3CHO^{br} configuration[29].

Next, we focus on possible elementary steps that proceeding from CH_3CHO^{br}-Ti^{cus} under the assumption that subsequent steps follow the path of least resistance, i.e., we eliminate pathways that involve significant barriers. For CH_3CHO^{br}-Ti^{cus}, there are four different possible bond scission steps (C-C, αC-H, ßC-H, and αC-O). The calculation of activation barriers for these four

different steps indicates that the αC-O bond scission (reaction O10 in Table 3-2) has the lowest E_a of 0.65 eV as shown in Figure 3-8(b), while the C-C bond breaking leading to CH_3-Ti^{cus} and CH-O^{br} has a much larger barrier of 2.11 eV. Therefore, further elementary steps following after C-C bond scission were not considered. The calculated ΔE of αC-O bond scission in bidentate CH_3CHO^{br}-Ti^{cus} (reaction O10 in Table 3-2) is exothermic by -0.08 eV. At the TS, the calculated $d_{O\text{-}C}$ is elongated from 1.31 Å to 2.08 Å.

To quantify the benefit of forming bidentate CH_3CHO^{br}-Ti^{cus}, we also investigated the αC-O bond scission that starts from monodentate CH_3CHO (CH_3CHO^{br}); however, we could not locate the TS, because the monodentate CH_3CHO^{br} always transforms into bidentate CH_3CHO^{br}-Ti^{cus} first before αC-O breaking occurs. Other competing C-H bond scissions, CH_3CHO^{br}-Ti^{cus} → CH_3CO^{br}-Ti^{cus} + H-Ti^{cus} and CH_3CHO^{br} → CH_2CHO^{br} + H-Ti^{cus}, are also kinetically limited with significant energy barrier of more than ca. 1.40 eV. As an alternative to these decomposition pathways, we even investigated the intramolecular H diffusion pathway expressed as CH_3CHO^{br} → $CH_2CH_{2(g)}$ + O^{br}, being considered as the most direct pathway for the formation of desired product ethylene gas (CH_2CH_2); however, it requires to overcome a barrier of E_a = 1.96 eV. A summary of all investigated elementary steps not depicted in Figure 3-8 is given in the Appendix.

After the αC-O bond scission, the ethylidene (CH_3CH^*) intermediate adsorbs on the Ti^{cus} site with E_{BE} = -0.50 eV, and the oxygen vacancy on the $TiO_{(2\text{-}x)}$ is healed by the stripped off oxygen from bidentate CH_3CHO^{br}-Ti^{cus} in accordance with the Mars and van Krevelen mechanism[147]. Without this healing step, the TiO_2(110) surface would continuously reduce further and further and eventually be converted into metallic Ti islands[148]. However, the deoxygenation of CH_3CHO can reoxideze the V_O site and counteracts the surface reduction. Subsequent to the αC-O bond scission, the reaction proceeds to the ßC-H scission of CH_3CH-Ti^{cus} (reaction O11 in Table 3-2). The calculated ΔE and E_a are -0.06 eV and 0.87 eV, respectively. At the TS, the bond lengths are 1.32 Å (ßC–H) and 1.37 Å (H–O^{br}). The regenerated O^{br} site in the previous step facilitates the ßC-H bond scission in CH_3CH-Ti^{cus}. In this step, the C-C axis of CH_3CH-Ti^{cus} tilts towards the O^{br} site as a hydrogen atom from the methyl group of CH_3CH-Ti^{cus} is transfered to the O^{br} site, forming bridging hydroxyl as shown in Figure 3-8(c). This is followed by the hydrogenation of the

vinyl intermediate ($CH_2CH\text{-}Ti^{cus}$) as shown in Figure 3-8(d) via the reaction O11 in Table 3-2, where the H atom from the neighboring HO^{br} formed the ßC-H bond with $CH_2CH\text{-}Ti^{cus}$, producing desired product ethylene (CH_2CH_2). At the TS, the bond lengths are 1.38 Å (O^{br}–H) and 1.52 Å (H–C), respectively. Once the H atom forms a bond with the αC of $CH_2CH\text{-}Ti^{cus}$, the product CH_2CH_2 spontaneously desorbs from the Ti^{cus} site. The calculated E_a and ΔE for reaction O11 are 0.42 eV and highly exothermic by -1.67 eV, respectively.

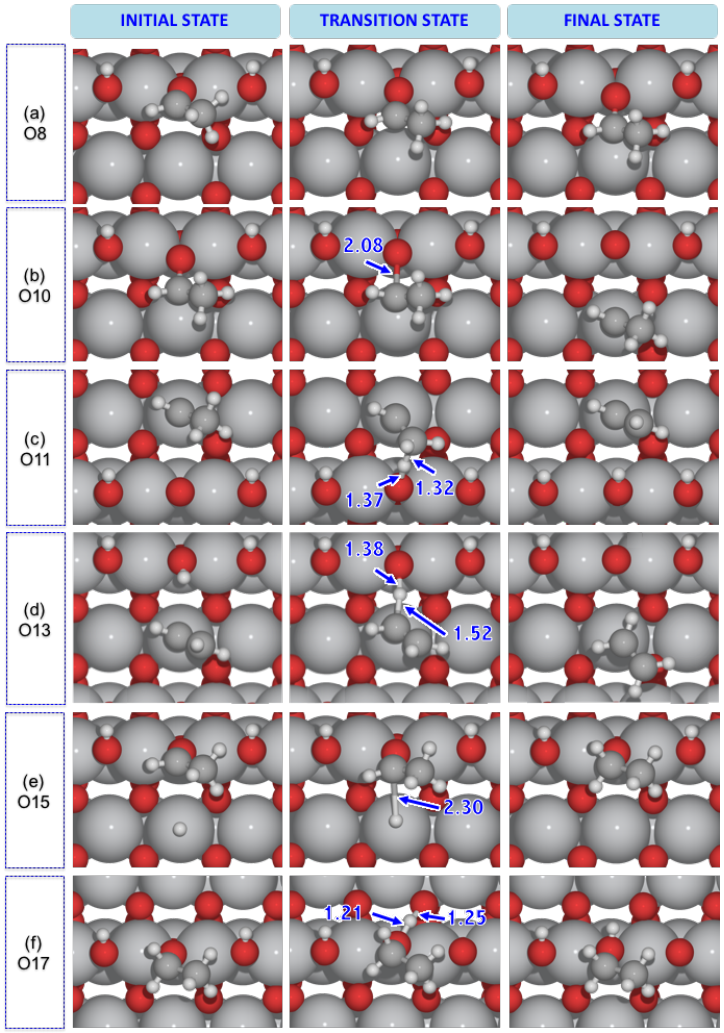

Figure 3-8. Calculated reaction pathways of CH_3CHO HDO on TiO_2(110) (white – hydrogen / red – oxygen / gray – titanium / dark-gray - carbon). Numerical values in blue represents bond distance in Å. (a) O8; (b) O10; (c) O11; (d) O13; (e) O15; (f) O17.

As an alternative to reaction O11, we also examined an intramolecular H diffusion pathway in $CH_3CH\text{-}Ti^{cus}$ (see reaction O12 in Table 3-2) to form CH_2CH_2 directly. This path involves simultaneous C-H bond scission and C-H bond formation; however, it needs to overcome a

barrier of E_a = 1.11 eV, which is considerably higher than the barrier of reaction O11. We note that despite the high activation barrier the step may occur due to the significant thermodynamic driving force (ΔE = -1.18 eV). This intramolecular H diffusion is also summarized in the Appendix. After CH_2CH_2 formation, the V_o site on TiO_2 needs to be regenerated to complete the catalytic cycle. These pathways were already discussed in the previous section 3.3.2.1.

Our proposed HDO mechanism on TiO_2 shows similarities but also differences to a published CH_3CHO HDO pathway on the MoO_3(010) surface by Mei's group[29]. In good agreement with our mechanism on TiO_2, CH_3CHO adsorbs on a vacancy site of MoO_3 with monodentate and bidentate adsorption configurations. The more plausible HDO pathway on MoO_3 is only initiated from monodentate CH_3CHO, whereas on TiO_2 the bidentate CH_3CHO is necessary. The bidentate CH_3CHO on MoO_3 leads to CH_3* and CO* with a significant energy barrier (ca. 1.43 eV), after αC-H bond cleavage in bidentate CH_3CHO[29]. In contrast, both CH_3CHO^{br} and bidentate CH_3CHO^{br}-Ti^{cus} intermediates on TiO_2 preferentially lead to αC-O bond scission in the subsequent step. The largest energy barrier along the HDO pathway on TiO_2 is 0.87 eV, which is for the dehydrogenation step of CH_3CH-Ti^{cus} (reaction O11 in Table 3-2), while on the MoO_3 surface a barrier of 1.39 eV needs to be overcome. These results would suggest that TiO_2 catalyst has a better selectivity and activity than the MoO_3 as long as oxygen vacancy sites on TiO_2 can be generated.

Hydrogenation (HYD) of CH_3CHO to ethanol on TiO_2 was also investigated similar to HYD on Ru(0001). Ethanol is formed via two successive hydrogenation steps. It begins with the hydrogenation of αC in CH_3CHO^{br} (reaction O15 in Table 3-2), forming an ethoxy ($CH_3CH_2O^{br}$) intermediate, followed by the second hydrogenation of the oxygen atom in $CH_3CH_2O^{br}$, forming surface ethanol ($CH_3CH_2O^{br}H$). The first hydrogenation step to form ethoxy is shown in Figure 3-8(e). At the IS, an H atom adsorbed on the Ti^{cus} site reacts with monodentate CH_3CHO^{br}. At the TS, the calculated bond lengths are 2.30 Å (αC–H), and 1.77 Å (H-Ti^{cus}), respectively. The calculated E_a and ΔE are 0.07 eV and -2.01 eV, suggesting that it can occur even at very low temperature and that the ethoxy intermediate is potentially the most abundant surface intermediate during CH_3CHO HDO.

We calculated two different hydrogenation pathways for the second hydrogenation in $CH_3CH_2O^{br}$. The first one is reaction O16 in Table 3-2. Similar to the IS of the first hydrogenation step, the H atom adsorbed on the Ti^{cus} site reacts with the oxygen atom in $CH_3CH_2O^{br}$. At the TS, the calculated bond lengths are 1.42 Å (O–H) and 2.13 Å (H-Ti^{cus}) and the calculated E_a and ΔE are 1.82 eV and 0.31 eV, respectively. The high energy barrier renders this step unlikely. There is, however, experimental evidence for the conversion of surface ethoxy intermediates adsorbed on the bridge vacancy of TiO_2 into ethanol via $CH_3CH_2O^{br} + HO^{br} \leftrightarrow CH_3CH_2O^{br}H + O^{br}$ at T = 250 ~ 400 K[144]. It was also reported that 25 % of surface ethoxy species were converted into ethanol:ethylene (=1:1) at T = 650 K[144]. The authors postulated that the activation of ethylene and ethanol at 650 K is initiated by αC-H bond scission in $CH_3CH_2O^{br}$ through interactions with a neighboring bare O^{br} site. Because we assumed that most O^{br} sites are hydroxylated under practical HDO reaction conditions (i.e. high pressure of H_2), the αC-H bond scission in $CH_3CH_2O^{br}$ has been ruled out in our calculations, i.e., this step (αC-H bond scission) is limited by the absence of O^{br} sites nearby ethoxy intermediates. However, the other hydrogenation pathway, reaction O17 in Table 3-2, is possible on TiO_2 and congruent with the observation that 75 % of ethoxy intermediates are converted into ethanol[144]. Two different elementary steps for this hydrogenation were investigated: (1) direct H atom diffusion from the neighboring HO^{br} site to $CH_3CH_2O^{br}$, reaction O19 Table 3-2, $CH_3CH_2O^{br} + HO^{br} \leftrightarrow CH_3CH_2O^{br}H + O^{br}$, and (2) the three-fold-oxygen (O^{3f}) site-assisted H diffusion, reaction O17 in Table 3-2, $CH_3CH_2O^{br} + HO^{br} + O^{3f} \leftrightarrow CH_3CH_2O^{br} + O^{br} + O^{3f}$-H $\leftrightarrow CH_3CH_2O^{br}H + O^{br} + O^{3f}$. The hydrogenation of ethoxy by direct H diffusion is unlikely because of a large activation energy of E_a = 1.5 eV. This finding is in consensus with other theoretical studies, reporting that atomic H diffusion along the O^{br} row on TiO_2 is kinetically hindered, while the later step, $CH_3CH_2O^{br} + O^{br}$-H + $O^{3f} \leftrightarrow CH_3CH_2O^{br} + O^{br} + O^{3f}$-H $\leftrightarrow CH_3CH_2O^{br}H + O^{br} + O^{3f}$, Figure 3-8(f), has a lower barrier of E_a = 0.89 eV. At the TS, the calculated $d_{Obr\text{-}H\text{-}O3f}$ are 1.21 Å (O^{br}-H) and 1.25 Å (H-O^{3f}), respectively. The calculated ΔE is endothermic by 0.60 eV. The formed $CH_3CH_2O^{br}H$ desorbs with ΔE = 0.16 eV and leaves a vacancy again, and completes catalytic cycle.

3.3.3. A Comparison of CH_3CHO HDO with Ru(0001) Surface

Before we discuss mechanistic difference of CH_3CHO HDO on oxide surfaces, we give a brief comparison of HDO between the TiO_2(110) surface and the metallic Ru(0001) surface. As eluded in section 3.3.2.2, TiO_2 preferentially catalyzes C-O scission over C-C scission. In contrast, the metallic Ru is more likely to catalyze DCN rather than DDO and HYD. CH_3CHO adsorbs on the Ru surface in the $\mu^2\eta^3$ configuration and decomposes into the CH_2CO* intermediate via two competing dehydrogenation steps. The C-C bond of CH_2CO* is more readily activated (E_a = 0.52 eV) than the C-O bond (E_a = 1.44 eV), resulting in the formation of CH_2* and CO* intermediates. Sequential hydrogenation or dehydrogenation of CH_2* intermediate can lead to $CH_{4(g)}$ or carbon deposition and catalyst deactivation. The more energetically favorable pathway, however, is dehydrogenation and coke formation, given by the following reaction (22),

$$CH_3CHO_{(g)} \leftrightarrow C^* + 2H_{2(g)} + CO_{(g)} \text{ with } \Delta E = -0.58 \text{ eV}. \quad (3\text{-}5)$$

This overall reaction is exothermic by -0.58 eV under the assumption of CO and H_2 desorption. The most activated step along the overall reaction (3-5) has an energy barrier of 1.00 eV, corresponding to the dehydrogenation of CH* (reaction M13 in Table 3-1). If $CH_{4(g)}$ is formed as a final product, the largest activation energy of 1.11 eV is needed for the final CH_3* hydrogenation to $CH_{4(g)}$. The overall reaction for methane production is given by reaction (23),

$$CH_3CHO_{(g)} \leftrightarrow CH_{4(g)} + CO_{(g)} \text{ with } \Delta E = 0.07 \text{ eV}. \quad (3\text{-}6)$$

For comparison, if we consider the nonselective HDO on metallic Ru, leading to the desired product ethylene, the most activated step is the removal of surface oxygen as H_2O (reaction M19 and M20) or even CO_2 (reaction M21). Both pathways require surmounting energy barriers of ca. 1.70 eV, which indicates the strong oxygen affinity of metallic Ru and its tendency to accumulate oxygen causing high oxygen coverage or even the formation of a surface oxide layer. In fact, it is experimentally well known that Ru can be easily oxidized and reduced depending on its environment, and the oxidation state of the surface under working conditions depends on the rates of oxygen delivery and removal to and from the surface. These results clearly indicate that ethylene formation is less selective on Ru(0001) compared to carbon deposition or methane

formation. Our preliminary conclusion at this point is that the HDO pathways on the TiO_2(110) surface favor DDO and HYD, while the reaction mechanism on metallic Ru(0001) shows complex reaction pathways that preferentially lead to DCN and the generation of CH_4 or more favorably carbon deposition.

3.3.4. A Comparison of CH_3CHO HDO between Metal Oxide Surfaces

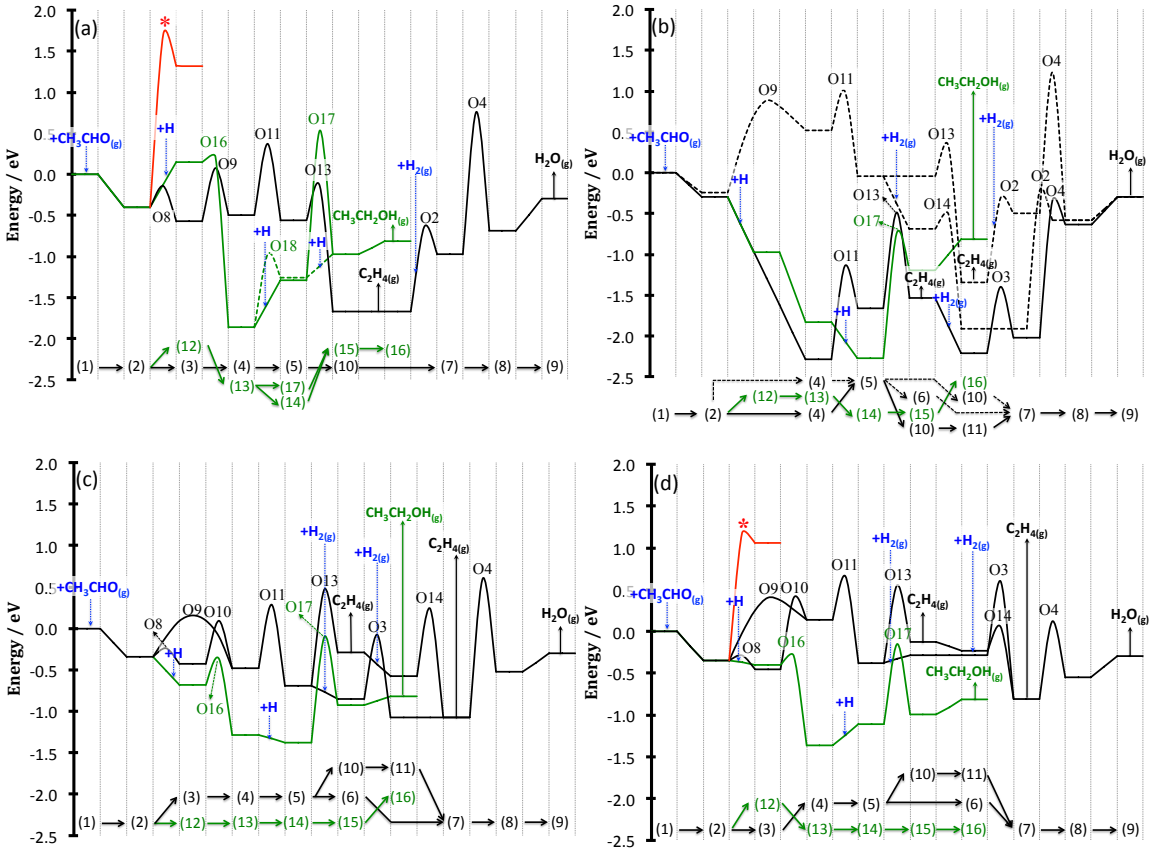

Figure 3-9. Potential energy surface of CH_3CHO HDO on (a) TiO_2(110), (b) Ru_1/TiO_2(110), (c) RuO_2/TiO_2(110), (d) RuO_2(110). The black, blue, and red lines represent the most preferred DDO, HYD, and DCN, respectively.

Having investigated all possible HDO pathways on the TiO_2(110) surface, we now compare them to the HDO pathways on Ru_1TiO_2, RuO_2/TiO_2, and RuO_2. First, CH_3CHO HDO on TiO_2 is summarized in Figure 3-9(a). Intermediate states are (1) V_o + $2HO^{br}$, (2) CH_3CHO^{br}+ $2HO^{br}$, (3) CH_3CHO^{br}-M^{cus} + $2HO^{br}$, (4) CH_3CH-M^{cus} + O^{br} + $2HO^{br}$, (5) CH_2CH-M^{cus} + $3HO^{br}$, (6) CH_2CH-M^{cus} + H_2-M^{cus} + $3HO^{br}$, (7) $CH_2CH_{2(g)}$ + H-M^{cus} + $3HO^{br}$, (8) H_2O^{br} + $2HO^{br}$, (9) V_o + $2HO^{br}$, (10) $CH_2CH_{2(g)}$ + O^{br} + $2HO^{br}$, (11) H_2-M^{cus} + $2HO^{br}$, (12) CH_3CHO^{br} + H-M^{cus} + $2HO^{br}$, (13) $CH_3CH_2O^{br}$

+ $2HO^{br}$, (14) $CH_3CH_2O^{br}$ + H-M^{cus} + $2HO^{br}$, (15) $CH_3CH_2O^{br}H$ + $2HO^{br}$, (16) V_o + $2HO^{br}$, (17) $CH_3CH_2O^{br}H$ + O^{br} + HO^{br}. It begins with CH_3CHO adsorption on the V_O site [state (2) in Figure 3-9(a)], followed by either DDO or HYD. The DDO path begins with isomerization, leading to the more stable bidentate-CH_3CHO^{br}-Ti^{cus} configuration [state (3) in Figure 3-9(a)]. The next step is the αC-O bond scission of bidentate-CH_3CHO^{br}-Ti^{cus}. This step simultaneously re-oxidizes the $TiO_{(2-x)}$ surface and heals the V_O site [state (4) in Figure 3-9(a)]. The CH_3CH-Ti^{cus} intermediate adsorbed on the Ti^{cus} site is dehydrogenated by interaction with the bare O^{br} site and decomposes into CH_2CH-Ti^{cus} and HO^{br} [state (5) in Figure 3-9(a)], which are then converted to our desired product ethylene (CH_2CH_2) via hydrogenation [state (10) in Figure 3-9(a)].

In order to complete the catalytic cycle, the V_O site needs be regenerated. The dissociative adsorption of an H_2 molecule leaves behind atomic H both at the Ti^{cus} and O^{br} site, forming H-Ti^{cus} and HO^{br} [state (7) in Figure 3-9(a)], which then convert into H_2O^{br} at the bridge site [state (8) in Figure 3-9(a)]. After H_2O^{br} desorbs the surface vacancy site is recreated [state (9) in Figure 3-9(a)].

The formation of ethanol via HYD requires an additional H atom at the Ti^{cus} site [state (12) in Figure 3-9(a)]. It initially forms $CH_3CH_2O^{br}$ [state (13) in Figure 3-9(a)] via reaction O16, followed by successive hydrogenation to form surface ethanol [state (15) in Figure 3-9(a)]. The H atom may originate either from H-Ti^{cus} or a neighboring HO^{br} site; the latter H source is kinetically preferred with a lower barrier by 0.9 eV. The desorption of ethanol completes the catalytic cycle.

Lastly, Figure 3-9(a) shows clearly that the C-C bond scission in CH_3CHO^{br} (red line with star) is kinetically and thermodynamically unfavorable (E_a = 2.11 eV, ΔE = 1.72 eV), and much more energetic than the αC-O bond scission. This preference of the αC-O bond breaking (E_a = 0.65 eV) over the C-C bond scission (E_a = 2.11 eV) on TiO_2(110) surface can be simply rationalized by bond length arguments, *i.e*. as bond distances increase, the bond strength decreases. Along with the HDO pathway of CH_3CHO from the gas phase molecule to the bidentate configuration, the C-O bond length in CH_3CHO is steadily increasing (gas phase = 1.224 Å → CH_3CHO^{br} = 1.31 Å → CH_3CHO^{br}-Ti^{cus} = 1.46 Å), whereas the C-C bond length is approximately constant (gas phase = 1.511 Å → CH_3CHO^{br} = 1.49 Å → CH_3CHO^{br}-Ti^{cus} = 1.52 Å). Hence, we conclude that TiO_2's

preference for the selective C-O scission over the C-C scission originates from this favorable bidentate configuration at the V_O site. The bond weakening can also be explained on the basis of electronic structure arguments similar to the Blyholder model commonly used to describe CO adsorption [149]. The hybridization of αC with the Ti^{cus} site leads to charge transfer from the αC to the Ti^{cus}. This is counteracted by electron back-donation to the anti-bonding σ^* orbital of C=O, which strengthens the adsorbates coupling with the substrate while at the same time the C=O bond is weakened.

Second, the PES for CH_3CHO HDO on Ru_1TiO_2, RuO_2/TiO_2, and RuO_2 is shown in Figure 3-9(b), (c), and (d). Because the HDO mechanism on the remaining surfaces shares most features with TiO_2, only the most salient aspects are discussed. Note that we investigated CH_3CHO HDO on both Ru^{cus} and Ti^{cus} sites of Ru_1TiO_2, because these two cus sites have a different electronic structure (see Figure 3-2). As for HDO on TiO_2, CH_3CHO adsorbs on the V_O site of each oxide surface [state (2) in Figure 3-9(b, c, d)], followed by isomerization or direct C-O bond scission. The calculated E_{BE} of CH_3CHO on each V_O site of metal oxide surfaces is -0.30 eV (V_o^{br-Ru} of Ru_1TiO_2), -0.24 eV (V_o^{br-Ti} of Ru_1TiO_2), -0.34 eV (RuO_2/TiO_2), and -0.45 eV (RuO_2), indicating that CH_3CHO is fairly stable at the V_O site. Among them, the RuO_2 has the highest affinity to oxygenated molecules, and its binding energy is comparable with the CH_3CHO binding energy on TiO_2.

On the Ru_1TiO_2 surface we find that C-O bond scission in CH_3CHO^{br} may proceed without undergoing isomerization at the V_o^{br-Ru} site. No TS for C-O bond scission was found at the promoted V_o^{br-Ru} site, while C-O bond scission was activated with E_a = 0.77 eV at the unpromoted V_o^{br-Ti} site (reaction O9 in Table 3-2). C-O bond scission on the other two oxide surfaces, (c) RuO_2/TiO_2 and (d) RuO_2, can proceed by either direct C-O bond scission or isomerization followed by C-O bond scission. The isomerization to bidentate-CH_3CHO^{br}-Ru^{cus} requires only small activation energies of 0.1 eV on RuO_2/TiO_2 and 0.06 eV on RuO_2, making it feasible even at low temperature. Subsequent C-O bond scission requires activation energies of 0.52 eV on RuO_2/TiO_2 and 0.83 eV on RuO_2. The alternative direct C-O bond scission from monodentate

CH_3CHO^{br}, is activated with energy barriers E_a = 0.50 eV on RuO_2/TiO_2 and E_a = 0.75 eV on RuO_2, respectively. We note that these pathways differ from what we observed for TiO_2. The C-O bond scission on TiO_2 only occurs through bidentate-CH_3CHO^{br}-Ti^{cus}, while on RuO_2/TiO_2 and RuO_2 a lower energy pathway is the direct C-O bond scission from monodentate CH_3CHO^{br}.

The intermediate CH_3CH-Ti^{cus} [state (4) in Figure 3-9(b, c and d)] after C-O scission is again identical for each oxide surface and is consecutively dehydrogenated via reaction O11 and hydrogenated via reaction O13. After the last hydrogenation step, the desired product ethylene is formed. The calculated E_a for the formation of CH_2CH-Ti^{cus} and HO^{br} by dehydrogenation of CH_3CH-Ti^{cus} [state (5) in Figure 3-9(b, c, and d)] is 1.14 eV (at V_o^{br-Ru} site of Ru_1TiO_2), 0.48 eV (at V_o^{br-Ti} site of Ru_1TiO_2), 0.77 eV (RuO_2/TiO_2), and 0.52 eV (RuO_2), respectively. The formation of the desired CH_2CH_2 product requires activation energies, E_a, of 1.17 eV at the V_o^{br-Ru} site of Ru_1TiO_2, 0.37 eV at the V_o^{br-Ti} site of Ru_1TiO_2, 1.17 eV on RuO_2/TiO_2, and 0.93 eV on RuO_2, respectively.

As alternative to reaction O13, The hydrogenation of CH_2CH-Ti^{cus} can also occur via reaction O14 in Table 3-2. In this case H_2 adsorbs on the Ru^{cus} site [state (6) in Fig. 9(b, c, and d)] and as it dissociates, one H atom reacts with CH_2CH-Ti^{cus} leaving the second one behind on the Ru^{cus} site [(7) in Fig. 9(b, c, d)]. The calculated E_a for this hydrogenation is 0.51 eV on the V_o^{br-Ti} site of Ru_1TiO_2, 0.77 eV on RuO_2/TiO_2 and 0.88 eV on RuO_2, respectively. For RuO_2/TiO_2, we find that this hydrogenation step is energetically more favorable than the hydrogenation by neighboring HO^{br}. Again, the H_2 molecule does not interact with the Ti^{cus} site and we can eliminate this step on the TiO_2 surface.

Vacancy regeneration is initiated with molecular H_2 adsorption on the Ru^{cus} site [(11) in Figure 3-9(b, c, and d)], followed by either successive H diffusion (reaction O3 → reaction O4 in Table 3-2) or disproportionation (not shown in Figure 3-9).

HYD pathways leading to by-product ethanol were also investigated on Ru_1TiO_2, RuO_2/TiO_2, and RuO_2. Note that the Ti^{cus} site of Ru_1TiO_2 has not been considered for HYD, because the HYD

mechanism on this site is expected to be similar to the HYD pathway on TiO_2. Also, the O^{3f} site-assisted HYD (reaction O17 in Table 3-2) was only investigated on RuO_2.

HYD is initiated with H diffusion from the Ru^{cus} site to CH_3CHO^{br} (reaction O16 in Table 3-2), forming ethoxy [state (13) in Figure 3-9(b, c, and d)]. Surprisingly, we could not locate a TS for this step on Ru_1TiO_2 as it occurs spontaneously without energy barrier and is exothermic by ΔE = -0.86 eV. For RuO_2/TiO_2 the calculated E_a of this step is 0.31 eV, and 0.11 eV for RuO_2, respectively.

The second hydrogenation step, reaction O16 in Table 3-2 leading to the formation of $CH_3CH_2O^{br}H$ [state (15) in Figure 3-9(b, c, and d)] has the calculated E_a of 1.54 eV on Ru_1TiO_2, 1.28 eV on RuO_2/TiO_2, and 0.96 eV on RuO_2, respectively. The O^{3f}-mediated HYD step, which is only calculated on RuO_2(110), shows a higher barrier of 1.35 eV than that of reaction O16. This result is contrary to TiO_2 where the O^{3f}-mediated HYD path has E_a = 0.93 eV, which is lower than the energy barrier for reaction O16.

We have also calculated C-C scission in CH_3CHO on RuO_2 to compare to the C-O scission or HYD [see red line in Figure 3-9(d)] and obtained a barrier of E_a = 1.52 eV and ΔE = 1.40 eV, indicating that it is less likely compared to C-O bond scission. This result is consistent with the result on TiO_2, where C-C scission highly energetic and endothermic.

We have summarized the most likely DDO and HYD pathways in Figure 3-10. For the sake of comparison, we used the simplest DDO, vacancy regeneration steps, and HYD, *i.e.*, $V_O \rightarrow$ HDO/HYD $\rightarrow$ Vacancy Regeneration $\rightarrow V_O$. The complexity of the mechanistic and kinetic differences was discussed above. For stable metal oxide HDO catalysts the rate of C-O scission and vacancy healing must be balanced with the rate of vacancy formation[115]. RuO_2, for example, is hardly stable and tends to reduce to metallic Ru, because as shown in Figure 3-10(a) surface reduction by vacancy formation is fast, whereas we find the highest barrier for C-O bond scission required to heal the vacancies.

C-O scission in CH_3CHO^{br} over Ru_1TiO_2 is remarkably facile, which means that Ru doping in TiO_2 alters the kinetics of C-O scission significantly [see Figure 3-10(a)]. In fact, several attempts

to locate the TS for C-O scission were unsuccessful even with different ionic optimizers and starting configurations. We suspect that the reason is the strong interaction between CH_3CH-Ru^{cus} and the Ru dopant in TiO_2[150]. This changes the electronic properties of TiO_2 as confirmed via Bader's analysis. We observe electron transfer from Ru to neighboring O^{3f} sites, which results in a positively charged Ru dopant and an associated stabilization of the TS for C-O scission in CH_3CHO^{br}. Subsequent surface intermediates adsorbed on the Ru dopant bind strongly. For instance, the binding energies of the other surface intermediates like CH_3CH-Ru^{cus} and CH_2CH-Ru^{cus} are even lower than -1.50 eV. This high stability of CH_3CH-Ru^{cus} makes (de)hydrogenation steps unfavorable with E_a > ca. 1.0 eV. This is rationalized in part by the Sabatier principle, which states that binding of reaction intermediates on catalysts should be neither too strong nor too weak[151].

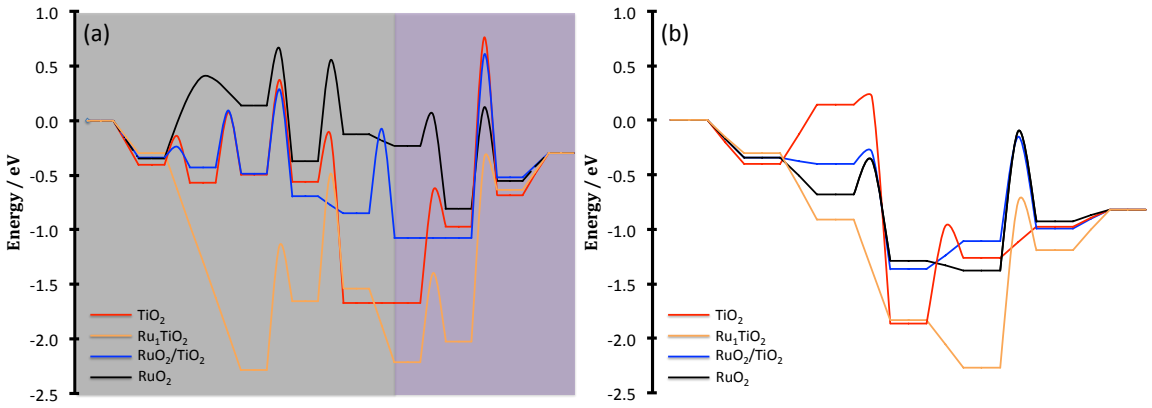

Figure 3-10. Potential energy surface (PES) of the most likely HDO pathway: (a) direct-deoxygenation (DDO, gray region) leading to desired product ethylene + vacancy formation steps (purple region), (b) hydrogenation (HYD) leading to ethanol.

Inspection of Figure 3-10 suggests that the DDO pathways on TiO_2 and RuO_2/TiO_2 exhibit relatively flat potential energy surfaces compared to Ru_1TiO_2 and RuO_2, i.e., the energy levels along the DDO pathway are neither too strong nor too weak. C-O bond scission occurs with a moderate activation energy barrier on both surfaces ($E_a \approx 0.60$ eV), but it appears as if surface vacancy formation on both oxide surfaces is difficult with an activation barrier of 1.7 eV as shown in the purple region of Figure 3-10(a). However, alternative vacancy formation pathways to the mechanism shown in Figure 3-10(a) could potentially resolve this issue. These are the WF1 on TiO_2 and the WF3 on RuO_2/TiO_2. These mechanisms require additional adsorption and diffusion

steps to complete the catalytic cycle of HDO. On RuO_2/TiO_2 the WF3 may lead to the formation of oxygen vacancy, but the WF1 on TiO_2 is still expected to be limited because of difficulties for the formation of surface hydroxyls on TiO_2[146] and data explained in section 3.3.2.1. Therefore, we conclude that the balance between vacancy formation (E_a = 0.65 eV) and C-O bond scission (E_a = 0.50 eV) makes RuO_2/TiO_2 the best candidate for DDO reactions among the considered metal-oxide surfaces.

As previously discussed, metal oxide surfaces can also activate HYD, which is shown in Figure 3-10(b). All investigated oxide surfaces have in common that they interact strongly with ethoxy (ca. E_{BE} > -1.5 eV) and the barrier for ethoxy formation is less than 0.2 eV, indicating that this intermediate may poison the V_O site during CH_3CHO HDO. In addition, the formation of surface ethanol has a higher barrier than ethoxy formation. Therefore, the calculated energy barrier for the formation of ethanol following the HYD mechanism is 0.89 eV on TiO_2, 1.53 eV on Ru_1TiO_2, 1.28 eV on RuO_2/TiO_2, and 0.96 eV on RuO_2, respectively.

Before we close this section, we highlight some key results. HYD and DDO are competitive pathways, but HYD is thermodynamically preferred over DDO and the HYD transition state energies are lower than any transition state energy along the DDO pathway. On RuO_2, the selectivity to ethylene is expected to be very low. The C-O bond scission occurs with lower a barrier on doped Ru_1TiO_2; however, the remaining elementary steps are kinetically limited due to strong binding of surface intermediates to the Ru^{cus} site.

On the basis of calculated energy barriers, RuO_2/TiO_2 is considered the best catalyst candidate for DDO, because the C-O bond cleavage and vacancy formation pathway are balanced. However, formation of ethylene on RuO_2/TiO_2 still competes with the formation of by-product ethanol. The slowest step on the basis of calculated barriers is the dehydrogenation of CH_3CH-Ru^{cus} with E_a = 0.77 eV during DDO and the second HYD step in $CH_3CH_2O^{br}$ with E_a = 1.28 eV during HYD. On TiO_2(110), DDO has a more favorable potential energy profile than RuO_2/TiO_2, but vacancy formation pathways are significantly hindered due to the weak interaction between the Ti^{cus} site and gas-phase H_2 molecules.

3.3.5. Hydrogen Delivery and Vacancy Formation on $Ru_{10}/TiO_2(110)$

The main limitation for TiO_2 as HDO catalyst is the slow delivery of H_2 onto the surface (section 3.3.4). The activation of H_2 and generation of surface hydroxyls has been attempted with different methods[152,153], but the best way appears to be a spillover process, which has been coined by Boudart *et al.* and describes the migration of hydrogen atoms from metal particles to the oxide support[154,155]. The concept of spillover has attracted significant research interest and several groups have attempted to prove spillover experimentally, and tried to apply this concept for catalysis[154,155].

One experimental example is given by Khoobiar *et al.* who reported that yellow WO_3 turns into blue WO_{3-x}, when WO_3 particles are contact with metal Pt clusters under H_2 atmosphere. The authors attribute this observation to surface reduction spill-over of hydrogen adsorbed on the Pt metal clusters to WO_3 ($WO_3 + H_2 \leftrightarrow WO_{3-x} + H_2O$)[154]. More recently, Boonyasuwat *et al*. implicated the hydrogen spillover process for vacancy formation during HDO of lignin-derived oxygenates on Ru/TiO_2 to explain enhanced catalytic activity and selectivity to desired products[156–158]. Temperature programmed reduction (TPR) profiles of Ru/TiO_2 under H_2 atmosphere showed surface reduction peaks at T = 180 ℃ and T = 310 ℃, which are associated with reduction of RuO_2 and partial reduction of TiO_2, respectively. In absence of metallic Ru, TiO_2 has a reduction peak at T = 570 ℃. Despite ample examples supporting that hydrogen spillover from metal clusters to reducible oxides surfaces mediates the creation of V_O sites, this mechanism remains speculative and has not been fully confirmed.

In this section, we are going to address the question of of hydrogen delivery from gas-phase to TiO_2 and focus specifically on the role of Ru metal clusters in this mechanism. As discussed in section 3.3.2.2, CH_3CHO HDO is feasible as long as a surface oxygen vacancy exists [158], and we shift our attention on how Ru clusters facilitie vacancy formation at the $Ru_{10}TiO_2$ interface. Such system is often called a multiphase catalyst where transition metals (Pt, Au, Cu, Pd, etc.) are supported on reducible supports (e.g. TiO_2, CeO_2, MoO_3, and Fe_3O_4, MnO, etc.) [159]. Each system has been tested for the water gas shift reaction, CO oxidation, and furfuraldehyde hydrogenation,

and showed enhanced catalytic activity and selectivity compared to transition metal catalysts such as Pt, Au, Cu, and Pd on inert support. The performance improvement is attributed to cooperative effects between each phase including transition metal, support, and the interface[160–162].

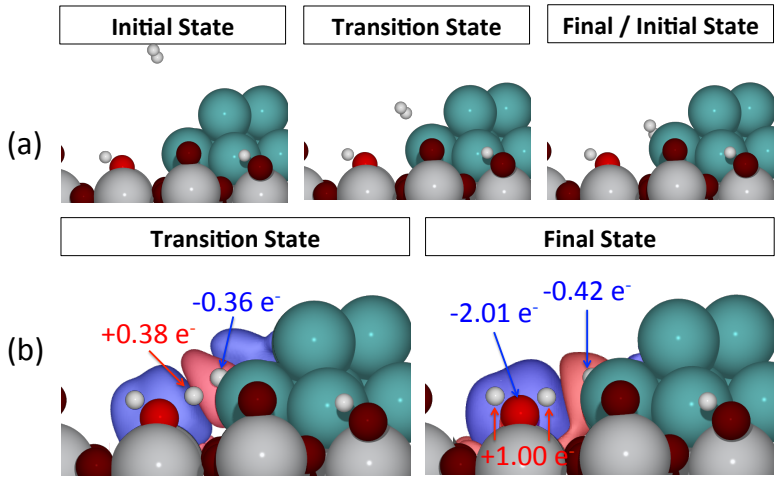

Figure 3-11. Hydrogen binding and heterolytic cleavage at the $Ru_{10}/TiO_2(110)$ interface. (a) H_2 adsorbs on the Ru particle; (b) Heterolytic dissociation of H_2-Ru occurs across the Ru/support interface. Color code: H - white; O - red; C - gray; Ru – teal; and Ti – light-gray.

To investigate the formation of an oxygen vacancy at the Ru_{10}/TiO_2 interface, several mechanistic possibilities were explored, including H_2 activation on a Ru site followed by spillover of atomic H. Although H_2 dissociation is nonactivated on Ru cluster, the spillover from Ru to TiO_2 requires an activation barrier of E_a = 1.15 eV. The most likely pathway according to our study is a TiO_2-assisted heterolytic cleavage of H_2, as illustrated in Figure 3-11. It is initiated with activated H_2 adsorption on the Ru cluster near the TiO_2 support, which has an E_a = 0.11 eV and ΔE = −0.05 eV [Figure 3-11(a)]. The adsorbed H_2 species then dissociates heterolytically across the Ru/TiO_2 interface to protonate a bridging hydroxyl group (HO^{br}) on TiO_2, as shown in the enlarged transition and final state of Figure 3-11(b). The charge density difference, $\Delta\rho = \rho_{H_2Ru/TiO_2} - (\rho_{RuTiO_2} + \rho_{H_2})$, shown with blue and red represent charge accumulation and depletion, respectively. The numerical values indicate the Bader charge at the transition state and final state. The protic character of the hydrogen being transferred to the support is evidenced by a fractional Bader charge of +0.38 e^- in the transition state. This dissociation mechanism generates

a support Brønsted acid site and an H adatom, with significant negative charge density, on the bridge site of two Ru atoms. The calculated energy barrier and reaction energy for this H_2 dissociation step are E_a = 0.47 eV and ΔE = 0.22 eV, respectively. After H_2O^{br} is formed at the interface, it may desorb as water and recreate the interfacial V_O site with Lewis acid character.

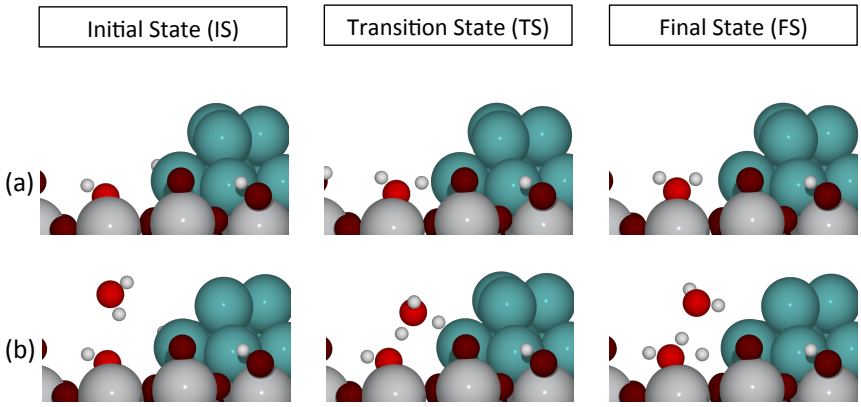

Figure 3-12. Side view of two different atomic hydrogen spillover mechanism at the Ru_{10}/h-TiO_2 interface: (a) atomic hydrogen spillover; (b) H_2O-assisted atomic hydrogen spillover. Color code: H - white; O - red; C - gray; Ru – teal; and Ti – light-gray.

H_2 dissociation on the Ru cluster followed by atomic hydrogen spillover to TiO_2 with or without the assistance of water as suggested by Xi *et al*. was also tested[163]; however, both atomic hydrogen spillover pathways involved at least one step with a barrier of ~ 1.1 eV or more as shown in Figure 3-12. Atomic hydrogen adsorbed on a bridge site of the Ru cluster diffuses to a neighboring bridging hydroxyl (HO^{br}) and forms a water molecule as shown in Figure 3-12(a). The calculated energy barrier and energy change are E_a = 1.15 eV and ΔE = 0.94 eV, respectively. Figure 3-12(b) shows the H_2O-assisted atomic hydrogen spillover mechanism, during which a hydronium (H_3O^+) ion is formed at the transition state. The calculated energy barrier and energy change are E_a = 1.73 eV and ΔE = 0.83 eV, respectively.

The most likely hydrogen spillover pathway, leading to formation of surface hydroxyls and a surface oxygen vacancy at the Ru_{10}/TiO_2 interface, is summarized in Figure 3-13. Intermediate states are (1) clean $Ru_{10}/TiO_2(110)$, (2) H_2-Ru^{br}, (3) H-Ru^{br} + H_2O^{br}, (4) $H_2O_{(g)}$ + H-Ru^{br}, (5) V_O site at Ru_{10}/TiO_2 interface. Binding energies are calculated with respect to gas-phase H_2, H_2O, and the Ru_{10}/TiO_2 model. Adsorption of molecular H_2 on the interface is activated with E_a = 0.11 eV on clean Ru_{10}/TiO_2 [state (2) in Figure 3-13], followed by H_2 dissociation with E_a = 0.47 eV [state (3)

in Figure 3-13], and finally forms H_2O^{br} and H-Ru^{br} [state (4) in Figure 3-13]. Once the formed H_2O^{br} desorbs, the V_O site can be created. Leftover H atom is able to recouple with another H atom or is expected to consume along with CH_3CHO HDO pathway. This PES clearly shows that vacancy formation pathway at the Ru_{10}/TiO_2 interface has much lower energy barrier than the vacancy formation pathway over TiO_2 itself (ca. E_a > 1.0 eV, see reaction O1 and O3 in Table 3-2). Therefore, it is concluded that Ru_{10}/TiO_2 interface facilitates the creation of V_O site that contributes to the selective DDO pathway as Ru/TiO_2 catalyst presents the better catalytic activity and selectivity for phenol and guaiacol HDO reaction [101,156].

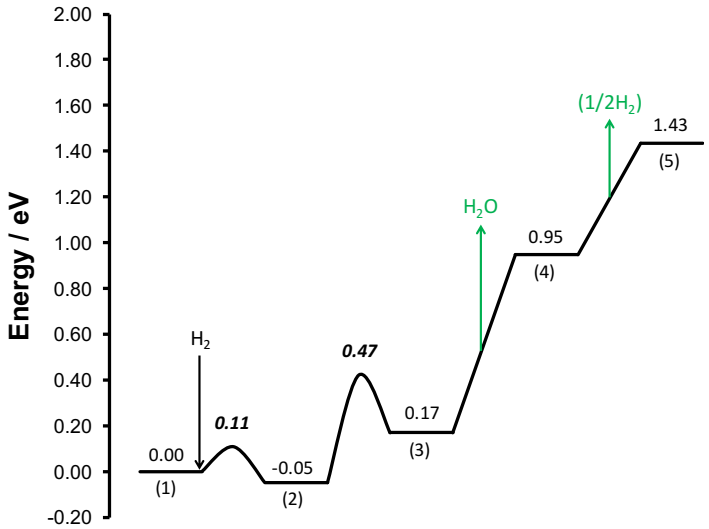

Figure 3-13. PES for vacancy formation pathway at the $Ru_{10}/TiO_2(110)$ interface. Activation energy barriers (E_a) in eV are shown in italic bold. Gas-phase species adsorbing to the surface are shown in black; products desorbing from the surface are shown in green.

3.4. Conclusions

We have investigated HDO mechanisms of acetaldehyde, a surrogate molecule among the ca. 400 oxygenated compounds in bio-oil obtained from the fast pyrolysis of biomass, on metallic Ru(0001), $TiO_2(110)$, $Ru_1TiO_2(110)$, 1 ML $RuO_2/TiO_2(110)$, $RuO_2(110)$, and $Ru_{10}/TiO_2(110)$. The binding energies of surface intermediates and the activation energies of a large number of different elementary steps were used to discern the preference for C-H, C-O, and C-C scission in CH_3CHO. On the metallic Ru(0001) surface, the C-C scission (DCN) leading to surface carbon rather than the C-O scission (DDO) was preferred. The thermodynamically and kinetically

preferred sequence of elementary steps on Ru(0001) are given by adsorption (CH_3CHO**)** → αC-H bond breaking (CH_3CO*) → ßC-H bond breaking (CH_2CO*) → C-C bond breaking (CH_2*) → C-H bond breaking (CH*) → C-H bond breaking (C*). Although desired product ethylene is formed, the removal of surface O* requires to surmount more than 1.7 eV.

For oxide surfaces, partially reduced surfaces determined via surface phase diagram in Chapter 2 were used as a reference surface for further mechanistic study. Upon further H_2 adsorption, the bridging hydroxyls form a water and leave behind a surface oxygen vacancy (V_O) site. The formation of V_O site becomes kinetically relevant as the Ru contents increase in TiO_2, indicating that the TiO_2 is the hardest surface to create a vacancy, while the RuO_2 is the easiest surface to form the V_O site. The formed V_O site not only plays an important role for CH_3CHO adsorption, but also is beneficial for the selective C-O scission over the C-C scission in CH_3CHO, leading to the desired product ethylene. Beside, the formation of ethanol is also predicted to be the major side reaction on oxide surfaces. The DDO pathway follows the sequence of elementary steps: adsorption on surface vacancy (CH_3CHO^{br}) → isomerization ($CH_3CHO^{br}Ti/Ru^{cus}$) → αC-O bond breaking (O^{br} + CH_3CH-Ti/Ru^{cus}) → ßC-H bond breaking (HO^{br} + CH_2CH-Ti/Ru^{cus}) → αC-H bond formation (O^{br} + $CH_2CH_{2(g)}$), while the sequence of HYD pathways is given as the adsorption on surface vacancy (CH_3CHO^{br}) → hydrogenation ($CH_3CH_2O^{br}$) → hydrogenation ($CH_3CH_2O^{br}H$). The highest catalytic activity to desired product ethylene is predicted on both 1 ML RuO_2/TiO_2(110) and TiO_2(110) along with byproduct ethanol formation; however, the dissociation of H_2 and the formation of hydroxyls which is the precursor to the formation of the required V_O site, are kinetically limited on TiO_2. This kinetic limitation on TiO_2 can be overcome by Ru cluster that facilitates hydrogen delivery from the gas-phase to TiO_2 support and create the V_O site at Ru/TiO_2 interface. Our DFT results suggest that the Ru/TiO_2 interface is the active sites for H_2 dissociation with $E_a \approx 0.4$ eV, forming a water on TiO_2 support. Once the V_O site on TiO_2 is formed, we expected that the desired DDO pathway shown in Figure 3-9 would be activated.

Chapter 4. Experimental and Theoretical Insights into the Hydrogen-efficient Direct Hydrodeoxygenation Mechanism of Phenol over Ru/TiO_2

4.1. Introduction

The complex, amorphous chemical structure of lignocellulosic biomass leads to hundreds of oxygenated bio-oil compounds and makes detailed HDO studies of this feedstock quite difficult [3]. Thus, phenol or substituted phenols, representative of a large fraction of oxygenated bio-oil compounds, are often used as model substrates[10,99,101,129,164,165]. Figure 4-1 schematically shows the two main reaction pathways by which oxygen can be removed from phenol. The upper pathway shows the direct deoxygenation (DDO) of phenol to benzene, which utilizes a single hydrogen equivalent for reduction. The lower pathway is initiated by a catalytic hydrogenation (HYD) of phenol to cyclohexanone. Additional reduction and dehydration steps are necessary to reach a deoxygenated product, cyclohexene, which under HDO reaction conditions is rapidly reduced by an additional hydrogen equivalent to cyclohexane[166,167].

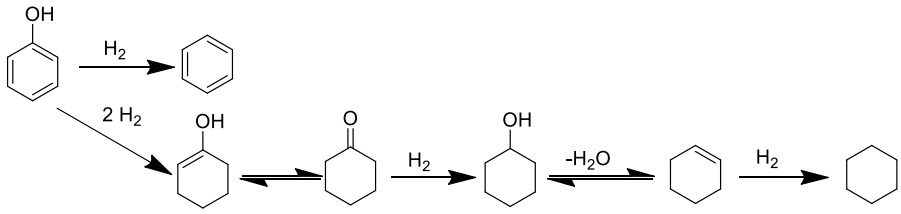

Figure 4-1. Two schematic HDO pathways for phenol. The top pathway represents the DDO route and utilizes hydrogen-reducing equivalents most efficiently. The lower pathway utilizes a total of four hydrogen-reducing equivalents to arrive at the final deoxygenated, but saturated product.

Overall, this process consumes four hydrogen equivalents for deoxygenation. For upgrading biofuels, it is desirable to selectively remove oxygen because hydrogenation of the double bonds uses expensive reduction equivalents while decreasing the octane value of the naphtha fraction of the product[168]. Selectivity in the context of the present work refers specifically to the extent to which reducing equivalents are used to directly remove oxygen, as opposed to the reduction of double bonds.

HDO catalyst design has been inspired by closely related hydrodesulfurization (HDS) catalysts used for decades in the petroleum industry to remove sulfur contaminants in crude oil and to meet low sulfur fuel standards[101,129,166,167,169,170]. MoS_2 catalysts are archetypal HDS catalysts whose catalytic activity relies on the formation of sulfide vacancies at the Mo-promoted edge sites [171]. Although many HDS catalysts are also effective at catalyzing HDO reactions, they require a continual feed of H_2S to prevent catalyst degradation. Lignocellulosic biomass inherently has little sulfur, so adding sulfur during an upgrading step is not desirable [169]. Recent efforts have turned instead to metal oxide- and supported metal particle-based catalysts, which do not require a sulfide regeneration step[101,169,172–174]. Rational catalyst design relies on understanding the mechanism by which catalysts operate. In our initial work in this area, we screened a number of supported Ru catalysts for HDO of liquefied phenol, which contains 10 wt % water[101]. Uncalcined Ru/TiO_2 catalysts with particle sizes of ~2nm showed the best activity and DDO selectivity of all the catalysts screened, consistent with several other literature reports[156,158,175]. Our findings supported the hypothesis that metallic Ru(0) was the primary ruthenium species in the active catalyst[101]. We and others hypothesized that TiO_2's superior support properties were attributable to its redox activity[101,158] which can be enhanced by hydrogen spillover. This interpretation was also suggested in literature reports on reducible ZrO_2 and Fe_2O_3 supports.

Conclusive information on the mechanism of catalytic direct deoxygenation (DDO) of phenolic compounds is scarce. Although the direct C-O bond scission pathway (Figure 4-2, mechanism A) is fully consistent with observed product distributions, it has been widely discarded because it requires breaking a strong C-O bond[176,177]. Indeed, density functional theory (DFT) calculations on the flat Ru(0001) surface support this assessment[15]. However, a recent DFT study on stepped Ru reported that C-O activation may occur with a moderate activation barrier of E_a = 0.78 eV[26]. Similarly, McEwen *et al.* identified direct C-O bond scission as the dominant pathway on Fe and Pd/Fe surfaces[164,178]. As an alternative to direct C-O bond scission, an initial hydrogenation (HYD) step was proposed to weaken the C-O bond, followed by an acid-catalyzed dehydration reaction (Figure 4-2, mechanism B)[179,180]. Resasco's group, however, convincingly argues that the product distributions observed on selective DDO catalysts, such as Ru/TiO_2, Pd/ZrO_2, Fe, and

bimetallic Ni−Fe catalysts are inconsistent with the hydrogenation/dehydration sequence [99,158,177]. They suggest instead that the DDO pathway is initiated by a tautomerization step leading to a keto intermediate, which undergoes hydrogenation and dehydration (Figure 4-2, mechanism C).

We have expanded our examination of the Ru/TiO_2 catalyst system using a combination of experimental work and first-principles calculations to resolve the debate regarding the mechanism of selective DDO catalysts. The addition of polar and nonpolar additives provides direct evidence for the crucial role of water in the activity and selectivity of these catalysts, and a series of isotopic labeling experiments imply that the phenolic hydroxyl is directly replaced by a single hydrogen atom.

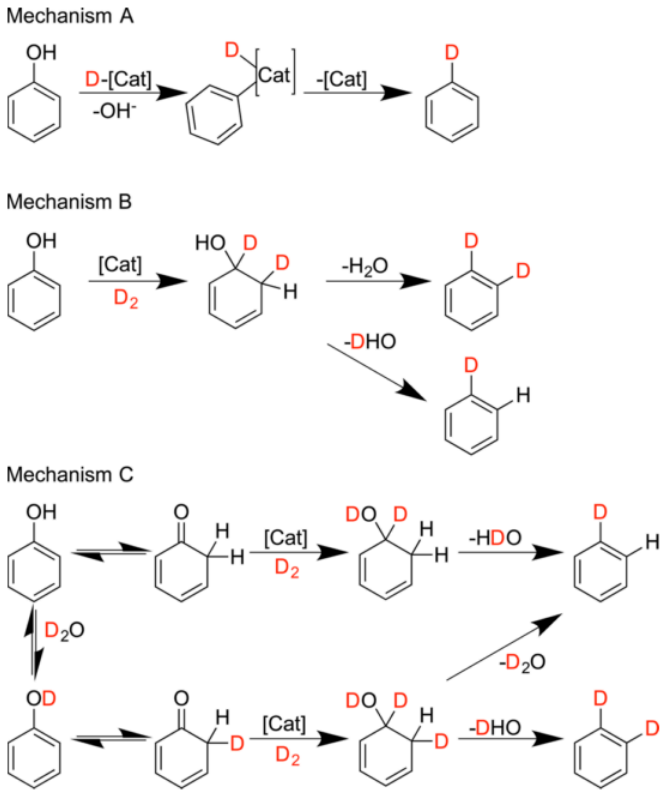

Figure 4-2. Three possible reaction mechanisms for DDO emphasizing the isotopic signature predicted for each pathway when starting with D_2 as the reductant. Reductive H/D equivalents and H/D atoms exchanged with water are highlighted in red.

Theoretical calculations indicate that H_2 undergoes heterolytic cleavage at an interfacial site between ruthenium nanoparticles and a basic bridging hydroxyl at the TiO_2 surface. The heterolytic cleavage of hydrogen generates an active site consisting of a Brønsted acid on the support in close proximity to a reductive ruthenium hydride.

The lowest energy reduction pathway is a proton-mediated, direct substitution of the aromatic hydroxyl with this ruthenium hydride. The exceptional activity and selectivity of TiO_2 is attributed to its amphoteric character rather than its reducibility. TiO_2 can both accept a proton from H_2 to generate the active site and donate a proton to assist in cleaving the C−O bond of phenol; both steps have almost identical activation energies. This novel mechanism, which does not require the formation of an oxygen vacancy site on TiO_2, is supported by theory and experiments using isotopically labeled reactants and is capable of explaining the observed activity and selectivity reported for other metal catalysts on amphoteric oxide supports.

We have expanded our examination of the Ru/TiO_2 catalyst system using a combination of experimental work and first principles calculations to resolve the debate regarding the mechanism of selective DDO catalysts. Solvent modifications provide direct evidence for the crucial role of water in the activity and selectivity of these catalysts, and a series of isotopic labeling experiments imply that the phenolic hydroxyl is directly replaced by a single hydrogen atom. Theoretical calculations indicate that H_2 undergoes heterolytic cleavage at an interfacial site between ruthenium nanoparticles and a basic bridging hydroxyl at the TiO_2 surface. The heterolytic cleavage of hydrogen generates an active site consisting of a Brønsted acid on the support in close proximity to a reductive ruthenium hydride. The lowest energy reduction pathway is a proton-mediated, direct substitution of the aromatic hydroxyl with this ruthenium hydride. The exceptional activity and selectivity of TiO_2 is attributed to its amphoteric character rather than its reducibility. TiO_2 can both accept a proton from H_2 to generate the active site and donate a proton to assist in cleaving the C-O bond of phenol; both steps have almost identical activation energies. This novel mechanism, which does not require the formation of an oxygen vacancy site on TiO_2, is supported by theory and experiments using isotopically labeled reactants, and is capable of explaining the observed activity and selectivity reported for other metal catalysts on amphoteric oxide supports.

4.2. Experimental

4.2.1. Materials

Titanium dioxide (Aldrich, 21 nm particle size, 33−55 $m^2\ g^{-1}$ surface area), $RuCl_3 \cdot 3H_2O$, phenol, hexadecane, cyclohexane, cyclohexene, cyclohexanol, cyclo-hexanone, hexamethyldisilazine, trace metal grade nitric acid, and trace metal grade hydrochloric acid were all purchased from Sigma-Aldrich. Deuterium oxide, deuterated phenol, and deuterated benzene were purchased from Cambridge Isotopes.

4.2.2. Catalyst Preparation

Supported ruthenium catalysts were prepared by a wet impregnation method, as previously reported, but without high-temperature calcination[101]. Catalysts were reduced in a 25 mL Parr reactor. After sealing an appropriate amount of catalyst in the reactor, the temperature of the system was increased under flowing H_2 gas at a rate of 20 K min^{-1} until it reached the 573 K set point. Upon temperature equilibration, the system was maintained under flowing H_2 for 0.5 h. At that point, the reactor was sealed and pressurized with H_2 to 550 psig and maintained at this temperature for 1 h. At the end of this reaction time, the reactor was cooled to room temperature before venting the remaining H_2. This reduced catalyst was quickly weighed in air before being immediately transferred back to the reactor along with the phenol.

4.2.3. Catalyst Characterization

4.2.3.1. Metal Determination

Ru content analysis was performed by Galbraith Laboratories or done using a Thermo Scientific iCAP 600 ICP- OES spectrometer with microwave-assisted digestion.

4.2.3.2. High-Resolution TEM (HRTEM)

High-resolution TEM was carried out at the MIT Center for Material Science and Engineering (CMSE) using the JEOL 2010 Advanced High Performance TEM. The catalysts were dispersed in isopropyl alcohol, and a drop of this suspension was placed on a lacey carbon Cu grid. Simultaneously with TEM analysis of the selected samples, energy dispersive X-ray

microanalysis (EDX) experiments were also performed on selected regions of the catalysts to confirm the presence of Ru metal and to demonstrate the absence of residual chlorine.

4.2.4. Catalytic Conversion of Phenol

4.2.4.1. Standard Reaction Conditions

The phenol HDO reactions were carried out in a 25 mL autoclave reactor operating in batch mode. In a typical reaction, liquefied phenol (5 g, ~10 wt % water, Fisher Scientific) was introduced into the reactor along with ~100 mg of freshly reduced catalyst. The system was closed, and to avoid any air contamination, H_2 was bubbled through the solution for 10 min. This was followed by three reactor purges with 75 psig of H_2. The closed reactor, still under H_2 atmosphere, was heated to the reaction temperature of 573 K while stirring at 700 rpm. When the reaction temperature was reached, the total pressure was adjusted to 650 psig (45.8 bar) by regulating the H_2 pressure. The pressure was kept constant during the progress of the 1 h experiment. After the reaction, the reactor was cooled to room temperature. Samples were immediately frozen until they could be analyzed by GC/MS.

4.2.4.2. Modified Reaction Conditions for Isotopic Labeling and Additive Effect Experiments.

These experiments were conducted as described above (section 2.4.1), except that either anhydrous D_0-phenol or anhydrous D_6-phenol (4.5 g) was added to the reactor along with an optional addition of water (deionized or deuterated) or octane. We use the notation D_x to indicate extent of deuteration, e.g. D_0-phenol is regular phenol, whereas D6-phenol is fully deuterated. In all cases, 0.5 g of additive was used for a final concentration of 90 wt % phenol. A catalytic experiment was also conducted with D_0- phenol (liquified, ~10 wt % water) and 200 µL of NMR quality D_6-benzene. This reaction was run for a total of 15 min. Samples from the isotopic labeling experiments were derivitized with trimethylsilane (TMS) by taking ~100 µL of the reaction mixture and mixing it with 50 µL of hexamethyldisilazine. After shaking the samples for 10 min, excess silylating agent was removed using a stream of argon gas.

4.2.4.3. Gas Chromatography Mass Spectrometry (GC-MS)

Two microliters of the reaction product were diluted in 1 mL of hexadecane. The samples were injected without a solvent delay. Samples were analyzed using an Agilent 689N Network GC System with a 6890 series injector and 5973N network mass selective detector with a HP-5MS cross-linked 5 % PH ME siloxane capillary column (dimensions of 30 m × 0.25 mm × 0.25 μm) using UHP He. The analysis method contained a 6 min hold at 308 K, followed by a ramp at 5 K min^{-1} to 398 K. This temperature was held for another 10 min before ramping at 30 K min^{-1} to 573 K, which was held for 10 min. The mass detector was turned off after the elution time of all potential products but before the solvent (hexadecane) eluted. Product yields were obtained from calibrated GC/MS spectra.

4.2.4.4. Isotopic Distribution Analysis

For HDO reactions conducted with isotopically labeled starting materials, the isotopologue distribution of the products and remaining starting materials were determined by non-negative least- squares fitting of a portion of the experimental MS data with a reference array of simulated isotopologue MS data. Experimental MS data were extracted from the GC/MS spectra of the reaction products. Under our GC/MS conditions, benzene and cyclohexane elute at very similar retention times, so the experimental MS intensity data for the entire elution region containing both compounds was considered simultaneously. Samples of TMS-protected phenol were prepared separately (see above), so the MS of this material was extracted and analyzed independently. The analysis window was 73−97 m/z for benzene/cyclohexane and 161−175 m/z for TMS-protected phenol. To prepare the reference MS matrices for all isotopologues, initial reference spectra were obtained from the NIST Webbook[181] for benzene and cyclohexane or from a MS of an authentic sample of TMS-protected phenol. The intensity values for the molecular ion and several lighter fragments were then extracted from this data: 73−78 m/z for benzene, 81−84 m/z for cyclohexane, and 161−166 m/z for TMS-protected phenol. MS data for heavier deuterium-containing isotopologues were simulated using a simple probability-based approach for loss of H or D in the molecular fragments, which was shown to give an approximation very close to the experimentally observed mass spectrum of D_1-benzene[182]. To account for heavier ^{13}C-containing

isotopologues, the reference MS data for each deuterium-containing isotopologue were convoluted with the ratios of the ^{13}C isotopologues calculated from the natural isotopic abundance of ^{12}C and ^{13}C.

4.2.5. Computational Approach

Density functional theory (DFT) calculations were carried out using the Vienna Ab-initio Simulation Package (VASP) in combination with the Atomic Simulation Environment (ASE)[63,64,103]. The projector augmented wave (PAW) method[106] and the generalized gradient approx- imation (GGA) with the revised Perdew−Burke−Ernzerhoff (RPBE) functional were employed to solve the Kohn−Sham equations[40,105]. All DFT calculations were performed with a cutoff energy of 400 eV and a Gaussian smearing of k_BT = 0.1 eV with subsequent extrapolation of the total energies to k_BT = 0 eV[71]. To correct for on-site Coulombic interaction of the localized Ti 3d state, we used the DFT+U approach by Dudarev *et al*. with U_{eff} = 2.0 eV[112]. This value is in good agreement with the value obtained by Hu and Metiu[114]. To model the Ru/TiO_2 interface, we emulated our previous approach to modeling the Au/TiO_2 interface[183]. We placed a 10 atom Ru cluster, initially in the hcp structure, on a fully hydroxylated rutile h-TiO_2(110) surface, the most stable surface facet of TiO_2, as shown in Figure 4-3. The Ru_{10} cluster was placed on three adjacent bridging oxygen vacancy sites, which can serve as nucleation sites for cluster growth[184]. The supported Ru_{10}/h-TiO_2(110) cluster model is representative for very small particles, whereas the more frequently used periodic Ru(0001) surface is a model for very large particles. Comparisons based on these two extreme models, neither one of which is an exact representation of the real catalyst, enable a computationally aided interpretation of the experimental measurements and allow rationalizing the observed particle size and support effect.

The optimized lattice constants for rutile TiO_2 are a = 4.712 Å, c/a = 0.640, and u = 0.306, in good agreement with experimental data[107,185]. The TiO_2(110) surface was represented in a 5 × 4 periodic unit cell with four TiO_2 layers, of which the top two layers were fully relaxed, while the bottom two layers were fixed at their bulk positions. Subsequent slabs were separated by 16 Å of vacuum space in the z direction, a dipole correction was applied to compensate for the effect of

adsorbing molecules only on one side of the surface[70], and spin polarization was included. The Brillouin zone was integrated using a (2 × 2 × 1) Monkhorst−Pack mesh[72], and geometries were optimized using a force convergence criterion of 0.05 eV $Å^{-1}$. Convergence with respect to the k-point set and the force criterion were confirmed.

The binding energies of stable intermediate states (E_{BE}) were calculated with respect to the clean surface and gas phase reference molecules according to $E_{BE} = E_{slab+adsorbate} - (E_{slab} + E_{gas})$, where $E_{slab+adsorbate}$ is the total energy of the slab with adsorbates; E_{slab} is the energy of the clean surface; and E_{gas} is a gas phase reference state based on phenol, water, and hydrogen.

All reported DFT energies are electronic energies at T = 0 K unless otherwise noted. Where the use of Gibbs free energies is indicated, those were calculated according to $\Delta G = \Delta E + E_{ZPE} - T\Delta S$ (E_{ZPE} = zero point energy) at T = 573 K, P_{phenol}= 11.43 bar, $P_{\mathrm{H_2}} = 33.37$ bar, and $P_{\mathrm{H_2O}}$ = 1.00 bar. The climbing image nudged elastic band (cNEB) method[72,186,187] was implemented to locate the transition state (TS) of each elementary reaction step with five or six intermediate images, which were fully optimized to a force criterion of 0.1 eV $Å^{-1}$. We confirmed that this convergence criterion is sufficient to obtain transition states within 0.1 eV accuracy, a generally accepted error bar in DFT calculations. Vibrational analysis was performed to confirm the existence of a single imaginary mode, corresponding to the reaction coordinate along the reaction pathway. For each calculated elementary reaction step, the hydrogen coverage was kept minimal by adding or removing $1/2H_2$ to or from the surface as needed. We note that the associated adsorption/desorption energy changes depend on lateral surface interactions within the local surface environment to or from which the H atom is added or removed. These interactions are included in the hydrogen adsorption/desorption energies, leading to variations of these values.

To study the effect of water on phenol HDO, we investigated three plausible scenarios, as shown in Figure 4-3: (1) water adsorbed in a bridging oxygen vacancy site ($V_{O^{br}}$) at the Ru_{10}/h-TiO_2 interface, (2) a single gas-phase water molecule near a $V_{O^{br}}$ site on h-TiO_2, and (3) water adsorbed on the Ru metal cluster. The binding energies (E_{BE}) for water in these positions are (1)

−0.06, (2) −0.11, and (3) −0.40 eV, respectively. For comparison, the water binding energy on the flat Ru(0001) surface is E_{BE} = −0.14 eV.

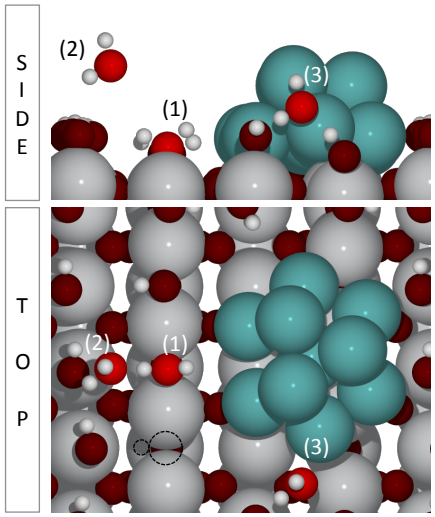

Figure 4-3. Side and top views of Ru_{10}/h-TiO_2(110) with enumerations at the locations used in the DFT calculations to investigate the effect of water. Color code: hydrogen, white; oxygen, red, ruthenium, teal; and titanium, light gray.

4.3. Results and Discussion

There are at least two separate reduction reaction pathways by which phenol can react on a supported Ru catalyst in the presence of hydrogen (see Figure 4-1)[166,188]. In the hydrogenation pathway (HYD), phenol is involved in a multistep hydrogenation sequence to form the ketone cyclohexanone and the alcohol cyclohexanol. Dehydration of cyclohexanol provides the first deoxygenated product cyclohexene, which is rapidly reduced to the ultimate deoxygented product cyclohexane[189–191]. The second pathway is a direct deoxygenation (DDO) that converts phenol into benzene without saturating its aromatic ring[192]. It has been suggested that HDO catalysts can have three distinct sites: a site for hydrogenation, a site for dehydration (these two sites would need to work in concert for HDO to occur), and a site for hydrogenolysis of the C−O bond for direct deoxygenation[8,193]. We postulate that HYD preferentially occurs on larger Ru particles and that DDO occurs at the interface between small Ru particles and an activated interfacial site. Below, we describe our use of HRTEM, isotopically labeled substrates, and DFT calculations to test this postulate.

4.3.1. Catalyst characterization with HRTEM

EXAFS and CO chemisorption measurements in our previous report indicated uncalcined Ru/TiO_2 catalysts with a particle size of ~ 2 nm showed the best DDO activity and selectivity [101]. In contrast, calcined Ru/TiO_2 catalysts had a particle size of 33 nm and were not selective for DDO, producing only 20% deoxygenated products from phenol[101].

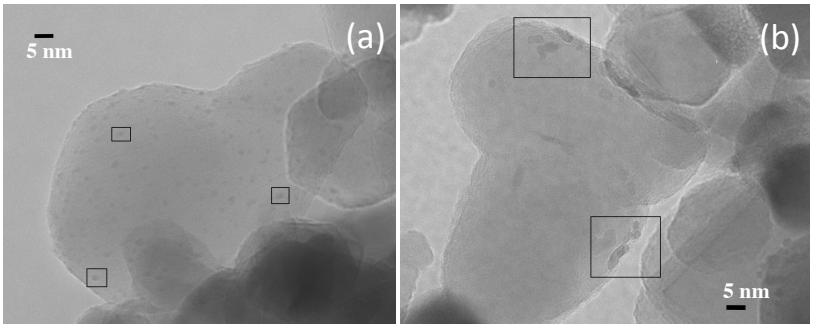

Figure 4-4. High-resolution transmission electron microscopy (HRTEM) images of Ru/TiO_2 (a) after H_2 reductive activation and (b) after a subsequent calcination. Both figures are magnified 200 000× at 200 kV. The black scale bar represents 5 nm.

To confirm the effect of calcination on the particle sizes, we acquired high-resolution transmission electron microscopy (HRTEM) images on selected catalysts (see Figure 4-4). These HRTEM images confirm the presence of small 2−3 nm Ru particles in catalysts treated only under a high-pressure reducing environment [see Figure 4-4(a)]. Upon calcination, the Ru particles aggregate to form much larger clusters of Ru metal [see Figure 4-4(b)], which is consistent with our previously reported chemisorption data[101].

4.3.2. The Effects of Additive on Catalytic Activity and Selectivity.

To explore the effects of polar and nonpolar additives as well as the possible role of water on the reaction mechanism, we conducted three sets of experiments: a reference experiment with liquefied phenol (10 wt % water); an experiment with anhydrous phenol; and an experiment with a nonpolar additive (octane).

The reference experiments (Table 4-1, entry 1) were done under conditions similar to our previously published work, with only a minor modification to the pretreatment conditions[101]. That is, the catalysts were activated by heating in an atmospheric pressure flow of 3:1 N_2/H_2 gas for several hours. A sample of unactivated catalyst was placed in a high-pressure Parr reactor and

heated up to 575 K in a static atmosphere (550 psig) of pure H_2 gas for 2 h. Upon cooling, the activated catalyst was weighed and immediately returned to the Parr reactor along with the phenol necessary for the reaction. The product selectivity is similar to that reported in our earlier work; however, slightly higher conversion is reported in this paper (30% conversion in this paper vs. 12% in prior work[101]), which we attribute to the more aggressive pretreatment conditions. In Table 4-1, the product distribution is reported as the average percent of each product formed relative to all phenol products. Percent conversion (% conv) gives the percentage of phenol converted to products. The percentage of all oxygen-free products (% deox) and the ratio of products that come from direct deoxygenation (benzene) to those that come from the hydrogenation pathway (all other products) are reported.

Table 4-1. Results of Catalytic Tests of Ru/TiO_2 for Phenol HDO.

Entry	Additive	% 	% 	% 	% OH 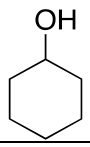	% O 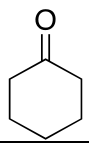	% Conv.	% deox	$\frac{DDO}{HYD}$
1	Water	95	2.5	0.8	0.8	0.8	30	98	19
2	None	38	40	5	3	14	22	83	0.8
3	Octane	40	24	1	15	20	13	65	1.6

Although the overall efficiency of the catalysts to deoxygenate phenol is similar whether water is present or absent in the reaction, the dominant deoxygenation reaction pathway is quite different. When water is excluded from the initial reaction, cyclohexane is the major deoxygenated product, with a DDO/HYD ratio of 0.8 (Table 4-1, entry 2). In the presence of water, benzene is the dominant product, with a DDO/HYD ratio of 19 (Table 4-1, entry 1).

When octane (10 wt %) is added to anhydrous phenol at the start of the reaction to reduce the polarity of the reaction medium, the reaction shows both lower conversion (13% conversion) and low selectivity toward DDO (DDO/HYD ratio of 1.6) (Table 4-1, entry 3). The presence of 10 wt % octane alters the reaction trajectory and slows the dehydration of cyclohexanol. Clearly, the presence of water plays an important role in the overall reaction, as these experiments done with and without water and with octane demonstrate.

The primary focus of this work is to develop catalysts that efficiently produce benzene directly from phenol; however, the pathway where phenol is hydrogenated and then dehydrated can also lead to products suitable for combustion. Different engines and different countries require fuels with differing compositions, so understanding the structural factors that control the HYD pathway is also of interest. As described in our prior work, under standard pressure at 573 K, both formation of cyclohexanone and reduction to cyclohexanol are thermo- dynamically unfavorable, but the subsequent steps in the HYD pathway are favorable[101]. The dehydration of cyclohexanol has been used as a probe of surface acidity of heterogeneous materials[194–196]. In this work, the ratio of cyclohexanol to cyclohexane varies from a low of 0.075 in the reaction with no water additive to a ratio of 0.63 in the reaction with octane additive, suggesting that there are fewer acidic sites suitable for catalyzing the dehydration of cyclohexanol when nonpolar octane is added as an additive.

4.3.3. Isotopic Labeling Experiments

To distinguish between the various proposed mechanisms for DDO, several reactions were carried out with isotopically labeled substrates. Figure 4-2 provides the expected isotopic signature of benzene from each pathway when the starting material is D_0-phenol and the reductant is D_2. Mechanism A, a direct substitution of a hydride for a hydroxide, should generate benzene with a single reductive hydrogen substituting the phenolic hydroxyl. The isotopic composition of benzene from mechanism B, ring hydrogenation followed by dehydration, and mechanism C, hydrogenation of the ketone tautomer of phenol followed by dehydration, is a bit more complicated to predict, but in each case, the isotopic composition of benzene should include more than one of the reductive hydrogen atoms. The isotopic labeling experiments in this work were conducted with different mixtures of isotopically labeled substrates, and the final isotopic compositions of the products were determined using simple least-squares fitting methods of the acquired GC/MS data. Phenol undergoes an inevitable H/ D exchange of the phenolic protons with ambient water during sample workup and GC/MS analysis [197]. To minimize the complications this induces in isotopic analysis, aliquots of each reaction sample were treated with

a silylating agent, which derivitizes free hydroxyl groups and leaves phenol with a maximum of five aromatic protons. These samples were used for isotopic distribution analysis of phenol.

4.3.3.1. H/D Ring Exchange in Phenol from Tautomerization

Phenol tautomerization provides a route to incorporate the isotopic signature of water into the aromatic ring [see Figure 4-5(a)][177]. DFT calculations estimate that the water-assisted tautomerization step at the Ru/TiO_2 interface is likely equilibrated with a moderate activation barrier of E_a= 0.38 eV and ΔE = -0.22 eV [see Figure 4-5(b)]. The extent of tautomerization expected under these reaction conditions was measured by a control reaction consisting of 10 wt % D_2O in D_0-phenol and a sample of activated Ru/TiO_2 catalyst. This reaction mixture was heated to the normal reaction temperature (573 K) under an atmosphere of inert gas (N_2). The isotopic distribution of phenol observed at the end of this reaction is shown in Figure 4-6(a). D_0-phenol remains the major isotopologue in this mixture; however, the presence of D_1-(~22%) and D_2-phenol (~4%) suggests that tautomerization occurs and that care must be taken in the interpretation of other isotopic labeling experiments.

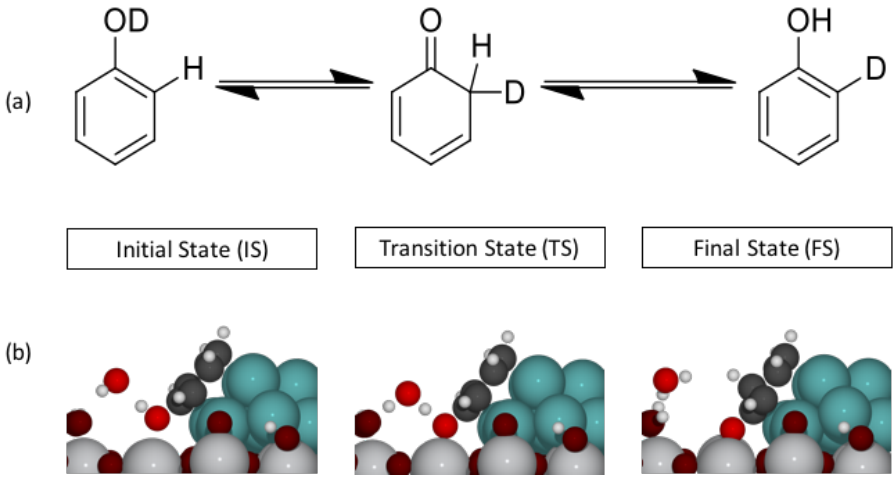

Figure 4-5. (a) Deuterium Incorporation into phenol through tautomerization. The initial deuterium is a result of H/D exchange with D_2O. (b) Side view of H_2O-assisted tautomerization of phenol at the Ru_{10}/h-TiO_2(110) interface.

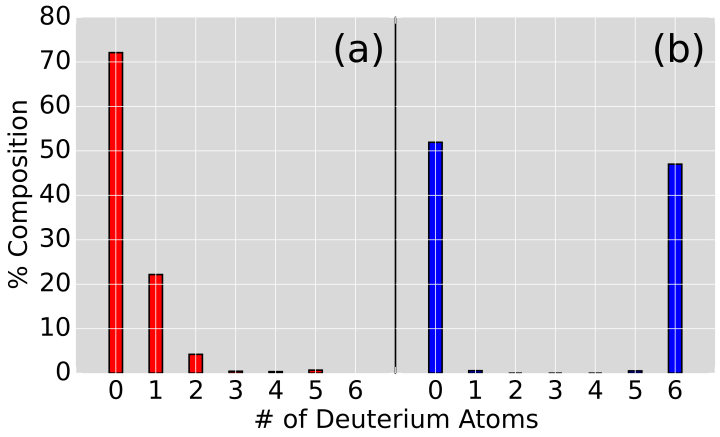

Figure 4-6. Isotopic distributions for benzene (blue) and phenol (red) for two control experiments. (a) The isotopologue distribution of phenol with D_0-phenol and D_2O; (b) The isotopologue composition of benzene with a spike of D_6-benzene, D_0-phenol, H_2O and H_2.

4.3.3.2. H/D Ring Exchange in Benzene under Reaction Conditions

Aromatic H/D exchange is commonly observed in metal hydride-catalyzed reactions (see Figure 4-7) [197,198] and has the potential to complicate mechanistic interpretations of isotopic distributions. To assess the extent of this process under our reaction conditions, a reaction was conducted in which 200 µL of D_6-benzene was added at the start of a standard HDO reaction. The isotopic composition of all benzene (spike + reaction product) at the end of this reaction is shown in Figure 4-6(b). This experiment indicates that H/D metal hydride exchange for the benzene product (see Figure 4-7) is very minor under these conditions. (Note: D_6-benzene overlaps with D_0- cyclohexane in the MS. However, very small amounts of cyclohexane are typically observed in reactions with this catalyst under these conditions, so it can be assumed that the majority of the intensity shown here comes from D_6-benzene)

(a) $H\text{-}[Cat] + D_2O \rightleftharpoons D\text{-}[Cat] + DHO$

(b) $XC_6H_5 + D\text{-}[Cat] \rightleftharpoons XC_6H_4D + H\text{-}[Cat]$

(c) $XC_6D_5 + H\text{-}[Cat] \rightleftharpoons XC_6D_4H + D\text{-}[Cat]$

Figure 4-7. Possible aromatic H/D scrambling pathways for phenol (X = OH) or benzene (X = H) (a) the H/D exchange of a metal hydride with water. (b, c) metal- catalyzed H/D ring exchange alters the isotopic composition of the aromatic ring.

The results of this experiment indicate that benzene is effectively inert to H/D ring exchange under these reaction conditions. D_0- and D_6-benzene are the two most prominent isotopologues

of benzene, each representing >40% of the product composition. D_0-benzene is the product of the catalytic DDO of D_0-phenol. The low levels of intermediate isotopologues are evidence that aromatic H/D exchange is a minor reaction pathway for benzene under these reaction conditions. It is also worth noting that this experiment confirms an assumption made in our earlier work: namely, that benzene is not fully hydrogenated under these reaction conditions, and therefore, the cyclohexane produced is entirely derived from the HYD pathway[199]. This is also confirmed by the lack of heavier cyclohexane isotopologues in this experiment.

4.3.3.3. H/D Ring Exchange in Phenol from Metal-catalyzed H/D Exchange

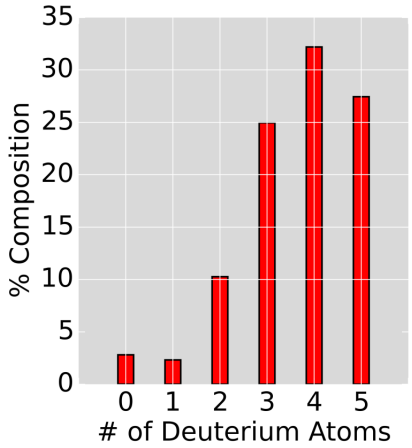

Figure 4-8. Isotopologue distribution for phenol in an HDO experiment with D_6-phenol and H_2 but without water showing that significant aromatic H/D exchange occurs for phenol.

Direct H/D exchange of the phenolic aromatic protons, in a manner analogous to that described above for benzene, would provide another route by which the isotopic composition of phenol could shift to reflect either the isotopic composition of the reducing gas or the isotopic composition of water (see Figure 4-7). An HDO experiment conducted with D_6- phenol and H_2 without water present at the start of the reaction was used to assess the level of aromatic H/D exchange in phenol. This reaction was stopped after only 15 min of total reaction time (rather than 1 h under normal conditions) to minimize side reactions with water, which is a reaction product. The distribution of phenol isotopologues in this experiment is shown in Figure 4-8. The phenol distribution shifts to lighter isotopologues as the reaction proceeds, which is indicative of metal-catalyzed H/D ring exchange.

4.3.3.4. Involvement of Water in H/D Exchange and Reduction Mechanism

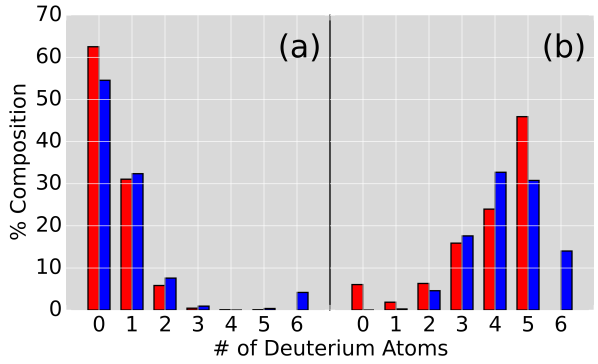

Figure 4-9. Isotopologue distributions for benzene (blue) and phenol (red) for two HDO isotopic labeling experiments. (a) Isotopologue composition from a reaction with D_0-phenol, 10 wt % D_2O, and H_2; (b) Isotopologue composition from a reaction with D_6-phenol, 10 wt % D_2O, and H_2.

To better understand both the mechanistic role played by water and its possible involvement in H/D exchange, an HDO reaction was conducted with 10 wt % D_2O, H_2, and anhydrous D_0-phenol. The isotopologue distributions for phenol (red bars) and benzene (blue bars) from this reaction are shown in Figure 4-9(a). Some deuterium incorporation into phenol is observed. The levels are slightly higher than the amount of deuterium incorporation from the tautomerization experiment (Figure 4-6(a)), suggesting that both tautomerization and metal-catalyzed H/D ring exchange in phenol (but not benzene) are operative (as illustrated in Figure 4-7) and lead to a change in the isotopic composition of phenol relative to its initial composition. Deuterium incorporation is also seen in benzene, but at levels that precisely mirror that of phenol starting material. The lack of additional deuterium incorporation into benzene leads to a mechanistic interpretation that water plays an important role in dictating activity and selectivity but does not directly participate in the reductive proton transfer.

4.3.3.5. Mechanistic Insights from Determining the Number of Reductive Hydrides Transferred to Product

The primary purpose of the isotope experiments was to elucidate the reduction mechanism by assessing the total number of hydrogen equivalents being transferred to benzene (Figure 4-2). To determine this, we compare the isotopologue distribution of benzene and phenol in HDO reactions that use either D_0-phenol or D_6-phenol in the presence of 10 wt % D_2O and H_2 (see

Figure 4-9). In both experiments, the isotopologue distribution of benzene mirrors that seen for phenol. Given that benzene is inert to H/D exchange under these reaction conditions, this result implies that the phenolic hydroxyl is being substituted by a single reductive hydrogen. Other mechanisms would lead to notably lighter distributions (i.e. more ^{1}H incorporation) of benzene isotopologues. Figure 4-9(a) shows the nearly identical distribution of benzene and phenol isotopologues. Taken in total, these data are consistent with the direct C−O bond cleavage pathway (Figure 4-2, mechanism A), but inconsistent with the mechanistic hypotheses that involve hydrogenation of the tautomerized keto form of phenol or multiple hydrogenation/dehydration steps (Figure 4-2, mechanisms B and C), which would be expected to add additional reductive equivalents to benzene.

4.3.4. First Principle Analysis of HDO Pathways on Ru/TiO_2

Table 4-2. Summary of key elementary steps at the Ru_{10}/h-TiO_2(110) interface model.[a]

No.	Elementary Steps	$^{1}\Delta E$	$^{2}E_a$	$^{3}\Delta G$	$^{4}\Delta G_a$	ΔE_{ZPE}	TΔS
I	$(C_6H_5)OH_{(g)}$ + $V_{O^{br}}$ + Ru → $(C_6H_5)OH$*	-1.60		-0.56		-0.04	-1.08
II	C_6H_6-Ru → $C_6H_{6(g)}$ + Ru	1.40		0.41		0.04	1.23
III	$H_2O_{(g)}$ + $V_{O^{br}}$ → H_2O^{br-}	-0.06		0.69		-	-
IV	H_2(g) + 2 Ru → 2 H-Ru	-0.25	~0.0[d]	[e]	[e]	-	-
V	H-Ru + HO^{br} → H_2O^{br} + Ru	0.94	1.15	[e]	[e]	-	-
VI(a)	$H_{2(g)}$ + Ru → H_2-Ru	-0.05	0.11	0.67	0.67[f]	0.43	-0.29
VI(b)	H_2-Ru + HO^{br} → H-Ru + H_2O^{br}	0.22	0.47	0.36	0.51	0.09	-0.02
VII	DDO1:$(C_6H_5)OH^*$ → (C_6H_5)-Ru + HO^{br}	-1.02	0.66	-1.09	0.65	-0.03	0.03
VIII	[6]DDO2:$(C_6H_5)OH^*$ + H_2O^{br}→ (C_6H_5)-Ru + HO^{br} + $H_2O_{(g)}$	-1.25	0.42	-1.25	0.58	-0.07	-0.06
IV	DDO3:$(C_6H_5)OH^*$ + $H_2O_{(g)}$ → (C_6H_5)-Ru + HO^{br} +$H_2O_{(g)}$	-0.83	0.94	[e]	0.90	-	-
X	DDO4:$(C_6H_5)OH^*$ + H_2O-Ru→ (C_6H_5)-Ru+HO^{br} +H_2O-Ru	-0.79	0.79	[e]	1.05	-	-
XI	(C_6H_5)-Ru + H-Ru → (C_6H_6)-Ru + Ru	-0.67	0.18	-0.52	0.19	0.14	-0.01

[a]The table shows the electronic energy change (ΔE), the activation energy (E_a), the Gibbs free energy change (ΔG), and the Gibbs free energy of activation (G_a) for each step. $V_{O^{br}}$ denotes the bridging oxygen vacancy site on h-TiO_2 near the interface. Species X bound only to the Ru cluster are shown as X−Ru. The simultaneous binding of phenol to both the $V_{O^{br}}$ site and the Ru cluster is indicated with an asterisk, for example,$(C_6H_5)OH^*$. [b]ΔE and E_a are the total energy change and activation energy barriers without zero point energy (E_{ZPE}) or entropy correction in electronvolts. [c]Gibbs free energies are calculated as $\Delta G = \Delta E + E_{ZPE} - T\Delta S$ at T = 573 K, P_{phenol} = 11.43 bar, P_{H_2} = 33.37 bar, and P_{H_2O} = 1.00 bar. [d]The H_2 molecule dissociated spontaneously upon adsorption on a Ru. metal site away from the Ru/TiO_2 interface. [e]Values were not calculated. [f]The Gibbs free energy of activation G_a is set equal to ΔG because entropy corrections render the calculated Gibbs free energy of the transition state more stable than the final state. [g]Instead of binding to the $V_{O^{br}}$ site, the phenolic OH group interacts with the H_2O^{br} molecule occupying the $V_{O^{br}}$ site.

To propose a DDO reaction mechanism that is consistent with our isotopic labeling experiments and can simultaneously explain the promotional effect of water, multiple pathways were explored using DFT calculations on a Ru_{10}/h-TiO_2(110) surface model. The key calculated energetics are summarized in Table 4-2. Guided by the experimental observation that a single reducing hydrogen equivalent is exchanged, the most probable DDO pathway for phenol in the absence of water is presented as DDO1 in Figure 4-10. The promotional effect of water on DDO activity and selectivity is then explored for three different cases (DDO2−DDO4), which are also summarized in Figure 4-13. Our results are contrasted with data on the thermodynamically most stable Ru(0001) facet, which is a good representation of larger Ru particles and has been used in several previous DFT investigations of HDO of phenolic compounds[15,200]. All of the most probable DDO mechanisms explored occur at interfacial sites between small Ru particles and the TiO_2 support. Such interfacial sites are known to play important roles in heterogeneous catalysis, and all of our computational results implicate them in the observed chemistry reported in this work[201].

4.3.4.1. Direct-deoxygenation (DDO) in the Absence of Water

The DDO of phenol without water is shown in Figure 4-10 and begins with its adsorption onto a Ru/TiO_2 interface site near a bridging oxygen vacancy ($V_{O^{br}}$) on TiO_2. The energy of the initial and final state is calculated with respect to phenol and the Ru_{10}/h-TiO_2 model with bridging oxygen vacancy site ($V_{O^{br}}$). At the transition state (TS), the activation barrier, E_a, is indicated in bold face. The calculated binding energy of phenol at the interface is exothermic by E_{BE} = −1.60 eV. In comparison, phenol binding to the flat Ru(0001) surface is weaker, with E_{BE} = −0.47 eV [see Figure 4-11(a)], indicating a preferential adsorption at the interface site. Binding occurs primarily by charge transfer from Ru metal to the adsorbate and strong π interactions between the aromatic ring and the d-states of the Ru cluster[202]. The binding of phenol is followed by direct C−O scission, which requires a moderate activation energy barrier of E_a = 0.66 eV. The cleaved OH group heals the $V_{O^{br}}$ site at the Ru/TiO_2 interface, rendering the reaction exothermic by ΔE = −1.02 eV. The same step on Ru(0001) is activated by E_a = 1.23 eV [see Figure 4-11(a)], which compares well with previously calculated values of E_a = 1.15 eV[200] and E_a = 1.29 eV[15].

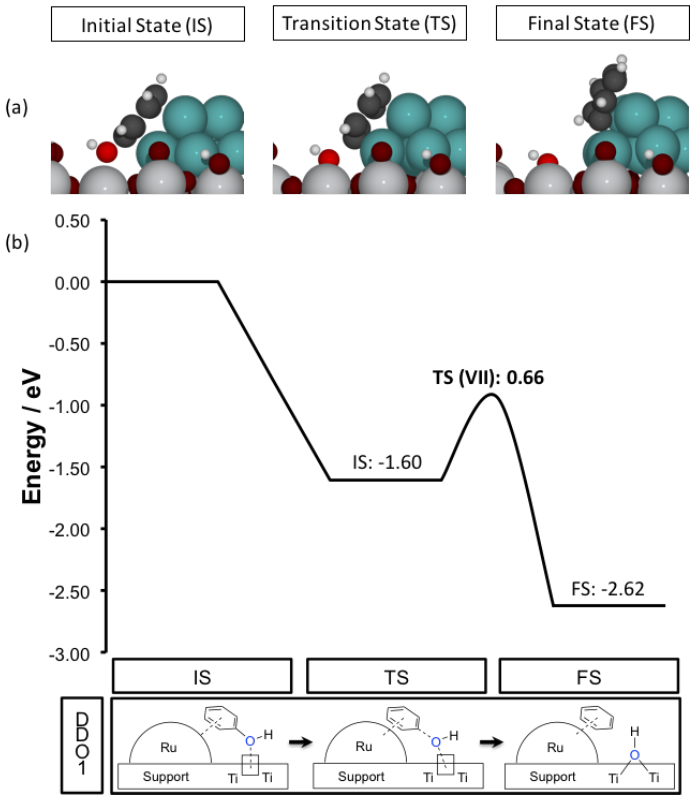

Figure 4-10. DDO1 pathway of phenol without water at the Ru_{10}/h-TiO_2(110) interface: (a) calculated geometries of the initial state, transition state, and final state; (b) potential energy surface. Color code: H-white; O-red; C-gray; Ru- teal; and Ti- light gray.

The resulting C_6H_5−Ru intermediate undergoes easy H atom transfer on the Ru cluster. The reaction C_6H_5−Ru + H−Ru → C_6H_6−Ru + Ru has an activation barrier of only E_a = 0.18 eV and is exothermic by ΔE = −0.67 eV (see Figure 4-12). On Ru(0001), the corresponding activation barrier increases to E_a = 0.55 eV[15,200]. Benzene is also strongly adsorbed on the Ru cluster, and its desorption requires ΔE = 1.40 eV from the Ru_{10}/h-TiO_2 interface and ΔE = 0.60 eV from the Ru(0001) surface. Thus, it may at first seem as if product desorption could be rate-limiting, but when Gibbs free energies (ΔG) are considered under realistic reaction conditions (e.g., conditions other than T = 0 K and ultrahigh vacuum), the adsorption and desorption steps are associated with a much smaller Gibbs free energy change. For example, Chiu *et al*. have calculated the ground state desorption energy for phenol and benzene from Ru(0001) as 1.35 and 1.41 eV and tabulated the Gibbs free energies at 523 K and 40 bar as 0.50 and 0.55 eV, respectively[15]. These values are in good agreement with the Gibbs free energies of adsorption of phenol and desorption of benzene shown in Table 4-2 obtained under the conditions of our experiments.

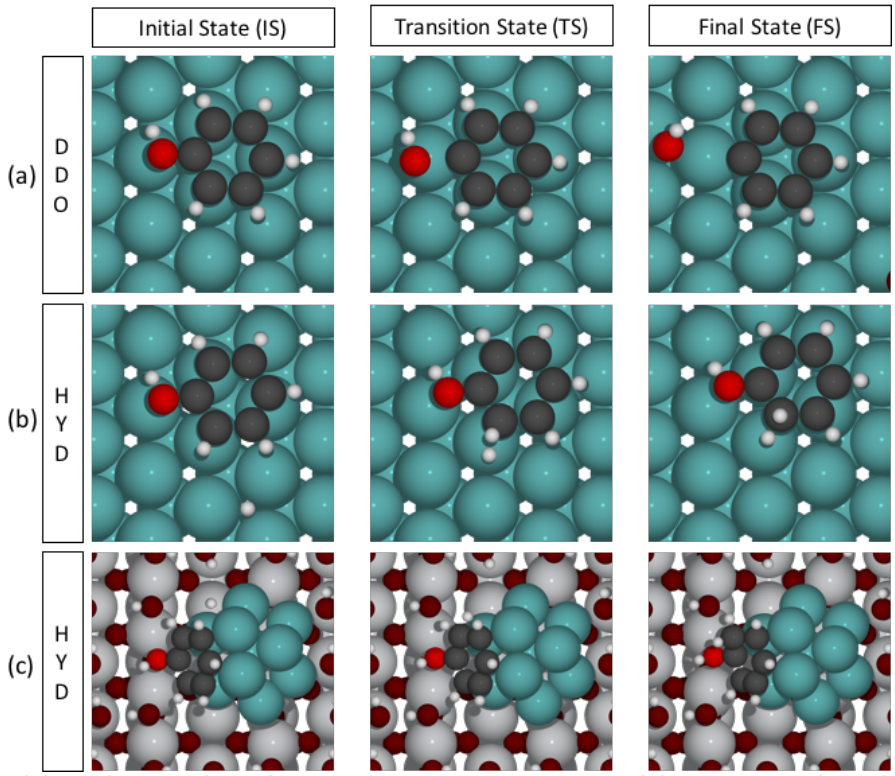

Figure 4-11. (a) DDO on Ru(0001), E_a = 1.23 eV, ΔE = 0.27 eV; (b) HYD on Ru(0001), E_a = 0.91 eV, ΔE = 0.29 eV; (c) HYD on the Ru_{10}/*h*-TiO_2(110) interface, E_a = 0.81 eV, ΔE = 0.31 eV, respectively. Color code: H-white; O-red; C-gray; Ru-teal; and Ti-light-gray.

Temperature and pressure effects on adsorbed intermediate and transition states are generally small[15]. As shown in Table 4-2, the Gibbs free energies change, and activation barriers for surface steps are similar to the ground state electronic energies. This allows us to neglect entropy contributions for our qualitative discussion of surface reaction mechanisms. Overall, our analysis suggests that the kinetics of the DDO pathway on Ru/TiO_2 and Ru(0001) are largely determined by the initial C−O scission step and that the Ru/TiO_2 interface site is more active than Ru(0001).

Phenol DDO on a $V_{O^{br}}$ vacancy site of the fully hydroxylated h-TiO_2(110) surface in the absence of a Ru cluster was also considered. Although vacancy formation by hydrogen activation and water elimination on h-TiO_2 is kinetically unfavorable[54], it has been suggested that a vacancy site may form via hydrogen spillover in the presence of transition metal clusters[146]. If such a vacancy site exists, then the calculated activation energy barrier of the direct C−O scission step is E_a = 1.02 eV [Figure 4-11(a)], which is lower than on Ru(0001), yet 0.36 eV larger than at the Ru/TiO_2 interface. Thus, the Ru/TiO_2 interface site remains the most favorable site for DDO.

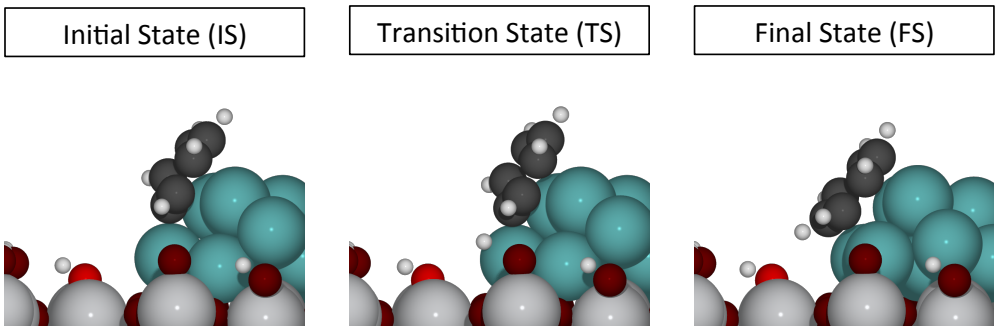

Figure 4-12. Side view of the benzene formation pathway at the Ru_{10}/*h*-TiO_2(110) interface. The calculated energy barrier and energy change are E_a = 0.18 eV and ΔE = -0.67 eV, respectively. Color code: H-white; O-red; C-gray; Ru-teal; and Ti-light-gray.

4.3.4.2. Site Regeneration: Vacancy Formation and Hydrogen Activation

It is fond that $V_{O^{br}}$ vacancy site at Ru/TIO_2 interface is facile as discussed in section 3.3.5. The sequence of the $V_{O^{br}}$ vacancy site is H_2 activated adsorption at the Ru/TIO_2 interface, followed by heterotic H_2 dissociation. The calculated energies for adsorption and dissociation are 0.11 and 0.47 eV. This dissociation mechanism generates a support Brønsted acid site and an H adatom, with significant negative charge density, on the bridge site of two Ru atoms (see Figure 3-12). After H_2O^{br} is formed at the interface, it may desorb as water and recreate the interfacial $V_{O^{br}}$ site with Lewis acid character. The H atom remaining on the Ru cluster is required for the hydrogenation of C_6H_5−Ru to benzene, as described earlier.

4.3.4.3. HYD Reactivity

Molecular hydrogen adsorbs dissociatively without barrier on a Ru site of Ru/TiO_2, and hydrogen delivery can be assumed to be quasi-equilibrated. Hence, to assess the HYD pathway, only the activation barrier for the first phenol hydrogenation step was calculated. On Ru(0001), hydrogen addition to the ortho position is more favorable than addition to either the meta and para positions on phenol. The calculated activation barrier for H addition at the ortho position is E_a = 0.91 eV on Ru(0001) [Figure 4-11(b)] and E_a = 0.81 eV on the supported Ru cluster [see Figure 4-11(c)]. These energetics are in line with the same reaction pathway studied on water-solvated Pt(111) and Ni(111), which fell between 0.84 and 1.00 eV[179].

4.3.4.4. DDO/HYD Selectivity and The Effect of Particle Size

Our calculations show that the Ru_{10}/h-TiO_2 interface with a bridging $V_{O^{br}}$ vacancy site, representative of small Ru particles on partially reduced TiO_2, has very good DDO activity (E_a = 0.66 eV) and moderate HYD activity (E_a = 0.81 eV). The Ru(0001) surface, representative of large Ru particles, has low HYD activity (E_a = 0.91 eV) and even lower DDO activity (E_a = 1.23 eV). Thus, small Ru particles with a large number of metal/support interface sites should have higher DDO/HYD selectivity and activity compared with large Ru particles with fewer interface sites.

This theoretical assessment of the DDO and HYD pathways and activity/selectivity trends for Ru_{10}/h-TiO_2 and Ru(0001) is consistent with the experimental data. The HRTEM images in Figure 4-4 showed fairly uniform 2−3 nm Ru particles on the H_2-activated catalysts. These small particles have relatively more Ru/TiO_2 interface area in comparison with bulk Ru, which is consistent with the most favorable DDO mechanism (DDO1). The aggregated Ru particles (~30 nm) obtained after calcination show reversed selectivity toward HYD, in agreement with our predictions for the Ru(0001) surface model. The proposed HYD and DDO pathways proceed independently, that is, ring hydrogenation is not necessary for C−O cleavage, which is consistent with observed product distributions[99]. Although this proposed mechanism and active site model is congruent with the vast majority of experimental observations, it cannot explicitly account for the promotional effect of water.

4.3.4.5. The Mechanistic Role of Water: Co-catalyzing C-O Cleavage

The additive exchange experiments clearly demonstrate a strong beneficial effect of water on DDO selectivity and are in agreement with the observations of others[156]. To investigate the mechanistic role of water during DDO, three scenarios were considered in which water might assist the C−O scission step.

In the first water-assisted scenario, DDO2, H_2O^{br} formed during the site regeneration process does not desorb from the $V_{O^{br}}$ site, that is, it remains in position 1 in Figure 4-3. This is likely to occur in water-rich environments that would shift the equilibrium to the surface-bound water state.

As explained earlier in section 4.3.4.2, this motif is created by heterolytic H_2 bond dissociation, which leads to the creation of a Brønsted acidic H_2O^{br} group. Brønsted acids can catalyze the elimination of OH groups from saturated reaction intermediates (*e.g.,* cyclohexanol) during HDO[180]. In the DDO2 pathway shown in Figure 4-13, H_2O^{br} was retained on the surface and acts as a proton donor to the hydroxyl group of phenol. Although phenol binding is weaker at this active site model (E_{BE} = −1.29 eV), the proton-assisted activation barrier is greatly reduced (E_a = 0.42 eV) compared with the non-assisted pathway, DDO1 (Figure 4-10). This mechanism is consistent with data from prior researchers[203,204] and supports the speculation that protonation of the lone pair orbital of oxygen could facilitate C−O bond cleavage. An important observation about this pathway is that the proton originating from H_2O^{br} is not incorporated into the aromatic ring. This is consistent with our isotopic labeling experiments using D_0-phenol, with or without D_2O, which exclude the possibility of direct water involvement during the reductive proton transfer, that is, the isotopic signature from water does not end up in benzene, except to the extent that it is exchanged into phenol through one of the two possible mechanisms discussed earlier. As discussed for DDO1, the benzene radical (C_6H_5−Ru) on the Ru particle reacts rapidly with the remaining H−Ru adatom.

The precise details of the C−O bond-breaking and C−H bond-forming steps are difficult to determine from our work and may depend on the hydrogen surface coverage. Lu and Heyden have considered the inverse sequence consisting of an initial hydride attack to the ispo carbon of phenol on Ru(0001) followed by C−O bond-breaking[200]. Their reported barriers along both alternative routes are within 0.1 eV, yet their microkinetic model predicts a ~2.5 times faster rate for C-H bond-forming followed by C-O bond-breaking, presumably caused by higher hydrogen coverage. In Figure 4-14, we present a similar sequence of HYD, followed by C-O scission for the water-assisted DDO2 mechanism at 1/9 ML hydrogen coverage; that is, one hydrogen atom is adsorbed on nine exposed Ru atoms. We find that hydrogen does not change the adsorption strength of phenol as long as it does not block the Ru sites near the $V_{O^{br}}$ vacancy. We also find that the adsorption complex after the ipso C-H bond formation step has a binding energy of -1.48 eV, which is even 0.19 eV stronger than phenol binding along the DDO2 pathway.

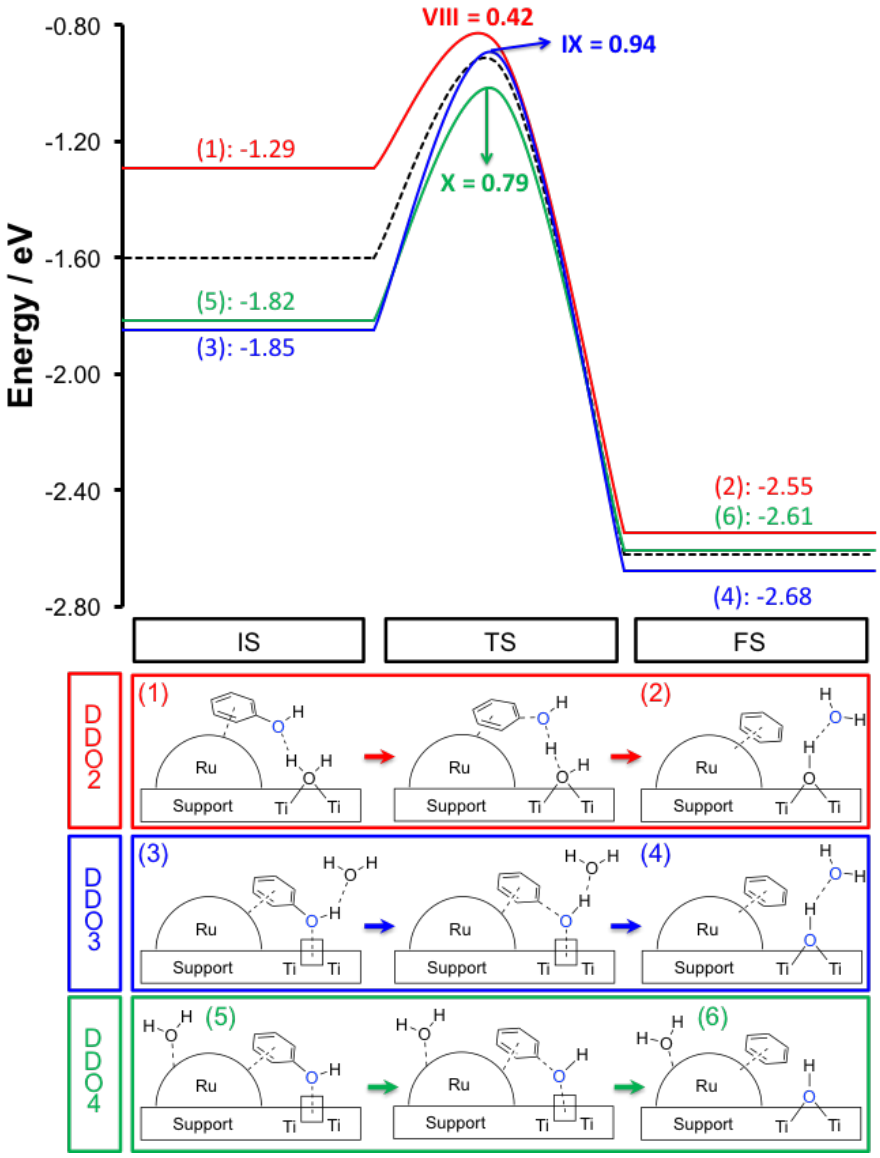

Figure 4-13. Potential energy surface of the H_2O-assisted DDO pathways. Initial and final state energies in electronvolts are given with respect to phenol and the respective (water-modified) Ru/TiO_2 model with oxygen vacancy (see Figure 4-3)..

Furthermore, the activation barrier for H_2O-assisted C-O scission remains identical at E_a = 0.42 eV. These findings do not implicate a strong hydrogen coverage dependence of the promotional effect of H_2O on the C-O dissociation barrier; yet a stronger effect at higher coverages cannot be excluded. Despite several attempts, a direct hydride attack pathway to generate a transition state, in which C-H bond formation and C-O bond breaking occur in concert, was not identified. In practice, both bond-forming/-breaking sequences are competitive, and the actual mechanism may depend on the extent of hydrogen coverage on Ru, which in turn depends on reaction conditions

[200]. A full microkinetic model, including all relevant steps, is required to address these details, but our main conclusion that the presence of H_2O lowers the C-O scission barrier appears to be independent of hydrogen coverage.

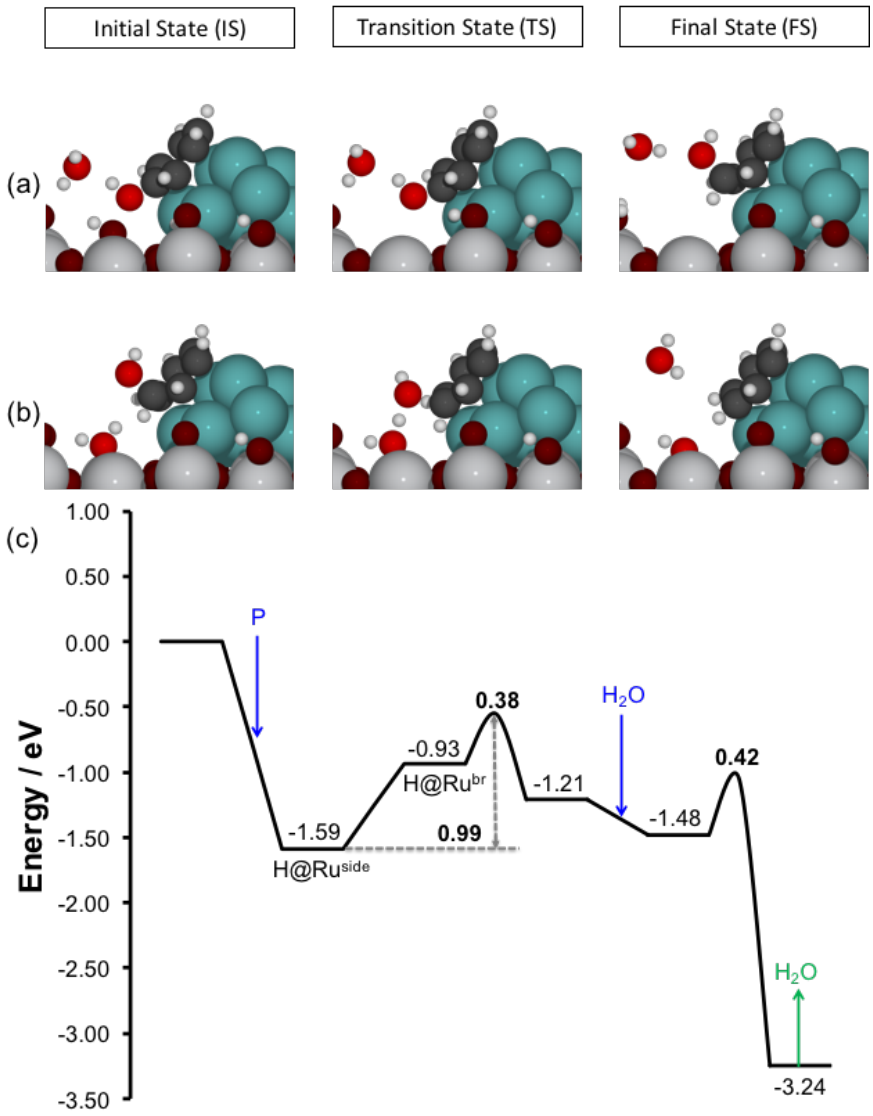

Figure 4-14. DDO2 pathway in reverse order: (a) HYD at the ipso position of phenol; (b) H_2O-assisted C-O scission; (c) alternative potential energy diagram for HYD followed by H_2O-assisted C-O scission. Color code: H-white; O-red; C-gray; Ru-teal; and Ti-light-gray.

4.3.4.6. Alternative Roles of Water: Phenol Stabilization

In addition to actively lowering the C-O scission barrier, water may passively stabilize reaction intermediates and transition states by pure solvation effects without transferring a proton[179]. Rather than attempting to fully model the aqueous reaction environment, two simplified systems

were considered: (1) physisorption of a single water molecule near the phenolic OH group (position 2 in Figure 4-3), and (2) water chemisorption on the Ru cluster (position 3 in Figure 4-3). These two pathways, DDO3 and DDO4, respectively, are illustrated in Figure 4-13. Activation energy barriers (E_a) in electronvolts are shown in bold face, and the roman numerals refer to the elementary steps in Table 4-2. The dotted black line serves as a reference to the DDO1 pathway in the absence of water, as shown in Figure 4-10. The final state energies vary slightly as a result of different binding orientations of benzene on the Ru particle and different binding environments, that is, the presence of H_2O. In the DDO3 pathway, a single physisorbed (≈ gas-phase) water molecule is located near the hydroxyl group of phenol, which adsorbs in the interfacial $V_{O^{br}}$ site (see the schematic of DDO3 in Figure 4-13). By acting as a hydrogen bond acceptor, the water molecule stabilizes the adsorbed phenol by -0.25 eV, resulting in a stronger phenol binding energy of E_{BE} = -1.85 eV, which is consistent with hydrogen bonding between water and the hydroxyl group of phenol. This stabilization, however, does not translate to a lower energy transition state barrier for C-O cleavage. The barrier for DDO3 (solid blue line in Figure 4-13) is E_a = 0.94 eV, therefore 0.28 eV higher than the barrier for DDO1 in the absence of water (E_a = 0.66 eV). Hence, this scenario, which approximates the effect of water on hydrogen bonding, is not alone capable of explaining the promotional effect of water on DDO activity.

The DDO3 pathway is, in fact, similar to the proton-assisted mechanism (DDO2), and the drastic activity difference between these two paths can qualitatively be understood in terms of reversed electronic interactions. In DDO2, hydrogen bond donation to the departing phenolic hydroxyl decreases the electron density in the C-O bond, facilitating its cleavage. In DDO3, however, the phenolic oxygen acts as a hydrogen bond donor, increasing the electron density in the C-O bond, making it more difficult to cleave.

Another potential role for water is modulating the density of states by binding to ruthenium near the active site (DDO4; see the schematic of DDO4 inFigure 4-13). Again, the presence of water stabilizes the initial binding of phenol by -0.22 eV relative to DDO1 (E_{BE} = -1.82 eV) while having relatively little effect on the activation energy (E_a = 0.78 eV for DDO4 vs E_a = 0.66 eV for DDO1). Overall, the potential energy diagram for DDO4 (solid green line in Figure 4-13) suggests

that water chemisorbed on the Ru cluster lowers the potential energy of the initial and transition state equally, without significantly changing the C−O bond breaking barrier. We note, however, that the effect of adsorbing water molecules on a Ru cluster will depend on the number of water molecules or size of the metal cluster, making it difficult to extrapolate the quantitative results of this pathway to other scenarios.

Calculations on the role of water in the DDO2 mechanism have led to a number of conclusions. Most importantly, a Brønsted acidic H_2O^{br} is able to act as a hydrogen bond donor to the ruthenium-bound phenol. This interaction decreases the activation barrier for C-O bond scission, which was thought to be the rate-determining step in our water-free model pathway DDO1. Notably, the formation of a vacancy site on TiO_2 is not required. This should lead to increased DDO activity in the presence of water, which mirrors the experimental increase in activity seen with water present (Table 4-1; compare entries 2 and 1). This observation is also in agreement with the conclusions of Behtash *et al*., who noted that polar solvents such as water and n-butanol not only increase the catalytic activity for HDO of propanoic acid but also stabilize the key intermediates[205]. When water acts as a hydrogen bond acceptor from bound phenol or is passively bound to the ruthenium cluster, decreased binding energies are observed, but the effect on the C−O cleavage energy barriers is minimal.

4.3.5. Kinetic Evaluation of Water-assisted DDO Pathways

A simple kinetic model was developed to discriminate between C−O scission mechanisms in the possible DDO pathways. This model should not be understood as a quantitative microkinetic model; it is rather a tool that allows us to predict whether the favorable binding and higher coverage of phenol in DDO3 and DDO4 can compensate for the larger C−O cleavage barrier when compared with DDO2. In this model, the adsorption of phenol is assumed to occur reversibly on the (water-modified) vacancy site at the interface of Ru/TiO_2 denoted as "*", followed by irreversible C-O scission[15]. Note that for weak phenol binding, the desorption of phenol may become faster than the C-O scission reaction, which will lower the consumption of phenol. Importantly, we do not assume that phenol adsorption is quasi-equilibrated, but that the fractional

phenol coverage is at steady-state (θ_{phenol} = constant). As indicated by our DFT analysis, the benzene radical formed after the C-O scission step is quickly hydrogenated to the final DDO product benzene. Because the hydrogenation barrier of E_a = 0.18 eV is so low, we make this last assumption irrespective of the presence or absence of water. Finally, it is sufficient for our purposes to consider only the intrinsic activity of each active site model, and we do not attempt to estimate the concentration of vacancy sites or water coverage. This reduces the kinetic analysis to the three elementary steps, of which only the first two is kinetically relevant. The simplified mechanism is then given by

$$\mathrm{phenol} + * \rightleftharpoons \mathrm{phenol}* \ \text{with}\ \mathrm{r}_1 = k_1^+ f_{\mathrm{phenol}}\theta^* - k_1^- \theta_{\mathrm{phenol}}, \tag{4-1}$$

$$\mathrm{phenol}* \rightarrow \mathrm{C_6H_5} - \mathrm{Ru} + \mathrm{HO^{br}}\ \text{with}\ \mathrm{r}_2 = k_2^+ \theta_{\mathrm{phenol}}, \tag{4-2}$$

$$\text{and}\ \mathrm{C_6H_5} - \mathrm{Ru} + \mathrm{HO^{br}} + \mathrm{H_2} \rightarrow \mathrm{benzene} + \mathrm{H_2O} + * \ (\mathrm{fast}). \tag{4-3}$$

Assuming steady state for the fractional coverage of phenol θ_{phenol} leads to $r_1 - r_2 = k_1^+ f_{\mathrm{phenol}}\theta^* - k_1^- \theta_{\mathrm{phenol}} - k_2^+ \theta_{\mathrm{phenol}} = 0$, which allows the estimation of θ_{phenol} as a function of the fugacity of phenol (f_{phenol}) as

$$\theta_{\mathrm{phenol}} = \frac{k_1^+ f_{\mathrm{phenol}}}{k_2^+ + k_1^- + k_1^+ f_{\mathrm{phenol}}}. \tag{4-4}$$

The site balance $\theta_{phenol} + \theta^* = 1$ was used to obtain Eq. (4-3). The reaction rate can then be approximated from Eqs. (4-1) and (4-3) as

$$\mathrm{r} = \mathrm{r}_2 = k_2^+ \frac{k_1^+ f_{\mathrm{phenol}}}{k_2^+ + k_1^- + k_1^+ f_{\mathrm{phenol}}}. \tag{4-5}$$

The fugacity of phenol at T = 573 K is approximated as its pure vapor pressure of 11.48 bar[206]. The DFT-derived energetics from Table 4-2 were used to calculate the expected reaction rates of the four different DDO pathways; the results are summarized in Table 4-3. Herein, the pre-exponential factors for the rate constants $k_{\mathrm{i}} = A_{\mathrm{i}}\, exp\left(\frac{-E_{\mathrm{a,i}}}{k_{\mathrm{b}}T}\right)$ were calculated as $A_{\mathrm{i}} = \frac{k_{\mathrm{b}}T}{h} \exp\left(\frac{\Delta S_{\mathrm{i}}^{\ddagger}}{k_{\mathrm{b}}}\right)$.

The simplified kinetic analysis clearly shows that the direct water-assisted pathway, DDO2, is the fastest reaction channel. Its rate is ~11 times faster than the reference rate for the DDO1

pathway without water, even though the phenol coverage decreases by one order of magnitude (Table 4-3). Without overemphasizing the quantitative agreement and assuming that the HYD rate is not altered by water, we note that the ca. 11-fold increase is similar to the experimentally obtained DDO/HYD ratio of 19 in the presence of water (Table 4-1, entry 1), whereas the DDO/HYD ratio is approximately unity in the absence of water (Table 4-1, entries 2 and 3). The less intuitive result of this analysis is that the stabilizing effect of water in pathways DDO3 and DDO4 is, in fact, detrimental because it slows the C-O scission rate, even though the phenol coverage is increased. The reason is that the phenol reactant in the initial state is stabilized with respect to the transition state, and although the surface coverage of phenol increases, the rate constant, k_2^+, becomes smaller.

Table 4-3. Estimated relative reaction rates at T = 573 K for the four different HDO pathways based on the DFT-calculated binding and activation energies tabulated in Table 4-2.

No	ΔG_{BE} / eV	E_a / eV	$\Delta S^{\#}$ / eVK^{-1}	k_1^+ / bar^{-1}s^{-1}	k_1^- / s^{-1}	k_2^+ / s^{-1}	θ_{phenol}	[a]r_{nrom}
DDO1	-0.56	0.66	-0.00012	8.86E+03	9.70E-02	4.28E+06	2.32E-02	1.0
DDO2	-0.37[b]	0.42	-0.00021	9.22E+04	5.06E+01	2.19E+08	4.80E-03	10.6
DDO3	-0.74[b]	0.94	-0.00007	2.06E+03	6.14E-04	2.79E+04	4.59E-01	0.1
DDO4	-0.78[b]	0.79	-0.00011	8.59E+03	1.22E-03	3.62E+05	2.14E-01	0.8

[a]Rate is normalized to DDO1. [b]Only the entropy change for phenol was considered in the calculation of ΔG_{BE}.

4.3.6. Active Site Formation for DDO Catalysis: The Specific Role of TiO_2

Titania has generated interest as a HDO support primarily as an alternative to alumina because alumina has known instability problems under typical HDO conditions of high temperatures and humidity[172,207]. In addition, titania is also a reducible support, which has been linked to ease of oxygen vacancy formation[156], and it has been noted that the use of reducible supports enhances the catalytic hydrogenation of carbonyls by group VIII metals[174]. The calculations presented in this work support this beneficial role of an oxygen vacancy in the energetics of C-O bond scission pathways in the absence of water (DDO1) or with passive water stabilization of phenol (DDO3 and DDO4). The HDO experiments of McEwen and Wang also support the hypothesis that DDO selectivity is enhanced by the combination of a reducible

support (Fe_2O_3) and the transition metal Pd[176]. A comparison of Pd/SiO_2, Pd/Al_2O_3, and Pd/ZrO_2 showed that only the reducible ZrO_2 support leads to selective DDO, because it has oxophilic undercoordinated Zr^{4+} sites with Lewis acid character[177], which is similar to the role our calculations indicate TiO_2 is playing. As an intrinsic biofuel component and a reaction product, water is a key player in phenolic HDO reactions, and as such, its presence on the catalyst surface cannot be avoided. Most previous studies have neglected to account for the presence of water, but our results confirm that water greatly enhances HDO activity and selectivity for the DDO pathway. On the basis of isotopic labeling studies and DFT simulations, we conclude that selective DDO of phenol occurs on a bifunctional reaction site at the interface between Ru nanoparticles and a Brønsted acidic surface hydroxyl/water on the TiO_2 support. In the proposed proton-assisted DDO mechanism (DDO2, Figure 4-13), phenol binds at this interfacial site. It is here that the acid site catalyzes C−O cleavage while the Ru metal component catalyzes the hydride attack. In this case, the active site motif is regenerated through heterolytic H-H bond cleavage, yielding a ruthenium hydride and Brønsted acidic water on the surface of hydroxylated TiO_2 (Figure 4-13). A number of homogeneous Ru-based hydrogenation catalysts, for example, Shvo's catalyst, show a similar ability to simultaneously transfer acidic and hydridic hydrogens in the reduction of carbonyl substrates and ultimately regenerate the active site through H_2 bond heterolysis[208]. The proposed proton-assisted DDO mechanism (DDO2) does not require formation of an oxygen vacancy site on the reducible TiO_2 support. Our newly obtained insights into the mechanism and active site location for DDO on Ru/TiO_2 allows us to revise the prevailing notion that the support reducibility is the key property for selective and hydrogen-efficient HDO catalysts. None of the intermediate states shown in the PES in Figure 4-15 or the most favorable DDO2 pathway involves an oxygen vacancy site. Instead of its reducibility, we propose that TiO_2 is unique among reducible metal oxide supports because of its amphoteric character, that is, it can act as both an acid and a base. In the full PES for the water-promoted DDO2 mechanism, shown in Figure 4-15, the two largest, and almost identical, activation barriers are obtained for proton-assisted dehydroxylation of phenol (E_a = 0.42 eV) and the regeneration of the acid site by heterolytic H_2 dissociation across the Ru/TiO_2 interface (E_a = 0.47 eV). These proton transfers to

and from the support are ideally balanced such that neither the acid- catalyzed dehydroxylation nor the active site regeneration step are highly activated. If TiO_2 had a higher proton affinity (lower acidity), the dehydroxylation step would require a higher activation energy; however, on the other hand, if TiO_2 was more acidic (lower proton affinity), the surface protonation during heterolytic H_2 dissociation would be more difficult.

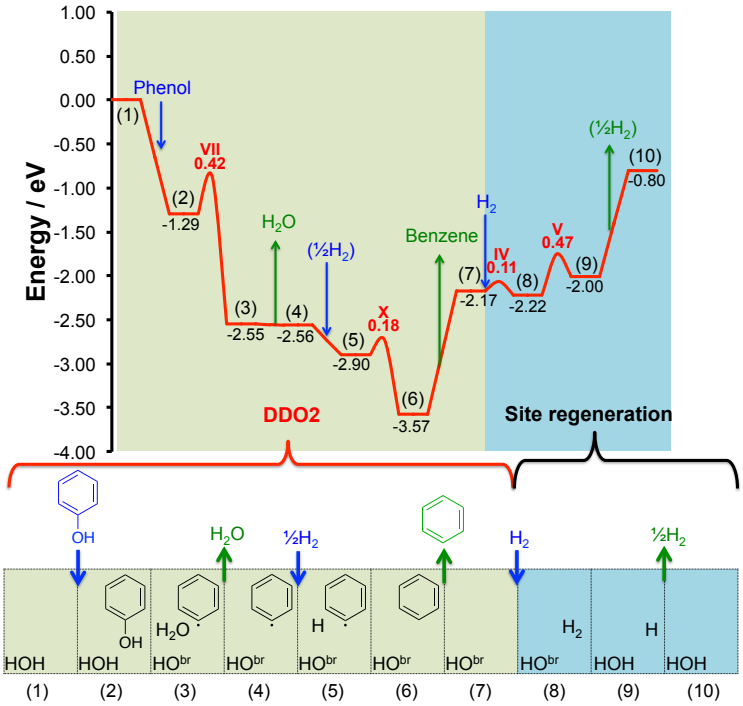

Figure 4-15. Full PES for the DDO2 pathway. The roman numerals refer to the elementary steps in Table 4-2. Reactants adsorbing to the surface are shown in blue; products desorbing from the surface are shown in green.

This explanation is congruent with the fact that ZrO_2, another amphoteric oxide with tunable Brønsted and Lewis acidity/basicity[209], has also been identified as a suitable support for transition metal catalysts for selective DDO[129,177]. The Lewis acid Zr^{4+} cations may be transformed to Brønsted acid sites in the presence of water and form an active site motif similar to what we propose for Ru/TiO_2. Similarly, Pd/Fe_2O_3 has shown high DDO selectivity, which was attributed to the reducibility of Fe_2O_3[210], but the authors did not investigate the role of water or support hydroxyl species. However, a combined STM/DFT study has shown that protons on iron oxide surfaces are highly mobile in the presence of water[211] and could assist the dehydration reaction,

as proposed here for TiO_2. Finally, the availability of mobile protons has also been implicated as a key mechanistic component during water-assisted CO oxidation on Au/TiO_2[183].

4.4. Conclusions

This work reports that the DDO selectivity of Ru/TiO_2 catalyst with small Ru particles is enhanced by the presence of water. At 573 K and 550 psig H_2, these catalysts show unprecedented activity (30% conversion) and selectivity for direct deoxygenation of phenol (DDO/HYD ratio of 19). In the absence of water or the presence of 10 % octane, there is a 10 ~ 20 - fold reduction in the ratio of DDO/HYD products and a 30 - 60 % reduction in the overall conversion of phenol to products.

We propose a novel DDO mechanism for phenol, which is consistent with the bulk of the experimental and theoretical literature and explains the co-catalytic effect of water. Isotopic labeling experiments indicate that a single reductive hydrogen atom is exchanged along the DDO path. This provides strong evidence against mechanisms involving multiple (de-)hydrogenation/dehydration steps (Figure 2, Mechanism B), because the overall number of reductive proton transfers would be expected to be greater than one. On the basis of product distributions, Resasco and co-workers proposed a reaction pathway initiated by a tautomerization step followed by hydrogenation and dehydration (Figure 2, Mechanism C). Isotopic labeling control experiments and low calculated activation barriers for water-assisted tautomerization in this work confirm the presence of phenol tautomerization. The hydrogenation/dehydration sequence along the tautomerization pathway, however, would increase the number of reductive H atoms transferred, which is not shown in our isotopic labeling data.

The novel mechanism we propose allows us to attribute the exceptional activity and selectivity of Ru/TiO_2 to the ability of TiO_2 to act as a conjugated acid/base pair rather than its reducibility. Water molecules adsorbed on hydroxylated or partially reduced TiO_2 can easily accept and donate protons across the Ru/TiO_2 interface and lower the C-O scission barrier by donating a proton during the abstraction of the phenolic OH group. The OH group is replaced in a hydride attack with a single reductive proton. Small Ru particles that create a maximal number of

interface sites are necessary for optimal DDO performance. Because of the strong C_{aryl}-O bond, the direct scission pathway has received very little attention in the past. The DFT results presented here, however, identified a bifunctional site with metal and Brønsted acid functionality at the Ru/TiO_2 interface that provides a lower C-O bond scission barrier (E_a = 0.42 eV) than the most favorable hydrogenation step (E_a = 0.81 eV). This proposed mechanism fully explains the beneficial effect of water (maintaining the Brønsted acid site) and small Ru particles (maximizing the ratio of interface/bulk Ru active sites) on DDO selectivity and the observation that a single reductive hydrogen is transferred to the product. While we have taken all necessary care in the pathway and active site determination, we have concentrated our theoretical efforts on pathways that are consistent with our catalytic and isotopic labeling experiments, and we acknowledge the possibility that other more complex reaction pathways or multi-site reactions may exist.

Ring hydrogenation (HYD) occurs preferentially on Ru particles as indicated by DFT simulations on the idealized Ru(0001). The lowest barrier to hydrogenation (E_a = 0.91 eV) occurs in the absence of the Ru/TiO_2 interface, and the direct C-O scission is more difficult (E_a = 1.23 eV). This is in line with previous results obtained using calcined Ru/TiO_2 catalysts, which have aggregated Ru particle sizes of about 30 nm. Higher amounts of cyclohexanone and cyclohexanol were also seen in this work when octane was added to the reaction mixture. This is consistent with the hypothesis that octane may occlude and reduce the number of dehydroxylation sites at the Ru/TiO_2 interface.

In conclusion, our detailed understanding of the DDO mechanism and novel interpretation of the role of the support material will aid future efforts to design more efficient, less expensive catalysts or catalytic processes for bio-oil upgrading by hydrodeoxygenation. Our results suggest that by tuning the support Brønsted acidity an optimal balance for proton acceptance and donation can be found, which is critical for selective C-O cleavage. Furthermore, the process conditions can be optimized to yield a desired DDO/HYD ratio by adjusting the amount of water present or modifying the Ru particle size.

Chapter 5. Mechanism and Active sites for Conversion of m-Cresol over Ru/TiO_2: An Experimental and DFT Study

5.1. Introduction

Our experimental corroborator, Crossleyl's group has recently studied the conversion of guaiacol over Ru on supports such as C, SiO_2, Al_2O_3 and TiO_2 and showed that the ability of Ru to activate hydrogen and create highly active sites on TiO_2 produced a more stable and active catalyst when compared to the other supports[212]. Results obtained from further studies where the effect of TiO_2 support phase (anatase vs. rutile) and pretreatment conditions on guaiacol conversion over Ru/TiO_2 catalysts led to the conclusion that the formation of monooxygenates such as phenol, cresols and xylenols occur on TiO_2 defect sites rather than at the Ru/TiO_2 interface. We also demonstrated that the rate of conversion of species containing two oxygen atoms, such as guaiacol and catechol, to monooxygenates is a much faster reaction than the subsequent conversion of monooxygenated phenolics such as cresol to aromatic hydrocarbons.

The cleavage of a phenolic C-O bond is perhaps the most difficult chemical transformation necessary for the removal of oxygen from bio-oil monomers en route to fuels and chemicals production. A number of metals supported on reducible, oxophilic, or amphoteric supports have been found promising for further conversion of monooxygenates to completely deoxygenated aromatic hydrocarbons, but the role of the metal/oxide perimeter sites is still not understood. For example, Ru/TiO_2 shows and increased rate and selectivity for aromatics production from phenolics when compared with Ru supported on other supports[101]. On the basis of density functional theory (DFT) simulations it was proposed that this observation can be explained by a water-assisted direct C-O cleavage mechanism across the Ru/TiO_2 interface and the amphoteric character of TiO_2, i.e., its ability to accept and donate protons[31]. Similar enhancements in the rate of aromatics formation have been observed in the literature for other metal/oxide systems such as Pt/TiO_2 and Pd/ZrO_2 and the improvement was attributed to support reducibility or oxophilicity[32,164,213–216]. In addition to the choice of metal/oxide support, the nature of the reactant

influences the location of the active site. In the case of the di-oxygenates catechol/guaiacol and furfural it was suggested that the conversion occurs on defect sites on the support, whereas the metal/support perimeter as has been suggested as the active site for HDO reactions of some mono-oxygenates, such as acetic acid[31,215].

While there appears to be a significant enhancement in deoxygenation rate and selectivity when metals are supported on reducible, oxophilic, or amphoteric supports such as TiO_2, two key questions remain unknown. What is the dominant site responsible for increased HDO of phenolics, and which support property, e.g. reducibility, oxophilicity or amphoteric character, is required to cause the rate enhancement? Because such great promise has been observed for this reaction upon the combination of metals with certain oxides it is essential to first understand the site requirements for this reaction to enable subsequent investigations of the key support characteristics.

In this paper, we focus on the conversion of an important monooxygenated phenolic compound, *m*-cresol over Ru/TiO_2 catalysts to quantify the role of perimeter vs. defect sites through a combined experimental/theoretical approach. Experimentally, the role of each type of site is determined by measuring m-cresol transformation rates in a vapor phase flow reactor over a series of Ru/TiO_2 catalysts spanning a wide range of metal particle sizes and perimeters. In addition to particle size and perimeter, the metal deposition methods and TiO_2 support phase are varied to determine how broadly applicable the conclusions derived from this study are. While results show a linear correlation between rates of *m*-cresol conversion to toluene and Ru perimeter, no such correlation was found between the reaction rates and Ru metal surface area. In addition, the rate of toluene formation over several Ru catalysts supported on inert SiO_2 demonstrate that C-O cleavage over Ru metal is structure insensitive. This suggests that the perimeter sites around the metal particle and not the Ru metal surface are the most important catalytic sites for m-cresol conversion to toluene over Ru/TiO_2. The fact that data obtained over both anatase and rutile TiO_2 supports fall on the same trend line also suggest that the active sites are not due to defects created on the TiO_2 support away from the Ru/TiO_2 interface. DFT calculations support the experimental observations and the role of the metal/oxide interface. The

lowest energy barrier for C-O scission in *m*-cresol was found at the Ru/TiO_2 interface model, while Ru metal favors hydrogenation and the formation of TiO_2 support vacancies is limited by hydrogen delivery. This result is interestingly in contrast to what has been proposed for catechol/guaiacol containing two oxygen atoms on the aromatic ring as well as the conversion of furfural[215]. This combined experimental/theoretical approach demonstrates the critical role of the metal/oxide perimeter for the cleavage of phenolic C-O bonds in cresol, and ultimately advance the field towards the development of HDO catalysts with tailored properties.

5.2. Experimental

5.2.1. Catalyst Preparation

Ru/TiO_2 (TiO_2: Aeroxide P25, pore volume: 0.25 ml g^{-1}, Ru loading: 1.1 ~ 4.4 wt %), Ru/TiO_2(TiO_2: Anatase, Ru loading: 0.4, 0.8 and 3.5 wt %), and Ru/SiO_2 (SiO_2: Hisil-210, pore volume 0.96 ml g^{-1}, Ru loading: 1.0, 5.3 and 9.4 wt %) were prepared by incipient wetness impregnation method in aqueous solution in which hexaammineruthenium (III) chloride (Sigma Aldrich, 98%), ruthenium (III) chloride hydrate (Sigma Aldrich, 99.98 % trace metals basis) were used for Ru/TiO_2 (P25) and Ru/SiO_2, and Ru/TiO_2 (Anatase), respectively. Anatase TiO_2 is purchased from Alfa Aesar (0.3175 cm pellet) and was crushed to a size bellow 500 μm dried overnight in an oven for 12 h before use. After impregnation, Ru/TiO_2 (P25) and Ru/SiO_2 were dried in air for 48 h at room temperature, followed by another drying in an oven at 120 °C for 12 h, and finally reduced in H_2 flow at 400 °C for 2 h. Ru/TiO_2 (anatase) was dried at 120 °C for 12 h, and then calcined in flowing air at 400 °C for 4 h. The Ru/TiO_2 (anatase) were pelletized and then sieved in order to obtain particle sizes in the 250 ~ 420 μm range (Mesh no. 40-60). Two samples, Ru/TiO_2 (P25, 0.5 and 0.6 wt % of Ru), were synthesized by the strong electrostatic adsorption (SEA) method in an aqueous solution of hexaammineruthenium (III) chloride (Sigma Aldrich, 98%) with a precursor concentration of 200 ppm in which acidity is controlled stepwise by additions of sodium hydroxide up to 11.7 pH. This aqueous solution was aged for 1h, and 12.5 g of TiO_2 (P25) was added into this solution. This mixed solution was stirred by shaking for 1 h and

was filtered out the precipitated solid, which was thoroughly washed, dried over night in flowing air, and finally reduced under mild conditions of 100 °C.

5.2.2. Catalyst Characterization

ICP (Galbraith Laboratories) was used to determine the Ru contents in the prepared catalysts. Particle size distribution was determined from Transmission Electron Microscopy (TEM, JEOL JEM-2100 model). Before the TEM measurement, all catalyst samples were prereduced in hydrogen flow at 400 °C for 1 h, dispersed in isopropanol, and then sonicated to produce a uniform suspension. Spent catalysts were dispersed in isopropanol without further reduction treatment. A few drops of the solution were dispersed on carbon-coated copper TEM grids. At least 200 particles were counted to obtain the particle size distribution.

5.2.3. Catalytic Activity Tests

Reaction measurements were determined in a ¼ in OD quartz reactor at atmospheric pressure in the vapor phase. In a typical experiment, the catalyst particles were diluted in inert glass beads (Sigma Aldrich, G1277) with a particle size range of 212 - 300 μm, which is similar to the particle size range of the catalyst pellets described above. The catalyst bed was placed between two layers of quartz wool in the reactor tube, while filling the empty space above the catalyst bed with 1 mm diameter glass beads to ensure that the m-cresol feed is vaporized uniformly starting from the heated inlet zone. Vapors were analyzed online via an Agilent 5890 FID GC. Products were identified and quantified with standards, with identification confirmed via GCMS in a Shimadzu QP-2010. The transfer line from the reactor outlet to the GC six port valve was heated to 300 °C to prevent condensation of compounds in the lines during reaction runs. The catalysts were reduced in situ with 100 ml min^{-1} hydrogen flow at 400 °C for 1 h before introducing the m-cresol feed. All m-cresol conversion reactions were carried out at 400 °C. The carbon balance for each of the runs reported was > 95%, with conversions reported at a time on stream of 10 minutes.

Ethylene hydrogenation reaction rates to verify particle sizes obtained via TEM were determined using the flow reactor system described above at 40 °C and atmospheric pressure.

The catalysts were reduced in hydrogen at 400 °C and cooled down to 40 °C prior to the introduction of the ethylene and hydrogen feed gases at a molar ratio of 1:50. The online gas chromatograph system (GC-GID) described above fitted with a PLOT column (Varian CP-Al_2O_3, 50 m, 0.32 μm) was utilized for analysis.

5.2.4. Computational Methods

All density functional theory (DFT) calculations for adsorption energies, activation energy barriers and vibrational frequencies used the projector augmented wave (PAW) method formalism [64,104] as implemented in the Vienna Ab-initio Simulation Package (VASP) in combination with the Atomic Simulation Environment (ASE)[63,65,103,104]. The revised Perdew – Burke – Ernzerhoff generalized gradient approximation (RPBE - GGA) was used as exchange-correlation functional[40,105], and the cut-off energy was set to 400 eV. Spin polarization was used for Ru/TiO_2(110) and TiO_2(110), but not for Ru(0001). A Fermi temperature (k_BT) of 0.1 eV and 0.01 eV was chosen for slab calculations and gas phase molecules (H_2, m-cresol, toluene), respectively, and the resulting energies were extrapolated to k_BT = 0 eV[23]. The conjugated gradient algorithm with a force convergence criterion of 0.05 eV/Å was used for ionic relaxations of equilibrium geometries.

It is well known that DFT fails to describe the correct electronic structure for strongly correlated systems due to errors associated with Coulomb and exchange interactions[113]. TiO_2, specifically when oxygen vacancy defects are present, has highly localized Ti 3d states; hence, we applied a Hubbard-U correction (DFT+U) with U_{eff} = 2.0 eV consistent with our earlier work[111,114].

Ruthenium (Ru) and titania (TiO_2) were modeled in their thermodynamically most stable hcp and rutile bulk structures and surfaces were cleaved in the Ru(0001) and TiO_2(110) direction. The optimized bulk lattice constants are a = 2.689 Å, c/a = 1.637 for Ru, and a = 4.712 Å, c/a = 0.640, u = 0.306 for TiO_2, which are all in good agreement with experimental data[107–110]. The metallic Ru(0001) surface was periodically repeated in a (4×4) unit cell, and we used a (3×2) unit cell for the fully hydroxylated TiO_2(110) surface [h-TiO_2(110)]. For both surfaces, the top two layers of the

four layer slabs were fully relaxed, while the bottom two layers were fixed at their bulk truncated positions. To avoid interaction between successive slabs due to periodic boundary conditions, the unit cell included 16 Å of vacuum along the normal direction of the surface. A dipole correction was applied to compensate the effect of adsorbing molecules only on one side of each surface [70]. The supported Ru/TiO_2 interface system was modeled as a 10 atom Ru cluster placed on three adjacent oxygen vacancy sites of a (5×4) TiO_2(110) unit cell[88,115]. This unit cell is large enough to separate periodically repeated images of the Ru cluster with at least 9 Å in the lateral direction. The remaining TiO_2 surface sites not occupied by Ru were terminated with hydroxyl species. The 10-atom cluster was chosen because it is computationally tractable, forms a defined hcp structure, is large enough to provide a hemispherical shape that has been observed in experiments[116], and closely resembles previously published models of metal/oxide interfaces. We refer to this model structure as Ru_{10}/h-TiO_2(110). The Brillouin zone was sampled using *k* point meshes of (4×4×1) for Ru(0001), (6×8×1) for TiO_2(110), and (2×2×1) for Ru/TiO_2(110) using the Monkhorst-Pack scheme[67]. Convergence with respect to *k* point sampling was confirmed.

Binding energies (E_{BE}) are calculated with respect to the clean surface and gas phase molecules (H_2, H_2O, and m-cresol) as $\mathrm{E_{BE}} = \mathrm{E_{slab+adsorbate}} - (\mathrm{E_{slab}} + \mathrm{E_{molecule}})$, where $E_{slab+adsorbate}$ is total energy of the slab with adsorbates, E_{slab} is energy of the clean surface, and $E_{molecule}$ is the energy of reference gas phase molecules. The climbing image nudged elastic band (cNEB) method[72] was used to determine transition states (TS) of elementary reaction steps, and the reaction path was sampled with five or six intermediate images, which were fully optimized until the residual force was below 0.1 eV $Å^{-1}$. We confirmed that this convergence criterion is sufficient to obtain TS within 0.1 eV accuracy, a generally accepted error bar in DFT calculations. Vibrational analysis was performed to confirm the existence of a single imaginary mode, corresponding to the reaction coordinate along the reaction path.

5.3. Results and Discussion

5.3.1. Reaction Mechanism

The mechanisms of m-cresol conversion have been reported in the literature to follow a hydrogenation (HYD)/dehydration(DHR) pathway[100,218,219] or a direct-deoxygenation (DDO) pathway[176,220]. In the HYD/DHR pathway, a catalyst with both metal and acid functionality is required. HYD of the aromatic ring of phenolic compounds to form alcohols can occur over the metal while the acid provides dehydration activity to remove the oxygen[20,221]. The direct deoxygenation pathway has been proposed over sulfides[193], carbides[222], and some transition metals in the absence of strong acidity through a tautomerization step and hydrogenation step[214].

The role of an oxophilic support has been proposed to accelerate deoxygenation of cresols and phenol over supported Pt and Pd catalysts[177,214]. It was speculated that the oxophilic support ZrO_2 can attract the surface tautomer and enhance its decomposition to eliminate oxygen. Asides from Pt and Pd based catalysts, the role of these oxophilic sites for *m*-cresol conversion to toluene has been demonstrated using other metal-based catalytic systems. In the first case, the reaction of *m*-cresol over Ni, Fe and Ni-Fe catalysts was studied[99]. While alcohols were seen as major products in supported Ni catalysts, the introduction of Fe either as a Ni-Fe alloy or as pure Fe resulted in a significant increase in selectivity to toluene[99].

In a recent investigation of the mechanism for the direct-deoxygenation (DDO) of phenol to benzene over Ru/TiO_2, we proposed a direct proton-assisted C_{aryl}-OH cleavage mechanism across the Ru/TiO_2 interface[31]. This mechanism was deduced from DFT calculations for key reaction steps on Ru(0001), TiO_2(110), and a 10-atom Ru cluster on TiO_2, Ru_{10}/h-TiO_2(110). Large Ru particles are well approximated as the Ru(0001) surface, while small and highly dispersed Ru metal clusters are best approximated with the Ru_{10}/h-TiO_2(110) model. We note that the Ru_{10} cluster has a diameter of ca. 0.7 nm, which is within the range of experimentally tested catalysts (see Table 5-3). The mechanism is congruent with experimentally observed product distributions[204] and the isotopic composition of the reaction product benzene[31]. An important feature of this novel mechanism are proton transfer steps across the Ru/TiO_2 interface

(see section 3.3.5): (i) upon heterolytic H_2 cleavage across the interface, the hydroxylated TiO_2 support is protonated, while the second H atom forms a Ru-hydride (Ru-H); (ii) during C_{aryl}-OH bond scission the support proton attacks the OH group of the Ru-bound phenol and aids its elimination as H_2O. Finally, the Ru-H forms a C-H bond with the benzene radical to form the final product benzene.

Table 5-1. Summary of key elementary steps on Ru(0001), h-TiO_2(110), and Ru_{10}/TiO_2(110).[a]

Surface	No.	Elementary Steps	[b]ΔE	[c]E_a	[d]ΔG	[e]ΔG_a
Ru	I	$C_6H_4(CH_3)OH_{(g)} + * \rightarrow C_6H_4(CH_3)OH*$	-0.28	-	-	-
	II	$C_6H_4(CH_3)OH* + * \rightarrow C_6H_4(CH_3)* + HO*$	0.00	1.42	-	-
	III	$C_6H_4(CH_3)OH* + H* \rightarrow C_6H_5(CH_3)OH*$	0.38	1.11	-	-
h-TiO_2	IV	$C_6H_4(CH_3)OH_{(g)} + V_{O^{br}} \rightarrow C_6H_4(CH_3)OH*$	-0.38	-	-	-
	V	$C_6H_4(CH_3)OH* \rightarrow C_6H_4(CH_3)* + HO^{br}$	0.13	0.99	-	-
Ru/TiO_2	VI	$H_{2(g)} + Ru \rightarrow H_2\text{-}Ru$	-0.05	0.11	0.93	1.05
	VII	$H_2\text{-}Ru + HO^{br} \rightarrow H\text{-}Ru + H_2O^{br}$	0.22	0.47	0.33	0.53
	VIII	$C_6H_4(CH_3)OH_{(g)} + V_{O^{br}} \rightarrow C_6H_4(CH_3)OH*$	-1.47	-	-0.20	-
	IX	$C_6H_4(CH_3)OH* + Ru \rightarrow C_6H_4(CH_3)\text{-}Ru + HO^{br}$	-0.78	0.71	0.70	-1.18
	X	$C_6H_4(CH_3)OH* + H_2O^{br} + Ru \rightarrow C_6H_4(CH_3)\text{-}Ru + HO^{br} + H_2O_{(g)}$	-0.79	0.30	-	-
	XI	$C_6H_4(CH_3) * + H\text{-}Ru \rightarrow C_6H_5(CH_3) * + Ru$	-0.75	0.10	-0.47	0.34

[a]$V_{O^{br}}$ denotes a bridging oxygen vacancy site on *h*-TiO_2. X-Ru refers to species X bound to a Ru site, while '*' is used to indicate interfacial binding requiring a Ru and $V_{O^{br}}$ site. [b, c]ΔE and E_a are total energy change and activation energy barrier without zero-point-energy (E_{ZPE}) or entropy correction in eV. [d, e]Gibbs free energies are calculated as $\Delta G = \Delta E + E_{ZPE} - T\Delta S$ at T = 673 K, pressure 1 atm.

The monooxygenates phenol, used in previous work, and m-cresol, used here, are chemically similar and we expect their DDO mechanisms to be identical. Nevertheless, we have repeated a series of DFT calculations for DDO of m-cresol on metallic Ru(0001), fully hydroxylated *h*-TiO_2(110), and the Ru_{10}/TiO_2(110) interface model to confirm this expectation. These results are summarized in Table 5-1. The initial heterolytic H_2 activation across the Ru/TiO_2 interface (step VII in Table 5-1) was described in detail in our earlier work[31] and section 3.3.5. This step remains unaltered when m-cresol is deoxygenated instead of phenol. The adsorption of m-cresol at the protonated interface site results in a binding energy of ΔE_{BE} = -1.85 eV, which is stronger than what we reported for phenol (ΔE_{BE} = -1.25 eV). Following step is the proton-assisted C_{aryl}-OH dehydroxylation (step X Table 5-1) forming in gas-phase H_2O and $C_6H_4(CH_3)$*. As in the case of

phenol, this proton-assisted C-O cleavage step in m-cresol has a relatively low barrier of 0.30 eV rather than direct C-O scission step (step IX Table 5-1).

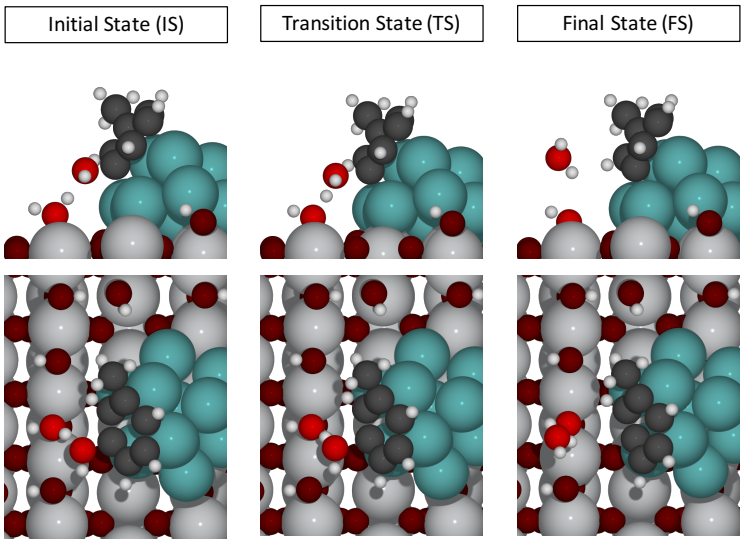

Figure 5-1. The most likely DDO pathway for m-cresol: $C_6H_4(CH_3)OH^* + H_2O^{br} \rightarrow C_6H_4(CH_3)^* + HO^{br} + H_2O_{(g)}$, E_a = 0.30 eV and ΔE = -0.79 eV. Color code: hydrogen - white; oxygen - dark red / bright red; titanium - gray; carbon - black; ruthenium - teal.

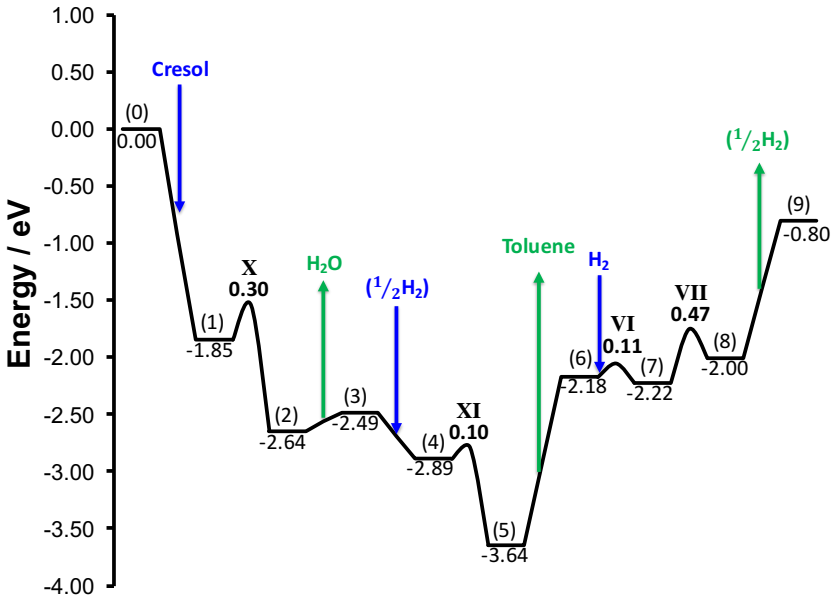

Figure 5-2. The proposed proton-assisted DDO mechanism of cresol at the Ru/TiO_2 interface. The numbers represent binding energy and energy barrier with respect to gas-phase m-cresol, H_2, H_2O, and Ru/TiO_2 with H_2O^{br} acid site, respectively.

Our proposed proton-assisted DDO pathway of m-cresol is summarized as a potential energy surface (PES) in Figure 5-2. The roman numerals indicate elementary steps in Table 5-1.

Reactants (m-cresol, H_2) adsorbing to the surface are shown in blue and products (toluene, H_2O) desorbing from the surface are shown in green. It starts with m-cresol adsorption on the Ru/TiO_2 interface where H_2O^{br} acid site exist [(1) in Figure 5-2]. Its calculated binding energy is -1.84 eV. The following steps is direct C-O scission in m-cresol by proton transfer mechanism [X in Figure 5-2]. The calculated barrier for this proton-mediated C-O scission is 0.30 eV. This step forms a gas-phase water and the $C_6H_4(CH_3)$* intermediate [(3) in Figure 5-2]. The $C_6H_4(CH_3)$* intermediate bound to the Ru cluster reacts quickly with H atom (E_a = 0.1 eV, ΔE = -0.75 eV), converted into surface toluene [(5) in Figure 5-2]. The desorption of toluene from the Ru cluster is significantly endothermic with ΔE = 1.46 eV [(6) in Figure 5-2]. This mechanism does not require any vacancy formation steps, but does require acid site, which is created by heterotic H_2 dissociation across the Ru/TiO_2 interface with E_a of 0.47 eV (section 3.3.5). Similar to our previous study, along the PES, two steps, C_{aryl}-OH dissociation and H_2 dissociation, are balanced with similar energy barriers[31], and it is attributed to the amphoteric character of TiO_2 support.

We should note here that the reported energies in Figure 5-2 account for electronic energy changes only; entropy effects to the free energy are not considered. However, entropy contributions are particularly important for adsorption and desorption steps. The significant toluene desorption barrier (ΔE_{des} = 1.46 eV) prompted us to estimate the free energy of toluene desorption ($\Delta G_{des} \approx \Delta E + E_{ZPE} - T\Delta S$), where E_{ZPE} and ΔS are zero-point energy and entropy change. We obtained ΔG_{des} = 0.27 eV at T = 673 K (same as experimental conditions). A similar result has also been reported in the Chie *et al*.'s work, in which the desorption energy of phenol decreases significantly after entropy corrections[15]. The entropy loss/gain during adsorption/desorption reduced the binding strength of m-cresol and toluene by similar amounts on the free energy landscape ($\Delta G \approx 1.2$ eV), but the activation barrier for C-O scission, toluene formation, and H_2 dissociation at the Ru/TiO_2 interface are less sensitive to entropy effects as listed in Table 5-1. Thus, at practical reaction temperatures we expect C-O scission, not toluene desorption, to be rate determining.

To conclude our argument for Ru/TiO_2 perimeter sites as potential active sites for the DDO of m-cresol, we refer to the data in Table 5-1. The direct C_{aryl}-OH dissociation (step II in Table 5-1)

on metallic Ru(0001), representative of large Ru particles in the absence of support effects, is E_a = 1.42 eV and considerably higher than the proton-assisted dehydroxylation. A bridging oxygen vacancy site ($V_{O^{br}}$) on TiO_2(110) is capable of breaking the C_{aryl}-OH bond with a somewhat lower barrier (step V in Table 5-1, E_a = 0.99 eV), but as discussed in our earlier work, the formation of $V_{O^{br}}$ sites on TiO_2(110) in the absence of a metal/TiO_2 interface is highly unfavorable. We also reported that atomic hydrogen spill-over from Ru to TiO_2 is a challenging process, requiring an activation barrier of > 1.2 eV, even if water-assisted pathways are considered (section 3.3.5). In concert, these calculations support the conclusion that proton transfer steps across the Ru/TiO_2 interface are responsible for the high DDO activity of this catalyst. In turn, the perimeter sites are implicated as the active sites of the m-cresol HDO reaction.

In addition to our DFT results, numerous prior studies have proposed that the metal/support perimeter sites play a paramount role for the direct deoxygenation of phenolic compounds. However, the exact role of these perimeter sites remains subject to speculation and unambiguous evidence for this active site assignment has not yet been provided. In the following we will address this question and show for the first time that for m-cresol conversion over Ru/TiO_2 the reaction rate varies systematically with the accessible metal perimeter.

5.3.2. Nature of Active Site

Table 5-2. Selectivity to toluene and rate of toluene formation per Ru surface area on Ru/TiO_2 and Ru/SiO_2. Reaction conditions are T = 400 ℃, P = 1 atm, and TOS = 10 mins. The rate and selectivity are reported at conversion below 25 %.

Catalyst	Particle Size (d_p) / nm	Toluene Selectivity mol % C	Toluene Rate (mol m^{-2}_{Ru} h)×10^6
3.5 % Ru/TiO_2	2.7±1.0	95.0	249
1.0 % Ru/SiO_2	2.3±1.3	69.9	133
5.3 % Ru/SiO_2	4.1±1.8	64.3	155
9.4 % Ru/SiO_2	5.3±3.3	57.5	151

When comparing the reaction rates of m-cresol conversion to toluene normalized to the Ru surface area of Ru/SiO_2 and Ru/TiO_2 catalysts of comparable particle size, we observe increased reaction rates by nearly a factor of two (Table 5-2). The results in Table 5-2 also show a great

selectivity enhancement to toluene from 58-70 % for Ru/SiO_2 to 95 % when TiO_2 is used as the support. Together, these results strongly suggest that active sites responsible for toluene production are created due to an interaction of Ru with the TiO_2 support, but the results are not sufficient to discriminate between modifications of the metal cluster due to support effects[101], actives sites on the support itself [223], or active sites at the metal/support interface[31].

Table 5-3. Perimeter and surface area per gam catalyst for various Ru catalysts estimated by Transmission Electron Microscopy (TEM) analysis, assuming a hemispherical shape of Ru cluster.

Ru Content %	Avg. Particle Size (d_p) nm	Ru perimeter (nm g^{-1})$\times 10^{-18}$	Ru surface Area (nm^2 g^{-1})$\times 10^{-18}$
0.4[a]	0.8±0.4	5.7	2.3
0.5	0.5±0.3	20.2	5.1
0.6	0.5±0.3	23.7	5.9
0.8[a]	0.7±0.4	15.5	5.3
1.1	1.8±1.8	3.3	2.9
1.6	2.3±1.2	2.9	3.4
1.7	2.4±1.5	2.9	3.5
2.3	3.0±1.2	2.4	3.7
3.5[a]	2.7±1.0	4.7	6.3
3.5	1.4±0.1	17.9	12.3
4.4	3.6±1.7	3.4	6.0

[a]It indicates anatase and Ru/TiO_2 corresponds to the P25.

To fully characterize the nature of the active sites responsible for selective toluene production, a series of catalysts with varying metal loading and particle sizes were prepared over both pure anatase and P25 TiO_2. By varying both the support phase and the particle size by over an order of magnitude, one can distinguish between actives sites on the Ru cluster (Ru surface area), at the Ru/TiO_2 interface (Ru perimeter), and on the two different supports (anatase and P25). To calculate the metal surface area and perimeter per gram catalyst presented in (Table 5-3) we use the Ru weight percent, particle size and catalyst amount, and assume hemispherical Ru particles on the TiO_2 support[224]. The wt% Ru for each catalyst was determined by ICP. The low loading (< 1 wt% Ru) catalysts used had sub-nanometer particle sizes as determined by TEM. While small particle sizes of this magnitude have been reported in the literature for this family of catalysts[225,226], additional verification of particle size was conducted with a probe reaction. The

classical structure-insensitive ethylene hydrogenation reaction probes the exposed Ru surface area. The rate per exposed metal atom on Ru/SiO_2 was used to estimate the exposed Ru surface area for several of the TiO_2 supported Ru catalysts. Particle sizes estimated via ethylene hydrogenation for various Ru/TiO_2 catalysts are presented in Table 5-4.

Table 5-4. Comparison of Ru particle sizes estimated from TEM and ethylene hydrogenation on Ru/TiO_2. External surface area of Ru in Ru/SiO_2 (1.0 wt %) was used as a reference at T = 40 ℃, C_2H_4:H_2 = 1:50, and P = 1 atm.

Ru Content		Avg.Particle size(d_p) / nm	
%		TEM	Ethylene Hydrogenation
Anatase	0.4%	0.8	0.7
P25	0.5%	0.5	0.4
	0.6%	0.5	0.4
	3.5%	2.7	2.3
	4.4%	3.6	3.2

Table 5-4, indicating excellent agreement between the two techniques. The fact that the two techniques agree further indicates that any TiO_x migration over the Ru nanoparticle during the reduction step does not lead to a significant loss in exposed surface area. Because these ethylene hydrogenation reactions were conducted with the smaller Ru nanoparticles, which are more prone to being covered by the TiO_x under high reduction temperatures, any migration of TiO_2 over the Ru surface was not enough to significantly modify the number of exposed metal sites.

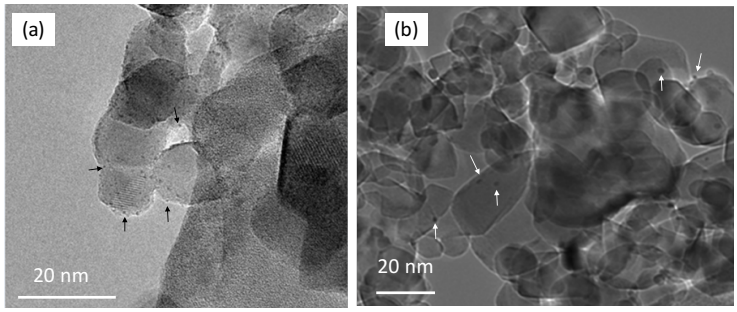

Figure 5-3. TEM images for selected Ru/TiO_2 catalysts (a) 0.6 % Ru/TiO_2 and (b) 4.4 % Ru/TiO_2. The white scale bar represents 20 nm. The black and white arrows represent Ru particles.

Representative TEM images for some of the Ru/TiO_2 catalysts are presented in Figure 5-3 and it is noticed that the Ru particle is evenly distributed over TiO_2 support.

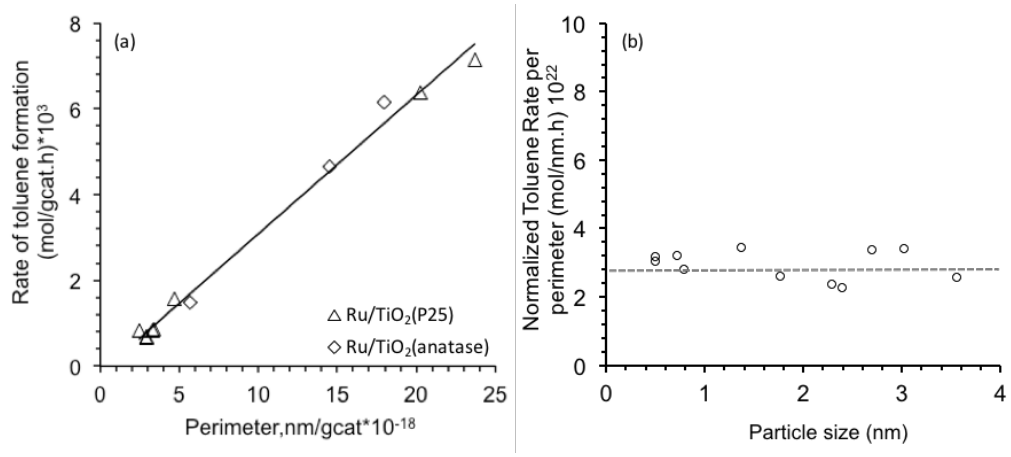

Figure 5-4. (a) The rate of toluene formation as a function of Ru perimeter. (b) Normalized rate of toluene formation per Ru perimeter versus particle size for several Ru catalysts. Reaction conditions are T= 400 ℃, P = 1 atm, and TOS = 10 mins. Rates are recorded at conversion below 15%.

Figure 5-4(a) shows the reaction rate of m-cresol conversion to toluene vs. the Ru perimeter for all of the catalysts listed in Table 5-2. The initial rates were all obtained at low conversions (< 15 %). The rate of toluene formation increases linearly with the Ru perimeter. It is important to note that toluene is the major product observed under these reaction conditions. Over 86 % selectivity to toluene is observed on a mol C basis for all TiO_2 supported catalysts under this range of conversions as a function of particle diameter.

This clear trend in rate per metal/support perimeter is rather remarkable considering that the range of catalysts studied spans both pure anatase as well as P25 TiO_2 supports, with P25 consisting of both anatase and rutile polymorphs. Under identical reaction conditions in a previous study, the catalyst support phase was found to have a significant impact on initial deoxygenation rates of a dioxygenated phenolic compound guaiacol[156]. This trend of increasing rate with increasing metal perimeter was not present upon the conversion of guaiacol under identical conditions, with activity correlating more strongly with the TiO_2 phase than the metal/support perimeter[156]. Based on the results presented in Figure 5-4(a), the active sites responsible for toluene formation scale linearly with the perimeter surrounding the metal particle. This plot alone, however, does not discern activity differences that may arise due to sites on the Ru particle with varying coordination numbers that result from the range of Ru particle sizes tested.

A plot of the normalized rate of toluene formation per Ru/TiO_2 perimeter [see Figure 5-4(b)] indicates that the trend is not dependent on the Ru particle size or the phase of the TiO_2 support. In fact, the graphs in Figure 5-4 provide strong evidence for the location of active site located at the Ru/TiO_2 interface for m-cresol conversion to phenol, and these perimeter sites are likely the active sites responsible for the reaction of other mono-oxygenated phenolics to form aromatic hydrocarbons such as toluene and benzene. This is a significant result as the promising enhancements in activity observed for guaiacol conversion to cresol when supporting Ru over TiO_2 in previous studies [158] were found to be highly dependent on the TiO_2 support (anatase vs. P25) under similar reaction conditions [156]. This implies that, although the combination of Ru with TiO_2 results in a synergy in activity for the conversion of phenolics containing one or two oxygen atoms, the active sites primarily responsible for each species may be different.

Based on our DFT results and experimental observations, we conclude that the perimeter sites at the Ru/TiO_2 interface are the active site for *m*-cresol DDO. The interface provides the following synergistic advantages: (1) It allows heterolytic H_2 activation and facilitates the formation of a protonated support site; (2) the support proton assists during the abstraction of OH leading to the formation of water; and (3) the interaction between Ru and the aromatic ring stabilizes the *m*-cresol molecular fragment after C-O scission.

The metal/support perimeter has been proposed as the active site for bond activation for a variety of reactions. In Ru/TiO_2 systems, perimeter sites for C-O bond activation have been implicated for phenol dehydroxylation[31] and in Fischer-Tropsch (FT) synthesis[227]. Also, normalized ethane and butane hydrogenolysis rates were found to follow a trend with the normalized perimeter and not the exposed metal surface area for Rh/TiO_2[228]. Finally, it was recently shown that surface water on TiO_2 donates protons across the Au/TiO_2 interface and thereby acts as a co-catalyst for CO oxidation on Au nanoparticles[183]. Collectively, these studies show that perimeter sites are significant for the conversion of various compounds in supported metal systems and an improved understanding of the phenomena occurring at metal/support interfaces is beneficial for a broad range of applications.

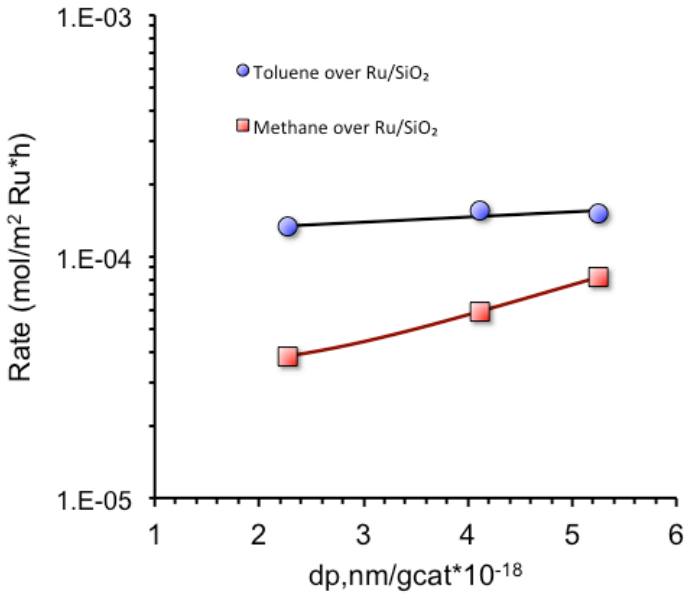

Figure 5-5. Rates for toluene and methane formation with regard to Ru particle diameter supported on SiO_2. Reaction conations are T= 400 ℃, P = 1 atm, and TOS = 10 mins. Rate are recorded at conversion below 25 %.

In addition to the activity enhancement for toluene formation, it is important to note that light gases such as methane were significant products for the reaction over Ru/SiO_2 with selectivity as high as 31 mol%. This is due to C-C bond hydrogenolysis over the Ru metal. This C-C hydrogenolysis activity is suppressed for the Ru/TiO_2 catalyst as indicated by the enhanced selectivity to toluene reported in Table 5-2. Figure 5-5 shows that irrespective of Ru metal loading or particle size for three Ru/SiO_2 catalysts compared, the rate of toluene formation per Ru surface area does not significantly change. Selectivity for light gases over the Ru/SiO_2 catalysts increases as Ru particle size is increased. Similar observations in hydrogenolysis selectivity over supported Ru catalysts have been reported in the literature[229]. The reduction in methane selectivity could be due to a combination of enhanced rates of toluene production on perimeter sites coupled with a decrease in sites necessary for C-C hydrogenolysis. While enhanced rates of toluene production due to the presence of new sites located near the perimeter will increase selectivity, it should be noted that the rate of methane formation is also decreased when Ru is supported on TiO_2. This could be due to the formation of water produced from the formation of toluene at the interface, which is known to suppress C-C hydrogenolysis in F-T reactions[230]. The decomposition of m-cresol over the Ru metal surface may instead yield CO. Alternatively, some small amount of TiO_2

decoration during high temperature reduction could inhibit sites required for C-C hydrogenolysis. Low coordination sites have been reported to be active sites for alkane hydrogenolysis over several metals[231,232]. Resasco and Haller[226] also found a drop in alkane hydrogenolysis rates after reduction at 500 °C of Rh supported on TiO_2. They attributed this to covering of active sites responsible for this reaction by the reduced TiO_2. This effect has also been demonstrated for Ru/TiO_2 systems upon the hydrogenolysis of n-butane[233] and n-hexane[234] after high temperature reduction. It should be noted, however, that any decoration that occurs in the present study is not sufficient to alter the ethylene hydrogenation activity, indicating that water may also play an important role.

5.4. Conclusions

Conversion of m-cresol over Ru/TiO_2 has been studied at atmospheric pressure and 400 °C in a vapor phase flow reactor to understand the active sites responsible for this reaction. Proposed sites were Ru metal and Ru/TiO_2 interface. Linear correlation for rate of m-cresol HDO to toluene with respect to the perimeter of Ru cluster was obtained, but not with regard to the surface area of Ru cluster. Hence, it is concluded that the Ru/TiO_2 interface is responsible for the enhanced the rate of m-cresol HDO on Ru/TiO_2. This conclusion agrees well with a series of DFT results in a way that the calculated energy barrier for direct C-O scission in m-cresol leading to desired product toluene is much lower than on Ru(0001) and TiO_2(110).

Chapter 6. Effects of Surface Intermediates (COOH*, O*, OH*) on Partial Oxidation of Methane, Complete Oxidation of Methane, and Methane Reforming: A Microkinetic Model Study

6.1. Introduction

Hydrodeoxygenation (HDO) requires large amounts of H_2 to upgrade bio-oils to oxygen free compounds. Venderbosch *et al.* reported that H_2 consumption increases drastically as it goes to deep deoxygenation[19]. H_2 consumption closely relates to both the level of deoxygenation and the saturation of double/triple bonds. Relatively reactive oxygenated molecules like ketone and alcohol are rapidly converted to oxygen free compounds under low pressure H_2 atmosphere, while more complex species like furan and substituted phenols often consume more H_2 than ideally necessary but to over-hydrogenation and saturation[1]. Therefore, we need to design a catalyst that uses H_2 efficiently (as discussed in Chapter 4) and a process to cheaply produce a sufficient amount of H_2 for bio-oil upgrading.

Currently, the commercialized catalytic process for H_2 production are methane steam reforming (MSR) to produce syngas and water gas shift (WGS) to further maximize H2 production and adjust the CO/CO_2 ratio[235–237]. While steam reforming can be done with many hydrocarbons sources, the most abundant and cheapest feedstock is methane (CH_4); thus its conversion into syngas through MSR is the most extensively studied reforming reaction[235,237,238]. In addition to MSR and WGS, partial oxidation of methane (POM) and methane dry reforming (MDR) are also investigated as a way to convert CH_4 to syngas[239]; however, they are still far from commercial application because of low selectivity toward H_2 production as a result of the deep oxidation that occurs in the presence of O_2 and catalyst deactivation[240]. Lastly, complete oxidation of methane (COM) is of interest in emissions control catalysis for natural gas powered vehicles.

Catalysts used for POM, COM, MSR and MDR are typically Ni, Pt, Pd, Rh, Ru, etc[238,241]. These are transition metals extensively used in heterogeneous catalysis to catalyze bond dissociation[4,55,238,242,243]. Transition metals belonging to groups VIB and VIII are effective in

dissociating X-H bonds (X=O, N, and C), whereas the IB group is less suited to activate these bonds. The he ability to activate bond dissociation on transition metals depends strongly on both electronic and geometrical effects[244,245]. The electronic structure of metal atoms is well described by the d-band model, which allows an estimation of stability of transition states and surface intermediates. On the other hand, the geometrical effects originate from the different geometries of surfaces such as kink, terrace, steps, defects, etc. and resulted in different structural environments for molecules to be activated in the transition state. Nowadays, these two effects are the key factors to design transition metal catalysts and tune their ability for the chemical bond activation.

Another factor influencing transition state energies and the stability of surface intermediates is the coverage of surface adsorbates such as surface oxygen (O*) and hydroxyl (OH*). For example, previous studies reported that pre-adsorbed O* and OH* change reaction kinetics and can alter the main reaction pathway for methane activation processes[239,246,247]. This effect especially stands out in the C-H bond dissociation of hydrocarbons. Maestri et al. revealed that the reaction pathways of POM on Rh are significantly influenced by the presence of surface O* and OH*[239]. Under excess coverage of surface O* and OH*, POM shifts to the complete combustion through oxidative dehydrogenation ($CH_x + O \rightarrow CH_{x-1} + HO$, $x = 1 \sim 4$). After depletion of surface O* and OH* COM is catalyzed through the pyrolytic mechanism ($CH_x \rightarrow CH_{x-1} + H$, $x = 4$) [239]. Similary, Yoo et al. reported similarly that the C-H dissociation in CH_4 on Ag, Au, and Cu becomes favorable in the presence of surface O*, but not on Pt-group metals[248]. More general trends for the effects of surface O* on the bond dissociation in X-H (X= O, N, C) were explored by Shustorovich et al., who studied the role of surface O* in the cleavage for X-H (X= O, N, C) on Ag, Cu, Ni, and W[249]. According to their data, surface O* facilitates the cleavage of X-H (X= O, N, C) on Ag and Au, whereas such processes are limited on Ni, Cu, W, and Mo[249]. Wise et al., on the contrary, revealed that rate of C-H dissociation in CH_4 significantly increased in the presence of surface O* on Ni(110) and Ni(111) surfaces[250,251].

The examples discussed above suggest that methane activation in the presence of surface O* and OH* is still under debate. It certainly depends on the nature of the metal surfaces as well as

on the reaction conditions. Hence, it requires a comprehensive study that can capture these effects to elucidate the effects of surface O* and OH* on the catalytic activity and production selectivity.

The aim of this study, therefore, is to study the effect of surface COOH*, O*, and OH* on C-H dissociation in CH_4 to explore how we can utilize the cheap and abundant natural gas to produce H_2 for bio-oil upgrading processes. In particular, we are interested in typical syngas processes such as partial oxidation of methane (POM), complete oxidation of methane (COM), methane steam reforming (MSR), and methane dry reforming (MDR), as well as the water-gas shift (WGS) reaction. A comprehensive descriptor-based microkinetic model (MKM) in conjunction with the web database CatApp and DFT calculations is used to explore systematically their effects. Overall, it is concluded that only surface O* alters the catalytic activity in POM and COM by increasing the CH_4 dissociation rate.

6.2. Computational Approach

The 28 elementary steps shown below were included in our microkinetic modeling to investigate the effect of surface O* and OH*. In this reaction scheme, "*" denotes a free surface sites, and X* is a X intermediate on surface.

Group	Elementary Step	Step No.
M1	$CH_{4(g)} + 2^* \leftrightarrow CH_3^* + H^*$	(1)
	$CH_3^* + ^* \leftrightarrow CH_2^* + H^*$	(2)
	$CH_2^* + ^* \leftrightarrow CH^* + H^*$	(3)
	$CH^* + ^* \leftrightarrow C^* + H^*$	(4)
	$H^* + O^* \leftrightarrow HO^* + ^*$	(5)
	$H^* + HO^* \leftrightarrow H_2O_{(g)} + 2^*$	(6)
	$2HO^* \leftrightarrow H_2O_{(g)} + O^* + ^*$	(7)
	$2H^* \leftrightarrow H_{2(g)} + 2^*$	(8)
	$O_{2(g)} + 2^* \leftrightarrow 2O^*$	(9)
	$C^* + O^* \leftrightarrow CO^* + ^*$	(10)
	$CO^* \leftrightarrow CO_{(g)} + ^*$	(11)
	$CO^* + O^* \leftrightarrow CO_{2(g)} + 2^*$	(12)
M2	$CO^* + OH^* \leftrightarrow COOH^* + ^*$	(13)
	$COOH^* \leftrightarrow CO_{2(g)} + H^*$	(14)

	$COOH^* + O^* \leftrightarrow CO_{2(g)} + HO^* + *$	(15)
	$COOH^* + HO^* \leftrightarrow CO_{2(g)} + H_2O_{(g)} + 2*$	(16)
M3	$CH_{4(g)} + O^* + * \leftrightarrow CH_3^* + HO^*$	(17)
	$CH_3^* + O^* \leftrightarrow CH_2^* + HO^*$	(18)
	$CH_2^* + O^* \leftrightarrow CH^* + HO^*$	(19)
	$CH^* + O^* \leftrightarrow C^* + HO^*$	(20)
	$CH^* + O^* \leftrightarrow HCO^* + *$	(21)
	$HCO^* \leftrightarrow H^* + CO^*$	(22)
M4	$CH_{4(g)} + HO^* + * \leftrightarrow CH_3^* + H_2O_{(g)} + *$	(23)
	$CH_3^* + HO^* \leftrightarrow CH_2^* + H_2O_{(g)} + *$	(24)
	$CH_2^* + HO^* \leftrightarrow CH^* + H_2O_{(g)} + *$	(25)
	$CH^* + HO^* \leftrightarrow C^* + H_2O_{(g)} + *$	(26)
	$HO^* + C^* \leftrightarrow COH^* + *$	(17)
	$COH^* \leftrightarrow H^* + CO^*$	(28)

To address the question whether the surface intermediates including COOH*, O*, and OH* have specific effects on the methane activation processes, the elementary steps are grouped as; M1: step 1 ~ 12, M2: step 13 ~ 16, M3: step 17 ~ 22, and M4: step 23 ~ 28. Group M1 includes pyrolytic methane activation (step 1 ~ 4), surface redox mechanism (step 5 ~ 12), and dissociative O_2 adsorption (step 9). In the many previous studies, these elementary steps included in M1 formed the mechanism for methanation, methane oxidation, and methane steam reforming[94,237]. The COOH-assisted water-gas shift (WGS) pathways being believed to be the most likely WGS steps are included in group M2 [252]. Group M3 consists of oxygen-assisted methane activation in the presence of surface O* (step 17 ~ 20) and the formation of formyl (HCO*, step 21 ~ 22), which have been implicated as key intermediate in steam reforming [253]. Group M4 is OH-assisted methane activation (step 23 ~ 26) and the formation of hydroxymethylidyne (COH*, step 27 ~ 28). The hydrogen insertion mechanism into CO along with COH formation is known to occur on Ni with a barrier of ca. 0.8 eV, well below the CO desorption energy, and is in turn considered as an important surface intermediate for CO production and methanation[254,255]. Five different reaction networks were assembled from these four groups to elucidate the effects of COOH-mediated WGS, surface O*, and OH* on methane activation based on the volcano (V) plots. The five combinations are, (1) V1: M1, (2) V2: M1+M2, (3) V3: M1+M3, (4) V4: M1+M4, and (5) V5: M1+M2+M3+M4. The first case, V1, is set to be our reference that

does not include any elementary steps involved in COOH*, O*, and OH*. The volcano plots, V2, V3, and V4 show the individual effects of COOH-mediated WGS, surface O*, and surface OH*, respectively. For example, a comparison of V1 with V3 and V4 helps us discern the effect of surface O* and OH*. Finally, we combined them all together to check any synergetic effects of these surface intermediates. The reason for the inclusion COOH-assisted WGS in V2 is that WGS is known as most likely side reaction during methane activation, methanation, reforming processes[252].

The reaction conditions for catalytic methane activation using all 28 elementary steps are according to:

POM: $CH_4 + 1/2O_2 \rightarrow CO + 2H_2$, (6-1)

COM: $CH_4 + 2O_2 \rightarrow CO_2 + 2H_2O$, (6-2)

MSR: $CH_4 + H_2O \rightarrow CO + 3H_2$, and (6-3)

MDR: $CH_4 + CO_2 \rightarrow 2CO + 2H_2$. (6-4)

These are partial oxidation of methane (POM, Eq. 29), complete oxidation of methane (COM, Eq. 30), methane steam reforming (MSR, Eq. 31), and methane dry reforming (MDR, Eq. 31). As a benchmark, H_2 and CO oxidation were tested to check the validity of our model and check for inconsistencies originating from mixing data from the online database CatApp and our own DFT calculations. The formation of syngas (CO and H_2) via Eq. 29 competes with the complete oxidation of methane, Eq. 30, leading to the CO_2 and H_2O production. Previous works related to the methane catalysis left the CO_2 production out of their model, and predicted only CO and H_2 production[94,256]. To better understand the selectivity (CO versus CO_2), we included both CO and CO_2 as final products. The effects of oxidative methane activation and COOH-assisted WGS during MSR and MDR on single metal catalyst has been presented by many groups[236,239,248,257]; however, to the best our knowledge a descriptor-based study across transition metals to obtain comprehensive understanding of such intermediates on methane activation hasn't yet been explored.

The results of microkinetic modeling were analyzed by means of a 2 dimensional volcano (V) in which the turn over frequency (TOF) is plotted as a function two descriptor values, carbon and oxygen binding energies. The descriptor-based approach to estimate electronic energies of surface intermediates and transition state energies has been employed as a way to reduce computational expenses and simultaneously increase the understanding of catalytic trends [258]. Similar to other works, the binding energy of carbon (E_C) and oxygen (E_O) on stepped (211) surfaces, enable us to obtain linear scaling relationships for the binding energies of surface intermediates and transition state energies[259–261]. Detailed information regarding these linear scaling correlations are summarized in the Appendix. All DFT energies were corrected with zero point energy (E_{ZPE}) and entropy (ΔS), because the reaction temperature (T) for those processes chosen in this study is relatively high (> 750 K). For gas phase species (CO, CO_2, H_2, H_2O, CH_4, and O_2), we used the Shomate equation to estimate their temperature-dependent Gibbs free energies (ΔG). Steady-state solutions under the reaction conditions summarized in Table 6-1 are solved with CapMAP, which facilitates the easy mapping of the catalytic activity and selectivity on the basis of volcano[258].

Table 6-1. Representative reaction conditions for H_2 oxidation, CO oxidation, water gas shift (WGS), partial oxidation of methane (POM), complete oxidation of methane (COM), methane steam reforming (MSR), and methane dry reforming (MDR).

Reaction	Overall Reaction	T / K	Feed Ratio
H_2 oxidation	$H_2 + \frac{1}{2}O_2 \leftrightarrow H_2O$	500	$H_2/O_2 = 2.0$
CO oxidation	$CO + \frac{1}{2}O_2 \leftrightarrow CO_2$	500	$CO/O_2 = 2.0$
WGS	$CO + H_2O \leftrightarrow CO_2 + H_2$	500	$CO/H_2O = 1.0$
POM	$2CH_4 + O_2 \leftrightarrow 2CO + 4H_2$	800	$CH_4/O_2 = 2.0$
COM	$CH_4 + 2O_2 \leftrightarrow CO + 2H_2$	800	$CH_4/O_2 = 0.5$
MSR	$CH_4 + H_2O \leftrightarrow CO + 3H_2$	773	$CH_4/H_2O = 1.0$
MDR	$CH_4 + CO_2 \leftrightarrow 2CO + 2H_2$	1000	$CH_4/CO_2 = 1.0$

Stepped (211) surfaces are chosen for Pt, Pd, Ru, Rh, Ni, Cu, Fe, Re, Au, and Ag. The four-site model, previously applied for various reactions on the stepped (211) facet, is adopted to describe the complexity of reactions occurring on stepped (211) surfaces[94,256,260].

The energetic input parameters to the MKM such as binding energies of surface intermediates and transition state energies for 20 elementary steps were taken from the literature and CatApp

[260,262]. Additional energies for 8 elementary steps including step 17 ~ 20 (CH_x + O* → CH_{x-1} + OH*, x = 4 ~ 1) and step 22 ~ 25 (CH_x + OH* → CH_{x-1} + H_2O, x = 4 ~ 1) were calculated using DFT on stepped (211) surfaces of Pd, Ni, and Au, and were used to estimate scaling lines. Energetic parameters on the other surfaces are predicted by using estimated scaling lines over Pd, Ni, and Ni surfaces. Energetic input for our microkinetic model is summarized in the Appendix.

For our density functional theory (DFT) calculations, we used the Vienna Ab initio Simulation Package (VASP) with the Atomic Simulation Environment (ASE)[63,103,263]. The electron-ion interaction is described with the projected-augmented wave (PAW) method, and the Perdew-Wang (PW91) exchange-correlation functional is employed with kinetic energy cut-off of 400 eV to solve the Kohn-Sham equations[41,106]. The (1 × 2) unit cells of Pd(211), Ni(211), and Au(211) are modeled with 4 layer slabs where the top two layers are allowed to fully relax until the forces acting on each atom are smaller than 0.05 eV $Å^{-1}$, and the bottom two layers are fixed at their bulk positions. Spin-polarized calculations are only performed for Ni. Transition-state energies are located using Nudged Elastic Band (NEB) method[72]. The vibrational frequencies to correct the zero-point energy (E_{ZPE}) and entropy corrections (ΔS) are obtained in the harmonic oscillator approximation as implemented in ASE.

6.3. Results and Discussion

This section is divided into three parts. First, we present MKM benchmark tests, because we used a database mixed with CatApp energies and our own DFT values. Inconsistencies between these sources may result in errors that could lead to incorrect interpretations of activity trends. Thus, a rigorous validation test prior to run any further MKM is necessary. In the second part, we introduce a simple approach to discern the most important surface intermediates from the series of elementary steps. It is a very important step when we investigate a new catalytic process, because this scheme can significantly reduce the amount of computational expenses. Finally, based on the observation of the second part we discuss the effects of COOH-mediated WGS, surface O*, and OH* on partial oxidation of methane (POM), complete oxidation of methane (COM), methane steam reforming (MSR), and methane dry reforming (MDR).

6.3.1. Validity Test with MKM

As noted, there are possible inconsistencies in our energetic input parameters. These originate from different exchange correlation functionals (PW91 vs. RPBE), potentials to represent atomic cores, and software packages (GPAW vs. VASP). Thus, we first confirm the validity of our energy inputs by running benchmark tests before proceeding to the methane activation reactions of interest. We assume that if the MKM reproduces previously published results, it is good enough to provide meaningful information in terms of catalytic activity trends and product selectivity. We used the well-studied H_2 oxidation and CO oxidation reaction for benchmark comparisons, because of the wealth of information that available for these reactions [93,109,115].

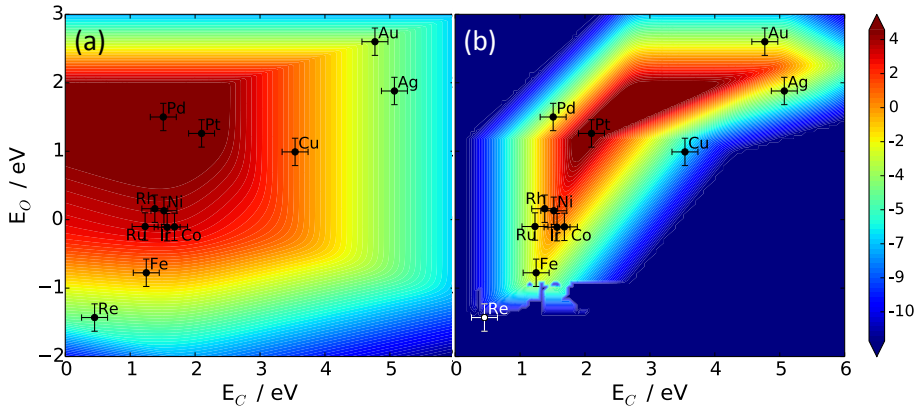

Figure 6-1. Calculated logarithmic turnover frequency (TOF) under prototype reactions: (a) H_2 oxidation, $H_2 + \frac{1}{2}O_2 \leftrightarrow H_2O$, T = 500 K, P_{H_2}/P_{O_2} = 2 ; (b) CO oxidation, $CO + \frac{1}{2}O_2 \leftrightarrow CO_2$, T = 500 K, P_{CO}/P_{O_2} = 2.

Overall, we found that our MKM produces identical results with previously published works under the same reaction conditions[93,264]. H_2 oxidizes rapidly to H_2O on Pt, Pd, Ru, Ru, etc. as shown in Figure 6-1(a), and Pt is predicted for the best catalyst for CO oxidation[93]. These consistent results suggest that our combined model has enough accuracy for the prediction of trends and product selectivity.

6.3.2. Discerning an Important Surface Intermediate with MKM

Unlike the prototype reactions used in section 6.3.1 (CO and H_2 oxidation), we often encounter a catalytic process consisting of 10 ~ 60 elementary steps. For example, Sun et al. investigated methane oxidative coupling reaction with 39 elementary steps by means of a MKM[265]. Santen et al. also included more than 20 elementary steps in their MKM to study Fischer-Tropsch (FT) reactions[266]. Lu et al. performed a MKM study for guaiacol hydrodeoxygenation (HDO) with 60 elementary steps and 39 surface intermediates[200]. It is true that the large number of elementary steps in a kinetic model increases the number of surface intermediates necessary for consideration. It is also true that we need to put more effort on the DFT calculations as the number of surface intermediates increases. We know, however, that not all the surface intermediates are catalytically important.

First, we are interested in determining which surface intermediates and elementary steps are potentially interesting. The definite answer is provided by performing a complete MKM, but it requires significant amount of computational expenses for the preparation of the complete input for MKM. Hence, we adopted a simple approach to screen important surface intermediates and elementary steps before running any DFT calculations. The procedure is the following. We started with the data collection for surface intermediates from CatApp, a web-based repository containing a large number of DFT-derived energies for many surface intermediates. With CatApp, we can easily build a full potential energy surface for many catalytic process such as formaldehyde, methanol, ethanol, methanation, CO oxidation, and H_2 oxidation as reported elsewhere[94,258,260,267]. Then, we added certain groups of elementary steps in a simplified MKM to determine their possible impact on activity and selectivity. Such screening test doesn't require kinetic information for elementary steps, but only takes the thermodynamic stabilities of surface intermediates. After this first screening we are able to eliminate unnecessary surface intermediate from kinetic model, and can focus on the catalytically important ones. The concept is similar to Liu et al.'s approach in which they plotted a free energy diagram for surface intermediates, and used this diagram to predict the most stable surface intermediates in the reaction network[268]. As they reported, the free energy diagram can be a practical alternative to a complete MKM[268].

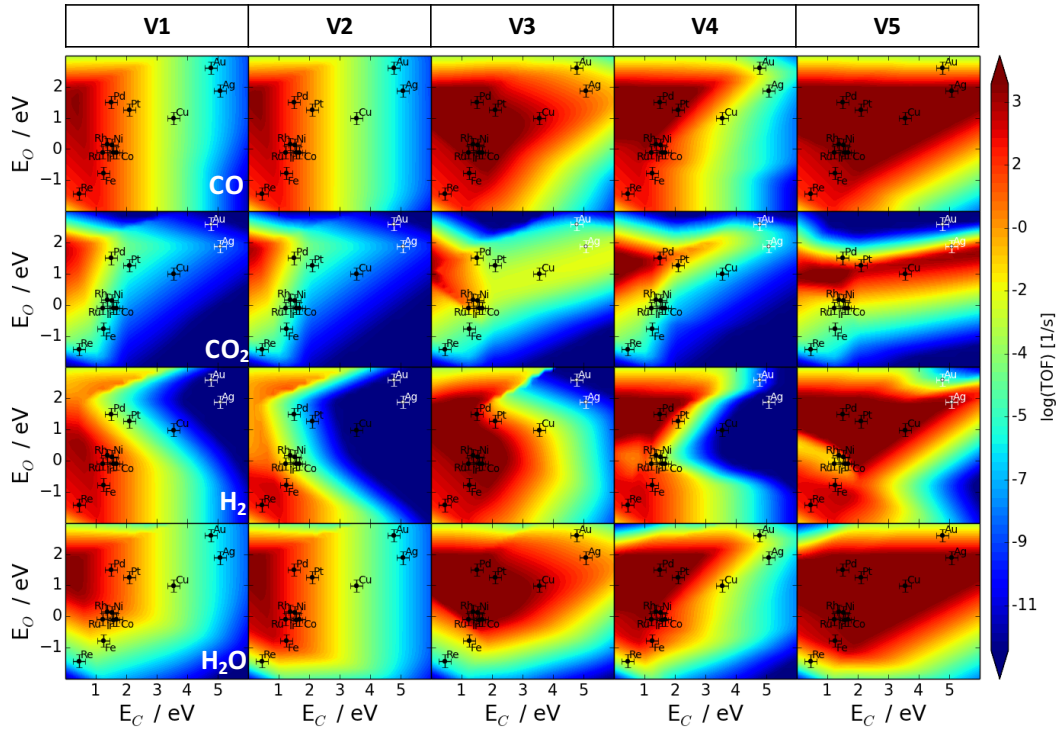

Figure 6-2. Calculated logarithmic turnover frequency (TOF) for partial oxidation of methane (POM) toward CO, CO_2, H_2, and H_2O. The error bars indicate an estimated error of 0.2 eV for E_O and E_C. Reaction conditions are T = 750 K and p = 1.0 bar with CH_4/O_2 = 2.0.

We performed this screening test to check if surface COOH*, O* and OH* play an important role in POM. First, we collected all energetic parameters from CatApp. Then, we ran a MKM with M1. Then, we add M2, M3, and M4 to M1 individually and analyze the differences. Note that except for M1, transition state energies in M2, M3, and M4 are not included for the purpose of screening. The final results are compared to each other as shown in Figure 6-2.

Volcano V1 in Figure 6-2 is our reference and shows the calculated TOF with the elementary steps (M1) for POM. When the MKM is modified with the steps of group M2 we obtain volcano V2 = M1 + M2. We observe minor changes in CO and CO_2 production, indicating that the effect of COOH-mediated WGS is small (see the V2 in Figure 6-2). On Rh, Ru, Ni, Co, and Fe we found that H_2O production became more active, but H_2 production became less active. These results indicate the occurrence of the reverse-WGS (rWGS, $CO_2 + H_2 \rightarrow CO + H_2O$) reaction over these catalysts. Volcano V3 in Figure 6-2 is the result after the inclusion of O-assisted methane activation (M3), and it exhibits significant differences to the volcano from the V1. First of all, the

center of each volcano shifts to the right (weak carbon binding), meaning that inactive catalysts such as Cu, Ag, and Au turn into, at least to a certain extent, active. We also noticed the significant increase in the rate of CO and CO_2 production on Rh, Ni, Ru, Co, Au and Ag. This effect is rationalized by faster methane activation on these metal surfaces. The addition of M4 to M1 induces similar results (see the V3 in Figure 6-2). The active region in the volcano plot for CO, CO_2, H_2, and H_2O production is enlarged. The area where Au and Ag are located increased the rate of CO_2 production, but shows not as much increase as shown in the V2. Interestingly, the area nearby Rh, Ni, Ru, and Co decreases the rate of CO_2 and H_2 production. It is again attributed to the effect of the rWGS. Volcano V5 in Figure 6-2 is the result of combining them all reaction step groups together (M2, M3, and M4), and it is completely different from volcano V1. The effects are even more pronounced than adding the three reaction groups M2, M3, M4 independently to M1, which is a strong indication of synergetic effects.

The preliminary conclusion we can reach by performing this screening analysis is that the surface O* and OH* may play a crucial role in POM, but COOH-mediated WGS does not significantly alter reactivity trends. At this point, we are advised to return to DFT calculations, and to calculate the energetic parameters for the elementary steps in M3 and M4.

6.3.3. MKM Trend Study for Partial/Complete Oxidation of Methane

After including scaled reaction barriers for all steps from groups M2, M3, and M4, we observed overall similar activity trends for POM and COM but with expected selectivity differences to CO and CO_2. Since MKM studies of POM and COM have produced similar trends, we mainly focused on POM here and summarize the results for COM in the Appendix. Particularly, none of the pure metal surfaces tested in this study is close to the top of each volcano. The CO_2 production volcano exhibits two distinct maxima, corresponding to two different methane activation mechanisms; one maximum is close to Pd with direct CH_4 activation as dominant mechanism, whereas the other one is close to Au and Ag and proceeds via O-assisted CH_4 activation. In general, the peak of the volcano shifts to the weak carbon binding after the inclusion of the O-assisted activation steps from group M3. In contrast, the trends in catalytic activity for COM and

POM after the inclusion of COOH-mediated WGS (M2) and OH-assisted CH_4 activation (M4) had a negligible effect on the volcano shape. POM has been studied by many groups, but the main pathway for syngas production is still debated. Two major pathways are suggested. One is direct oxidative mechanism where H_2 and CO are directly produced after complete dissociation of CH_4 and O_2. The other pathway is the indirect route in which some CH_4 is totally oxidized to CO_2 and H_2O, followed by reforming to H_2 and CO as long as there is accessible surface O* for methane[269,270].

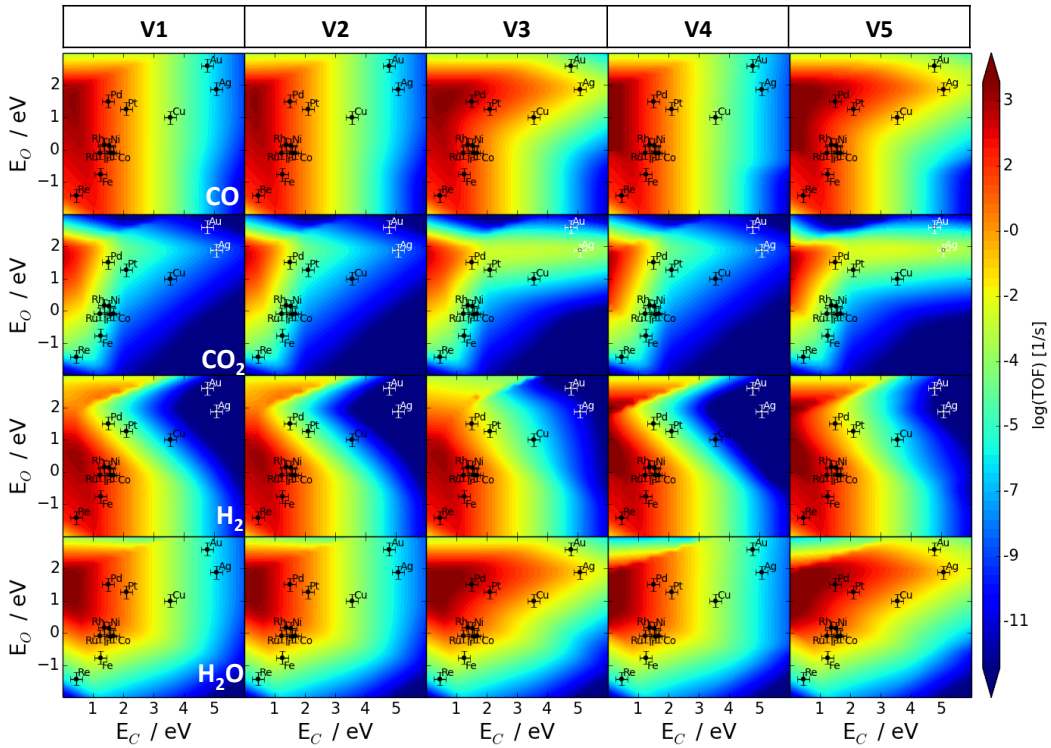

Figure 6-3. Calculated logarithmic turnover frequency (TOF) for partial oxidation of methane (POM) toward CO, CO_2, H_2, and H_2O. The error bars indicate an estimated error of 0.2 eV for E_O and E_C. Reaction conditions are T = 750 K and p = 1.0 bar with CH_4/O_2 = 2.

Delgado et al. have proposed that the indirect route is the dominant pathway for POM on Ni, Rh, and Pt [271]. At the reactor entrance which is rich in oxygen, only CO_2 and H_2O are detected, and the catalyst surface is completely covered with surface O*. Further down the length of the reactor they found a region where oxygen is completely consumed, and detected a rapid increase in the production of H_2 and CO. Their data implies that surface O* plays an important role in the

production distribution of POM, and can possibly alter the product selectivity to CO and H_2 from CO_2 and H_2O.

Figure 6-3 shows the calculated logarithmic TOF of POM. When only the basic mechanism M1 is included, no monometallic transition metals are located on the top of the volcano plot, but transition metals such as Rh, Ru, Ni, Co, and Pd are close to the top (V1 in Figure 6-3). We also notice that the most active region for the production of CO and CO_2 lies in the region of strong carbon binding and weak oxygen binding. This observation is consistent with the indirect route for POM at the volcano's top where CO_2 is produced rapidly and then converted to CO via reforming. At the volcano's top in CO production, we notice that H_2 formation is slower than CO formation, despite the feed stoichiometry of $CH_4/O_2 = 2$. We reason that the formed H_2 is consumed through the rWGS reaction in the region where CO_2 formation is active. Pt and Pd have the highest selectivity toward CO formation among others catalysts, but shows low product selectivity toward H_2, because H_2 is rapidly consumed via rWGS on Pt and Pd as reported[272].

Volcano V2 (M1 + M2) is presented in Figure 3-V2. We found that adding the COOH-mediated WGS reaction steps from group M2 has little effect on POM trends and the volcano peaks remain almost identical to V1. This result indicates that M2 is unlikely to affect the overall trends of POM as predicted in the section 6.3.2.

As shown in Figure 6-3 – V3, the calculated TOF after adding the O-assisted steps of group M3 differs significantly from the basic mechanism only (V1). First, Pd turns into the most active catalyst among others. It is because the rate of step 17 becomes as fast as the rate of step 1 on Pd. The calculated energy barrier for the step 17 is 0.13 eV lower than the barrier of step 1. Second, the rate of both CO and CO_2 production increases significantly on Ag and Au, and interestingly two distinctive peaks appear in the volcano of CO_2 production; one at $E_c < 0.5$ eV and $E_O > 0.0$ eV, and the other one is close to Au and Ag. The first peak corresponds to the CH_4 pyrolytic pathways included in group M1, and the second peak, which is less active than the first peak, corresponds to oxidative methane dehydrogenation as captured by the steps in group M3.

These differences with V3 are fully explained by the promotional effect of surface O* on CH_4 activation. The weak oxygen binding on metals like Au and Ag makes C-H scission in CH_4 more favorable as reported by Yoo *et al* [248]. Hence, the increased catalytic activity near Ag and Au can be rationalized by the lowered energy barrier of step 17 as similarly shown on Pd. For example, the calculated energy barriers for C-H dissociation in CH_4 on the Au in the presence and absence of surface O* are 0.85 eV and 1.58 eV, respectively. It indicates that CH_4 on Au(211) is more easily activated through the oxidative mechanism, step 17, rather than step 1. Recent DFT work also reveals a consistent result with ours[248].

Contrary to what we predicted in the section 6.3.2 in the absence of activation barriers, surface OH* is not as effective as the surface O* on POM. The predicted TOFs for V4 are almost identical to V1, which demonstrates that the purely thermodynamic screening approach is limited, but it does not exclude potentially interesting reaction steps. After we account for reaction barriers for the steps of group 4, we find that they do not significantly contribute to the overall catalytic activity of POM.

Volcano V5 in Figure 6-3 illustrates the synergetic effects of surface O*, OH* and COOH-assisted WGS. We expected to see the interplay between COOH-assisted WGS and surface O* or OH*, but did not find any synergetic effects. Volcano V5 is nearly identical to V3, which includes only steps from groups M3 and M1, indicating that only surface O* plays an important role during POM.

To better understand the catalytic activity predicted in Figure 6-3, we inspect the coverage of surface carbon, oxygen, and hydroxyl (see Figure 6-4). These are taken from the MKM with all 28 elementary steps. Note that surface C* binds strongly to the four-fold site, while surface O* and OH* compete for the adsorption on the on-top site (see SI). As shown in Figure 6-4(a), metals like Re bind strongly to carbon and oxygen, leading to surface poisoning by covering step sites (on-top and four-fold sites) predominantly with both surface O* and C*. Catalysts with a binding energy for oxygen (E_O) below 1.0 eV are completely covered with surface O* as shown in Figure 6-4(b).

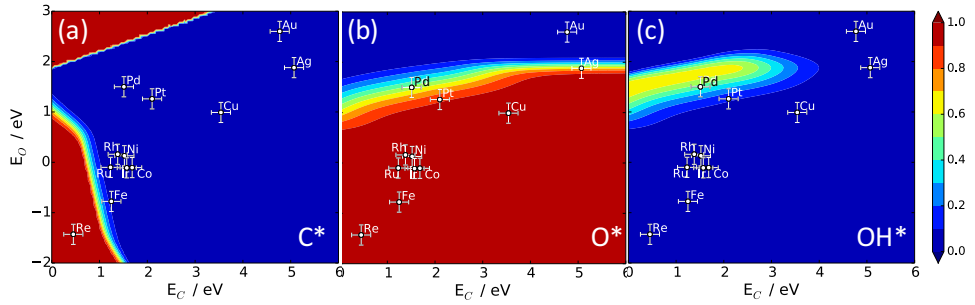

Figure 6-4. Stead-state coverages of (a) C*, (b) O*, and (c) OH* as a function of E_C and E_O, obtained after POM with the M1+M2+M3+M4+M5. Both oxygen and hydroxyl bind to the top of step sites of (211) surfaces.

The coverage results indicate that surface O* is the most abundant reaction intermediate (MARI) during POM. By examining both calculated TOFs (Figure 6-3) and coverages of major surface intermediates (Figure 6-4), we have noticed that the most active metals for CO production have θ_{OH} and $\theta_O \approx 0.5$ ML. The moderate coverage θ_{OH} nearby Pd and Pt is consistent with rapid activation of step 17. As previously reported, above a certain coverage threshold (e.g. 0.2 ~ 0.5 ML), strong interactions between surface intermediates can be induced, potentially resulted in the change of predicted reaction rate by altering the transition state energies[94,256]. The predicted reaction trends, however, are often unaltered because the induced interactions have a similar effect on the stability of surface intermediates across the different transition metals[93,94]. In addition, at the region where oxygen and carbon bind very strongly, there is a chance for the adsorbate-induced surface reconstruction that can also alter the predicted rates for POM; however, this is beyond the scope of this study.

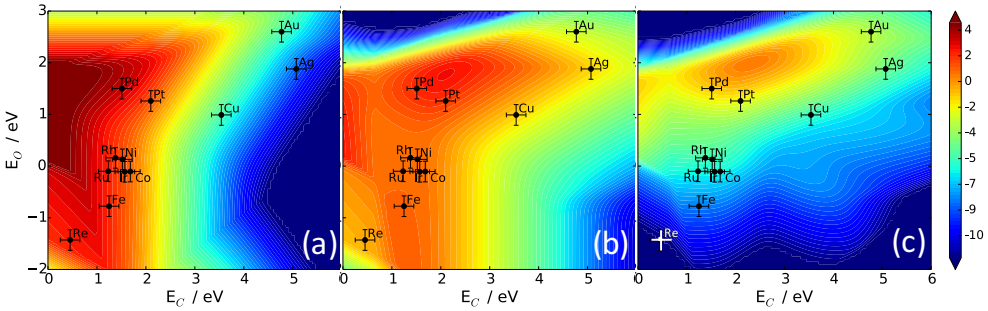

Figure 6-5. Three different pathways for C-H dissociation of methane during the partial oxidation of methane (POM): (a) step 1, $CH_{4(g)} + 2^* \leftrightarrow CH_3^* + H^*$, (b) step 17, $CH_{4(g)} + O^* + * \leftrightarrow CH_3^* + HO^*$, and (c) step 23, $CH_{4(g)} + OH^* + * \leftrightarrow CH_3^* + H_2O_{(g)}$.

To study the effect of surface O* during POM, we extracted the rate of C-H dissociation in CH_4 (step 1) and its rate in the presence of surface O* (step 17) and OH* (step 23) after a MKM with all 28 steps. The comparison is shown in Figure 6-5. In the region where carbon binds strongly to metals (E_C < 1.0 eV), the calculated rate of step 1 is much faster than the rate of step 17 or step 23. This region corresponds to the metals Ru, Rh, Ni, and Co as shown in Figure 6-5(a). On the other hand, in the region of weaker oxygen binding (E_O > 1.0 eV), step 17 became as fast as step 1 over Pt and Pd, or is faster than step 1 over Cu, Ag, and Au [see Figure 6-5(b)]. Such effect on methane activation has been speculated upon by experimental groups and our results are by and large consistent with their data[4,239,273]. Our results also agree with the most recent DFT study on this topic, except that they neglected to account for surface coverages and postulated that the O-assisted C-H dissociation in CH_4 is not favorable on both Pt and Pd [248].

6.3.4. MKM Trend Study for Methane Reforming Processes

We also explored the effects of surface O*, OH*, COOH* on methane steam reforming (MSR) and dry reforming (MDR), but did not find any effects of these intermediates on MSR and MDR, i.e., almost identical TOF were predicted after the inclusion of elementary steps from groups M2, M3, and M4. As in the previous section, we focus on just one process, which is MSR, and summarize the results of MDR in the Appendix.

The SR process is the most well developed process used for inexpensive syngas production[238,271]. Experimentally, the highest reforming rates have been measured for Rh, Ru, Ni, Pt, Pd, and Ir[238,273,274]. Among them, Ni-based catalysts are typically used in industry, because they are the least expensive materials compared to others[4,243]. As expected, the highest rate for CO and H_2 production are predicted from our MKM for Rh, Ru, Ir, Pd, Pt, and Ni, and much lower rates are predicted for Cu, Ag, and Au as shown in Figure 6-6. Contrary to the effect of surface O* on POM, we could not find any notable effects of COOH-assisted WGS, surface O*, and OH* on the overall production rates in MSR. Namely, the predicted volcano trends are essentially identical each other (see V1, V2, V3, V4, and V5 in Figure 6-6). Interestingly, we observed small amounts of O_2 production in the region where oxygen binds weaker than 0.5 eV, but the

production rate is much slower compared to the rates of CO and H_2 production. Our results suggest that MSR is insensitive reaction steps requiring surface COOH*, O*, and OH* species. Xu *et al.* investigated MSR under the same reaction conditions and reported similar activity trends for CO and H_2 production[256]. One thing we noted is that step 9 (oxygen coupling reaction) and step 12 (CO_2 formation) were not included in their model.

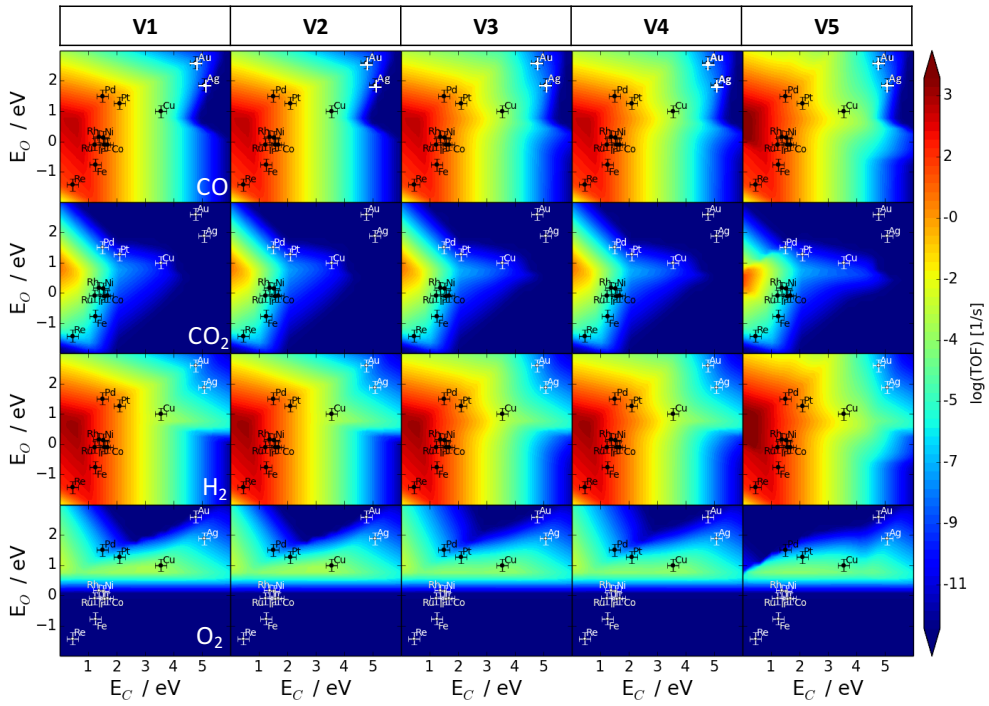

Figure 6-6. Calculated logarithmic turnover frequency (TOF) for methane steam reforming (MSR) toward CO, CO_2, H_2, and O_2. Reaction conditions are T = 773 K and p = 1.0 bar with CH_4/H_2O = 1.

To explain the ineffectiveness of surface COOH*, O*, and OH* on MSR, we turn our attention to θ_O and θ_{OH}. Unlike the oxygen coverage θ_O shown in Figure 6-4, Figure 6-7 shows complete oxygen coverage for metal surfaces with E_O < 0.5 eV. No significant surface coverage of OH* was predicted throughout the volcano, which is explained by fast consumption of OH* to O* and H* via step 5.

Three C-H activation steps in CH_4 (step 1, step 17, and step 23) are compared in Figure 6-8. When E_c < 1.0 eV, the highest rate for C-H dissociation in CH_4 is predicted for step 1 consistent with our results shown in Figure 6-5. In that region, the predicted rates for step 17 [Figure 6-8(b)]

and step 23 [Figure 6-8(c)] are much slower than the rate of step 1. Even on Pd, the rate of step 17 in (b) is approximately 4 orders of magnitude slower than rate of step 1.

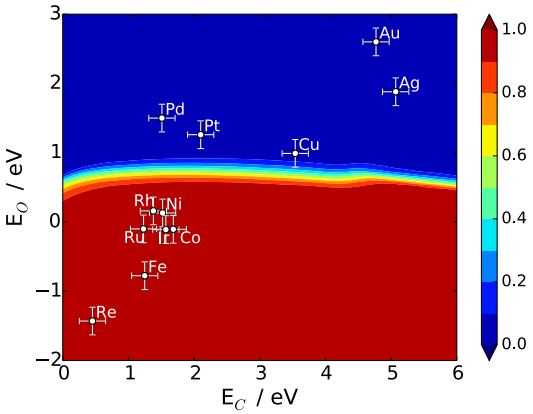

Figure 6-7. Stead-state coverages of O* as a function of E_C and E_O, obtained after MSR with the V5 (M1+M2+M3+M4). Both oxygen and hydroxyl bind to the top of step sites of (211) surfaces.

It is mainly because the predicted oxygen coverage is very low on Pd as observed in Figure 6-7, indicating that step 17 is limited by the availability of O* even though its energy barrier is lower than the energy barrier of step 1. Therefore, based on the results shown in Figure 6-6 and Figure 6-7 we conclude that surface O* and OH* do not play a crucial role in the prediction of catalytic activity of MSR, because surface O* is no longer available on the weak oxygen binding metals like Pd, Pt, Au, and Ag.

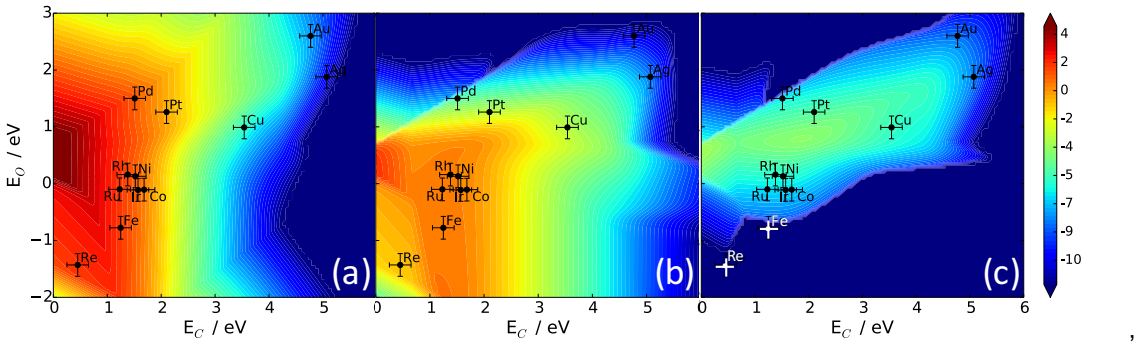

Figure 6-8. Three different pathways for C-H dissociation of methane during the methane steam reforming process (MSR): (a) step 1, $CH_{4(g)} + 2^* \leftrightarrow CH_3^* + H^*$, (b) step 17, $CH_{4(g)} + O^* + * \leftrightarrow CH_3^* + HO^*$, and (c) step 23, $CH_{4(g)} + OH^* + * \leftrightarrow CH_3^* + H_2O_{(g)}$. Conclusions

A descriptor-based microkinetic model consisting of a total of 11 surface intermediates and 28 elementary steps was studied to elucidate the effects surface intermediates (COOH, O, OH) on

partial oxidation of methane, complete oxidation of methane, methane steam reforming, and methane dry reforming. Two descriptor values, the binding energies of carbon and oxygen on (211) stepped surfaces, are sufficient to linearly scale the 28 transition state energies and 11 binding energies. We calculated the energy barrier for oxidative methane activation (8 steps: CH_x + O*/OH* → CH_{x-1} + OH*/H_2O, x =1 ~ 4) on Pd, Ni, and Au, and combined them with the data collected from CatApp. Hence, the sensitivity to inconsistencies caused by this data mixing, was initially investigated by comparing our model with well studied H_2 and CO oxidation. We obtained almost identical trends in catalytic activity and product selectivity for H_2 and CO oxidation, which confirms the robustness of our model. A simple screening test has been adopted to check if surface COOH*, O*, OH* truly play an important role in methane oxidation. It turns out that only surface O* and OH* can alter the overall trends and product distribution. After this screening, we ran a complete microkinetic model for methane oxidation and reforming processes. As predicted by the screening test, we observed that surface O* plays an important role in methane oxidation over the relatively weak oxygen binding metals such as Pd, Pt, Au, and Ag. It is mainly attributed to the decreased energy barrier of C-H dissociation in the presence of surface O*, further leading to the increase in the rate of CO and CO_2. However, we could not find any significant effects of COOH* and OH* on any methane activation processes we studied, because these steps are limited by the availability of the required surface species.

Chapter 7. Summary and Future Works

In this dissertation, I studied acetaldehyde, phenol, and m-cresol hydrodeoxygenation (HDO) over Ru/TiO_2 catalyst using density functional theory (DFT). Particularly, my focus was on finding an active site and reaction mechanisms over Ru(0001), TiO_2(110), $RuTiO_2$(110), RuO_2/TiO_2(110), RuO_2(110), and Ru_{10}/TiO_2(110).

Information on the atomistic scale surface termination of rutile surfaces including MO_2(110) with M = Ru, Ti, Ir, Rh, Sn, Pt, Pd, V, and a mixed binary RuO_2/TiO_2, was obtained through the investigation of surface phase diagrams. Energetic parameters necessary for the prediction of a surface phase diagram were calculated by using linear scaling relationships with a single descriptor value, ΔE_v: $O^{br} + H_2 \leftrightarrow H_2O + V_o$. Thus, this descriptor reduces greatly the amount of DFT calculations necessary to develop a full phase diagram. The most stable surface termination of rutile surfaces under typical HDO conditions is predicted to be a fully hydroxylated surface at bridging oxygen atoms. We also derived a kinetic phase diagram using kinetic Monte Carlo (kMC) simulations and compared it with the phase diagram derived from scaled binding energies. Both phase diagrams predicted similar phase behavior, indicating that our linear relations have sufficient accuracy for the prediction of dominant surface terminations. Notably, the linear scaling relations can be extended to treat mixed oxides, as we have demonstrated for the RuO_2/TiO_2(110) surface.

The HDO mechanism on metallic Ru(0001) led to undesired coke and saturated aromatic formations. C-C bond scission in acetaldehyde is preferentially catalyzed over C-O bond scission, leading to surface carbon or methane formation. In the case for phenolic compounds such as phenol and m-cresol, hydrogenation (HYD) is preferred rather than direct C-O scission, converting them to saturated aromatic compounds.

On the metal oxide surfaces, TiO_2(110), $RuTiO_2$(110), RuO_2/TiO_2(110), and RuO_2(110), vacancies not only play an important role for acetaldehyde adsorption, but also are beneficial for the preferential activation of C-O scission over C-C scission, leading to the desired product ethylene. Ethanol is predicted as a primary by-product due to the fact that ethanol formation is

thermodynamically preferable over ethylene formation. Moreover, it is also found that the rates between vacancy formation and C-O scission should be balanced with each other. Namely, if surface reduction was too facile, metal oxides would be completely reduced; however, if surface reduction was kinetically hindered, the rate for C-O scission would be slow due to the limitation of available sites. For instance, RuO_2(110) has the lowest energy barrier for vacancy formation, but the highest barrier for C-O scission, indicating that this surface is subject to facing a severe phase transition during HDO reaction. Relatively, high DDO selectivity is shown on TiO_2(110), but the formation of hydroxyls, the precursor to form a vacancy site, is kinetically limited, because of the difficulty of H_2 activation. These results clearly suggest that TiO_2 needs a site for H_2 activation, which facilitates the formation of hydroxyls and oxygen vacancies.

The site to activate H_2 molecules can be provided by a Ru metal cluster supported on TiO_2(110) [Ru_{10}/TiO_2]. Hydrogen activation occurs through heterolytic H_2 dissociation across the Ru/TiO_2 interface with a barrier of 0.4 eV, which is much lower than the calculated barrier on TiO_2(110). One proton from the Ru cluster transfers to the nearby bridging hydroxyl (HO^{br}) of TiO_2, forming H_2O^{br} at the Ru/TiO_2 interface. This formed water has Brønsted acid character, which prompts a proton-assisted direct C-O scission in phenolics, preferentially leading to DDO mechanism. This DDO mechanism is proven by isotopic labeling experiments showing that only a single hydrogen is transferred to the product benzene during phenol HDO. The calculated barriers for this proton-assisted direct C-O scission in phenol and m-cresol are E_a = 0.42 eV and and E_a = 0.30 eV, respectively. These energy barriers are lower than energy barriers on Ru(0001) and TiO_2(110), indicating that the Ru/TiO_2 is the most active site for phenolic HDO reactions. Experimentally, we also found that the rate of m-cresol conversion to toluene is linearly proportional to the perimeter of Ru cluster, but not to the surface area of Ru cluster, which is in good agreement with our DFT calculations.

This new mechanism, proton-assisted C-O scission does not require any vacancy formation steps, but is related to acid/base chemistry derived by the amphoteric character of TiO_2, which can act as both an acid (proton donator) and a base (proton acceptor). This result suggests that the support Brønsted acidity plays an important role for selective C-O scission during HDO

mechanism. By tuning this support acidity, we expect to design more efficient and less expensive HDO catalysts for bio-oil upgrading, i.e., if the support had a higher proton affinity (lower acidity), the dehydroxylation step would require a higher activation energy; however, on the other hand, if the support was more acidic (lower proton affinity), the surface protonation would be more difficult.

Previously, experimental data showed that the conversion of species containing two oxygen atoms like catechol and guaiacol occurs at the TiO_2 defect sites and is much faster than the subsequent conversion of monooxygenated phenolics such as cresol to aromatic hydrocarbons. However, it has not been fully understood whether this new mechanism is applicable for the other pyrolyzed oxygenated molecules such as furans, aldehydes, acids, etc., or if it is only applicable for alcohols. It is essential for novel HDO catalysts to activate the different oxygenated functional, because bio-oil contains more than ca. 300 ~ 400 different molecules.

In conclusion, future efforts should be put on tuning support acidity to find the optimal balance between proton acceptance and donation. These efforts should be accompanied with a screening for different oxygenated molecules over different metal/support catalysts.

Bibliography

[1] Mortensen, P. M.; Grunwaldt, J.-D.; Jensen, P. A.; Knudsen, K. G.; Jensen, A. D. A Review Of Catalytic Upgrading Of Bio-oil To Engine Fuels. *Applied Catalysis A: General* **2011**, *407* (1-2), 1–19.

[2] Saidur, R.; Abdelaziz, E.; Demirbas, A.; Hossain, M. S.; Mekhilef, S. A Review On Biomass As A Fuel For Boilers. *Renewable and Sustainable Energy Reviews* **2011**, *15* (5), 2262–2289.

[3] Huber, G. W.; Iborra, S.; Corma, A. Synthesis Of Transportation Fuels From Biomass: Chemistry, Catalysts, And Engineering. *Chemical reviews* **2006**, *106* (9), 4044–4098.

[4] Christian Enger, B.; Lødeng, R.; Holmen, A. A Review Of Catalytic Partial Oxidation Of Methane To Synthesis Gas With Emphasis On Reaction Mechanisms Over Transition Metal Catalysts. *Applied Catalysis A: General* **2008**, *346*, 1–27.

[5] Choudhary, T. V.; Phillips, C. B. Renewable Fuels Via Catalytic Hydrodeoxygenation. *Applied Catalysis A: General* **2011**, *397* (1-2), 1–12.

[6] Jones, S. B.; Valkenburg, C.; Walton, C. W.; Elliott, D. C.; Holladay, J. E.; Stevens, D. J.; C.Kinchin; Czernik, S. Production Of Gasoline And Diesel From Biomass Via Fast Pyrolysis, Hydrotreating, And Hydrocracking: A Design Case. **2009**, PNNL – 18284.

[7] Hoang, T. Q.; Zhu, X.; Danuthai, T.; Lobban, L. L.; Resasco, D. E.; Mallinson, R. G. Conversion Of Glycerol To Alkyl-aromatics Over Zeolites. *Energy & Fuels* **2010**, *24* (7), 3804–3809.

[8] Şenol, O.; Viljava, T.-R.; Krause, A. Hydrodeoxygenation Of Aliphatic Esters On Sulphided NiMo/γ-Al2O3 And CoMo/γ-Al2O3 Catalyst: The Effect Of Water. *Catalysis Today* **2005**, *106* (1-4), 186–189.

[9] Dupont, C.; Lemeur, R.; Daudin, A.; Raybaud, P. Hydrodeoxygenation Pathways Catalyzed By MoS2 And NiMoS Active Phases: A DFT Study. *Journal of Catalysis* **2011**, *279* (2), 276–286.

[10] Badawi, M.; Paul, J.-F.; Cristol, S.; Payen, E. Guaiacol Derivatives And Inhibiting Species Adsorption Over MoS2 And CoMoS Catalysts Under HDO Conditions: A DFT Study. *Catalysis Communications* **2011**, *12* (10), 901–905.

[11] Adjaye, J. D.; Katikaneni, S. P. R.; Bakhshi, N. N. Catalytic Conversion Of A Biofuel To Hydrocarbons: Effect Of Mixtures Of HZSM-5 And Silica-alumina Catalysts On Product Distribution. *Fuel Processing Technology* **1996**, *48* (2), 115–143.

[12] Katikaneni, S.; Adjaye, J.; Bakhshi, N. Performance Of Aluminophosphate Molecular Sieve Catalysts For The Production Of Hydrocarbons From Wood-derived And Vegetable Oils. *Energy & fuels* **1995**, N. 7, 1065–1078.

[13] Mohan, D.; Pittman, C. U.; Steele, P. H. Pyrolysis Of Wood/Biomass For Bio-oil: A Critical Review. *Energy & Fuels* **2006**, *20* (3), 848–889.

[14] Bridgwater, A. V. Review Of Fast Pyrolysis Of Biomass And Product Upgrading. *Biomass and Bioenergy* **2012**, *38*, 68–94.

[15] Chiu, C.; Genest, A.; Borgna, A.; Ro, N. Hydrodeoxygenation Of Guaiacol Over Ru (0001): A DFT Study. *ACS Catalysis* **2014**, *4* (0001), 4178–4188.

[16] Resasco, D. E. What Should We Demand From The Catalysts Responsible For Upgrading Biomass Pyrolysis Oil? *The Journal of Physical Chemistry Letters* **2011**, *2* (18), 2294–2295.

[17] Gangadharan, A.; Shen, M.; Sooknoi, T.; Resasco, D. E.; Mallinson, R. G. Condensation

Reactions Of Propanal Over CexZr1−xO2 Mixed Oxide Catalysts. *Applied Catalysis A: General* **2010**, *385* (1-2), 80–91.

[18] French, R. J.; Stunkel, J.; Baldwin, R. M. Mild Hydrotreating Of Bio-oil: Effect Of Reaction Severity And Fate Of Oxygenated Species. *Energy and Fuels* **2011**, *25*, 3266–3274.

[19] Venderbosch, R. H.; Ardiyanti, A. R.; Wildschut, J.; Oasmaa, A.; Heeres, H. J. Stabilization Of Biomass-derived Pyrolysis Oils. *Journal of Chemical Technology & Biotechnology* **2010**, *85* (5), 674–686.

[20] Wang, H.; Male, J.; Wang, Y. Recent Advances In Hydrotreating Of Pyrolysis Bio-Oil And Its Oxygen-Containing Model Compounds. *ACS Catalysis* **2013**, *3* (5), 1047–1070.

[21] Popa, C.; Offermans, W. K.; van Santen, R. A.; Jansen, A. P. J. Ab Initio Density-functional Theory Study Of NHx Dehydrogenation And Reverse Reactions On The Rh(111) Surface. *Physical Review B* **2006**, *74* (15), 1–10.

[22] Honkala, K.; Hellman, A.; Remediakis, I. N.; Logadottir, A.; Carlsson, A.; Dahl, S.; Christensen, C. H.; Nørskov, J. K. Ammonia Synthesis From First-principles Calculations. *Science* **2005**, *307* (5709), 555–558.

[23] Grabow, L. C.; Mavrikakis, M. Mechanism Of Methanol Synthesis On Cu Through CO2 And CO Hydrogenation. *ACS Catalysis* **2011**, *1* (4), 365–384.

[24] Lu, J.; Behtash, S.; Heyden, A. Theoretical Investigation Of The Reaction Mechanism Of The Decarboxylation And Decarbonylation Of Propanoic Acid On Pd (111) Model Surfaces. *The Journal of Physical Chemistry C* **2012**, *116* (27), 14328–14341.

[25] Vorotnikov, V.; Mpourmpakis, G.; Vlachos, D. G. DFT Study Of Furfural Conversion To Furan, Furfuryl Alcohol, And 2-Methylfuran On Pd(111). *ACS Catalysis* **2012**, *2* (12), 2496–2504.

[26] Chiu, C.; Genest, A.; Borgna, A.; Rösch, N. C–O Cleavage Of Aromatic Oxygenates Over Ruthenium Catalysts. A Computational Study Of Reactions At Step Sites. *Phys. Chem. Chem. Phys.* **2015**, *17* (23), 15324–15330.

[27] de Brimont, M. R.; Dupont, C.; Daudin, A.; Geantet, C.; Raybaud, P. Deoxygenation Mechanisms On Ni-promoted MoS2 Bulk Catalysts: A Combined Experimental And Theoretical Study. *Journal of Catalysis* **2012**, *286*, 153–164.

[28] Guo, N.; Caratzoulas, S.; Doren, D. J.; Sandler, S. I.; Vlachos, D. G. A Perspective On The Modeling Of Biomass Processing. *Energy & Environmental Science* **2012**, *5* (5), 6703.

[29] Mei, D.; Karim, A. M.; Wang, Y. Density Functional Theory Study Of Acetaldehyde Hydrodeoxygenation On MoO 3. *The Journal of Physical Chemistry C* **2011**, *115*, 8155–8164.

[30] Ren, H.; Yu, W.; Salciccioli, M.; Chen, Y.; Huang, Y.; Xiong, K.; Vlachos, D. G.; Chen, J. G. Selective Hydrodeoxygenation Of Biomass-derived Oxygenates To Unsaturated Hydrocarbons Using Molybdenum Carbide Catalysts. *ChemSusChem* **2013**, *6* (5), 798–801.

[31] Nelson, R. C.; Baek, B.; Ruiz, P.; Goundie, B.; Brooks, A.; Wheeler, M. C.; Frederick, B. G.; Grabow, L. C.; Austin, R. N. Experimental And Theoretical Insights Into The Hydrogen-Efficient Direct Hydrodeoxygenation Mechanism Of Phenol Over Ru/TiO2. *ACS Catalysis* **2015**, *5*, 6509–6523.

[32] Hong, Y.; Zhang, H.; Sun, J.; Ayman, K. M.; Hensley, A. J. R.; Gu, M.; Engelhard, M. H.; McEwen, J.-S.; Wang, Y. Synergistic Catalysis Between Pd And Fe In Gas Phase Hydrodeoxygenation Of M -Cresol. *ACS Catalysis* **2014**, *4* (10), 3335–3345.

[33] Moses, P. G.; Hinnemann, B.; Topsøe, H.; Nørskov, J. K. The Effect Of Co-promotion On MoS2 Catalysts For Hydrodesulfurization Of Thiophene: A Density Functional Study. *Journal of Catalysis* **2009**, *268* (2), 201–208.

[34] SCOPUS www.scopus.com.

[35] Hafner, J. Ab-Initio Simulations Of Materials Using VASP: Density-functional Theory And Beyond. *Journal of computational chemistry* **2008**, *29*, 2044–2078.

[36] Sholl, D. S.; Steckel, J. A. *Density functional theory: a practical introduction*, 1° ed.; JohnWiley & Sons, Inc.: Hoboken, New Jersey, 2009.

[37] Oppenheimer R, B. M. On The Quantum Theory Of Molecules. *Annalen der Physik* **1927**, *84* (20), 457–484.

[38] Wellendorff, J.; Lundgaard, K. T.; Møgelhøj, A.; Petzold, V.; Landis, D. D.; Nørskov, J. K.; Bligaard, T.; Jacobsen, K. W. Density Functionals For Surface Science: Exchange-correlation Model Development With Bayesian Error Estimation. *Physical Review B* **2012**, *85* (23), 235149.

[39] Studt, F.; Abild-Pedersen, F.; Varley, J. B.; Nørskov, J. K. CO And CO2 Hydrogenation To Methanol Calculated Using The BEEF-vdW Functional. *Catalysis Letters* **2012**, *143* (1), 71–73.

[40] Hammer, B.; Hansen, L.; Nørskov, J. Improved Adsorption Energetics Within Density-functional Theory Using Revised Perdew-Burke-Ernzerhof Functionals. *Physical Review B* **1999**, *59* (11), 7413–7421.

[41] Perdew, J. P.; Wang, Y. Pair-distribution Function And Its Coupling-constant Average For The Spin-polarized Electron Gas. *Physical Review B* **1992**, *46* (20), 947–954.

[42] V. E. Henrich; P. A. Cox. *The surface science of metal oxides*; Cambridge University Press, Cam- bridge, 1996.

[43] Lun Pang, C.; Lindsay, R.; Thornton, G. Chemical Reactions On Rutile TiO2(110). *Chemical Society reviews* **2008**, *37* (10), 2328–2353.

[44] Novell-Leruth, G.; Carchini, G.; López, N. On The Properties Of Binary Rutile MO2 Compounds, M = Ir, Ru, Sn, And Ti: A DFT Study. *The Journal of chemical physics* **2013**, *138* (19), 194706.

[45] Over, H.; Muhler, M. Catalytic CO Oxidation Over Ruthenium—bridging The Pressure Gap. *Progress in Surface Science* **2003**, *72* (1-4), 3–17.

[46] Weaver, J. F. Surface Chemistry Of Late Transition Metal Oxides. *Chemical reviews* **2013**, *113* (6), 4164–4215.

[47] Wang, C.; Siao, S.; Jiang, J. Density Functional Theory Study Of NH X (x= 0− 3) And N2 Adsorption On IrO2 (110) Surfaces. *The Journal of Physical Chemistry …* **2010**, *2* (114), 18588–18593.

[48] Liu, Z.-P.; Jenkins, S. J.; King, D. A. Car Exhaust Catalysis From First Principles: Selective NO Reduction Under Excess O2 Conditions On Ir. *Journal of the American Chemical Society* **2004**, *126* (34), 10746–10756.

[49] Ono, S.; Brodholt, J. P.; Price, G. D. Structural Phase Transitions In IrO 2 At High Pressures. *Journal of Physics: Condensed Matter* **2008**, *20* (4), 045202.

[50] Hamad, B. A. First-principle Calculations Of Structural And Electronic Properties Of Rutile-phase Dioxides (MO2), M = Ti, V, Ru, Ir And Sn. *The European Physical Journal B* **2009**, *70* (2), 163–169.

[51] Wang, J.; Fan, C. Y.; Sun, Q.; Reuter, K.; Jacobi, K.; Scheffler, M.; Ertl, G. Surface Coordination Chemistry: Dihydrogen Versus Hydride Complexes On RuO2(110). *Angewandte Chemie* **2003**, *42* (19), 2151–2154.

[52] Xia, Y.; Ye, J.; Murray, P.; Ali, A.; Ge, Q.; Zhang, Z. Imaging Reactions Of Acetone With Oxygen Adatoms On Partially Oxidized TiO2(110). *Phys. Chem. Chem. Phys.* **2013**, *15* (33), 13897–13901.

[53] Houtman, C. J.; Barteau, M. A. Divergent Pathways Of Acetaldehyde And Ethanol Decarbonylation On The Rh(111) Surface. *Journal of Catalysis* **1991**, *130* (2), 528–546.

[54] Hammer, B.; Wendt, S.; Besenbacher, F. Water Adsorption On TiO2. *Topics in Catalysis* **2010**, *53* (5-6), 423–430.

[55] Madey, T. E.; Engelhardt, A.; Menzel, D. Adsorption Of Oxygen And Oxidation Of CO On The Ruthenium(001) Surface. *Surface Science* **1975**, *48*, 304–328.

[56] Dinter, N.; Rusanen, M.; Raybaud, P.; Kasztelan, S.; Silva, P. Da; Toulhoat, H. Temperature-programmed Reduction Of Unpromoted MoS2-based Hydrodesulfurization Catalysts: First-principles Kinetic Monte Carlo Simulations And Comparison With Experiments. *Journal of Catalysis* **2010**, *275* (1), 117–128.

[57] Bollinger, M.; Jacobsen, K.; Nørskov, J. Atomic And Electronic Structure Of MoS2 Nanoparticles. *Physical Review B* **2003**, *67* (8), 085410.

[58] Getman, R. B.; Schneider, W. F.; Smeltz, A. D.; Delgass, W. N.; Ribeiro, F. H. Oxygen-Coverage Effects On Molecular Dissociations At A Pt Metal Surface. *Physical Review Letters* **2009**, *102* (7), 4.

[59] Reuter, K.; Scheffler, M. Oxide Formation At The Surface Of Late 4d Transition Metals: Insights From First-principles Atomistic Thermodynamics. *Applied Physics A: Materials*

Science & Processing **2004**, *78* (6), 793–798.

[60] Stamatakis, M.; Vlachos, D. G. Unraveling The Complexity Of Catalytic Reactions Via Kinetic Monte Carlo Simulation: Current Status And Frontiers. *ACS Catalysis* **2012**, *2* (12), 2648–2663.

[61] Wu, C.; Schmidt, D. J.; Wolverton, C.; Schneider, W. F. Accurate Coverage-dependence Incorporated Into First-principles Kinetic Models: Catalytic NO Oxidation On Pt (111). *Journal of Catalysis* **2012**, *286*, 88–94.

[62] Stamatakis, M.; Chen, Y.; Vlachos, D. G. First-Principles-Based Kinetic Monte Carlo Simulation Of The Structure Sensitivity Of The Water À Gas Shift Reaction On Platinum Surfaces. *The Journal of Physical Chemistry C* **2011**, *115*, 24750–24762.

[63] Bahn, S. R.; Jacobsen, K. W. An Object-oriented Scripting Interface To A Legacy Electronic Structure Code. *Computing in Science & Engineering* **2002**, *4* (3), 56–66.

[64] Kresse, G.; Furthmüller, J. Efficiency Of Ab-initio Total Energy Calculations For Metals And Semiconductors Using A Plane-wave Basis Set. *COMPUTATIONAL MATERIALS SCIENCE* **1996**, *6*, 15–50.

[65] Kresse, G.; Hafner, J. Ab Initio Molecular-dynamics Simulation Of The Liquid-metal-amorphous-semiconductor Transition In Germanium. *Physical Review B* **1994**, *49* (20), 251–269.

[66] Fernández, E. M.; Moses, P. G.; Toftelund, A.; Hansen, H. A.; Martínez, J. I.; Abild-Pedersen, F.; Kleis, J.; Hinnemann, B.; Rossmeisl, J.; Bligaard, T.; Nørskov, J. K. Scaling Relationships For Adsorption Energies On Transition Metal Oxide, Sulfide, And Nitride Surfaces. *Angewandte Chemie* **2008**, *47* (25), 4683–4686.

[67] Monkhorst, H. J.; Pack, J. D. Special Points For Brillouin-zone Integrations. *Physical*

Review B **1976**, *13* (12), 5188–5192.

[68] Mellan, T. a; Grau-Crespo, R. Density Functional Theory Study Of Rutile VO2 Surfaces. *The Journal of chemical physics* **2012**, *137* (15), 154706.

[69] Bolzan, A. A.; Fong, C.; Kennedy, B. J.; Howard, C. J. Structural Studies Of Rutile-Type Metal Dioxides. *Acta Crystallographica Section B Structural Science* **1997**, *53* (3), 373–380.

[70] Bengtsson, L. Dipole Correction For Surface Supercell Calculations. *Physical Review B* **1999**, *59* (19), 12301–12304.

[71] Stevens, E. D.; Rys, J.; Coppens, P. Quantitative Comparison Of Theoretical Calculations With The Experimentally Determined Electron Density Distribution Of Formamide. *J Am Chem Soc* **1978**, *100*, 2324–2328.

[72] Sheppard, D.; Terrell, R.; Henkelman, G. Optimization Methods For Finding Minimum Energy Paths. *The Journal of chemical physics* **2008**, *128* (13), 134106.

[73] WebBook, N. C. NIST Chemistry WebBook http://webbook.nist.gov/cgi/fluid.cgi?T=600&PLow=0&PHigh=300&PInc=100&Digits=5&ID=C1333740&Action=Load&Type=IsoTherm&TUnit=K&PUnit=MPa&DUnit=mol%2Fl&HUnit=kJ%2Fmol&WUnit=m%2Fs&VisUnit=uPa*s&STUnit=N%2Fm&RefState=DEF.

[74] NIST Chemistry WebBook http://webbook.nist.gov/cgi/fluid.cgi?T=600&PLow=0&PHigh=400&PInc=50&Digits=5&ID=C7732185&Action=Load&Type=IsoTherm&TUnit=K&PUnit=MPa&DUnit=mol%2Fl&HUnit=kJ%2Fmol&WUnit=m%2Fs&VisUnit=uPa*s&STUnit=N%2Fm&RefState=DEF (accessed gen 1, 2012).

[75] Temel, B.; Meskine, H.; Reuter, K.; Scheffler, M.; Metiu, H. Does Phenomenological

Kinetics Provide An Adequate Description Of Heterogeneous Catalytic Reactions? *The Journal of chemical physics* **2007**, *126* (20), 204711.

[76] Xu, L.; Henkelman, G. Adaptive Kinetic Monte Carlo For First-principles Accelerated Dynamics. *The Journal of chemical physics* **2008**, *129* (11), 114104.

[77] Reuter, K.; Scheffler, M. First-principles Kinetic Monte Carlo Simulations For Heterogeneous Catalysis: Application To The CO Oxidation At RuO2(110). *Physical Review B* **2006**, *73* (4), 045433.

[78] Hoffmann, M. J.; Matera, S.; Reuter, K. Kmos : A Lattice Kinetic Monte Carlo Framework. **2014**.

[79] Over, H.; Muhler, M.; Seitsonen, A. P. Comment On «CO Oxidation On Ruthenium: The Nature Of The Active Catalytic Surface» By D.W. Goodman, C.H.F. Peden, M.S. Chen. *Surface Science* **2007**, *601* (23), 5659–5662.

[80] Lobo, A.; Conrad, H. Interaction Of H2O With The RuO2(110) Surface Studied By HREELS And TDS. *Surface Science* **2003**, *523*, 279–286.

[81] Knapp, M.; Crihan, D.; Seitsonen, A. P.; Over, H. Hydrogen Transfer Reaction On The Surface Of An Oxide Catalyst. *Journal of the American Chemical Society* **2005**, *127* (10), 3236–3237.

[82] Ugur, D.; Storm, A.; Verberk, R. Kinetics Of Reduction Of A RuO2 (110) Film On Ru (0001) By H2. *The Journal of Physical Chemistry C* **2012**, *116* (110), 26822–26828.

[83] Reuter, K.; Scheffler, M. Composition And Structure Of The RuO2(110) Surface In An O2 And CO Environment: Implications For The Catalytic Formation Of CO2. *Physical Review B* **2003**, *68* (4), 045407.

[84] Fernandez, E. M.; Moses, P. G.; Toftelund, A.; Hansen, H. A.; Martinez, J. I.; Abild-Pedersen, F.; Kleis, J.; Hinnemann, B.; Rossmeisl, J.; Bligaard, T.; Nørskov, J. K. Scaling Relationships For Adsorption Energies On Transition Metal Oxide, Sulfide, And Nitride Surfaces. *Angewandte Chemie-International Edition* **2008**, *47* (25), 4683–4686.

[85] Todorova, M.; Reuter, K.; Scheffler, M. Oxygen Overlayers On Pd(111) Studied By Density Functional Theory †. *The Journal of Physical Chemistry B* **2004**, *108* (38), 14477–14483.

[86] Inderwildi, O. R.; Lebiedz, D.; Deutschmann, O.; Warnatz, J. Coverage Dependence Of Oxygen Decomposition And Surface Diffusion On Rhodium 111: A DFT Study. *The Journal of chemical physics* **2005**, *122* (3), 34710.

[87] Miller, S. D.; Kitchin, J. R. Relating The Coverage Dependence Of Oxygen Adsorption On Au And Pt Fcc(111) Surfaces Through Adsorbate-induced Surface Electronic Structure Effects. *Surface Science* **2009**, *603* (5), 794–801.

[88] Martinez, J. I.; Hansen, H. A.; Rossmeisl, J.; Nørskov, J. K. Formation Energies Of Rutile Metal Dioxides Using Density Functional Theory. *Physical Review B* **2009**, *79* (4), 5.

[89] Nomiyama, R. K.; Piotrowski, M. J.; Silva, J. L. F. Da. Bulk Structures Of PtO And PtO2 From Density Functional Calculations. *Physical Review B* **2011**, *84* (10), 1–3.

[90] Suntivich, J.; Gasteiger, H.; Yabuuchi, N. Design Principles For Oxygen-reduction Activity On Perovskite Oxide Catalysts For Fuel Cells And Metal – Air Batteries. *Nature Chemistry* **2011**, *3* (July), 546–551.

[91] Calle-Vallejo, F.; Inoglu, N. G.; Su, H.-Y.; Martínez, J. I.; Man, I. C.; Koper, M. T. M.; Kitchin, J. R.; Rossmeisl, J. Number Of Outer Electrons As Descriptor For Adsorption Processes On Transition Metals And Their Oxides. *Chemical Science* **2013**, *4* (3), 1245.

[92] Lee, Y.-L.; Kleis, J.; Rossmeisl, J.; Shao-Horn, Y.; Morgan, D. Prediction Of Solid Oxide Fuel Cell Cathode Activity With First-principles Descriptors. *Energy & Environmental Science* **2011**, *4* (10), 3966.

[93] Grabow, L. C.; Hvolbæk, B.; Nørskov, J. K. Understanding Trends In Catalytic Activity: The Effect Of Adsorbate-Adsorbate Interactions For CO Oxidation Over Transition Metals. *Topics in Catalysis* **2009**, *53* (5-6), 298–310.

[94] Lausche, A. C.; Medford, A. J.; Khan, T. S.; Xu, Y.; Bligaard, T.; Abild-Pedersen, F.; Nørskov, J. K.; Studt, F. On The Effect Of Coverage-dependent Adsorbate–adsorbate Interactions For CO Methanation On Transition Metal Surfaces. *Journal of Catalysis* **2013**, *307*, 275–282.

[95] Sun, Q.; Reuter, K.; Scheffler, M. Hydrogen Adsorption On RuO2(110): Density-functional Calculations. *Physical Review B* **2004**, *70* (23), 1–12.

[96] Jacobi, K.; Wang, Y.; Ertl, G. Interaction Of Hydrogen With RuO2(110) Surfaces: Activity Differences Between Various Oxygen Species. *The Journal of Physical Chemistry. B* **2006**, *110* (12), 6115–6122.

[97] Fan, C. Y.; Wang, J.; Jacobi, K.; Ertl, G. The Oxidation Of CO On RuO2(110) At Room Temperature. *The Journal of Chemical Physics* **2001**, *114* (22), 10058–10062.

[98] Rogal, J.; Reuter, K.; Scheffler, M. CO Oxidation On Pd(100) At Technologically Relevant Pressure Conditions: First-principles Kinetic Monte Carlo Study. *Physical Review B* **2008**, *77* (15), 155410.

[99] Nie, L.; de Souza, P. M.; Noronha, F. B.; An, W.; Sooknoi, T.; Resasco, D. E. Selective Conversion Of M-cresol To Toluene Over Bimetallic Ni–Fe Catalysts. *Journal of Molecular Catalysis A: Chemical* **2014**, *388-389*, 47–55.

[100] Wan, H.; Chaudhari, R. V; Subramaniam, B. Aqueous Phase Hydrogenation Of Acetic Acid And Its Promotional E Ff Ect On P‐Cresol Hydrodeoxygenation. *Energy & Fuels* **2013**, *27*, 487–493.

[101] Newman, C.; Zhou, X.; Goundie, B.; Ghampson, I. T.; Pollock, R. A.; Ross, Z.; Wheeler, M. C.; Meulenberg, R. W.; Austin, R. N.; Frederick, B. G. Effects Of Support Identity And Metal Dispersion In Supported Ruthenium Hydrodeoxygenation Catalysts. *Applied Catalysis A: General* **2014**, *477*, 64–74.

[102] Christiansen, M.; Mpourmpakis, G.; Vlachos, D. Density Functional Theory-Computed Mechanisms Of Ethylene And Diethyl Ether Formation From Ethanol On Γ-Al2O3 (100). *ACS Catalysis* **2013**, *3* (100).

[103] Kresse, G.; Hafner, J. Ab Initio Molecular Dynamics For Liquid Metals. *Physical Review B* **1993**, *47* (1), 558–561.

[104] Kresse, G.; Furthmüller, J. Efficient Iterative Schemes For Ab Initio Total-energy Calculations Using A Plane-wave Basis Set. *Physical review. B, Condensed matter* **1996**, *54* (16), 11169–11186.

[105] Perdew, J. P.; Burke, K.; Ernzerhof, M. Generalized Gradient Approximation Made Simple. *Physical Review Letters* **1996**, *77* (18), 3865–3868.

[106] Blöchl, P. Projector Augmented-wave Method. *Physical Review B* **1994**, *50* (24), 953–979.

[107] Chueh, B. Y.-L.; Hsieh, C.-H.; Chang, M.-T.; Chou, L.-J.; Lao, C. S.; Song, J. H.; Gan, J.-Y.; Wang, Z. L. RuO2 Nanowires And RuO2/TiO2 Core/Shell Nanowires: From Synthesis To Mechanical, Optical, Electrical, And Photoconductive Properties. *Advanced Materials* **2007**, *19* (1), 143–149.

[108] Pan, Y.; Zhang, H.; Shi, D.; Sun, J.; Du, S.; Liu, F.; Gao, H. Highly Ordered, Millimeter-

Scale, Continuous, Single-Crystalline Graphene Monolayer Formed On Ru (0001). *Advanced Materials* **2009**, *21* (27), 2777–2780.

[109] Chrétien, S.; Metiu, H. Density Functional Study Of The CO Oxidation On A Doped Rutile TiO2(110): Effect Of Ionic Au In Catalysis. *Catalysis Letters* **2006**, *107* (3-4), 143–147.

[110] del Rosal, I.; Truflandier, L.; Poteau, R.; Gerber, I. C. A Density Functional Theory Study Of Spectroscopic And Thermodynamic Properties Of Surfacic Hydrides On Ru (0001) Model Surface: The Influence Of The Coordination Modes And The Coverage. *The Journal of Physical Chemistry C* **2011**, *115* (5), 2169–2178.

[111] Lutfalla, S.; Shapovalov, V.; Bell, A. T. Calibration Of The DFT/GGA+U Method For Determination Of Reduction Energies For Transition And Rare Earth Metal Oxides Of Ti, V, Mo, And Ce. *Journal of Chemical Theory and Computation* **2011**, *7* (7), 2218–2223.

[112] Dudarev, S.; Botton, G. Electron-energy-loss Spectra And The Structural Stability Of Nickel Oxide: An LSDA+ U Study. *Physical Review B* **1998**, *57* (3), 1505–1509.

[113] Ferrari, A. M.; Pisani, C.; Cinquini, F.; Giordano, L.; Pacchioni, G. Cationic And Anionic Vacancies On The NiO(100) Surface: DFT+U And Hybrid Functional Density Functional Theory Calculations. *The Journal of chemical physics* **2007**, *127* (17), 174711.

[114] Hu, Z.; Metiu, H. Choice Of U For DFT+U Calculations For Titanium Oxides. *The Journal of Physical Chemistry C* **2011**, *115*, 5841–5845.

[115] Kim, H.; Lee, H. CO Oxidation By Rutile TiO2 (110) Doped With V, W, Cr, Mo, And Mn. *The Journal of Physical Chemistry C* **2008**, *112* (110), 12398–12408.

[116] Hong, S.; Rahman, T. S. Rationale For The Higher Reactivity Of Interfacial Sites In Methanol Decomposition On Au13/TiO2(110). *Journal of the American Chemical Society* **2013**, *135* (20), 7629–7635.

[117] Hirschl, R. Hydrogenation Of Ethylene And Formaldehyde On Pt (111) And Pt80Fe20 (111): A Density-functional Study. *Journal of Catalysis* **2004**, *226* (2), 273–282.

[118] Delbecq, F.; Vigné, F. Acetaldehyde On Pt(111) And Pt/Sn(111): A DFT Study Of The Adsorption Structures And Of The Vibrational Spectra. *The journal of physical chemistry. B* **2005**, *109* (21), 10797–10806.

[119] Shekhar, R.; Barteau, M. Adsorption And Reaction Of Aldehydes On Pd Surfaces. *The Journal of Physical Chemistry B* **1997**, *101*, 7939–7951.

[120] Panagiotopoulou, P.; Kondarides, D. I.; Verykios, X. E. Mechanistic Study Of The Selective Methanation Of CO Over Ru / TiO 2 Catalyst : Identification Of Active Surface Species And Reaction Pathways. *J. Phys. Chem. C* **2011**, *115*, 1220–1230.

[121] Starr, D. E.; Bluhm, H. Surface Science CO Adsorption And Dissociation On Ru (0001) At Elevated Pressures. *Surface Science* **2013**, *608*, 241–248.

[122] Ciobica, I. M.; Frechard, F.; van Santen, R. A.; Kleyn, A. W.; Hafner, J. A Theoretical Study Of CHx Chemisorption On The Ru(0001) Surface. *Chemical Physics Letters* **1999**, *311* (September), 185–192.

[123] Cheng, J.; Hu, P.; Ellis, P.; French, S.; Kelly, G.; Lok, C. M. An Energy Descriptor To Quantify Methane Selectivity In Fischer−Tropsch Synthesis: A Density Functional Theory Study. *The Journal of Physical Chemistry C* **2009**, *113* (20), 8858–8863.

[124] Geerlings, J. J. C.; Zonnevylle, M. C.; de Groot, C. P. . Studies Of The Fischer-Tropsch On Co (0001). *Surface Science* **1991**, *241* (2), 302–314.

[125] Geerlings, J. J. C.; Zonnevylle, M. C.; de Groot, C. P. M. Studies Of The Fischer-Tropsch Reaction On Co(0001). *Surface Science* **1991**, *241* (3), 302–314.

[126] Nørskov, J.; Rossmeisl, J. Origin Of The Overpotential For Oxygen Reduction At A Fuel-cell Cathode. *The Journal of Physical Chemistry B* **2004**, *108*, 17886–17892.

[127] Pan, M.; Flaherty, D. W.; Mullins, C. B. Low-Temperature Hydrogenation Of Acetaldehyde To Ethanol On H-Precovered Au(111). *The Journal of Physical Chemistry Letters* **2011**, *2* (12), 1363–1367.

[128] Lee, J.; Xu, Y.; Huber, G. W. High-Throughput Screening Of Monometallic Catalysts For Aqueous-Phase Hydrogenation Of Biomass-Derived Oxygenates. *Applied Catalysis B: Environmental* **2013**, *141*, 98–107.

[129] Mortensen, P. M.; Grunwaldt, J.-D.; Jensen, P. A.; Jensen, A. D. Screening Of Catalysts For Hydrodeoxygenation Of Phenol As A Model Compound For Bio-oil. *ACS Catalysis* **2013**, *3* (8), 1774–1785.

[130] Sun, Q.; Reuter, K.; Scheffler, M. Effect Of A Humid Environment On The Surface Structure Of RuO2(110). *Physical Review B* **2003**, *67* (20), 205424.

[131] Mirwald, J. W.; Inderwildi, O. R. Unraveling The Fischer-Tropsch Mechanism: A Combined DFT And Microkinetic Investigation Of C-C Bond Formation On Ru. *Physical chemistry chemical physics : PCCP* **2012**, 7028–7031.

[132] Zhuo, M.; Tan, K. F.; Borgna, A.; Saeys, M. Density Functional Theory Study Of The CO Insertion Mechanism For Fischer−Tropsch Synthesis Over Co Catalysts. *The Journal of Physical Chemistry C* **2009**, *113* (19), 8357–8365.

[133] Panagiotopoulou, P.; Kondarides, D. I.; Verykios, X. E. Mechanistic Study Of The Selective Methanation Of CO Over Ru / TiO 2 Catalyst : Identification Of Active Surface Species And Reaction Pathways †. *J. Phys. Chem. C* **2011**, *115*, 1220–1230.

[134] López, N.; Novell-Leruth, G. Rules For Selectivity In Oxidation Processes On RuO2(110).

Physical chemistry chemical physics : PCCP **2010**, *12* (38), 12217–12222.

[135] Santiago, M.; Kondratenko, V. A.; Kondratenko, E. V.; López, N.; Pérez-Ramírez, J. Mechanistic Analysis Of Direct N2O Decomposition And Reduction With H2 Or NH3 Over RuO2. *Applied Catalysis B: Environmental* **2011**, *110*, 33–39.

[136] Bollinger, M.; Jacobsen, K.; Nørskov, J. Atomic And Electronic Structure Of MoS2 Nanoparticles. *Physical Review B* **2003**, *67* (8), 1–17.

[137] Wendt, S.; Matthiesen, J.; Schaub, R.; Vestergaard, E.; Lægsgaard, E.; Besenbacher, F.; Hammer, B. Formation And Splitting Of Paired Hydroxyl Groups On Reduced TiO2(110). *Physical Review Letters* **2006**, *96* (6), 066107.

[138] Henrich, V. E.; Kurtz, R. L. Surface Electronic Structure Of TiO2: Atomic Geometry, Ligand Coordination, And The Effect Of Adsorbed Hydrogen. *Physical Review B* **1981**, *23* (100), 6280–6287.

[139] Suzuki, S.; Fukui, K.; Onishi, H.; Iwasawa, Y. Hydrogen Adatoms On TiO2(110)-(1x1) Characterized By Scanning Tunneling Microscopy And Electron Stimulated Desorption. *Physical review letters* **2000**, *84* (10), 2156–2159.

[140] Wendt, S.; Matthiesen, J.; Schaub, R.; Vestergaard, E.; Lægsgaard, E.; Besenbacher, F.; Hammer, B. Formation And Splitting Of Paired Hydroxyl Groups On Reduced TiO2(110). *Physical Review Letters* **2006**, *96* (6), 66107.

[141] Wendt, S.; Schaub, R.; Matthiesen, J.; Vestergaard, E. K.; Wahlström, E.; Rasmussen, M. D.; Thostrup, P.; Molina, L. M.; Lægsgaard, E.; Stensgaard, I.; Hammer, B.; Besenbacher, F. Oxygen Vacancies On TiO2(110) And Their Interaction With H2O And O2: A Combined High-resolution STM And DFT Study. *Surface Science* **2005**, *598* (1-3), 226–245.

[142] Mayernick, A.; Janik, M. Methane Activation And Oxygen Vacancy Formation Over CeO2

And Zr, Pd Substituted CeO2 Surfaces. *The Journal of Physical Chemistry C* **2008**, *112*, 14955–14964.

[143] Sundell, P. G.; Björketun, M. E.; Wahnström, G. Thermodynamics Of Doping And Vacancy Formation In BaZrO3 Perovskite Oxide From Density Functional Calculations. *Physical Review B* **2006**, *73* (10), 104112.

[144] Gamble, L.; Jung, L. S.; Campbell, C. T. Decomposition And Protonation Of Surface Ethoxys On TiO2(110). *Surface Science* **1996**, *348*, 1–16.

[145] Knapp, M.; Crihan, D. Complex Interaction Of Hydrogen With The RuO2 (110) Surface. *The Journal of Physical Chemistry C* **2007**, *2* (110), 5363–5373.

[146] Rekoske, J.; Barteau, M. Isothermal Reduction Kinetics Of Titanium Dioxide-based Materials. *The Journal of Physical Chemistry B* **1997**, *101* (96), 1113–1124.

[147] Mars, P.; van Krevelen, D. W. Oxidations Carried Out By Means Of Vanadium Oxide Catalysts. *Chemical Engineering Science* **1954**, *3*, 41–59.

[148] Over, H. Surface Chemistry Of Ruthenium Dioxide In Heterogeneous Catalysis And Electrocatalysis: From Fundamental To Applied Research. *Chemical reviews* **2012**, *112* (6), 3356–3426.

[149] Blyholder, G. Molecular Orbital View Of Chemisorbed Carbon Monoxide. *The Journal of Physical Chemistry* **1964**, *68* (1), 2722–2777.

[150] Yunarti, R. T.; Lee, M.; Hwang, Y. J.; Choi, J.-W.; Suh, D. J.; Lee, J.; Kim, I. W.; Ha, J.-M. Transition Metal-doped TiO2 Nanowire Catalysts For The Oxidative Coupling Of Methane. *Catalysis Communications* **2014**, *50*, 54–58.

[151] Falsig, H.; Hvolbaek, B.; Kristensen, I. S.; Jiang, T.; Bligaard, T.; Christensen, C. H.;

Nørskov, J. K. Trends In The Catalytic CO Oxidation Activity Of Nanoparticles. *Angewandte Chemie* **2008**, *47* (26), 4835–4839.

[152] Fujino, T.; Katayama, M.; Inudzuka, K.; Okuno, T.; Oura, K.; Hirao, T. Surface Hydroxyl Formation On Vacuum-annealed TiO2(110). *App. Phys. Lett.* **2001**, *79* (17), 2716–2718.

[153] Yu, J.; Qi, L.; Jaroniec, M. Hydrogen Production By Photocatalytic Water Splitting Over Pt/TiO2 Nanosheets With Exposed (001) Facets. *J. Phys. Chem. C* **2010**, *114* (001), 13118–13125.

[154] Prins, R. Hydrogen Spillover. Facts And Fiction. *Chemical reviews* **2012**, *112* (5), 2714–2738.

[155] Conner, W. C.; Falconer, J. L. Spillover In Heterogeneous Catalysis. *Chemical Reviews* **1995**, *95* (3), 759–788.

[156] Omotoso, T.; Boonyasuwat, S.; Crossley, S. P. Understanding The Role Of TiO2 Crystal Structure On The Enhanced Activity And Stability Of Ru/TiO2 Catalysts For The Conversion Of Lignin-derived Oxygenates. *Green Chemistry* **2014**, *16* (2), 645–652.

[157] Pham, T. N.; Shi, D.; Sooknoi, T.; Resasco, D. E. Aqueous-phase Ketonization Of Acetic Acid Over Ru/TiO2/carbon Catalysts. *Journal of Catalysis* **2012**, *295*, 169–178.

[158] Boonyasuwat, S.; Omotoso, T.; Resasco, D. E.; Crossley, S. P. Conversion Of Guaiacol Over Supported Ru Catalysts. *Catalysis Letters* **2013**, *143* (8), 783–791.

[159] Ammal, S. C.; Heyden, A. Origin Of The Unique Activity Of Pt/TiO2 Catalysts For The Water–gas Shift Reaction. *Journal of Catalysis* **2013**, *306*, 78–90.

[160] Aranifard, S.; Ammal, S. C.; Heyden, A. Nature Of Ptn/CeO2(111) Surface Under Water–Gas Shift Reaction Conditions: A Constrained Ab Initio Thermodynamics Study. *The*

Journal of Physical Chemistry C **2012**, *116* (16), 9029–9042.

[161] Evans, J.; Park, J.; Liu, P.; Hrbek, J.; Sanz, J. F. High Water - Gas Shift Activity In TiO 2 (110) Supported Cu And Au Nanoparticles : Role Of. *J. Phys. Chem. C* **2009**, *113* (17), 7364–7370.

[162] Baker, L. R.; Kennedy, G.; Van Spronsen, M.; Hervier, A.; Cai, X.; Chen, S.; Wang, L.-W.; Somorjai, G. a. Furfuraldehyde Hydrogenation On Titanium Oxide-supported Platinum Nanoparticles Studied By Sum Frequency Generation Vibrational Spectroscopy: Acid-base Catalysis Explains The Molecular Origin Of Strong Metal-support Interactions. *Journal of the American Chemical Society* **2012**, *134* (34), 14208–14216.

[163] Xi, Y.; Zhang, Q.; Cheng, H. On The Mechanism Of Hydrogen Spillover On WO3 (001) And Formation Of HxWO3 (x= 0.125, 0.25, 0.375 And 0.5). *The Journal of Physical Chemistry C* **2013**, *3* (118), 494–501.

[164] Hensley, A. J. R.; Wang, Y.; Mcewen, J.-S. Phenol Deoxygenation Mechanisms On Fe(110) And Pd(111). *ACS Catalysis* **2014**, *5* (110), 523–536.

[165] Leiva, K.; Sepúlveda, C.; García, R.; Fierro, J. L. G.; Escalona, N. Effect Of Water On The Conversions Of 2-methoxyphenol And Phenol As Bio-oil Model Compounds Over ReS2/SiO2 Catalyst. *Catalysis Communications* **2014**, *53*, 33–37.

[166] Echeandia, S.; Pawelec, B.; Barrio, V. L.; Arias, P. L.; Cambra, J. F.; Loricera, C. V.; Fierro, J. L. G. Enhancement Of Phenol Hydrodeoxygenation Over Pd Catalysts Supported On Mixed HY Zeolite And Al2O3. An Approach To O-removal From Bio-oils. *Fuel* **2014**, *117*, 1061–1073.

[167] Laurent, E.; Delmon, B. Influence Of Oxygen-, Nitrogen-, And Sulfur-containing Compounds On The Hydrodeoxygenation Of Phenols Over Sulfided Cobalt-

molybdenum/.gamma.-alumina And Nickel-molybdenum/.gamma.-alumina Catalysts. *Industrial & Engineering Chemistry Research* **1993**, *32* (11), 2516–2524.

[168] Albahri, T. A.; Riazi, M. R.; Alqattan, A. A. Octane Number And Aniline Point Of Petroleum Fuels. *Division of Fuel Chemistry* **2002**, *47*, 710–711.

[169] Boullosa-Eiras, S.; Lødeng, R.; Bergem, H.; Stöcker, M.; Hannevold, L.; Blekkan, E. a. Catalytic Hydrodeoxygenation (HDO) Of Phenol Over Supported Molybdenum Carbide, Nitride, Phosphide And Oxide Catalysts. *Catalysis Today* **2014**, *223*, 44–53.

[170] Yoon, Y.; Rousseau, R.; Weber, R. S.; Mei, D.; Lercher, J. A. First-Principles Study Of Phenol Hydrogenation On Pt And Ni Catalysts In Aqueous Phase. *Journal of the American Chemical Society* **2014**, 10287–10298.

[171] Moses, P. G.; Grabow, L. C.; Fernandez, E. M.; Hinnemann, B.; Topsøe, H.; Knudsen, K. G.; Nørskov, J. K. Trends In Hydrodesulfurization Catalysis Based On Realistic Surface Models. *Catalysis Letters* **2014**, *144* (8), 1425–1432.

[172] Pucher, H.; Schwaiger, N.; Feiner, R.; Pucher, P.; Ellmaier, L.; Siebenhofer, M. Catalytic Hydrodeoxygenation Of Dehydrated Liquid Phase Pyrolysis Oil. *International Journal of Energy Research* **2014**, *38* (15), 1964–1974.

[173] Gao, D.; Schweitzer, C.; Hwang, H. T.; Varma, A. Conversion Of Guaiacol On Noble Metal Catalysts: Reaction Performance And Deactivation Studies. *Industrial & Engineering Chemistry Research* **2014**, *53* (49), 18658–18667.

[174] Mendes, M. J.; Santos, O. A. A.; Jordão, E.; Silva, A. M. Hydrogenation Of Oleic Acid Over Ruthenium Catalysts. *Applied Catalysis A: General* **2001**, *217* (1-2), 253–262.

[175] Wildschut, J.; Mahfud, F. H.; Venderbosch, R. H.; Heeres, H. J. Hydrotreatment Of Fast Pyrolysis Oil Using Heterogeneous Noble-Metal Catalysts. *Industrial & Engineering*

Chemistry Research **2009**, *48* (23), 10324–10334.

[176] Furimsky, E. Catalytic Hydrodeoxygenation. *Applied Catalysis A: General* **2000**, *199* (2), 147–190.

[177] de Souza, P. M.; Rabelo-Neto, R. C.; Borges, L. E. P.; Jacobs, G.; Davis, B. H.; Sooknoi, T.; Resasco, D. E.; Noronha, F. B. Role Of Keto Intermediates In The Hydrodeoxygenation Of Phenol Over Pd On Oxophilic Supports. *ACS Catalysis* **2015**, *5* (2), 1318–1329.

[178] Hensley, A. J. R.; Wang, Y.; McEwen, J.-S. Adsorption Of Phenol On Fe (110) And Pd (111) From First Principles. *Surface Science* **2014**, *630*, 244–253.

[179] Yoon, Y.; Rousseau, R.; Weber, R. S.; Mei, D.; Lercher, J. a. First-Principles Study Of Phenol Hydrogenation On Pt And Ni Catalysts In Aqueous Phase. *Journal of the American Chemical Society* **2014**.

[180] Zhao, C.; Kou, Y.; Lemonidou, A. A.; Li, X.; Lercher, J. A. Highly Selective Catalytic Conversion Of Phenolic Bio-oil To Alkanes. *Angewandte Chemie (International ed. in English)* **2009**, *48* (22), 3987–3990.

[181] Stein, S. E. Mass Spectra. *NIST Chemistry WebBook, NIST Standard Reference Database Number 69*.

[182] Mohler, F. L.; Dibeler, V. H.; Williamson, L.; Dean, H. Mass Spectra Of Deuteroacetylene, Monodeuterobenzene, And Deuteronaphthalenes. *Journal of Research of the National Bureau of Standards* **1952**, *48* (3), 188–192.

[183] Saavedra, J.; Doan, H. A.; Pursell, C. J.; Grabow, L. C.; Chandler, B. D. The Critical Role Of Water At The Gold-titania Interface In Catalytic CO Oxidation. *Science* **2014**, *345* (6204), 1599–1602.

[184] Campbell, C. T. The Energetics Of Supported Metal Nanoparticles: Relationships To Sintering Rates And Catalytic Activity. *Accounts of chemical research* **2013**, *46* (8), 1712–1719.

[185] Morgan, B.; Watson, G. A Density Functional Theory+ U Study Of Oxygen Vacancy Formation At The (110),(100),(101), And (001) Surfaces Of Rutile TiO2. *The Journal of Physical Chemistry C* **2009**, N. 110, 7322–7328.

[186] Saavedra, J.; Doan, H. A.; Pursell, C. J.; Grabow, L. C.; Chandler, B. D. The Critical Role Of Water At The Gold-titania Interface In Catalytic CO Oxidation. *Science* **2014**, *345*, 1599–1602.

[187] Farberow, C. A.; Dumesic, J. A.; Mavrikakis, M. Density Functional Theory Calculations And Analysis Of Reaction Pathways For Reduction Of Nitric Oxide By Hydrogen On Pt(111). *ACS Catalysis* **2014**, *4* (111), 3307–3319.

[188] Hong, D.-Y.; Miller, S. J.; Agrawal, P. K.; Jones, C. W. Hydrodeoxygenation And Coupling Of Aqueous Phenolics Over Bifunctional Zeolite-supported Metal Catalysts. *Chem. Commun.* **2010**, *46* (7), 1038–1040.

[189] Romero, Y.; Richard, F.; Renème, Y.; Brunet, S. Hydrodeoxygenation Of Benzofuran And Its Oxygenated Derivatives (2,3-dihydrobenzofuran And 2-ethylphenol) Over NiMoP/Al2O3 Catalyst. *Applied Catalysis A: General* **2009**, *353* (1), 46–53.

[190] Elliott, D. C.; Hart, T. R. Catalytic Hydroprocessing Of Chemical Models For Bio-oil. *Energy & Fuels* **2009**, *23* (2), 631–637.

[191] Bunch, A. Y.; Wang, X.; Ozkan, U. S. Adsorption Characteristics Of Reduced Mo And Ni–Mo Catalysts In The Hydrodeoxygenation Of Benzofuran. *Applied Catalysis A: General* **2008**, *346* (1-2), 96–103.

[192] Zhao, H. Y.; Li, D.; Bui, P.; Oyama, S. T. Hydrodeoxygenation Of Guaiacol As Model Compound For Pyrolysis Oil On Transition Metal Phosphide Hydroprocessing Catalysts. *Applied Catalysis A: General* **2011**, *391* (1-2), 305–310.

[193] Massoth, F. E.; Politzer, P.; Concha, M. C.; Murray, J. S.; Jakowski, J.; Simons, J. Catalytic Hydrodeoxygenation Of Methyl-substituted Phenols: Correlations Of Kinetic Parameters With Molecular Properties. *The journal of physical chemistry. B* **2006**, *110* (29), 14283–14291.

[194] El-Sharkawy, E.-S. A. Non Aqueous Titration And Catalytic Conversion Of Cyclohexanol As A Test Of Surface Acidity. *Monatshefte für Chemie - Chemical Monthly* **2006**, *137* (12), 1487–1498.

[195] Martin, D.; Duprez, D. Evaluation Of The Acid-base Surface Properties Of Several Oxides And Supported Metal Catalysts By Means Of Model Reactions. *Journal of Molecular Catalysis A: Chemical* **1997**, *118* (1), 113–128.

[196] Datka, J.; Gil, B.; Vog, O.; Rakoczy, J. *Porous materials in environmentally friendly pocesses, Proceedings of the 1st international FEZA conference*; Studies in Surface Science and Catalysis; Elsevier, 1999; Vol. 125.

[197] Sajiki, H.; Ito, N.; Esaki, H.; Maesawa, T.; Maegawa, T.; Hirota, K. Aromatic Ring Favorable And Efficient H–D Exchange Reaction Catalyzed By Pt/C. *Tetrahedron Letters* **2005**, *46* (41), 6995–6998.

[198] Ito, N.; Watahiki, T.; Maesawa, T.; Maegawa, T.; Sajiki, H. Synergistic Effect Of A Palladium-on-Carbon/Platinum-on-Carbon Mixed Catalyst In Hydrogen/Deuterium Exchange Reactions Of Alkyl-Substituted Aromatic Compounds. *Advanced Synthesis & Catalysis* **2006**, *348* (9), 1025–1028.

[199] Moreau, C.; Aubert, C.; Durand, R.; Zmimita, N.; Geneste, P. Structure-activity Relationships In Hydroprocessing Of Aromatic And Heteroaromatic Model Compounds Over Sulphided NiO-MoO3/γ-Al2O3 And NiO-WO3/ Γ -Al2O3 Catalysts; Chemical Evidence For The Existence Of Two Types Of Catalytic Sites. *Catalysis Today* **1988**, *4* (1), 117–131.

[200] Lu, J.; Heyden, A. Theoretical Investigation Of The Reaction Mechanism Of The Hydrodeoxygenation Of Guaiacol Over A Ru(0001) Model Surface. *Journal of Catalysis* **2015**, *321*, 39–50.

[201] An, K.; Alayoglu, S.; Musselwhite, N.; Plamthottam, S.; Melaet, G.; Lindeman, A. E.; Somorjai, G. A. Enhanced CO Oxidation Rates At The Interface Of Mesoporous Oxides And Pt Nanoparticles. *Journal of the American Chemical Society* **2013**, *135* (44), 16689–16696.

[202] Hensley, A. J. R.; Wang, Y.; McEwen, J.-S. Adsorption Of Phenol On Fe (110) And Pd (111) From First Principles. *Surface Science* **2014**, *630*, 244–253.

[203] Zhu, X.; Lobban, L. L.; Mallinson, R. G.; Resasco, D. E. Bifunctional Transalkylation And Hydrodeoxygenation Of Anisole Over A Pt/HBeta Catalyst. *Journal of Catalysis* **2011**, *281* (1), 21–29.

[204] Zhu, X.; Nie, L.; Lobban, L. L.; Mallinson, R. G.; Resasco, D. E. Efficient Conversion Of M‑Cresol To Aromatics On A Bifunctional Pt/HBeta Catalyst. *Energy & Fuels* **2014**, *28*, 4104–4111.

[205] Behtash, S.; Lu, J.; Faheem, M.; Heyden, A. Solvent Effects On The Hydrodeoxygenation Of Propanoic Acid Over Pd(111) Model Surfaces. *Green Chemistry* **2014**, *16* (2), 605.

[206] Green, D. W.; Perry, R. H. *Perry's Chemical Engineering's Handbook*; McGraw-Hill: New

York, 2008.

[207] Boullosa-Eiras, S.; Lødeng, R.; Bergem, H.; Stöcker, M.; Hannevold, L.; Blekkan, E. A. Catalytic Hydrodeoxygenation (HDO) Of Phenol Over Supported Molybdenum Carbide, Nitride, Phosphide And Oxide Catalysts. *Catalysis Today* **2014**, *223*, 44–53.

[208] Conley, B. L.; Pennington-Boggio, M. K.; Boz, E.; Williams, T. J. Discovery, Applications, And Catalytic Mechanisms Of Shvo's Catalyst. *Chemical reviews* **2010**, *110* (4), 2294–2312.

[209] Arce-Ramos, J.-M.; Grabow, L. C.; Handy, B. E.; Cárdenas-Galindo, M.-G. Nature Of Acid Sites In Silica-Supported Zirconium Oxide: A Combined Experimental And Periodic DFT Study. *The Journal of Physical Chemistry C* **2015**, *119* (27), 15150–15159.

[210] Hensley, A. J. R.; Hong, Y.; Zhang, R.; Zhang, H.; Sun, J.; Wang, Y. Enhanced Fe2O3 Reducibility Via Surface Modi Fi Cation With Pd: Characterizing The Synergy Within Pd / Fe Catalysts For Hydrodeoxygenation Reactions. *ACS Catalysis* **2014**, *4*, 3381–3392.

[211] Merte, L. R.; Peng, G.; Bechstein, R.; Rioboldt, F.; Farberow, C. A.; Grabow, L. C.; Kudernatsch, W.; Wendt, S.; Laegsgaard, E.; Mavrikakis, M.; Besenbacher, F. Water-mediated Proton Hopping On An Iron Oxide Surface. *Science* **2012**, *336* (May), 889–893.

[212] Coq, B.; Bittar, A.; Figueras, F. Hydrogenolysis And Isomerization Of Alkanes On Ru/Al2O3 Catalysis Of Varying Dispersions. *Applied Catalysis* **1990**, *59* (1), 103–121.

[213] Komaya, T.; Bell, A. T.; Wengsieh, Z.; Gronsky, R.; Engelke, F.; King, T. S.; Pruski, M. Effects Of Dispersion And Metal-Metal Oxide Interactions On Fischer-Tropsch Synthesis Over Ru/Tio2 And Tio2-Promoted Ru/Sio2. *Journal of Catalysis*. 1994, pagg 400–406.

[214] de Souza, P. M.; Nie, L.; Borges, L. E. P.; Noronha, F. B.; Resasco, D. E. Role Of Oxophilic Supports In The Selective Hydrodeoxygenation Of M-Cresol On Pd Catalysts.

Catalysis Letters **2014**, *144* (12), 2005–2011.

[215] Climent, M. J.; Corma, A.; Iborra, S. Conversion Of Biomass Platform Molecules Into Fuel Additives And Liquid Hydrocarbon Fuels. *Green Chemistry* **2014**, *16* (2), 516.

[216] Hong, Y.; Zhang, H.; Sun, J.; Ayman, K. M.; Hensley, A. J. R.; Gu, M.; Engelhard, M. H.; McEwen, J.-S.; Wang, Y. Synergistic Catalysis Between Pd And Fe In Gas Phase Hydrodeoxygenation Of M -Cresol. *ACS Catalysis* **2014**, *4* (10), 3335–3345.

[217] Ammal, S. C.; Heyden, A. Origin Of The Unique Activity Of Pt/TiO2 Catalysts For The Water–gas Shift Reaction. *Journal of Catalysis* **2013**, *306*, 78–90.

[218] Zhao, C.; Kasakov, S.; He, J.; Lercher, J. A. Comparison Of Kinetics, Activity And Stability Of Ni/HZSM-5 And Ni/Al2O3-HZSM-5 For Phenol Hydrodeoxygenation. *Journal of Catalysis* **2012**, *296*, 12–23.

[219] He, J.; Zhao, C.; Lercher, J. a. Impact Of Solvent For Individual Steps Of Phenol Hydrodeoxygenation With Pd/C And HZSM-5 As Catalysts. *Journal of Catalysis* **2014**, *309*, 362–375.

[220] Yoosuk, B.; Tumnantong, D.; Prasassarakich, P. Unsupported MoS2 And CoMoS2 Catalysts For Hydrodeoxygenation Of Phenol. *Chemical Engineering Science* **2012**, *79*, 1–7.

[221] Zhao, C.; Yu, Y.; Jentys, A.; Lercher, J. A. Understanding The Impact Of Aluminum Oxide Binder On Ni/HZSM-5 For Phenol Hydrodeoxygenation. *Applied Catalysis B: Environmental* **2013**, *132-133*, 282–292.

[222] Ren, H.; Yu, W.; Salciccioli, M.; Chen, Y.; Huang, Y.; Xiong, K.; Vlachos, D. G.; Chen, J. G. Selective Hydrodeoxygenation Of Biomass-derived Oxygenates To Unsaturated Hydrocarbons Using Molybdenum Carbide Catalysts. *ChemSusChem* **2013**, *6* (5), 798–

801.

[223] de Souza, P. M.; Rabelo-Neto, R. C.; Borges, L. E. P.; Jacobs, G.; Davis, B. H.; Sooknoi, T.; Resasco, D. E.; Noronha, F. B. Role Of Keto Intermediates In The Hydrodeoxygenation Of Phenol Over Pd On Oxophilic Supports. *ACS Catalysis* **2015**, *5* (2), 1318–1329.

[224] Campbell, C. T. The Energetics Of Supported Metal Nanoparticles: Relationships To Sintering Rates And Catalytic Activity. *Accounts of chemical research* **2013**, *46* (8), 1712–1719.

[225] Wang, Y.; Ren, J.; Deng, K.; Gui, L.; Tang, Y. Preparation Of Tractable Platinum, Rhodium, And Ruthenium Nanoclusters With Small Particle Size In Organic Media. *Chemistry of Materials* **2000**, *12* (6), 1622–1627.

[226] Coq, B.; Figueras, F. Structure–activity Relationships In Catalysis By Metals: Some Aspects Of Particle Size, Bimetallic And Supports Effects. *Coordination Chemistry Reviews* **1998**, *178-180*, 1753–1783.

[227] Ojeda, M.; Li, A.; Nabar, R.; Nilekar, A. U.; Mavrikakis, M.; Iglesia, E. Kinetically Relevant Steps And H 2 /D 2 Isotope Effects In Fischer−Tropsch Synthesis On Fe And Co Catalysts. *The Journal of Physical Chemistry C* **2010**, *114* (46), 19761–19770.

[228] Resasco, D. E.; Haller, G. L. A Model Of Metal-oxide Support Interaction For Rh On TiO2. *Journal of Catalysis* **1983**, *82* (2), 279–288.

[229] Lam, Y. L.; Sinfelt, J. H. Cyclohexane Conversion On Ruthenium Catalysts Of Widely Varying Dispersion. *Journal of Catalysis* **1976**, *42* (2), 319–322.

[230] Madon, R. J.; Reyes, S. C.; Iglesia, E. Primary And Secondary Reaction Pathways In Ruthenium-catalyzed Hydrocarbon Synthesis. *The Journal of Physical Chemistry* **1991**, *95*

(20), 7795–7804.

[231] Blakely, D. W.; Somorjai, G. A. The Dehydrogenation And Hydrogenolysis Of Cyclohexane And Cyclohexene On Stepped (high Miller Index) Platinum Surfaces. *Journal of Catalysis* **1976**, *42* (2), 181–196.

[232] Shi, H.; Li, X.; Haller, G. L.; Gutiérrez, O. Y.; Lercher, J. A. Active Sites And Reactive Intermediates In The Hydrogenolytic Cleavage Of C–C Bonds In Cyclohexane Over Supported Iridium. *Journal of Catalysis* **2012**, *295*, 133–145.

[233] Bond, G. C.; Yide, X. Hydrogenolysis Of Alkanes. Part 1.—Hydrogenolysis Of Ethane, Propane And N-butane On 6 Percent Pt/SiO2(EUROPT-1). *Journal of the Chemical Society, Faraday Transactions 1* **1984**, *80* (4), 969.

[234] Bond, G. C.; Rajaram, R. R.; Burch, R. Hydrogenolysis Of Propane, N-butane, And Isobutane Over Variously Pretreated Ruthenium/titanium Dioxide Catalysts. *The Journal of Physical Chemistry* **1986**, *90* (20), 4877–4881.

[235] Ammal, S. C.; Heyden, A. Nature Of Pt N/TiO2 (110) Interface Under Water-Gas Shift Reaction Conditions: A Constrained Ab Initio Thermodynamics Study. *The Journal of Physical Chemistry C* **2011**, *2* (110), 19246–19259.

[236] Schädel, B. T.; Duisberg, M.; Deutschmann, O. Steam Reforming Of Methane, Ethane, Propane, Butane, And Natural Gas Over A Rhodium-based Catalyst. *Catalysis Today* **2009**, *142* (1-2), 42–51.

[237] Xu, Y.; Lausche, A. C.; Wang, S.; Khan, T. S.; Abild-Pedersen, F.; Studt, F.; Nørskov, J. K.; Bligaard, T. In Silico Search For Novel Methane Steam Reforming Catalysts. *New Journal of Physics* **2013**, *15*, 1–18.

[238] Jones, G.; Jakobsen, J. G.; Shim, S. S.; Kleis, J.; Andersson, M. P.; Rossmeisl, J.; Abild-

Pedersen, F.; Bligaard, T.; Helveg, S.; Hinnemann, B.; Rostrup-Nielsen, J. R.; Chorkendorff, I.; Sehested, J.; Nørskov, J. K. First Principles Calculations And Experimental Insight Into Methane Steam Reforming Over Transition Metal Catalysts. *Journal of Catalysis* **2008**, *259*, 147–160.

[239] Maestri, M.; Vlachos, D. G.; Beretta, A.; Forzatti, P.; Groppi, G.; Tronconi, E. Dominant Reaction Pathways In The Catalytic Partial Oxidation Of CH4 On Rh. *Topics in Catalysis* **2009**, *52*, 1983–1988.

[240] Aboul-Gheit, A. K.; El-Masry, M. S.; Awadallah, A. E. Oxygen Free Conversion Of Natural Gas To Useful Hydrocarbons And Hydrogen Over Monometallic Mo And Bimetallic Mo–Fe, Mo–Co Or Mo–Ni/HZSM-5 Catalysts Prepared By Mechanical Mixing. *Fuel Processing Technology* **2012**, *102*, 24–29.

[241] Catapan, R. C.; Oliveira, A. A. M.; Chen, Y.; Vlachos, D. G. DFT Study Of The Water − Gas Shift Reaction And Coke Formation On Ni (111) And Ni (211) Surfaces. *The Journal of Physical Chemistry C* **2012**, *116* (111), 20281–20291.

[242] Tan, P.; Leung, Y.; Lai, S.; Au, C. Methane Aromatization Over 2 Wt% Mo/HZSM-5 In The Presence Of O2 And NO. *Catalysis letters* **2002**, *78* (March), 251–258.

[243] Pakhare, D.; Spivey, J. A Review Of Dry (CO2) Reforming Of Methane Over Noble Metal Catalysts. *Chem. Soc. Rev.* **2014**, *43*, 7813–7837.

[244] Nørskov, J. K.; Bligaard, T.; Rossmeisl, J.; Christensen, C. H. Towards The Computational Design Of Solid Catalysts. *Nature Chemistry* **2009**, *1*, 37–46.

[245] Nørskov, J. K.; Bligaard, T.; Hvolbaek, B.; Abild-Pedersen, F.; Chorkendorff, I.; Christensen, C. H. The Nature Of The Active Site In Heterogeneous Metal Catalysis. *Chemical Society reviews* **2008**, *37* (10), 2163–2171.

[246] Valden, M.; Pere, J.; Xiang, N.; Pessa, M. Influence Of Preadsorbed Oxygen On Activated Chemisorption Of Methane On Pd(110). *Chemical Physics Letters* **1996**, *257* (3-4), 289–296.

[247] Maestri, M.; Vlachos, D. G.; Beretta, A.; Groppi, G.; Tronconi, E. A C1 Microkinetic Model For Methane Conversion To Syngas On Rh/Al2O3. *AIChE* **2009**, *55*, 993–1008.

[248] Yoo, J. S.; Khan, T. S.; Abild-pedersen, F.; Nørskov, J. K.; Studt, F.; Road, S. H.; Park, M. On The Role Of The Surface Oxygen Species During A-H (A = C, N, O) Bond Activation: A Density Functional Theory Study. *Chem. Commun.* **2015**, *51*, 2621–2624.

[249] Shustorovich, E.; Bell, A. T. Oxygen-assisted Cleavage Of O-H, N-H, And C-H Bonds On Transition Metal Surfaces: Bond-order-conservation-Morse-potential Analysis. *Surface Science* **1992**, *268*, 397–405.

[250] Krishnan, G.; Wise, H. Interaction Of Methane And Carbon Monoxide With Oxygen Adspecies On Ni(111). *Applied Surface Science* **1989**, *37*, 244–249.

[251] Quinlan, A.; Wood, B. J.; Wise, H. Detection Of Surface Intermediates In The Oxidation Of Methane On Ni(100) By Electron Energy Loss Spectroscopy. *Chemical Physics Letters* **1985**, *118*, 478–480.

[252] Grabow, L. C.; Gokhale, A. A.; Evans, S. T.; Dumesic, J. A.; Mavrikakis, M. Mechanism Of The Water Gas Shift Reaction On Pt: First Principles, Experiments, And Microkinetic Modeling. *Journal of Physical Chemistry C* **2008**, *112*, 4608–4617.

[253] Zhu, Y. A.; Chen, D.; Zhou, X. G.; Yuan, W. K. DFT Studies Of Dry Reforming Of Methane On Ni Catalyst. *Catalysis Today* **2009**, *148* (3-4), 260–267.

[254] Shetty, S.; Jasen, A. P. J.; Santen, R. A. Direct Versus Hydrogen-assisted CO Dissociation. *J Am Chem Soc* **2009**, *131*, 12874.

[255] Chen, Y.; Vlachos, D. G. Density Functional Theory Study Of Methane Oxidation And Reforming On Pt(111) And Pt(211). *Ind. Eng. Chem. Res.* **2012**, *51*, 12244–12252.

[256] Xu, Y.; Lausche, A. C.; Wang, S.; Khan, T. S.; Abild-Pedersen, F.; Studt, F.; Nørskov, J. K.; Bligaard, T. In Silico Search For Novel Methane Steam Reforming Catalysts. *New Journal of Physics* **2013**, *15* (12), 125021.

[257] Kahle, L. C. S.; Roussière, T.; Maier, L.; Delgado, K. H.; Wasserschaff, G.; Schunk, S. A.; Deutschmann, O. Methane Dry Reforming At High Temperature And Elevated Pressure: Impact Of Gas-phase Reactions. *Industrial and Engineering Chemistry Research* **2013**, *52* (34), 11920–11930.

[258] Medford, A. J.; Shi, C.; Hoffmann, M. J.; Lausche, A. C.; Fitzgibbon, S. R.; Bligaard, T.; Nørskov, J. K. CatMAP: A Software Package For Descriptor-Based Microkinetic Mapping Of Catalytic Trends. *Catalysis Letters* **2015**, 794–807.

[259] Mhadeshwar, A.; Vlachos, D. Microkinetic Modeling For Water-promoted CO Oxidation, Water-gas Shift, And Preferential Oxidation Of CO On Pt. *The Journal of Physical Chemistry B* **2004**, *108*, 15246–15258.

[260] Medford, A. J.; Lausche, A. C.; Abild-Pedersen, F.; Temel, B.; Schjødt, N. C.; Nørskov, J. K.; Studt, F. Activity And Selectivity Trends In Synthesis Gas Conversion To Higher Alcohols. *Topics in Catalysis* **2013**, *57*, 135–142.

[261] Lausche, A. C.; Falsig, H.; Jensen, A. D.; Studt, F. Trends In The Hydrodeoxygenation Activity And Selectivity Of Transition Metal Surfaces. *Catalysis Letters* **2014**, *144* (11), 1968–1972.

[262] Hummelshøj, J. S.; Abild-Pedersen, F.; Studt, F.; Bligaard, T.; Nørskov, J. K. CatApp: A Web Application For Surface Chemistry And Heterogeneous Catalysis. *Angewandte*

Chemie **2012**, *51* (1), 272–274.

[263] Rohrbach, A.; Hafner, J.; Kresse, G. Ab Initio Study Of The (0001) Surfaces Of Hematite And Chromia: Influence Of Strong Electronic Correlations. *Physical Review B* **2004**, *70* (12), 125426.

[264] Jiang, T.; Mowbray, D. J.; Dobrin, S.; Falsig, H.; Hvolbœk, B.; Bligaard, T.; Nørskov, J. K. Trends In CO Oxidation Rates For Metal Nanoparticles And Close-packed, Stepped, And Kinked Surfaces. *Journal of Physical Chemistry C* **2009**, *113* (111), 10548–10553.

[265] Sun, J.; Thybaut, J.; Marin, G. Microkinetics Of Methane Oxidative Coupling. *Catalysis Today* **2008**, *137* (1), 90–102.

[266] van Santen, R. A.; Ghouri, M.; Hensen, E. M. J. Microkinetics Of Oxygenate Formation In The Fischer-Tropsch Reaction. *Physical chemistry chemical physics : PCCP* **2014**, *16* (21), 10041–10058.

[267] Lausche, A. C.; Hummelshoj, J. S.; Abild-Pedersen, F.; Studt, F.; Norskov, J. K. Application Of A New Informatics Tool In Heterogeneous Catalysis: Analysis Of Methanol Dehydrogenation On Transition Metal Catalysts For The Production Of Anhydrous Formaldehyde. *Journal of Catalysis* **2012**, *291*, 133–137.

[268] Liu, B.; Greeley, J. Density Functional Theory Study Of Selectivity Considerations For C–C Versus C–O Bond Scission In Glycerol Decomposition On Pt(111). *Topics in Catalysis* **2012**, *55* (5-6), 280–289.

[269] Dissanayake, D.; Rosynek, M. P.; Kharas, K. C. C.; Junsford, J. H. Partial Oxidation Of Methane To Carbon Monoxide And Hydrogen Over A Ni/Al2O3 Catalyst. *Journal of Catalysis* **1991**, *132* (1), 117–127.

[270] Schwiedernoch, R.; Tischer, S.; Correa, C.; Deutschmann, O. Experimental And

Numerical Study On The Transient Behavior Of Partial Oxidation Of Methane In A Catalytic Monolith. *Chemical Engineering Science* **2003**, *58* (3-6), 633–642.

[271] Delgado, K. H.; Maier, L.; Tischer, S.; Zellner, A.; Stotz, H.; Deutschmann, O. Surface Reaction Kinetics Of Steam- And CO2-Reforming As Well As Oxidation Of Methane Over Nickel-Based Catalysts. *Catalysts* **2015**, *5* (2), 871–904.

[272] Hickman, D. A.; Schmidt, L. D. Production Of Syngas By Direct Catalytic Oxidation Of Methane. *Science* **1993**, *259* (5093), 343–346.

[273] Ferreira-Aparicio, P. Mechanistic Aspects Of The Dry Reforming Of Methane Over Ruthenium Catalysts. *Applied Catalysis A: General* **2000**, *202*, 183–196.

[274] Zhu, T.; van Grootel, P. W.; Filot, I. A. W.; Sun, S.-G.; Santen, R. A. van; Hensen, E. J. M. Microkinetics Of Steam Methane Reforming On Platinum And Rhodium Metal Surfaces. *Journal of Catalysis* **2013**, *297*, 227–235.

Appendix

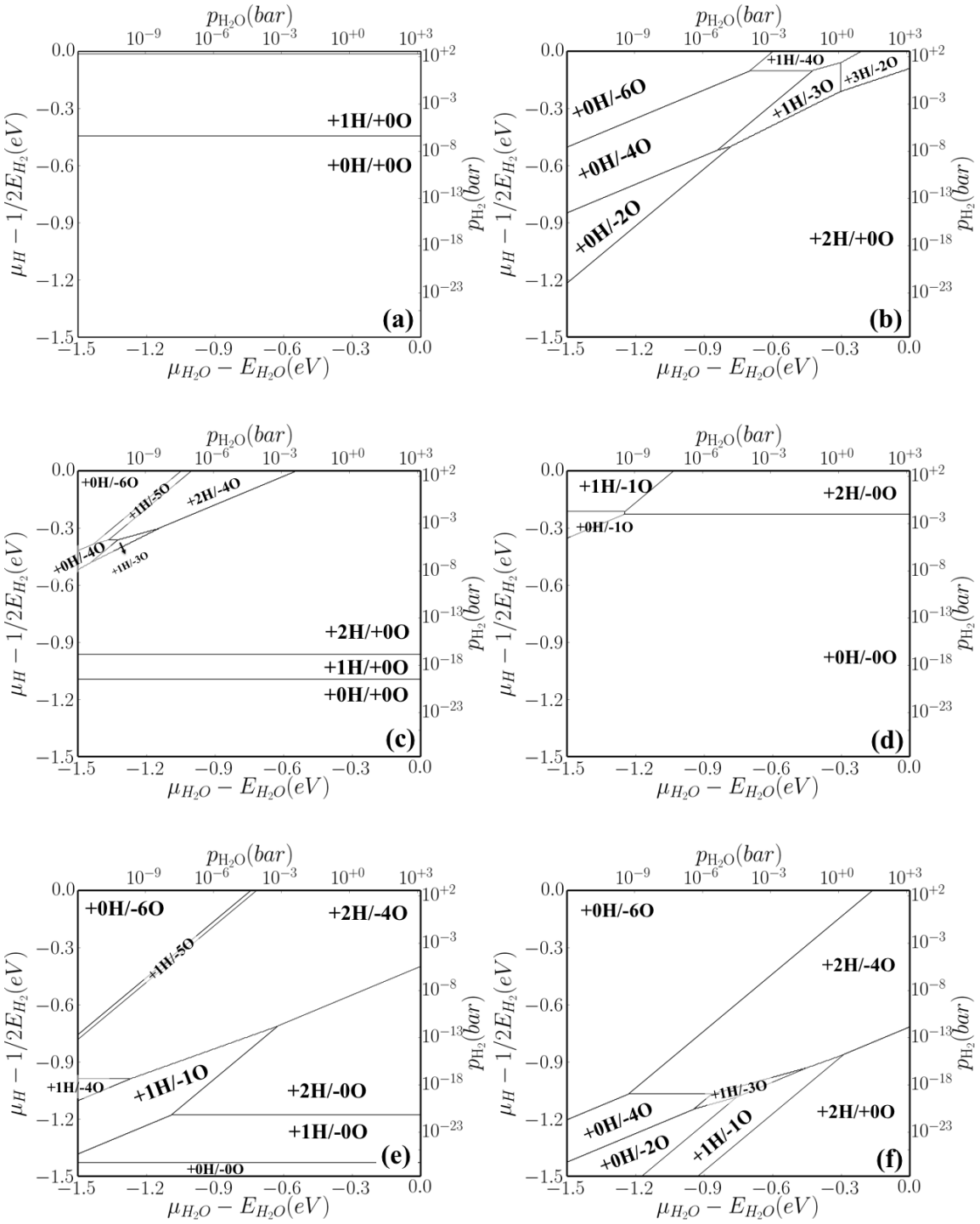

A-Figure 1. Thermodynamic phase diagram for (a) TiO_2, (b) RhO_2, (c) IrO_2, (d) VO_2, (e) PtO_2, and (f) PdO_2 as a function of H_2 and H_2O chemical potentials at T= 500 K.

A-Table 1. Slope and y-axis intercept for linear correlations.

Ref Figure 2-2	Color in Figure 2-2	Coordinate	Linear correlation	R^2
(a)	Blue	+0H/-6O	$E = 6.58\Delta E_v+5.51$	0.96
(b)	Green	+1H/-5O	$E = 6.10\Delta E_v+4.31$	0.96
	Blue	+0H/-5O	$E = 5.48\Delta E_v+4.07$	0.96
(c)	Red	+2H/-4O	$E = 5.66\Delta E_v+3.19$	0.95
	Green	+1H/-4O	$E = 4.96\Delta E_v+2.86$	0.96
	blue	+0H/-4O	$E = 4.42\Delta E_v+2.50$	0.98
(d)	aquamarine	+3H/-3O	$E = 4.85\Delta Ev+2.66$	0.97
	red	+2H/-3O	$E = 4.37\Delta E_v+1.90$	0.96
	green	+1H/-3O	$E = 3.89\Delta E_v+1.45$	0.97
	blue	+0H/-3O	$E = 3.20\Delta E_v+1.74$	0.98
(e)	Cyan	+4H/-2O	$E = 3.96\Delta E_v+2.32$	0.99
	Aquamarine	+3H/-2O	$E = 3.69\Delta E_v+1.11$	0.98
	red	+2H/-2O	$E = 3.07\Delta E_v+1.09$	0.97
	Green	+1H/-2O	$E = 2.58\Delta E_v+0.67$	0.98
	Blue	+0H/-2O	$E = 2.16\Delta E_v+0.28$	0.99
(f)	Black	+5H/-1O	$E = 3.29\Delta E_v+2.27$	0.99
	cyan	+4H/-1O	$E = 2.94\Delta E_v+0.99$	0.99
	aquamarine	+3H/-1O	$E = 2.49\Delta E_v+0.22$	0.99
	Red	+2H/-1O	$E = 1.98\Delta E_v-0.33$	0.98
	green	+1H/-0O	$E = 1.53\Delta E_v-0.79$	0.99
(g)	Black	+6H/-0O	$E = 2.57\Delta E_v+2.38$	0.98
	Cyan	+5H/-0O	$E = 2.15\Delta E_v+1.00$	0.97
	aquamarine	+4H/-0O	$E = 1.76\Delta E_v-0.30$	0.97
	Red	+3H/-0O	$E = 1.36\Delta E_v-1.02$	0.97
	Green	+2H/-0O	$E = 0.95\Delta E_v-1.64$	0.95
	Blue	+1H/-0O	$E = 0.48\Delta E_v-0.93$	0.90

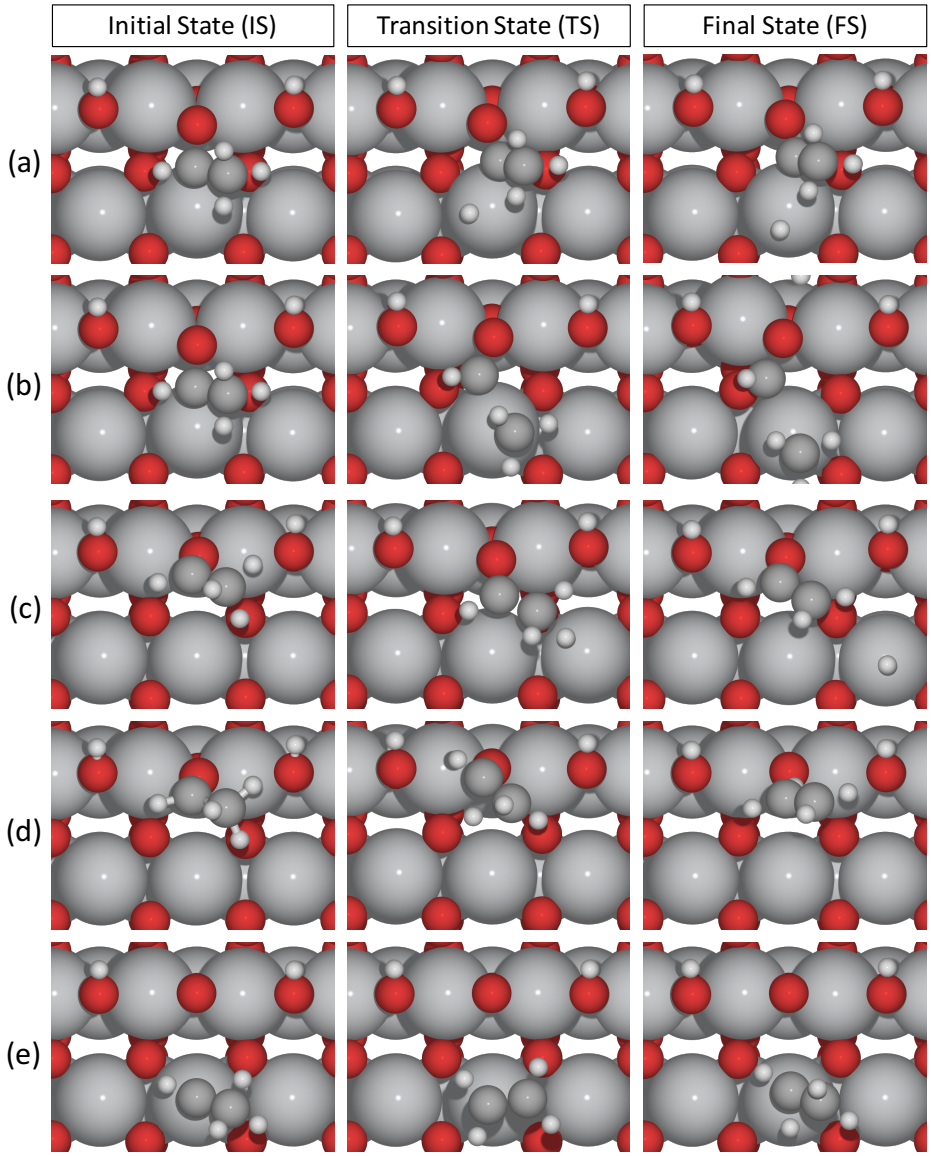

A-Figure 2. Calculated reaction pathways of CH_3CHO HDO on $TiO_2(110)$ (white – hydrogen / red – oxygen / gray – titanium / dark-gray - carbon). (a) $CH_3CHO^{br} \rightarrow CH_3CO^{br}\text{-}Ti^{cus} + H\text{-}Ti^{cus}$, isomerization; (b) $CH_3CHO^{br}\text{-}Ti^{cus} \rightarrow CH_3\text{-}Ti^{cus}{}_+CHO^{br}$; (c) $CH_3CHO^{br} + Ti^{cus} \rightarrow CH_2CHO^{br} + H\text{-}Ti^{cus}$; (d) $CH_3CHO^{br} \rightarrow CH_2CH_{2(g)} + O^{br}$; (e) $CH_3CH\text{-}Ti^{cus} \rightarrow CH_2CH_{2(g)} + Ti^{cus}$.

A-Table 2. List of energies and frequencies used for microkinetic modeling.

Surface	Site Name	Specie Name	ΔE / eV	Frequency / cm-1
None	gas	CO	2.740	[2170]
None	gas	H2	0.000	[4401]
None	gas	H2O	0.000	[3657, 1595, 3756]
None	gas	CH4	0.000	[2917,1534,1534,3019,3019,3019,1306,1306,1306]
None	gas	CO2	2.450	[1333,2349,667,667]
None	gas	O2	5.420	[1580]
Ni	211	H	-0.390	[801,838,986]
Cu	211	H	-0.090	[]
Pd	211	H	-0.400	[]
Pt	211	H	-0.350	[]
Ag	211	H	0.240	[]
Ir	211	H	-0.220	[]
Rh	211	H	-0.320	[]
Ru	211	H	-0.440	[]
Au	211	H	0.170	[]
Ni	211	CO	1.470	[44,144,208,260,280,2004]
Cu	211	CO	2.500	[]
Pd	211	CO	1.440	[]
Pt	211	CO	1.330	[]
Ag	211	CO	3.090	[]
Ir	211	CO	0.890	[]
Rh	211	CO	1.290	[]
Ru	211	CO	1.200	[]
Au	211	CO	2.800	[]
Ni	211	C-O	3.350	[363,449,453,516,579]
Cu	211	C-O	5.430	[]
Pd	211	C-O	4.510	[]
Pt	211	C-O	4.060	[]
Ag	211	C-O	7.860	[]
Rh	211	C-O	2.810	[]
Ru	211	C-O	2.740	[]
Au	211	C-O	8.170	[]
Ni	211	C	1.520	[267,563,576]
Cu	211	C	3.540	[]
Pd	211	C	1.510	[]
Pt	211	C	2.100	[]
Ag	211	C	5.070	[]
Ir	211	C	1.570	[]
Rh	211	C	1.380	[]
Ru	211	C	1.230	[]
Au	211	C	4.770	[]
Ni	211	OH	-0.500	[73,296,379,497,664,3843]

A-Table 2 continued

Cu	211	OH	-0.040	[]
Pd	211	OH	0.340	[]
Pt	211	OH	0.360	[]
Ag	211	OH	0.490	[]
Ir	211	OH	-0.400	[]
Rh	211	OH	-0.370	[]
Ru	211	OH	-0.690	[]
Au	211	OH	0.940	[]
Ni	211	CH	1.220	[354,396,410,632,668,2987]
Cu	211	CH	2.700	[]
Pd	211	CH	1.570	[]
Pt	211	CH	1.190	[]
Ag	211	CH	3.960	[]
Ir	211	CH	0.690	[]
Rh	211	CH	1.010	[]
Ru	211	CH	0.710	[]
Au	211	CH	3.430	[]
Ni	211	O	0.130	[309,398,437]
Cu	211	O	0.990	[]
Pd	211	O	1.500	[]
Pt	211	O	1.260	[]
Ag	211	O	1.880	[]
Ir	211	O	-0.110	[]
Rh	211	O	0.160	[]
Ru	211	O	-0.100	[]
Au	211	O	2.600	[]
Ag	211	O-O	5.340	[141,228,340,372,389]
Au	211	O-O	6.180	[]
Pt	211	O-O	4.900	[]
Pd	211	O-O	4.600	[]
Cu	211	HCO	2.750	[2866,1464,1216,558,375,187,127,108,96]
Pd	211	HCO	1.840	[]
Pt	211	HCO	1.790	[]
Ag	211	HCO	3.210	[]
Rh	211	HCO	1.830	[]
Au	211	HCO	2.880	[]
Ni	211	CH2	1.440	[148,209,396,431,451,672,1296,2976,3030]
Cu	211	CH2	2.350	[]
Pd	211	CH2	1.640	[]
Pt	211	CH2	1.210	[]
Ag	211	CH2	3.040	[]
Ir	211	CH2	1.160	[]
Rh	211	CH2	1.330	[]
Ru	211	CH2	1.170	[]

A-Table 2 continued

Au	211	CH2	2.650	[]
Ni	211	CH3	0.930	[12,101,111,301,495,588,1099,1365,1380,2967,3043,3088]
Cu	211	CH3	1.300	[]
Pd	211	CH3	0.920	[]
Pt	211	CH3	0.550	[]
Ag	211	CH3	1.600	[]
Ir	211	CH3	0.650	[]
Rh	211	CH3	0.840	[]
Ru	211	CH3	0.730	[]
Au	211	CH3	1.350	[]
Cu	211	H-H	0.780	[12,493,654,1187,1224]
Pd	211	H-H	0.120	[]
Pt	211	H-H	0.190	[]
Au	211	H-H	1.150	[]
Cu	211	CO-H	4.300	[35,204,394,386,435,667,1277,1583]
Pd	211	CO-H	2.590	[]
Pt	211	CO-H	2.500	[]
Ag	211	CO-H	5.300	[]
Rh	211	CO-H	2.900	[]
Cu	211	C-H	4.310	[227,496,527,812,1127]
Pd	211	C-H	2.250	[]
Pt	211	C-H	3.060	[]
Ag	211	C-H	5.990	[]
Rh	211	C-H	1.970	[]
Ru	211	C-H	1.740	[]
Au	211	C-H	5.780	[]
Ni	211	CH-H	1.930	[256,353,382,620,759,834,1231,3019]
Cu	211	CH-H	3.270	[]
Pd	211	CH-H	2.050	[]
Pt	211	CH-H	2.350	[]
Ag	211	CH-H	4.740	[]
Rh	211	CH-H	1.540	[]
Ru	211	CH-H	1.070	[]
Au	211	CH-H	4.580	[]
Ni	211	CH2-H	1.730	[12,123,377,450,569,676,836,1297,1408,2971,3039]
Cu	211	CH2-H	2.870	[]
Pd	211	CH2-H	1.950	[]
Pt	211	CH2-H	1.530	[]
Ag	211	CH2-H	3.990	[]
Rh	211	CH2-H	1.440	[]
Ru	211	CH2-H	1.430	[]
Au	211	CH2-H	3.450	[]
Ni	211	CH3-H	1.270	[12,86,102,282,371,677,753,1091,1327,1380,1398,3018,3117,3160]
Cu	211	CH3-H	1.940	[]

A-Table 2 continued

Pd	211	CH3-H	1.130	[]
Pt	211	CH3-H	1.060	[]
Ag	211	CH3-H	2.490	[]
Rh	211	CH3-H	1.080	[]
Ru	211	CH3-H	1.060	[]
Au	211	CH3-H	2.230	[]
Ni	211	O-H	0.680	[188,293,421,583,1071]
Cu	211	O-H	1.630	[]
Pd	211	O-H	1.750	[]
Pt	211	O-H	1.600	[]
Ag	211	O-H	2.800	[]
Ir	211	O-H	0.600	[]
Rh	211	O-H	0.730	[]
Ru	211	O-H	0.270	[]
Au	211	O-H	3.180	[]
Ni	211	H-OH	0.350	[51,141,184,327,486,790,1613,3805]
Cu	211	H-OH	0.800	[]
Pd	211	H-OH	0.820	[]
Pt	211	H-OH	0.720	[]
Ag	211	H-OH	1.390	[]
Ir	211	H-OH	0.240	[]
Rh	211	H-OH	0.490	[]
Ru	211	H-OH	-0.010	[]
Au	211	H-OH	1.820	[]
Ni	211	O-HOH	0.330	[50,110,233,302,425,427,629,683,14339,1496,3870]
Cu	211	O-HOH	0.920	[]
Pd	211	O-HOH	1.830	[]
Pt	211	O-HOH	1.560	[]
Ag	211	O-HOH	1.860	[]
Ir	211	O-HOH	0.370	[]
Rh	211	O-HOH	0.450	[]
Ru	211	O-HOH	-0.100	[]
Au	211	O-HOH	2.900	[]
Cu	211	H-CO	3.110	[1871,1676,499,413,56,148,193,220]
Pd	211	H-CO	1.970	[]
Pt	211	H-CO	1.850	[]
Ag	211	H-CO	3.700	[]
Rh	211	H-CO	1.820	[]
Au	211	H-CO	3.300	[]
Cu	211	H-HCO	3.200	[2918,1658,1558,1185,871,699,376,188,175,56]
Pd	211	H-HCO	2.470	[]
Pt	211	H-HCO	2.120	[]
Ag	211	H-HCO	3.740	[]
Rh	211	H-HCO	1.850	[]

A-Table 2 continued

Cu	211	HC-O	5.090	[92,208,359,405,490,787,1019,3054]
Pt	211	HC-O	4.770	[]
Ag	211	HC-O	6.970	[]
Rh	211	HC-O	3.290	[]
Ru	211	HC-O	2.590	[]
Au	211	HC-O	7.290	[]
Cu	211	COOH	2.590	[3614,1772,1147,851,582,575,352,241]
Pd	211	COOH	1.960	[]
Pt	211	COOH	1.870	[]
Rh	211	COOH	1.670	[]
Cu	211	COO-H	3.910	[2058,1311,888,811,594,294,228]
Pd	211	COO-H	2.690	[]
Pt	211	COO-H	2.870	[]
Rh	211	COO-H	2.680	[]
Cu	211	OC-OH	3.000	[3810,2060,721,516,348,322,274,223]
Pd	211	OC-OH	2.940	[]
Pt	211	OC-OH	3.050	[]
Rh	211	OC-OH	2.480	[]
Ni	211	C-O-H	3.426	[322, 370,453,482,516,682,996,1595]
Pd	211	C-O-H	3.366	[]
Au	211	C-O-H	6.440	[]
Ni	211	CH3-HOH	1.195	[90,112,132,149,258,315,412,469,567,605,720,1073,1108,1375,1414,1466,2903,2974,3043,3655]
Pd	211	CH3-HOH	1.442	[]
Au	211	CH3-HOH	1.966	[]
Ni	211	CH2-HOH	1.518	[52,22,84,287,292,359,485,556,633,698,827,1070,1255,1470,2935,3040,3622]
Pd	211	CH2-HOH	2.366	[]
Au	211	CH2-HOH	3.071	[]
Ni	211	CH-HOH	2.141	[154,158,283,398,424,438,548,594,659,754,1041,1326,2734,3640]
Pd	211	CH-HOH	2.408	[]
Au	211	CH-HOH	4.488	[]
Ni	211	C-HOH	2.160	[76,265,354,405,448,501,670,724,1138,1310,3636]
Pd	211	C-HOH	2.581	[]
Au	211	C-HOH	5.356	[]
Cu	211	COH	3.560	[3689, 1273,1085,336,322,287,222,198,18]
Pd	211	COH	1.890	[]
Pt	211	COH	1.900	[]
Ag	211	COH	4.580	[]
Rh	211	COH	1.930	[]
Cu	211	C-OH	4.740	[87,165,359,547,581,633,707,4273]
Pd	211	C-OH	2.350	[]
Pt	211	C-OH	2.980	[]
Ag	211	C-OH	6.540	[]

A-Table 2 continued

Rh	211	C-OH	1.990	[]
Ni	211	CO-O	2.968	[27,171,240,292,329,381,557,671]
Cu	211	CO-O	4.118	[]
Pd	211	CO-O	4.192	[]
Pt	211	CO-O	3.728	[]
Ag	211	CO-O	5.299	[]
Rh	211	CO-O	2.759	[]
Ru	211	CO-O	2.551	[]
Au	211	CO-O	5.648	[]

A-Figure 3. Linear scaling correlation for the binding energies of surface intermediates and transition state energies with regard to binding energy of carbon (E_C) and oxygen (E_O).

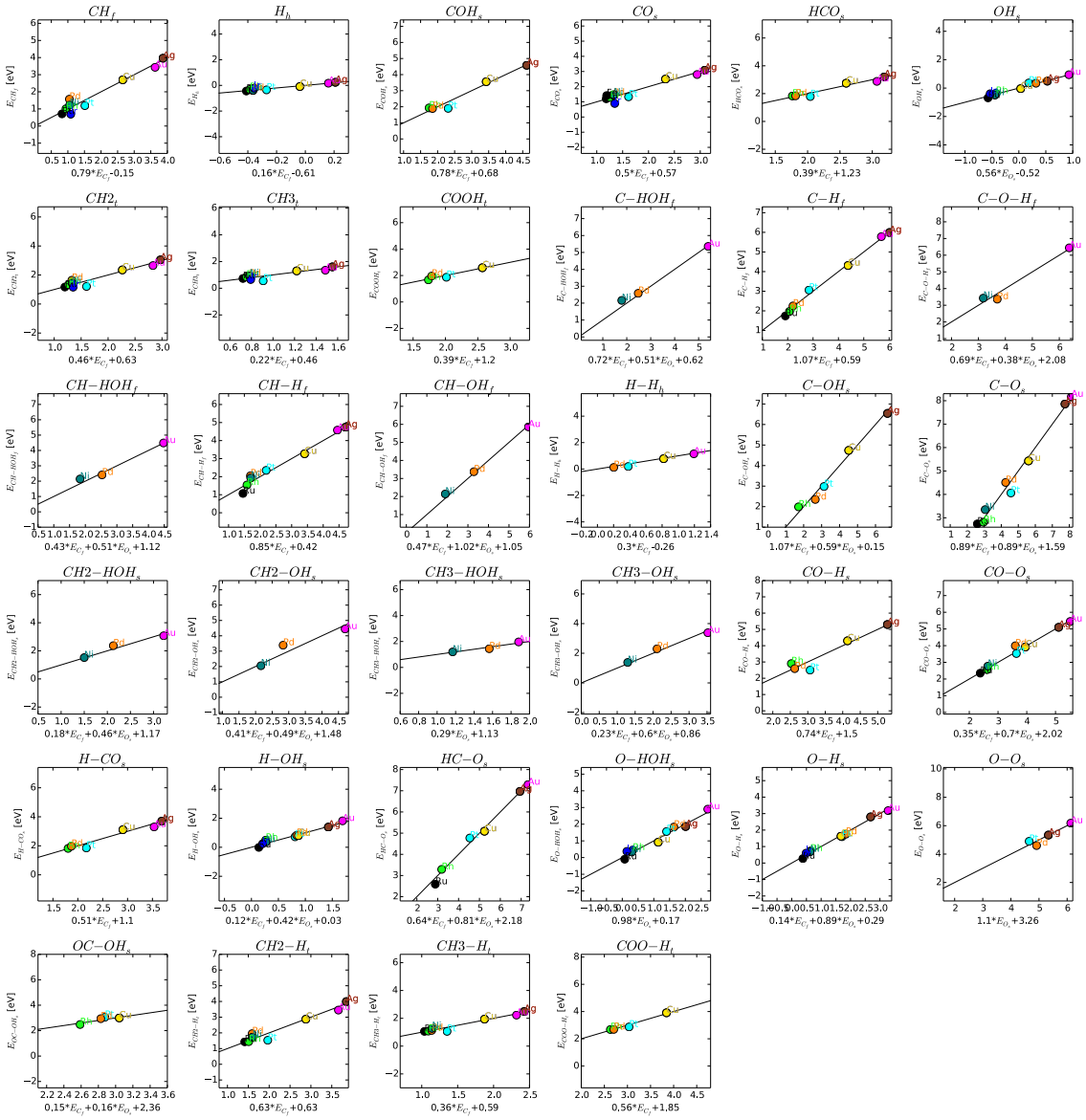

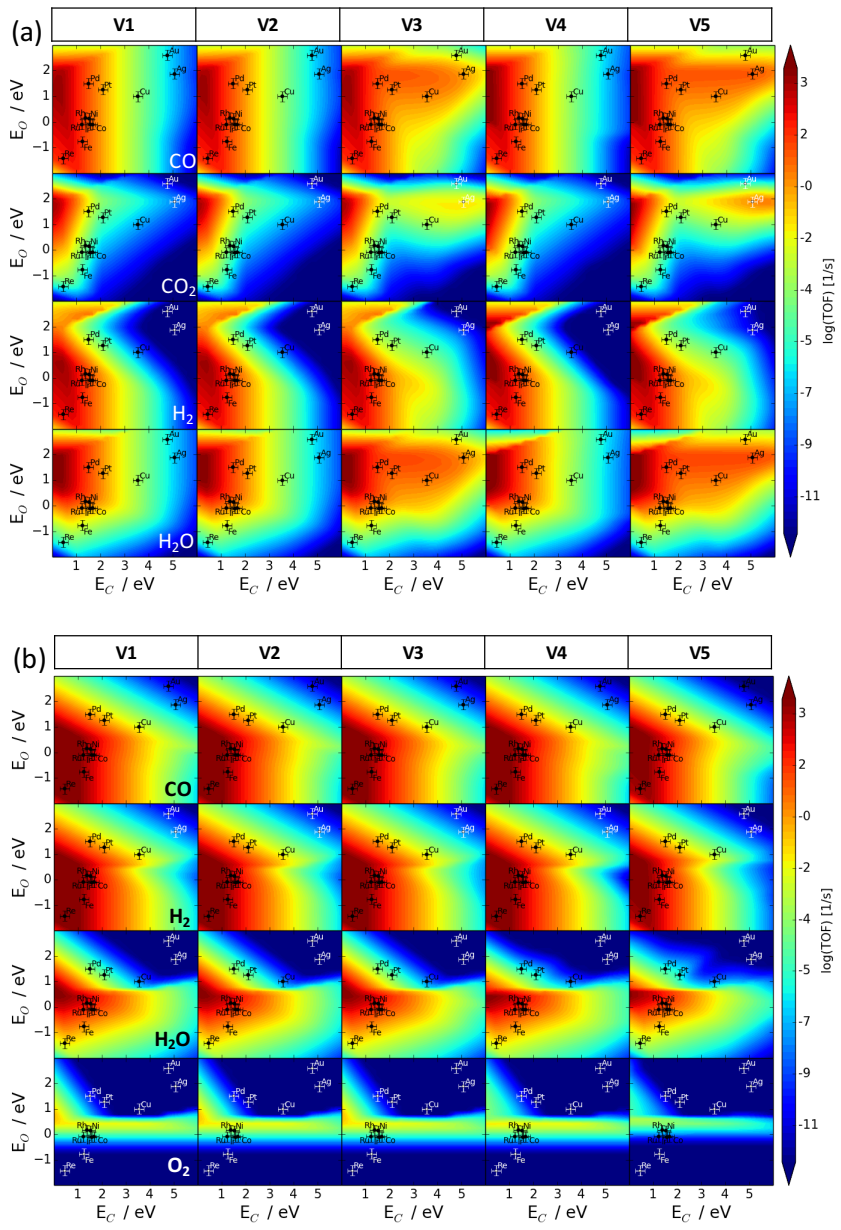

A-Figure 4. Calculated logarithmic turnover frequency (TOF): (a) complete oxidation of methane (COM) toward CO, CO_2, H_2, and H_2O. Reaction conditions are T = 750 K and p = 1.0 bar with CH_4/O_2 = 0.5; and (b) methane dry reforming (MDR) toward CO, H_2, H_2O, and O_2. Reaction conditions are T = 1000 K and p = 1.0 bar with CH_4/CO_2 = 1.